Czech Technical University in Prague
Faculty of Nuclear Sciences and Physical Engineering

Dissertation Thesis

Photoproduction of J/ψ in ultra-peripheral p-Pb and Pb-Pb collisions with the ALICE detector at the LHC

Prague, 2016

Jaroslav Adam

To Lenka, Jaroslav and Zuzana

Bibliografický záznam

Autor	Ing. Jaroslav Adam České vysoké učení technické v Praze Fakulta jaderná a fyzikálně inženýrská Katedra fyziky
Název práce	Fotoprodukce J/ψ v ultra-periferálních p-Pb a Pb-Pb srážkách v experimentu ALICE na LHC
Studijní program	Aplikace přírodních věd
Studijní obor	Jaderné inženýrství
Školitel	doc. RNDr. Vojtěch Petráček, CSc. České vysoké učení technické v Praze Fakulta jaderná a fyzikálně inženýrská Katedra fyziky
Školitel specialista	prof. Guillermo Contreras Nuno, Ph.D. České vysoké učení technické v Praze Fakulta jaderná a fyzikálně inženýrská Katedra fyziky
Akademický rok	2015/2016
Počet stran	192
Klíčová slova	QCD, fotoprodukce J/ψ, gluonová saturace, gluonové stínění, ultra-periferální srážky, ALICE

Bibliographic Entry

Author	Ing. Jaroslav Adam Czech Technical University in Prague Faculty of Nuclear Sciences and Physical Engineering Department of Physics
Title of Dissertation	Photoproduction of J/ψ in ultra-peripheral p-Pb and Pb-Pb collisions with the ALICE detector at the LHC
Degree Programme	Application of Natural Sciences
Field of Study	Nuclear Engineering
Supervisor	doc. RNDr. Vojtěch Petráček, CSc. Czech Technical University in Prague Faculty of Nuclear Sciences and Physical Engineering Department of Physics
Supervisor specialist	prof. Guillermo Contreras Nuno, Ph.D. Czech Technical University in Prague Faculty of Nuclear Sciences and Physical Engineering Department of Physics
Academic Year	2015/2016
Number of Pages	192
Keywords	QCD, J/ψ photoproduction, gluon saturation, gluon shadowing, ultra-peripheral collisions, ALICE

Abstrakt

V první části práce je shrnuta fyzikální problematika ultra-periferálních srážek společně se základními koncepty různých teoretických modelů. Měření fotoprodukce vektorových mezonů na protonech a jádrech olova umožňuje studium kvantově-chromodynamické struktury těchto objektů při energiích dříve nedosažitelných. Měření, výsledky, a fyzikální diskuse výsledků jsou popsány v následujících částech.

Cílem práce je prezentace analýzy koherentní fotoprodukce J/ψ v dopředné rapiditě v ultra-periferálních Pb-Pb srážkách a analýzy exkluzivní fotoprodukce J/ψ v ultra-periferálních p-Pb srážkách v dopředné, kvazi-dopředné a centrální rapiditě.

Osobním příspěvkem autora k analýze v Pb-Pb je určení účinnosti koherentních, nekoherentních a dvou-fotonových procesů a korekce pro feed-down. V analýzách v p-Pb přispěl autor přípravou a správou oficiálních a pomocných MC simulací pro všechny tři rapiditní intervaly, a s výjimkou určení luminozity autor provedl úplný rozsah analýz v kvazi-dopředné a centrální rapiditě.

Abstract

The physics of ultra-peripheral collisions is introduced in the first part along with the fundamental concepts of several theoretical models. The measurement of photoproduction of vector mesons off proton and lead nucleus allows to study the QCD structure of these targets at energies that have never been measured before. The next parts of the text describe the measurements, the results, and present the physics discussion of the results.

The aim of the thesis is to present the analysis of coherent J/ψ photoproduction in the forward rapidity in ultra-peripheral Pb-Pb collisions and the analysis of exclusive J/ψ photoproduction in ultra-peripheral p-Pb collisions in the forward, semi-forward and central rapidity.

The personal contribution of the author in the Pb-Pb analysis consists in the determination of the efficiency of coherent, incoherent and two-photon processes and computations of the feed-down correction. In the case of the p-Pb analyses, the author has prepared and managed the official and auxiliary MC productions for all three rapidity intervals, determined the efficiency and feed-down corrections for the forward rapidity, and, with the exception of

the luminosity calculation, conducted the full scope of the analyses in the semi-forward and central rapidities.

Declaration

I do solemnly declare that I have written the presented research thesis by myself under the direction of my supervisor and my supervisor specialist, and without the aid of unfair or unauthorized resources.

Jaroslav Adam

Acknowledgements

Foremost I express my great gratitude for the supervision by Guillermo Contreras and Vojtěch Petráček for their support, guidance and help in all aspects of this work.

Many thanks go to the ALICE UPC group, especially to Daniel Tapia Takaki, Eugenio Scapparone and Joakim Nystrand for their encouragement and helpful ideas they have patiently provided.

I would like to thank all my friends and colleagues for the stimulating atmosphere and the encouragement throughout my study, during research work or while supervising seminars.

Last but not least, I would like to thank my parents, my dearest wife and my beautiful kids for their support in my life.

Table of contents

Preface

Ultra-peripheral Collisions (UPC) are collision of highly accelerated protons or nuclei mediated by strong electromagnetic fields, allowing us to study interactions of photons with hadrons at high energies using proton or nuclei beams. At the LHC we can study phenomena accessible by photon-hadron interactions which were before measured at facilities with lepton beams, but now at unprecedentedly higher energies. The measurements at the LHC are also a very valuable input to specify the scientific agenda of future facilities being designed now.

The main physics motivation for the study of interactions of photons and hadrons is the measurement of the internal gluonic structure of hadrons, which is hard to describe theoretically due to its complexity. The UPC processes provide here very clean probes into special kinematic regions which cannot be reached by conventional hadronic interactions. Moreover, measurements of photon-photon interactions may reveal the existence of exotic particles and couplings, whose signatures could be hidden in the substantial background present in hadronic collisions.

The purpose of this thesis is to present in detail the analysis steps that were followed to produce ALICE results on coherent J/ψ photoproduction in Pb-Pb UPC [1] and exclusive J/ψ photoproduction in p-Pb [2], as well as to describe yet unpublished results on J/ψ photoproduction in p-Pb and the novel rapidity intervals now accessible by ALICE. The results from Pb-Pb UPC have put strong constraints on models for this process and can be considered as the first direct observation of gluon shadowing. The results from p-Pb UPC extended to more than twice higher energies than ever reached before in other accelerators, and offer one of the best measurements to look for gluon saturation in the proton. The impact of these results on our understanding of physics is discussed in Chapter 5 and Chapter 7 for Pb-Pb and p-Pb, respectively.

More in detail, the structure of this thesis is the following. In Chapter 1 a review of the physics mechanisms of photon-proton, photon-nucleus and photon-photon interactions is given. This chapter also includes a summary of previous experimental results on J/ψ photoproduction and the description of theoretical models for which predictions for LHC kinematics are available. Chapter 1 closes with a list of open problems and motivations for future studies of UPC physics.

Chapter 2 provides the reader with a description of the ALICE experiment focusing on aspects important for the UPC analyses to be described here. Besides the technical description of the apparatus, the overview of the collaboration organizational structure and the common workflow is presented.

The main experimental result, which may be compared to a theoretical prediction, is the cross section for a given physics process. Chapter 3 contains the description of the essential ingredients which are needed in order to calculate the experimental cross section. The general procedures how to obtain them are presented.

Chapter 4 is devoted to a detailed description of the analysis of coherent J/ψ photoproduction in Pb-Pb UPC at $\sqrt{s_{\rm NN}}$ = 2.76 TeV at the forward rapidity. (Natural units, $\hbar = c = 1$, will be used throughout the text.) This is followed by the physics discussion of coherent J/ψ photoproduction in Chapter 5, where the quality of agreement between predictions and measurements is presented, emphasizing the assumptions made by the models.

As the input data to the discussion, ALICE results from the forward rapidity and also from mid-rapidity will be used together with recent preliminary results made by the CMS collaboration.

In Chapter 6 there is a detailed description of the analysis of exclusive J/ψ photoproduction in p-Pb UPC at $\sqrt{s_{\rm NN}}$ = 5.02 TeV. The corresponding discussion of the physics results on J/ψ photoproduction in photon-proton interactions, presented in Chapter 7, concentrates on ALICE results and also on the model dependent results, so called solutions, provided by the LHCb experiment.

The conclusions, presented in Chapter 8, consist of qualitative remarks about UPC results by ALICE and other LHC experiments and their physics implications. The overview of the current status of the ALICE experiment and a proposal for future UPC studies is given. Appendices A – D contain technical and supplementary details to the presented analyses.

The measurements presented in this work have resulted in several publications which are listed in Appendix E.

Chapter 1

Physics of ultra-peripheral collisions

A mainly qualitative description of the physics processes occurring in ultra-peripheral collisions (UPC) will be given throughout this chapter, with special emphasis on the production mechanisms of the J/ψ mesons (bound state of the charm "c" quark and antiquark with mass $\sim$3 GeV) in photon-proton and photon-nucleus interactions, because these processes are the focus of the experimental results presented in the following sections. Excellent reviews of the physics of UPC are given in [3–6].

The essential requirement for a collision to be classified as an UPC is the presence of a strong electromagnetic field with the simultaneous suppression of hadronic processes mediated by the strong interaction. Such circumstances are achieved by selecting collisions with impact parameter larger than the sum of radii of the interacting particles. The situation is

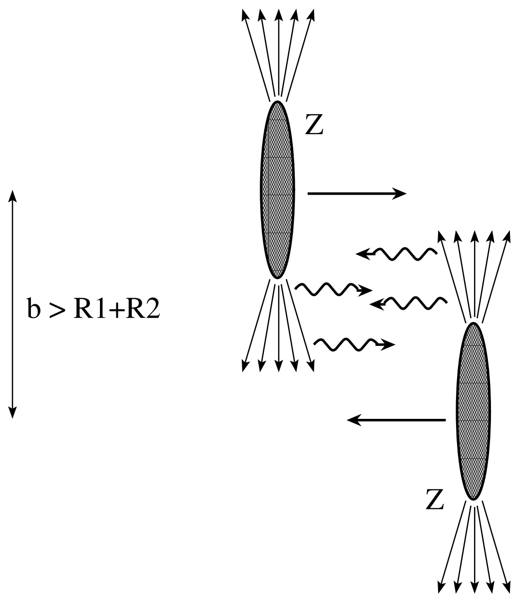

Fig. 1.1 Schematic view of an ultra-peripheral collision of relativistic nuclei.

shown in Fig. 1.1, where the two relativistically contracted nuclei of charge Ze and radii $R_{1,2}$ are passing each other at the impact parameter b. The electromagnetic field is concentrated in the direction perpendicular to the direction of movement and can be considered as a flux of virtual photons [7–9].

Besides the production of J/ψ, in photon-hadron interactions other heavy mesons (ψ' or Υ) or light mesons (ρ^0, ϕ and ω) or jets may be produced. Interactions of two photons may not only lead to lepton pair production driven by quantum electrodynamics, but also η_c or χ_{c0} or pairs of $W^{\pm}$ bosons can be produced. This is to illustrate that the field of UPC physics is very wide and particles in a wide range of mass can be studied. In the following, only the case of J/ψ photoproduction will be treated.

1.1 Interactions of photons and hadrons at high energies

In the UPC of two hadrons, the final state X can be produced in the interaction of a photon and a hadron (Fig. 1.2a) or by photon-photon interaction (Fig. 1.2b). The interactions are treated as interactions of individual photons on the target hadron or another photon, while the emission of photons by the source hadron is described by the flux of photons.

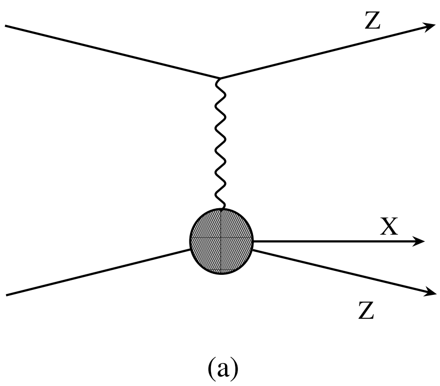

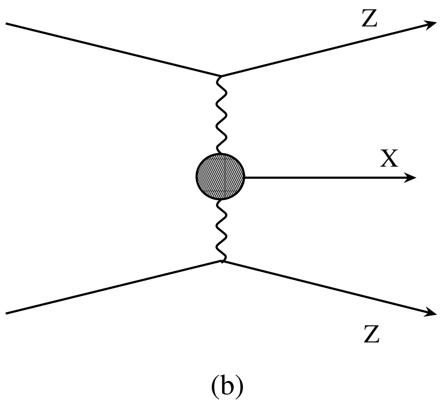

Fig. 1.2 Photon-hadron (1.2a) and photon-photon (1.2b) interactions.

1.1.1 Cross section of photoproduction reactions

The photoproduction cross section σ_X of a state X is given by

$$\sigma_X = \int d\omega \frac{n(\omega)}{\omega} \sigma_X^{\gamma}(\omega), \tag{1.1}$$

where $\sigma_X^{\gamma}(\omega)$ is the photon-nucleus photoproduction cross section and the flux of photons is expressed as the number of photons $n(\omega)$ with energy ω.

The two-photon processes are characterized by the simultaneous presence of two photon fluxes $n(\omega_1)$ and $n(\omega_2)$, the corresponding photoproduction cross section is

$$\sigma_X = \int d\omega_1 \omega_2 \frac{n(\omega_1)}{\omega} \frac{n(\omega_1)}{\omega} \sigma_X^{\gamma\gamma}(\omega_1, \omega_2), \tag{1.2}$$

where $\sigma_X^{\gamma\gamma}(\omega_1, \omega_2)$ is the two-photon cross section of the process $\gamma\gamma \rightarrow X$.

The energy of the photons is limited by the dimensions of the emitting source, because the wavelength of the photon cannot be lower than this size. If we imagine a static target irradiated by a photon from a passing ultra-relativistic nucleus, the maximal photon energy ω_{max} will be given by the Lorentz contraction of the nucleus,

$$\omega_{max} \approx \frac{\gamma_L}{R}, \tag{1.3}$$

where γ_L is the Lorentz factor of the nucleus. The nuclear radius, R, is approximately $R = 1.2A^{1/3}$[fm], where A is the nucleon number.

Although the photons in the diagrams in Fig. 1.2 are internal lines and therefore virtual, their virtuality is limited by the nuclear radius, $-q^2 \lesssim (1/R)^2$, and is negligible in ultra-relativistic UPC collisions. The photons can be treated as real and often they are called "quasi-real".

1.1.2 Probing the gluon distribution by virtual photons

The current theory of hadrons describes them as objects composed of the massive quarks, fermions with fractional electric charge, which are bound together by the massless field of the strong interaction. The strong interaction of individual quarks and gluons is described by perturbative Quantum Chromodynamics (QCD).

The hadron is a composition of virtual quarks and gluons too complicated to be accurately modeled up to the interaction of each individual quark and gluon. Instead, the notion of partons with a given density within the hadron is used [10].

In the infinite momentum frame, each parton contributes to the longitudinal momentum $\boldsymbol{p}$ of the hadron by its momentum fraction $x < 1$. The momentum of the parton is $\boldsymbol{k} = x\boldsymbol{p} + \boldsymbol{k_t}$ with $\boldsymbol{k_t}$ transversal to $\boldsymbol{p}$. Where m is the mass of the parton, the transversal mass is $m_\perp^2 = m^2 + k_t^2$.

The lifetime of the parton is constrained as $\tau_{\text{parton}} \sim 2k_z/m_\perp$. The longer living partons may form new partons of smaller momentum fractions x and cascades of partons develop in the hadron.

When the virtual photon of four-momentum q and virtuality $Q^2 = -q^2$ interacts with the hadron, interacts with a parton and the fraction of momentum carried by the parton is changed, $x \rightarrow x + x'$. The number of partons which are available for the interaction is described by the density function $F_i(x, Q^2)$, where i denotes the type of parton.

Due to the development of new parton cascades, the parton density increases with decreasing momentum fraction x. This is known from the extraction of F_i using DIS measurements from HERA [11, 12]. This rise would eventually violate the unitarity of the cross section, so at some point it has to be reduced. One mechanism to achive this within pQCD is to consider the interaction of partons in a recombination process first introduced in [13]. The amount of the reduction directly affects the cross section of photoproduction reactions.

The quasi-real photon γ at high energy can fluctuate into a pair of quark and antiquark, $\gamma \to q\bar{q}$. Due to the conservation of quantum numbers the photon fluctuates into a vector state. The wave function of the photon fluctuates in most cases to a vector meson. The wave function of the photon can be decomposed as [14]

$$|\gamma\rangle = c_0|\gamma_0\rangle + \sum_{V=\rho^0,\omega,\phi,J/\psi,\Upsilon} c_V|V\rangle + \sum c_q|q\bar{q}\rangle, \tag{1.4}$$

where $|\gamma_0\rangle$, $|V\rangle$ and $|q\bar{q}\rangle$ denote the wave function of the point-like photon, vector meson and quark-antiquark pair respectively, weighted by the coupling coefficients c_0, c_V and c_q. In the Vector Dominance Model (VDM) [15], the coefficients c_V are given as

$$c_V^2 = 4\pi\alpha_{\rm em}/f_V^2, \tag{1.5}$$

where $\alpha_{\rm em} = 1/137$ is the electromagnetic coupling constant and f_V is determined experimentally in terms of the mass of the meson M_V and the leptonic decay width $\Gamma_{V\to l^+l^-}$. In the case of the J/ψ, $f^2_{J/\psi}/4\pi = 11.5$ [5].

The factors c_V in Eq. (1.4) give the photon coupling to the particular vector meson V, but a correction is required to describe the elastic scattering on the hadronic target. The photon may fluctuate into a higher vector meson V' which makes, during the interaction, the transition into a lower meson V appearing in the final state.

With the hadronic target A, both processes $V'A \to VA$ (non-diagonal) and $VA \to VA$ (elastic) contribute to the cross section. The corresponding correction of the c_V is provided by the Generalized VDM (GVDM) [16].

If the quasi-real photon interacts with the hadron via the $|V\rangle$ component, elastic scattering on the gluon field of the hadron may occur, producing the vector meson V as a free particle which can be detected experimentally. In the case of the J/ψ, such interaction can be described by pQCD [17]. The leading order contribution is the exchange of two gluons in the color singlet state.

In conclusion, the cross section of J/ψ photoproduction in photon-nucleus/nucleon interactions ($X = J/\psi$ in Eq. (1.1)) depends on the gluon structure function $xg(x,Q^2)$ associated with the parton distribution function of gluons $g(x,Q^2)$ at the scale Q^2 where the scale is normally taken as $Q^2 \approx (M_{J/\psi}/2)^2$.

1.2 The flux of quasi-real photons

The idea of describing the electromagnetic field of a moving source by virtual photons was formulated for the first time by E. Fermi [7] in 1924, when he described the excitation of atoms by an electron beam. A relativistic generalization of the equivalent photon method was developed by Weizsäcker [8] and Williams [9].

If there is a projectile nucleus of atomic and mass numbers A_1, Z_1 passing at the speed $v \simeq 1$ along the static target nucleus A_2, Z_2 in the direction z at impact parameter b, the electromagnetic field of the projectile is [18]

$$\begin{aligned} E_z &= -Z_1 e \gamma_L v t / [b^2 + \gamma_L^2 v^2 t^2]^{3/2} \\ \boldsymbol{E_T} &= -Z_1 e \gamma_L \boldsymbol{b} / [b^2 + \gamma_L^2 v^2 t^2]^{3/2} \\ \boldsymbol{B_T} &= \boldsymbol{v} \times \boldsymbol{E_T}, \text{ and } B_z = 0, \end{aligned} \tag{1.6}$$

where $\gamma_L = (1 - v^2)^{-1/2}$ and T denotes the direction perpendicular to z.

The situation is shown in Fig. 1.3. The collective vibration of the nuclear charges and the equivalent pulses of radiation are shown. The pulses are the plane-polarized electromagnetic radiation projected to the target in the direction parallel to the projectile (P1) and perpendicular (P2) to it.

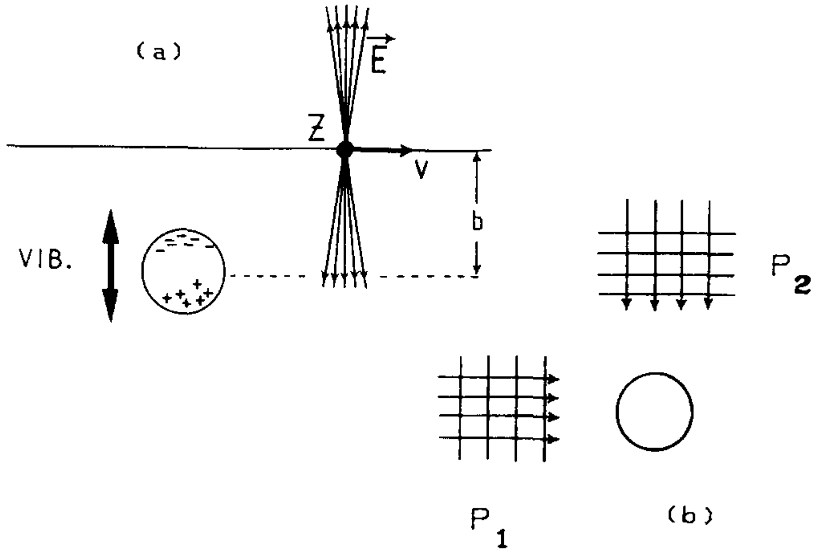

Fig. 1.3 Electromagnetic field projected to the static target by the ultra-relativistic charge (a) and corresponding plane waves (b) [18].

Applying the Fourier transform on the time-varying fields $\boldsymbol{E}$ and $\boldsymbol{B}$ in Eq. (1.6), we are left with the amount of energy projected to the target per unit of area in terms of the frequency spectrum of the field,

$$I(\omega, b) = (1/4\pi) |\boldsymbol{E}(\omega) \times \boldsymbol{B}(\omega)|. \tag{1.7}$$

Probability for an electromagnetic process of the cross section $\sigma_\gamma(\omega)$ to be generated by an equivalent pulse of light for the photon energy $E_\gamma = \hbar\omega$ is

$$P(b) = \int I(\omega,b)\sigma_\gamma(\hbar\omega)\mathrm{d}(\hbar\omega) = \int N(\omega,b)\sigma_\gamma(\omega)\frac{\mathrm{d}\omega}{\omega}, \tag{1.8}$$

where the integral runs over the full frequency spectrum of the virtual radiation. By the quantity $N(\omega,b)$ we have introduced the flux of the virtual photons as the number of equivalent photons incident on the target per unit area.

Putting the Fourier transforms of Eq. (1.6) into Eq. (1.7) and using the definition in Eq. (1.8), we obtain the virtual photon flux as

$$N(\omega,b) = \frac{Z_1^2\alpha_{\mathrm{em}}\omega^2}{\pi^2\gamma_L^2 v^2}\left[K_1^2(x) + \frac{1}{\gamma_L^2}K_0^2(x)\right], \tag{1.9}$$

where $K_{0,1}$ are the modified Bessel functions and $x = \omega b/\gamma_L v$. The term with K_1^2 gives the flux of the transversally polarized photons, dominating in the ultra-relativistic limit. The flux drops exponentially at $\omega > \gamma_L v/b$, which corresponds to the kinematic relation in Eq. (1.3).

The flux at an impact parameter b in Eq. (1.9) is related to the flux $n(\omega)$ in the cross section in Eq. (1.1) by $n(\omega) = \int 2\pi b N(\omega,b)\mathrm{d}b$. If we integrate over $b > b_{\mathrm{min}} = R_1 + R_2$ with $R_A = 1.2A^{1/3}$fm (hard-sphere approximation), we get

$$n(\omega) = \frac{2Z_1^2\alpha_{\mathrm{em}}}{\pi\beta^2}\left[\xi K_0(\xi)K_1(\xi) - \frac{\xi^2}{2}\left(K_1^2\xi - K_0^2\xi\right)\right], \tag{1.10}$$

where $\xi = \omega b_{\mathrm{min}}/\gamma_L v$.

Following the equations for the flux, we may make two observations. First, the flux is proportional to the square power of the projectile electric charge Z_1^2 due to the nature of Eq. (1.7), and, second, the energy of the projectile translates into the flux via the Lorentz factor γ_L of the projectile.

1.3 Exclusive photoproduction of J/ψ

From now on, we will deal with the exclusive photoproduction of J/ψ on protons or nuclei. The J/ψ is the only new particle in the final state, the colliding protons or nuclei remain intact. The J/ψ is detected via its dilepton decay, $J/\psi \to l^+l^-$, with l for electron or muon. The leptons are the only final products of the collision and can be measured in an experimental apparatus in order to reconstruct the kinematics of the J/ψ.

The polarization of the J/ψ affects the angular distribution of the decay leptons of the J/ψ which then has consequences for the acceptance of the experimental apparatus. As the quasi-real virtual photons are predominantly transversely polarized, also the J/ψ has mainly transversal polarization. The angular distribution of the leptons is in this case given by

$$\frac{\mathrm{d}n}{\mathrm{d}\cos\theta} = 1 + \cos^2(\theta), \tag{1.11}$$

where θ is the polar angle of the positive lepton in the rest frame of the J/ψ, given with respect to the flight direction of the J/ψ in the centre-of-mass of the colliding beams (the helicity frame [19]).

1.3.1 Photoproduction of J/ψ in photon-proton interactions

The photoproduction reaction on a proton target may leave the proton intact in the so-called elastic interaction, or the proton may dissociate into a low-mass system, or the proton may break with transfer of color in the inelastic collision case. We will deal now with the elastic photoprodution process: $\gamma\mathrm{p} \to J/\psi\,\mathrm{p}$.

The elastic photoproduction of the J/ψ meson in proton-Pb interactions is shown in Fig. 1.4. The photon γ is most likely produced by the Pb-ion because of the charge-squared proportionality of the photon flux (Section 1.2), the pair of virtual $c\bar{c}$ quarks interact with the gluon parton distribution function of the proton and a J/ψ meson is produced.

The kinematical description of the process in Fig. 1.4 is provided by the square of the center-of-mass energy of proton and lead ion s, the center-of-mass energy of photon and proton $W_{\gamma\mathrm{p}}$, the absolute value of the four-momentum transfer squared at the Pb-γ vertex Q^2, and the four-momentum transfer squared of the proton t. In the elastic photoproduction, the values of Q^2 and t are small and usually the proton and Pb-ion are not detected by the experimental apparatus.

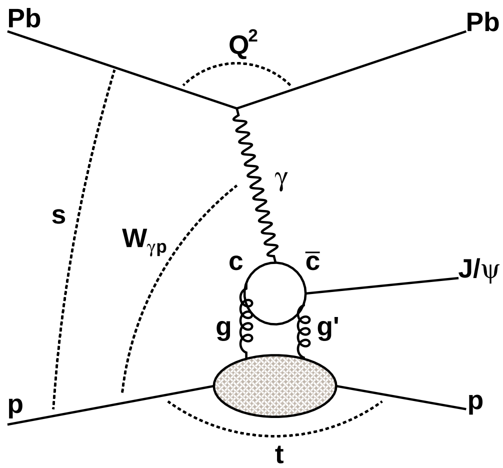

Fig. 1.4 Elastic J/ψ photoproduction in ultra-peripheral p-Pb collision.

Experimental observables of the J/ψ are the transverse momentum p_T (transversal to the direction of the proton beam) and the rapidity of the J/ψ. The p_T is related to t as $t \simeq -p_T^2$. The rapidity variable y can be calculated using the J/ψ four-momentum p as

$$y = \frac{1}{2}\ln((p_0+p_z)/(p_0-p_z)). \tag{1.12}$$

For any particle fulfill the high-energy limit $p \gg m$ where m is the rest mass of the particle, the rapidity of such a particle becomes equal to the pseudorapidity $\eta = -\ln \tan \theta/2$, where θ is the polar angle relative to the axis of the beam.

Because the J/ψ is the only produced particle, the photon-proton center-of-mass energy $W_{\gamma\mathrm{p}}$ can be reconstructed by the rapidity of the J/ψ:

$$W_{\gamma\mathrm{p}}^2 = 2E_p M_{J/\psi}\exp(-y), \tag{1.13}$$

where E_p is the energy of the proton beam and $M_{J/\psi}$ is the mass of the J/ψ.

In terms of perturbative QCD, the photoproduction in Fig. 1.4 is described by the exchange of a colourless system of the gluons g and g'. The cross section in the leading logarithmic (LO) approximation, at zero momentum transfer $t = 0$ and negligible photon virtuality is [17, 20]

$$\left.\frac{\mathrm{d}\sigma}{\mathrm{d}t}(\gamma\mathrm{p} \to J/\psi\mathrm{p})\right|_{t=0} = \frac{\Gamma_{ee}\pi^3\alpha_\mathrm{s}^2}{3M_{J/\psi}\alpha_\mathrm{em}}\left[xg(x,Q^2)\right]^2, \tag{1.14}$$

where Γ_{ee} is the width of the dielectron decay, α_s is the strong coupling constant, $Q^2 = M_{J/\psi}^2/4$ and $xg(x,Q^2)$ is the gluon parton distribution function.

As we can see, the cross section given by Eq. (1.14) depends on the square power of the gluon distribution.

Given the cross section at $t = 0$, the t-dependence of the cross section follows the exponential proportionality

$$\frac{\mathrm{d}\sigma}{\mathrm{d}t} = A\exp(-bt) \tag{1.15}$$

with the slope parameter b measured experimentally.

The momentum fraction of the proton, x, probed by the J/ψ in the elastic photoproduction is

$$x = \left(\frac{M_{J/\psi}}{W_{\gamma\mathrm{p}}}\right)^2, \tag{1.16}$$

or

$$x = \left(\frac{M_{J/\psi}}{\sqrt{s}}\right) \exp(-y) \tag{1.17}$$

using the beams center-of-mass energy $\sqrt{s}$ and rapidity y of the J/ψ.

Having the relation between $W_{\gamma p}$ and x, we can probe $xg(x, Q^2)$ at different x by measuring the cross section of $\gamma p \to J/\psi p$ at various $W_{\gamma p}$.

However, there are two gluons interacting with the proton gluon distribution, as shown in Fig. 1.4 where the gluons g and g' are coupled to the shaded area representing the gluon distribution.

Each gluon may carry a different momentum fraction and therefore the cross section in Eq. (1.14) is in fact proportional to the generalized (or skewed or off-diagonal) gluon distribution. Nonetheless, for this process the standard gluon distribution can be used, provided that a correction factor is included [21].

The measurement of the cross section of photoproduction off protons is of interest both for different $W_{\gamma p}$ and also with different final vector mesons, since these allow to constrain the gluon distribution over different range in x and also at different scales Q^2.

1.3.2 Photoproduction of J/ψ in coherent photon-nucleus interactions

The photoproduction on a nuclear target follows the same kinematics as shown in Fig. 1.4, but here the photon may couple coherently to the whole nucleus without resolving the internal structure, leading to coherent photoproduction, or the photon may couple to a single nucleon resulting in incoherent photoproduction.

The nucleus normally breaks-up after incoherent photoproduction. In this case the nucleus gets excited and normally breaks-up emitting forward neutrons. For the coherent case, in a few cases, an independent soft electromagnetic interaction may dissociate one of the nucleus, producing also one or few forward neutrons.

The main distinction between the coherent and incoherent processes is the transverse momentum p_T of the J/ψ. The mean value of the p_T is inversely proportional to the transverse size of the target, leaving substantially lower p_T for the coherent photoproduction ($\langle p_T \rangle \simeq 60$MeV) than for the incoherent ($\langle p_T \rangle \simeq 500$MeV).

The coherent photoproduction cross section depends on the nuclear gluon distribution in a similar manner as the photon-proton cross section on the proton gluon distribution. The calculation of the cross section at zero momentum transfer ($t = 0$) may be based on Eq. (1.14) with explicit notion of the gluon distribution, or may use the parametrization of the photon-proton cross section followed by the generalization to the nucleus.

The dependence of the coherent cross section on the momentum transfer t is determined by the nuclear form-factor $F(t)$, which is the Fourier transform of the nuclear density distribution. Starting with the cross section at $t = 0$, the t-dependence is

$$\frac{\mathrm{d}\sigma_{\gamma\mathrm{A}\to J/\psi\mathrm{A}}}{\mathrm{d}t} = |F(t)|^2 \left.\frac{\mathrm{d}\sigma_{\gamma\mathrm{A}\to J/\psi\mathrm{A}}}{\mathrm{d}t}\right|_{t=0}. \tag{1.18}$$

The measurement of the coherent cross section of $\gamma\mathrm{A} \to J/\psi\mathrm{A}$ provides not only a constraint to the nuclear gluon distribution at the x and Q^2 given by the experiment, but also to its relation to the proton gluon distribution, allowing us to extract the modification of the gluon distribution from the proton to the more complex system of the nucleus.

1.3.3 Two photon production of dilepton pairs

Since the exclusive production of J/ψ mesons in elastic photon-proton or coherent photon-nucleus interactions is measured in the dilepton decay of the J/ψ, $J/\psi \to l^+l^-$ with l^+l^- standing for e^+e^- or $\mu^+\mu^-$ the process of exclusive dilepton production in photon-photon interactions, $\gamma\gamma \to l^+l^-$, will contribute to the signal of the J/ψ. The $\gamma\gamma$ interaction may also lead to a $(C = \text{even})$ meson, or a pair of mesons in the final state.

Moreover, the two-photon processes are a probe to many aspects of the Standard Model, covering quantum electrodynamics (QED) by the dielectron and dimuon production, $\gamma\gamma \to \mu^+\mu^-$ and $\gamma\gamma \to e^+e^-$ and electroweak theory in two-photon production of the W-mesons, $\gamma\gamma \to W^+W^-$. Dilepton production in the $\gamma\gamma$ interactions may be used to measure the beam luminosity or to extract the efficiency of the particular trigger aimed for exclusive events with dilepton decay of the J/ψ.

The production of a fermion pair (quarks or leptons) in a $\gamma\gamma$ interaction, at the lowest order of the QED, is shown in Fig. 1.5. With m_f the mass of the fermion, the invariant mass of the $\gamma\gamma$ system $\sqrt{s}$ should be above the threshold $\sqrt{s} > 2m_f$.

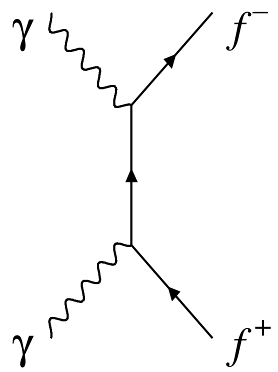

Fig. 1.5 Fermion pair production in $\gamma\gamma$ interaction in the lowest order QED [5].

The cross section of dilepton production in lowest order QED is given by [5]

$$\sigma(\gamma\gamma \to l^+l^-) = \frac{\pi\alpha_{\mathrm{em}^2}}{4s}\beta\left[\frac{3-\beta^4}{2\beta}\ln\frac{1+\beta}{1-\beta} - 2 + \beta^2\right], \tag{1.19}$$

where $\beta = \sqrt{1-4m_l^2/s}$ is the velocity of the lepton in the rest frame of the $\gamma\gamma$ system.

Since the cross section in Eq. (1.19) is inversely proportional to the square of the mass of the lepton, the production cross section of heavier pairs ($\mu^+\mu^-$ and $\tau^+\tau^-$) is much lower than for e^+e^-.

1.4 Previous experimental results on J/ψ photoproduction

The first measurements of photoproduction of J/ψ were performed using photon beams incident on fixed targets of liquid nitrogen or deuterium, or on solid targets of carbon and beryllium.

The first high energy photoproduction measurement has been reported in [22]. The beam of bremsstrahlung photons of 5.5 GeV, produced by the Cambridge electron accelerator, was incident on the hydrogen and carbon targets. Pairs of charged π mesons were detected using the spectrometer capable of measuring the angles and momenta. The spectrometer measured the di-pions in the range of invariant mass of $0.3 < M_{\pi^+\pi^-} < 1.5$ GeV, showing a clear signal of elastically produced ρ mesons (Fig. 1.6). The hypothesis of transversal polarization of the photoproduced ρ mesons (Eq. (1.11)) was confirmed by this experiment.

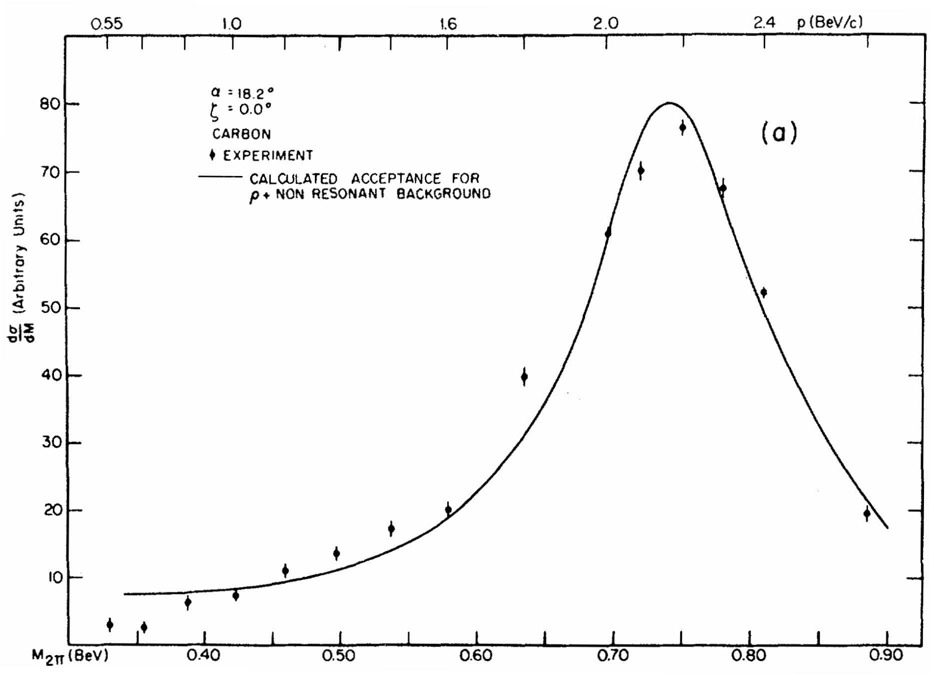

Fig. 1.6 Photoproduction of ρ mesons by a 5.5 GeV photon beam on a carbon target. The units of BeV are equivalent to GeV [22].

The first experiments measuring the photoproduction of J/ψ used the beams of bremsstrahlung photons incident on hydrogen, deuterium or beryllium targets. Review of these results is given in [23].

A wide variety of experiments worked with photon beams of energies up to 55 GeV. The J/ψ mesons were reconstructed via the $\mu^+\mu^-$ and e^+e^- decays with electrons and muons reconstructed in spectrometers or Čerenkov or scintillator hodoscopes. All of the production modes, coherent, incoherent, elastic and inelastic were measured using proton, neutron (in deuterium) and hadronic targets.

The cross section of $\gamma N \to J/\psi N$ at zero momentum transfer ($t = 0$) was used to test the Vector Dominance Model (Section 1.1.2), the dependence of the cross section on the momentum transfer, $\mathrm{d}\sigma/\mathrm{d}t$, justified the exponential parametrization in Eq. (1.15), see Fig. 1.7. As an important result it was quoted that the production from neutron and proton targets were similar.

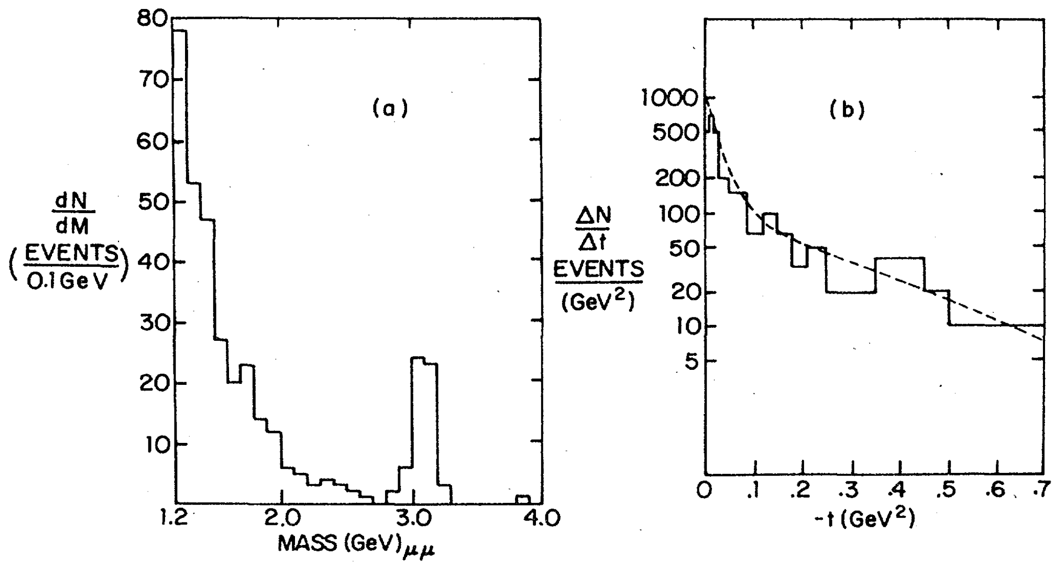

Fig. 1.7 J/ψ photoproduction in photon-berylium interactions. (a) Invariant mass distribution of the dimuons showing clear peak of the J/ψ around 3 GeV. (b) Measured t distribution of events in (a) with invariant mass $2.8 < M_{\mu\mu} < 3.4$ GeV. The peak at low values of |t| is clear evidence for coherent photoproduction of J/ψ [23].

Later the energy of photons was extended up to 300 GeV. Measurements of J/ψ photoproduction from liquid hydrogen and deuterium targets are reported in [24]. Further tests of the transversal polarization of J/ψ and of the exponential parametrization of $\mathrm{d}\sigma/\mathrm{d}t$ were done, and the dependence of the cross section on the photon energy was studied. Elastic photoproduction was extracted via the measurement of exclusive J/ψ, such events were called as *two-track events* at that time.

Higher states of charmonia were also measured at fixed-target experiments. The measurement of ψ' is described in [25]. A photon beam with energies in the range 60 - 160 GeV was interacting with a liquid hydrogen target. The events with ψ' were reconstructed as $\psi' \to J/\psi\pi^+\pi^-$.

1.4.1 Exclusive J/ψ photoproduction off protons

The first measurements of the J/ψ photoproduction on collider experiments were carried with beams of electrons (positrons) and protons or in the collisions of protons on protons or anti-protons.

Exclusive photoproduction of J/ψ in the process of $\gamma\mathrm{p} \to J/\psi\,\mathrm{p}$ using colliding beams of positrons and protons was measured at HERA by ZEUS [26]. The center-of-mass energy of the photon-proton system was $20 < W_{\gamma\mathrm{p}} < 290$ GeV. The J/ψ mesons were reconstructed both in the dielectron and dimuon channels using the tracking detectors.

The dependence of the differential cross section on the momentum transfer t was studied, in particular the dependence of the slope parameter b in Eq. (1.15) on $W_{\gamma\mathrm{p}}$ was measured. The results showed a little shrinkage of b with increasing $W_{\gamma\mathrm{p}}$.

The photoproduction cross section was measured as a function of $W_{\gamma\mathrm{p}}$ with no selection on t. An steep rise of the cross section $\sigma(\gamma\mathrm{p} \to J/\psi\mathrm{p})$ with increasing $W_{\gamma\mathrm{p}}$ was observed, confirming thus results from fixed-target experiments. The measurement by ZEUS provided constraints to the generalized gluon parton distribution of the proton.

Another measurement of the exclusive J/ψ photoproduction in electron-proton collisions at HERA was reported by the H1 experiment. The energy range probed by H1 is $40 < W_{\gamma\mathrm{p}} < 305$ GeV [27] and a more precise measurement was performed at $25 < W_{\gamma\mathrm{p}} < 110$ GeV [28]. The J/ψs have also been reconstructed in dielectron and dimuon decays.

Besides the elastic photoproduction, the proton-dissociative photoproduction was measured, the proton p dissociates in this case to a system of remnants Y of mass $m_p < M_Y < 10$ GeV.

The differential cross section $\mathrm{d}\sigma/\mathrm{d}t$ was measured in the range $40 < W_{\gamma\mathrm{p}} < 305$ GeV and $|t| < 1.2$ GeV^2. The data were parametrized using the exponential form $\mathrm{d}\sigma/\mathrm{d}t \propto e^{bt}$ (Eq. (1.15)) in different bins of $W_{\gamma\mathrm{p}}$. The dependence of the exponential slope parameter b on the energy was found to follow

$$b(W_{\gamma\mathrm{p}}) = b_0 + 4\alpha' \ln(W_{\gamma\mathrm{p}}/W_0), \tag{1.20}$$

with the constants determined by the fit as $b_0 = 4.63$ GeV^{-1} and $\alpha' = 0.164$ GeV^{-1} at very low virtuality $Q^2 \lesssim 1$ GeV^2. The parameter W_0 was arbitrarily chosen as 90 GeV.

The elastic cross section of $\gamma\mathrm{p} \to J/\psi\,\mathrm{p}$ was parametrized by the empirical power law proportionality

$$\sigma = N \left(\frac{W_{\gamma\mathrm{p}}}{W_0} \right)^{\delta}. \tag{1.21}$$

The data together with the power law fit is shown in Fig. 1.8. The parameter of the fit is $\delta = 0.67 \pm 0.03$.

Using the results from the power law fit, the gluon density at the leading order was parametrized as [29]

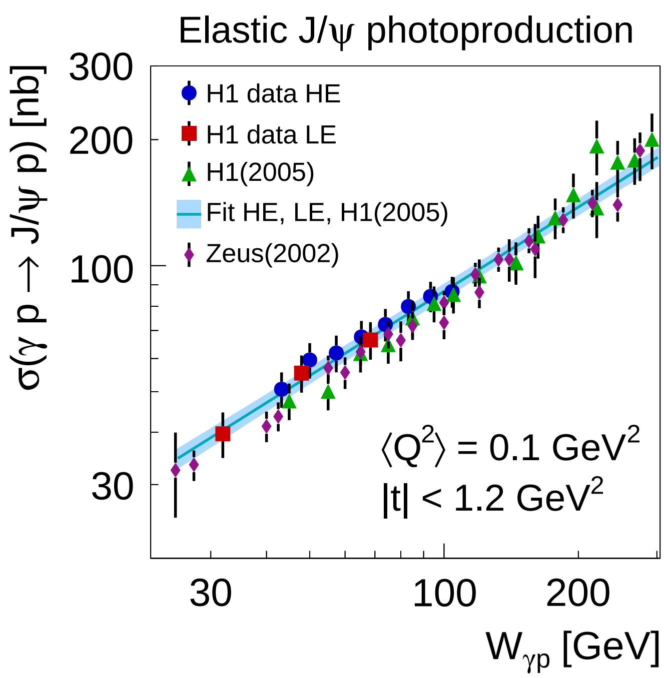

Fig. 1.8 Cross section of elastic J/ψ photoproduction and the fit with uncertainty shown as the shaded band [28].

$$x \cdot g(x,\mu^2) = N \cdot x^{-\lambda} \tag{1.22}$$

at the scale $\mu^2 = M^2_{J/\psi}/4 = 2.4$ GeV^2 and $\delta \approx 4 \cdot \lambda$. With the present data, $\lambda_{J/\psi} = 0.168 \pm 0.008$. The skewing effects are neglected in the present formula, the distribution in Eq. (1.22) is treated as diagonal.

The momentum fraction x carried by the gluons is proportional to the energy square as $x = (M_{J/\psi}/W_{\gamma p})^2$ (Eq. (1.16)), which means that we can probe smaller parts of the proton using larger energy.

Extrapolation of Eq. (1.22) to lower-x values shows an increase of the number of gluons with decreasing momentum fraction. It is expected that, at some energy threshold (or limiting x), the gluon density will saturate and no more gluons will emerge.

The onset of gluon saturation would present itself by a deflection from Eq. (1.22) and consequently the elastic photoproduction cross section would move into a lower value of the δ parameter in the power law dependency.

The power law proportionality of the elastic photoproduction cross section $\sigma \propto W^{\delta}_{\gamma p}$ was used in an indirect measurement by the LHCb experiment in proton-proton collisions at $\sqrt{s} = 7$ TeV [30].

The J/ψ have been reconstructed via the dimuon decays in the pseudorapidity range $2 < \eta < 5$. As we are dealing with a symmetric collision system, unlike the positron-proton collision, each of the protons may act as a photon source or as a target. Consequently, the rapidity of the J/ψ may have positive or negative sign in each event, leading to an ambiguous determination of the energy $W_{\gamma p}$. The low-energy (W_-) and high-energy components (W_+) are present in the data together.

The differential cross section $d\sigma/dy$ was measured directly, each of the components was extracted in a model-dependent approach by postulating the power law results from H1 for the other. The photoproduction cross section together with HERA and fixed target data is given in Fig. 1.9.

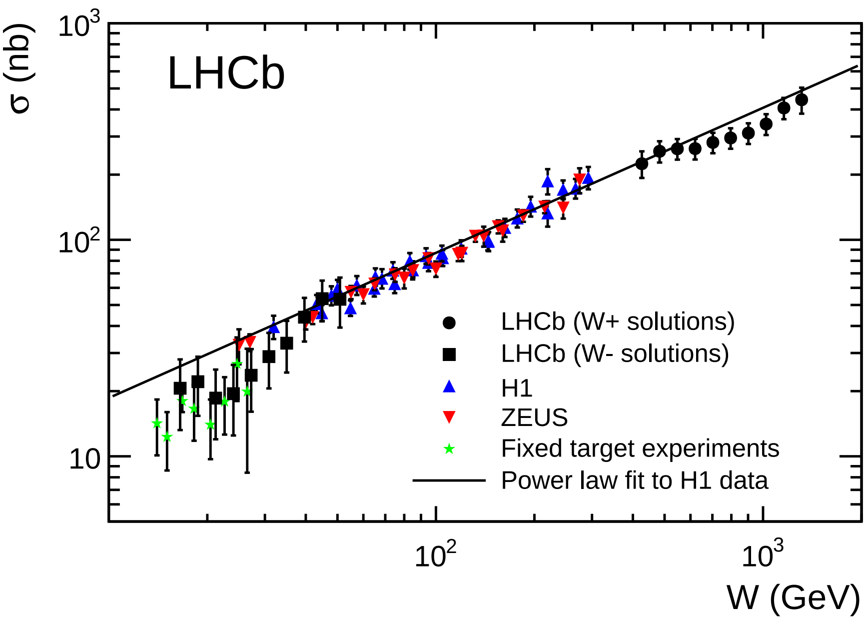

Fig. 1.9 Cross section of J/ψ photoproduction in elastic photon-proton interactions with the LHCb solutions $W_+(W_-)$ extracted by assuming the power law validity for $W_-(W_+)$ [30].

The CDF experiment at the Tevatron measured exclusive photoproduction of J/ψ and heavier species in proton-antiproton collisions at $\sqrt{s} = 1.96$ TeV [31]. The J/ψs have been reconstructed in the dimuon channel with both muon tracks in the central pseudorapidity $|\eta| < 0.6$. The measurement by CDF was the first exclusive photoproduction measurement in hadron-hadron collisions. The results include also elastic QED production of dimuons in the reaction $\gamma\gamma \to \mu^+\mu^-$.

The main motivation for the CDF measurement was to test the hypothesis on 3-gluon exchange mechanism of J/ψ photoproduction. Such process would enhance the photoproduction cross section, the CDF results provide an upper limit of the 3-gluon contribution.

The photoproduction cross section of J/ψ was in agreement with HERA results, the cross section of $\gamma\gamma \to \mu^+\mu^-$ was found to be consistent with the QED expectation. The results by the CDF experiment have shown the feasibility of photoproduction measurements in hadron colliders.

1.4.2 Coherent J/ψ photoproduction in heavy-ion UPC

The first measurement of exclusive J/ψ and e^+e^- photoproduction in nucleus-nucleus collisions was reported by the PHENIX experiment at RHIC [32]. The measurement was performed using Au-Au collisions at $\sqrt{s_{NN}} = 200$ GeV. The J/ψs have been identified through their dielectron decay $J/\psi \rightarrow e^+e^-$ in central rapidity $|y| < 0.35$.

The measurement corresponds to photon-nucleon center-of-mass energy $21 < W_{\gamma\mathrm{p}} < 30$ GeV with a mean value of $\langle W_{\gamma\mathrm{p}} \rangle = 24$ GeV, giving thus $x = (M_{J/\psi}/W_{\gamma\mathrm{p}})^2 \approx 1.5 \times 10^{-2}$.

The main objective of the measurement was to get the nuclear gluon density $G^A(x, Q^2)$ from the photoproduction cross section and discuss its relation to the nucleon gluon distribution $g(x, Q^2)$ at low values of x.

At first approximation we may suppose scaling of nuclear gluon density with the number of nucleons. The nucleus would be treated as a simple superposition of nucleon gluon densities and the nuclear gluon density would be

$$G^A(x, Q^2) = A \cdot g(x, Q^2). \tag{1.23}$$

Experimental evidence of a deviation from such a scaling, at a given x and Q^2, is called gluon shadowing at small-x [33], because the gluon distribution of nuclei is less that expected from Eq. (1.23). The main physics motivation for photoproduction measurements off nuclear targets is then the search for deviations from hypothesis in Eq. (1.23).

The events of exclusive vector meson photoproduction in nucleus-nucleus collisions are very rare compared to the yield of hadronic events and therefore require special triggering at the level of data taking. The PHENIX experiment utilized the presence of additional soft photons in the same event where the photoproduction reaction had occurred. Such photons have energy too low to produce particles, but may excite the nuclei, dominantly to a Giant-Dipole Resonance, which emits very forward neutrons. The neutrons can be used to trigger for UPC events by detecting them in the Zero-Degree Calorimeters (ZDC). The probability of neutron emission in at least one direction, coincident with coherent J/ψ production was established as $55\% \pm 6\%$ for the kinematic conditions in the experiement.

The UPC trigger of PHENIX required (i) veto in the forward Cherenkov detectors on both sides of the interaction point, (ii) energy deposition in the electromagnetic calorimeter consistent with electron-positron pair and (iii) energy deposition in one or both ZDCs consistent with forward neutrons emission from excited Au nuclei.

After the event selection, the yield of exclusive J/ψ candidates was about 10 J/ψ with the dielectron p_T distribution consistent with the presence of coherent and incoherent contributions. The measured photoproduction cross section included both contributions due to limited statistics.

The measured cross section of J/ψ photoproduction is shown in Fig. 1.10, where the statistical uncertainty is represented as the error bars and systematical as the boxes. The theoretical predictions are in agreement with the data within the errors. Unfortunately, the large uncertainties prevent any definite conclusions regarding the amount of nuclear gluon shadowing.

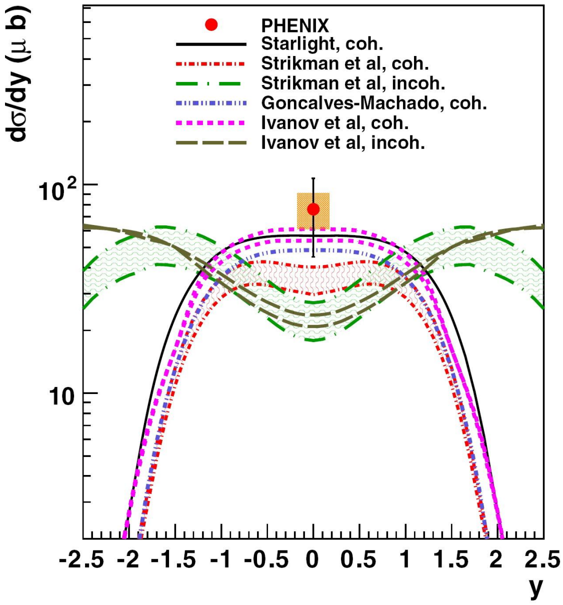

(a)

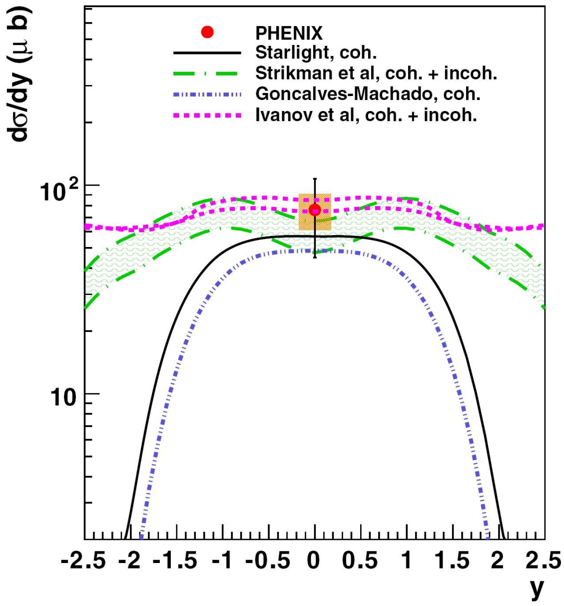

(b)

Fig. 1.10 Measured cross section of J/ψ photoproduction with neutron emission by the PHENIX experiment. The theoretical calculations for coherent and incoherent contributions are shown (a) separately and (b) summed up [32].

Using the equivalent photon spectrum, the cross section of photon-nucleus photoproduction was obtained from the differential photoproduction cross section in Au-Au, allowing to construct the ratio to the photon-proton cross section measured at HERA at the same $\langle W_{\gamma p}\rangle$. The ratios $\sigma(\gamma+\mathrm{Au}\to J/\psi)/\sigma(\gamma+\mathrm{p}\to J/\psi)$ for coherent and incoherent contributions, though with errors of about 50%, are consistent with scaling of the cross sections by the number of nucleons (A = 179 for gold), expressed as $\sigma(\gamma+\mathrm{Au}\to J/\psi) = A^{\alpha}\sigma(\gamma+\mathrm{p}\to J/\psi)$ with α = 1.01 ± 0.07 and 0.92 ± 0.08 for coherent and incoherent contributions respectively.

The publication by PHENIX also reports the measurement of electron-positron production in photon-photon interactions in the invariant mass interval $2.0 < m_{e^+e^-} < 2.8$ GeV. The prediction of leading order QED is in agreement with the measured cross section.

1.5 STARLIGHT event generator

The STARLIGHT event generator [34] provides inputs to the Monte-Carlo (MC) simulations of various photoproduction processes. The simulation may serve as a baseline for acceptance and efficiency corrections and/or as the source of samples of elemental processes contributing to the signal from real data. STARLIGHT has become a generally used MC among UPC analyses, because it allows to generate various mesons in photon-proton or coherent or incoherent interactions as well as two-photon production of mesons or dilepton pairs, all of these under arbitrarily defined colliding beams.

As the generator may not precisely predict the resulting cross section of a given process, and the analysis of real data should be model-independent, the ability of the generator to describe the data can be tested by comparing the distributions of kinematic and technical parameters obtained from the MC to those from the data. The systematic error resulting from using a specific MC is determined either by varying the parameters of the generation or by using another theoretical model as an input to the MC.

In the preceding sections, the basic ideas of the virtual photons and kinematics and dynamics of the photoproduction reactions were outlined. However, corrections are required to get a more accurate physics picture. STARLIGHT is one of the *models* supposed to give such more accurate picture, the following sections describe other models.

The photonuclear cross section of the process $A+A \to A+A+V$ with A the nucleus and V the produced vector meson uses here the experimental cross section of photon proton production $\gamma p \to Vp$ as an input for the Glauber calculation of $\gamma A \to VA$ [35]. The calculation is carried out in the rest frame of one of the nuclei (target nucleus), the total production is the sum of the contributions from both nuclei. The flux of virtual photons is calculated separately, the total cross section of $A+A \to A+A+V$ is given by the integration of the cross section of $\gamma A \to VA$ over the spectrum of virtual photons.

1.5.1 Calculation of the photon flux

In Section 1.2 the electromagnetic field of a moving source is described as a flux of virtual photons $n(\omega)$ with energy ω. The hard-sphere approximation for $n(\omega)$ of an ultra-relativistic source was formulated in Eq. (1.10) using the Weizsäcker-Williams method.

In the hard-sphere approach the nucleus is treated as a sphere with well defined boundary at the radius $R_A = 1.2A^{1/3}$ with A the nucleon number. Hadronic interactions, which would spoil the exclusivity requirements, are immediately suppressed at an impact parameter $b > 2R_A$.

STARLIGHT describes the photon flux using the non-interaction probability resulting from the overlap of two Woods-Saxon distributions. The Woods-Saxon distribution describes the nucleus as a continuous-shaped object. The overlap of the two nuclei is then calculated as the convolution of the two distributions in the direction of the impact parameter.

The probability of no interaction at a given impact parameter follows a Poisson distribution with mean taken as the multiplication of the impact-parameter dependent overlap function and the total nucleon-nucleon interaction cross section.

The total photon flux is provided as the distribution of photons of momentum k as $\mathrm{d}N_\gamma(k)/\mathrm{d}k$. The photon flux at a given impact parameter obtained by Weizsäcker-Williams method is integrated over the surface of the nucleus and modulated by the non-interaction probability.

As the range of strong interactions is much smaller than the dimensions of the nucleus, a possible correction to the electric field inside the nucleus by the form factor is neglected.

1.5.2 Vector meson photoproduction in heavy-ion collisions

Several steps are carried out in order to obtain the desired heavy-ion cross section $\sigma(AA \to VA)$ of photoproduction of vector meson V in collision of nuclei A.

First the observed cross section of photon-proton photoproduction $\sigma(\gamma p \to Vp)$ is parameterized and used as input for the vector meson dominance model (VDM) calculation of elastic meson-proton scattering $\sigma(Vp \to Vp)$. In the case of the J/ψ, the parametrization on the center-of-mass energy W reads as

$$\left.\frac{d\sigma(\gamma p \to Vp)}{dt}\right|_{t=0} = 4 \times 0.0015 \times W^{0.8} \tag{1.24}$$

The optical theorem is then applied to find the total cross section $\sigma_{\text{tot}}(Vp)$.

A Glauber calculation is used for the total cross section of vector meson and nucleus interaction $\sigma_{\text{tot}}(VA)$ from the $\sigma_{\text{tot}}(Vp)$, using the nuclear thickness function $T_A(\vec{r})$:

$$\sigma_{\text{tot}}(VA) = \int d^2\vec{r} \left(1 - e^{-\sigma_{\text{tot}}(Vp)T_A(\vec{r})}\right), \tag{1.25}$$

where the thickness function is obtained by integrating the Woods-Saxon nuclear density over the direction of travel. Again the optical theorem and vector meson dominance is applied to obtain the photon-nucleus cross section $\sigma(\gamma A \to VA)$.

The total cross section of $\gamma A \to VA$ depends on the slope of the cross section with the square of momentum transfer of the target nucleus. The relation is given by the nuclear form factor, which is the Fourier transform of the nuclear density. An accurate description of the nuclear density is given by the Woods-Saxon distribution, but, unfortunately, the corresponding Fourier transform is not an analytic function. An alternative approach was used in STARLIGHT, a convolution of a hard sphere and the Yukawa potential was used as a very good approximation to the nuclear density.

Finally, the photoproduction cross section $\sigma(AA \to VA)$ is found by integrating the photon-nucleus cross section over the photon flux. The rapidity of the final state is given by the photon momentum in the rest frame of the target and the mass of the vector meson.

1.5.3 Two-photon production of lepton pairs

The cross section of lepton pair production, $\gamma\gamma \to l^+l^-$with l for e, μ or τ, is determined by the Breit-Wheeler formula [36]. The formula provides the cross section for a pair with given mass in the final state when there was a two-photon pair of a given center-of-mass energy in the initial state.

As each of the nuclei is the source of virtual photons, the two-photon luminosity is given by the convolution of photon fluxes of the two nuclei. The full QED calculation of the process would require to treat the photon as virtual, but at high energy the virtuality can be neglected and the equivalent photon approach can be used.

The rapidity of the final state is given by the photon energies, the transverse momentum is the vector sum of the photon's perpendicular momenta $k_{\perp}$. The spectrum of $k_{\perp}$ for a given photon momentum is obtained using the nuclear form factor.

1.6 Models for J/ψ photoproduction in photon-proton interactions

The task for the models is to describe the cross section of the photoproduction reaction $\gamma p \to J/\psi p$ using a minimal set of free parameters. The parameters can be obtained either from other physics processes, or by fitting the photoproduction cross section to the data.

One possibility to calculate the cross section is by constructing the Feynman diagrams of the process [17]. The reaction is described by the exchange of a colourless two-gluon system, as shown in Figure 1.11. The amplitude of the process is the sum of the two diagrams.

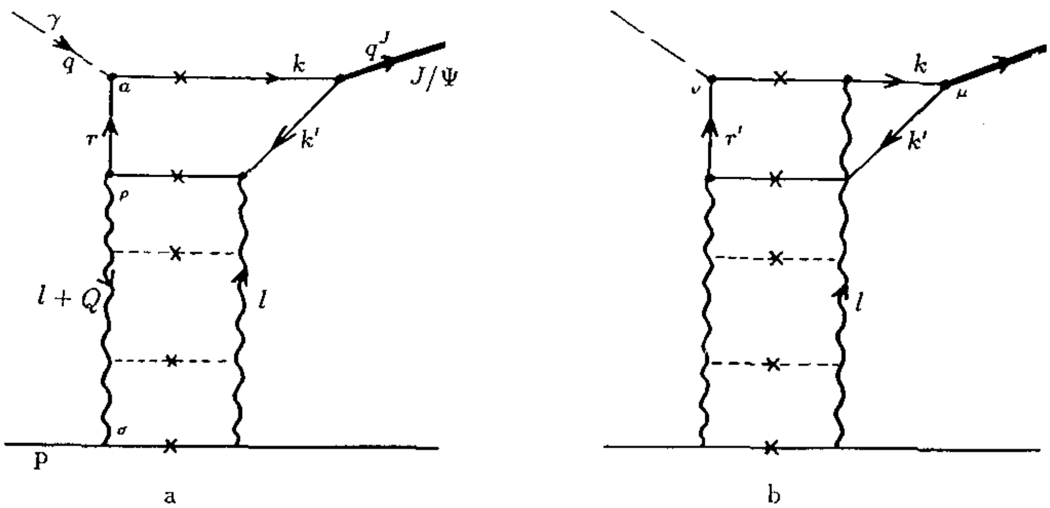

Fig. 1.11 Feynman diagrams for J/ψ photoproduction [17].

Other possibility is splitting the entire process into three consecutive sub-processes. First the photon fluctuates into a quark-antiquark pair. The pair is characterized as the color dipole [37, 38]. The dipole then scatters elastically on the gluon cloud of the proton and after the scattering it may recombine back into the photon or a vector meson can be formed. The situation is shown in Figure 1.12.

In both cases the cross section is related to the square power of the skewed gluon distribution of the proton (see Section 1.3.1). The gluon must be introduced via a suitable functional form, experimental data impose constraints upon the parameters of the form. The physics message of the measurement of the process $\gamma p \to J/\psi p$ is therefore the knowledge of the gluon distribution in the proton.

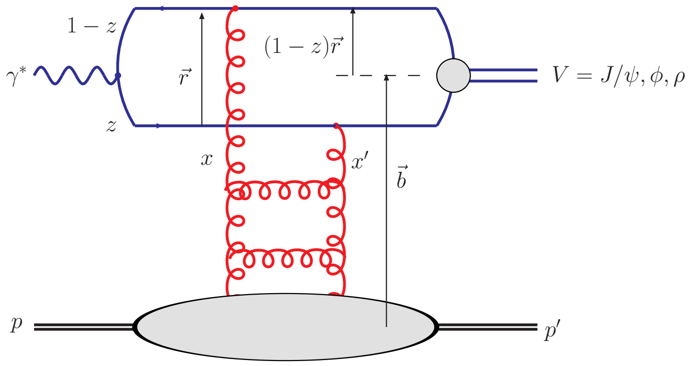

Fig. 1.12 Scattering of a color dipole on a proton [39].

1.6.1 Model by S.P. Jones, A.D. Martin, M.G. Ryskin and T. Teubner ("JMRT")

The model [40] uses perturbative QCD to calculate the cross section according to the Feynman diagram on Figure 1.11, parameters of the gluon distribution are constrained by fitting the prediction to the data.

In the lowest order, the corresponding Feynman diagram is shown in Figure 1.13, where x and x' denote the momentum fractions carried by the gluons and k_T is the transverse momentum of the virtual quarks c and $\bar{c}$.

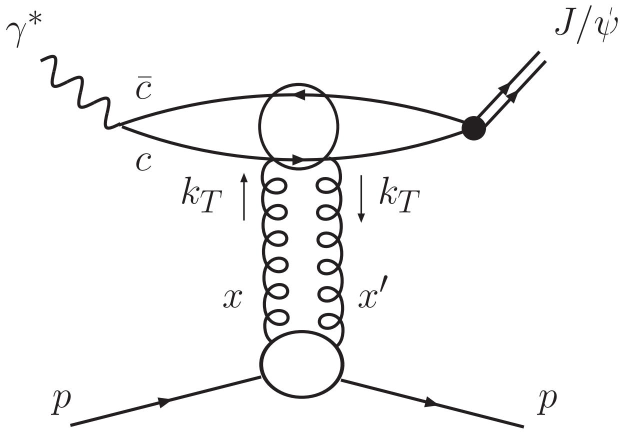

Fig. 1.13 High energy J/ψ production modeled by the two-gluon exchange [40].

The cross section according to the diagram in Figure 1.13 in leading logarithmic (LO) approximation is [17]

$$\frac{\mathrm{d}\sigma}{\mathrm{d}t}(\gamma \mathrm{p} \to J/\psi \mathrm{p})\bigg|_{t=0} = \frac{\Gamma_{ee} M_{J/\psi}^3 \pi^3}{48\alpha} \left[\frac{\alpha_s(\bar{Q}^2)}{\bar{Q}^4} x g(x, \bar{Q}^2) \right]^2 \left(1 + \frac{Q^2}{M_{J/\psi}^2} \right), \tag{1.26}$$

where

$$\bar{Q}^2 = (Q^2 + M_{J/\psi}^2)/4, \qquad x = (Q^2 + M_{J/\psi}^2)/(W^2 + Q^2). \tag{1.27}$$

W is the center-of-mass energy of photon-proton system, Q^2 is the virtuality the photon and Γ_{ee} and $M_{J/\psi}$ are the electronic width and the rest mass of the J/ψ.

Equation (1.26) provides with the cross section at zero momentum transfer at the proton vertex, where $t = 0$. The integration over t assumes the proportionality $\sigma \sim \exp(-Bt)$ (Eq. (1.15)).

As we can see from Eq. (1.26), measurement of the cross section allows to extract the gluon density $xg(x, \bar{Q}^2)$, profiting from the square-power proportionality.

Several corrections are required to the LO Eq. (1.26). Relative momenta of the quarks (Fermi motion), Coulombic and short-distance corrections are covered by the measured width of the J/ψ electronic decay Γ_{ee}. The electronic width is related to the wave function of the J/ψ at the origin.

The gluon distribution $xg(x, \bar{Q}^2)$ in Eq. (1.26) is in fact the skewed (or generalized or off-diagonal) distribution, since the two gluons are exchanged. According to the arrows of k_T in Figure 1.13, the momentum fractions carried by the two gluons are ordered as $x' \ll x \ll 1$. The diagonal and skewed gluon distributions are connected via the Shuvaev transform [21].

Some of the next-to-leading order (NLO) corrections are implemented by integration of the gluon distribution over k_T^2. Starting with the unintegrated gluon distribution $f(x, k_T^2)$, the integrated distribution is obtained as

$$xg(x, \mu^2) = \int_{Q_0^2}^{\mu^2} \frac{\mathrm{d}k_T^2}{k_T^2} f(x, k_T^2) + c(Q_0^2). \tag{1.28}$$

To describe the data and obtain constraints to the gluon distribution, a parametrization of the gluon should be selected. At the leading order (LO), the following simple formula is sufficient:

$$xg(x, \mu^2) = N x^{-\lambda} \qquad \text{and} \qquad \lambda = a + b \ln(\mu^2/0.45\ \text{GeV}), \tag{1.29}$$

where N, a and b are free parameters to be determined by the fit to the data on exclusive J/ψ photoproduction.

For the calculation including some NLO effects the specific feature of QCD, running coupling constant α_s, should be taken into account. The parametric form of the gluon is in this case

$$xg(x, \mu^2) = N x^{-a} (\mu^2)^b \exp\left[\sqrt{16 N_c/\beta_0 \ln(1/x) \ln(G)}\right] \qquad \text{with} \qquad G = \frac{\ln(\mu^2/\Lambda_{\mathrm{QCD}}^2)}{\ln(Q_0^2/\Lambda_{\mathrm{QCD}}^2)}. \tag{1.30}$$

Again, N, a and b are free parameters to be extracted by a fit to data.

The developed framework which is based on perturbative QCD for the cross section and Shuvaev transform for the skewing effect can be used to predict the cross section of Υ exclusive photoproduction. The rest mass and electronic width have to be replaced by the values corresponding to the Υ.

Parameters of gluon distributions in Eq. (1.29) and Eq. (1.30) have been determined using experimental data on exclusive J/ψ photoproduction and predictions for the Υ photoproduction have been calculated.

1.6.2 Generalized impact parameter dipole saturation ("b-Sat") model

The model describes exclusive photoproduction processes using a QCD dipole (Figure 1.12), parameters of the gluon distribution are constrained using deep inelastic scattering (DIS) of electrons on protons [39]. The framework calculates photoproduction cross sections of J/ψ, ϕ and ρ mesons as well as the deeply virtual Compton scattering (DVCS.)

The photoproduction process is described in several stages as the fluctuation of an initial virtual photon into a quark - antiquark pair forming the dipole, the elastic interaction of the dipole with the proton and the recombination of the dipole into the final vector meson or real photon in the case of DVCS.

The differential cross section to produce the final state E at squared momentum transfer at the proton vertex t is

$$\frac{d\sigma_{T,L}^{\gamma p \to Ep}}{dt} = \frac{1}{16\pi} |\mathscr{A}_{T,L}^{\gamma p \to Ep}|^2 \tag{1.31}$$

for transverse T or logitudinal L polarization of the photon γ. The amplitude $\mathscr{A}$ characterizes the whole process as shown in Figure 1.14, where $V = E$. The dipole here is characterized by its transverse size $\boldsymbol{r}$, fraction of photon's light-cone momentum carried by a quark z and impact parameter of the interaction $\boldsymbol{b}$.

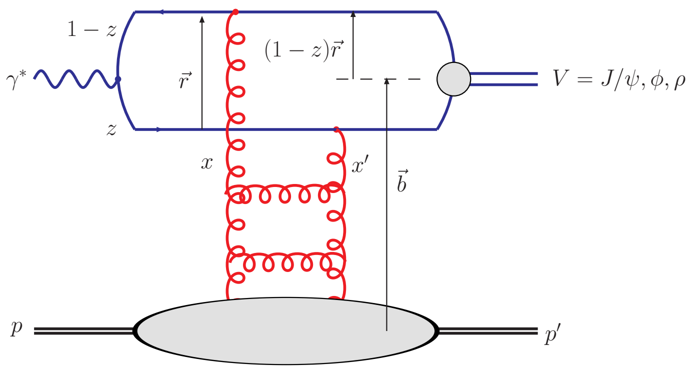

Fig. 1.14 The amplitude of elastic scattering for vector meson production [39].

The amplitude is found by integrating over all dipole radii and momentum fractions,

$$\mathscr{A}_{T,L}^{\gamma p \to E p}(x, Q, \Delta) = \int \mathrm{d}^2 \boldsymbol{r} \int_0^1 \frac{\mathrm{d}z}{4\pi} (\Psi_E^* \Psi)_{T,L} \mathscr{A}_{q\bar{q}}(x, r, \Delta) \tag{1.32}$$

as a function of x of the gluon, photon virtuality Q^2 and transverse momentum lost by the proton $\Delta^2 = -t$. $(\Psi_E^* \Psi)_{T,L}$ is the overlap of the photon and final state wave functions, describing thus fluctuation of the photon into the dipole and recombination of the dipole into the final state E.

The elastic amplitude $\mathscr{A}_{q\bar{q}}$ is defined via the cross section of elastic scattering of the $q\bar{q}$ dipole on the proton:

$$\frac{\mathrm{d}\sigma_{q\bar{q}}}{\mathrm{d}t} = \frac{1}{16\pi} |\mathscr{A}_{q\bar{q}}(x, r, \Delta)|^2 \tag{1.33}$$

The model is supposed to deliver the cross section of the dipole interaction at a given impact parameter. Such dependence should be put into the basic amplitude in Eq. (1.32).

The $q\bar{q}$ amplitude in Eq. (1.33) is related to the impact-parameter dependent amplitude as

$$\begin{aligned} \mathscr{A}_{q\bar{q}}(x, r, \Delta) &= \int \mathrm{d}^2 \boldsymbol{b} e^{-i\mathbf{b}\cdot\boldsymbol{\Delta}} \mathscr{A}_{q\bar{q}}(x, r, b) \\ &= i \int \mathrm{d}^2 \boldsymbol{b} e^{-i\mathbf{b}\cdot\boldsymbol{\Delta}} 2[1 - S(x, r, b)], \end{aligned} \tag{1.34}$$

where $S(x, r, b)$ is the S-matrix element of the dipole scattering.

The optical theorem is used to replace the term with the S-matrix element with the impact parameter differential cross section. The theorem gives the total cross section from the imaginary part of the forward scattering amplitude (no momentum lost by the proton):

$$\sigma_{q\bar{q}}(x, r) = \mathrm{Im}\mathscr{A}_{q\bar{q}}(x, r, \Delta = 0) = \int \mathrm{d}^2 \boldsymbol{b} 2[1 - \mathrm{Re}S(x, r, b)]. \tag{1.35}$$

The integrand in Eq. (1.35) is equal to the desired impact parameter differential cross section:

$$\frac{\mathrm{d}\sigma_{q\bar{q}}}{\mathrm{d}^2 \boldsymbol{b}} = 2[1 - \mathrm{Re}S(x, r, b)]. \tag{1.36}$$

Now it is enough to substitute the term with S-matrix element $2[1 - S(x, r, b)]$ in the amplitude in Eq. (1.34) by $\mathrm{d}\sigma_{q\bar{q}}/\mathrm{d}^2\boldsymbol{b}$ and put it to the basic amplitude in Eq. (1.32). The assumption to be made in doing the substitution is that the S-matrix element $S(x, r, b)$ is mostly real, with imaginary part negligible.

The final amplitude used in the b-Sat cross section in Eq. (1.31) is then

$$\mathscr{A}_{T,L}^{\gamma p\to Ep}(x,Q,\Delta) = \int \mathrm{d}^2\boldsymbol{r} \int_0^1 \frac{\mathrm{d}z}{4\pi} \int \mathrm{d}^2\boldsymbol{b} (\Psi_E^*\Psi)_{T,L} \times e^{-i[\boldsymbol{b}-(1-z)\boldsymbol{r}]\cdot\boldsymbol{\Delta}} \times \frac{\mathrm{d}\sigma_{q\bar{q}}}{\mathrm{d}^2\boldsymbol{b}}. \quad (1.37)$$

The term $[\boldsymbol{b}-(1-z)\boldsymbol{r}]$ in the exponential factor in Eq. (1.37) extends the forward wave functions Ψ_E and Ψ (Δ or $t = 0$) to the nonforward wave functions [41].

The forward photon wave function Ψ is calculated within perturbative QED. The wave function of the vector meson, $\Psi_{E=V}$ is modeled treating the meson as a quark-antiquark bound state with the spin and polarization same as the photon, input to the vector meson wave function are quark masses and charges. Several constraints are imposed by normalization and experimental electronic decay width Γ_{ee}. The scalar part of the vector meson wave function assumes the Gaussian form.

The initial idea to use the dipole model in the description of the total inclusive and diffractive DIS cross sections was formulated by Golec-Biernat and Wüsthoff [42, 43]. The GBW dipole cross section integrated over impact parameter was

$$\sigma_{q\bar{q}}^{\mathrm{GBW}}(x,r) = \sigma_0(1-e^{-r^2Q_s^2(x)/4}), \quad (1.38)$$

where σ_0 is constant and $Q_s(x)$ is the saturation scale defined as $Q_s^2(x) = (x_0/x)^{\lambda_{\mathrm{GBW}}}\ \mathrm{GeV}^2$. Parameters of the GBW cross section are $\sigma_0 = 29$ mb, $\lambda_{\mathrm{GBW}} = 0.28$ and $x_0 = 3\times10^{-5}$ with contribution of charm quark. When the dipole becomes large compared to $1/Q_s$, the cross section saturates at σ_0 and is further independent of λ_{GBW}.

The dipole cross section in the b-Sat model, $\mathrm{d}\sigma_{q\bar{q}}/\mathrm{d}^2\boldsymbol{b}$ in the amplitude in Eq. (1.37), is

$$\frac{\mathrm{d}\sigma_{q\bar{q}}}{\mathrm{d}^2\boldsymbol{b}} = 2(1-e^{-(\Omega/2)}), \quad (1.39)$$

where Ω is the opacity of the proton, which is given by the gluon density $xg(x,\mu^2)$ and the transverse profile of the proton $T(b)$:

$$\Omega = \frac{\pi^2}{N_c} r^2 \alpha_s(\mu^2)\cdot xg(x,\mu^2)\cdot T(b), \quad (1.40)$$

where N_c is number of colors of the quarks.

The cross section in Eq. (1.39) together with the opacity in Eq. (1.40), known as the Glauber-Mueller cross section, is the base of the b-Sat model [39].

The gluon density at the scale μ^2, $xg(x,\mu^2)$, is evolved from an initial scale μ_0^2 using the LO DGLAP evolution [44–46]. The scale is related to the dipole size r as $\mu^2 = 4/r^2 + \mu_0^2$. The evolution scheme provides the prescription for the derivative of the gluon density with respect to the scale, $\partial xg(x,\mu^2)/\partial \ln\mu^2$.

The gluon density at the initial scale μ_0^2 is parametrized as

$$xg(x,\mu_0^2) = A_g x^{-\lambda_g}(1-x)^{5.6}, \tag{1.41}$$

where μ_0^2, A_g and λ_g are free parameters of the model, which are fixed using the measured DIS data.

The proton transverse profile $T(b)$ in the opacity in Eq. (1.40) is assumed as a Gaussian shape

$$T(b) = \frac{1}{2\pi B_G} e^{-(b^2/2B_G)} \tag{1.42}$$

with B_G the fourth free parameter of the b-Sat model. The value of B_G was fixed using the measured differential cross section as $\mathrm{d}\sigma/\mathrm{d}t \propto e^{-B_g|t|}$.

Several phenomenological corrections are required for the cross section. Implementation of the impact parameter dependent cross section into the amplitude in Eq. (1.37) with use of the optical theorem in Eq. (1.35) was done assuming the S-matrix element predominantly real, giving the amplitude purely imaginary. The correction is added via the ratio of real to imaginary parts of the amplitude.

Similarly to the model by JMRT [40] (Section 1.6.1), the interaction of the dipole with the proton proceeds via the two gluons carrying different momentum fractions x and x', as indicated in Figure 1.14. The skewing effect for the fractions $x' \ll x \ll 1$ is implemented via the Shuvaev transform [21].

The 4 free parameters of the model, parameters of the initial gluon density μ_0^2, A_g and λ_g in Eq. (1.41) and width of the Gaussian proton profile B_G in Eq. (1.42) have been fixed using the experimental data on DIS and the differential cross section, assuming the quark masses $m_{u,d,s} = 0.14$ GeV and $m_c = 1.4$ GeV. The quark masses are inputs to the photon and vector meson wave functions in the amplitude in Eq. (1.37).

The parameters of the b-Sat model are then $\mu_0^2 = 1.17$ GeV^2, $A_g = 2.55$, $\lambda_g = 0.02$ and $B_G = 4$ GeV^{-2}.

The dipole approach adopted by the b-Sat model [39] is self-consistent in the sense that the same calculational framework is first used to obtain the gluon density from the inclusive processes and then the framework is applied to the exclusive processes.

The minimal set of four parameters, three for the gluon density and one for the proton shape is used for a variety of processes, exclusive photoproduction of the ρ, ϕ and J/ψ mesons and deeply virtual Compton scattering under various kinematical conditions. Contribution of transversal and logitudinal polarizations to the cross section is also discussed. The 1-pomeron version of the b-Sat model was presented in the proposal of the LHeC project [47] as an example calculation without the saturation effects.

1.7 Models for J/ψ photoproduction in coherent photon-nucleus interactions

As the nucleus is a composite object, the calculations of coherent cross section have to treat the photonuclear interaction and also incorporate the nuclear effects. The nuclear effects influence the observed gluon density and hence the predicted cross section.

The models for coherent J/ψ photoproduction can be divided into two main groups. The partonic models (AB, RSZ and GSZ) are based on Eq. (1.14) with an explicit dependence on the square of the nuclear gluon distribution.

The second group use the dipole calculations to model the photonucleon interaction, while the nuclear cross section is obtained via the Glauber approach [35]. The group consists of GM, CSS, LM and also of STARLIGHT (see Section 1.5).

1.7.1 Model by A. Adeluyi and C. A. Bertulani ("AB")

The model [48] is designed to use data on exclusive vector meson photoproduction to constrain the nuclear gluon distribution. The cross section for coherent photoproduction is explicitly dependent on the square power of the gluon distribution, making this process a very sensitive probe to nuclear effects.

The photon flux, giving the number of virtual photons with given energy k, $\mathrm{d}N/\mathrm{d}k$, is calculated using the analytical hard-sphere approximation in Eq. (1.9), integrated over the impact parameter in the region $b > 2R_A$ with R_A the nuclear radius.

The total photoproduction cross section in nucleus-nucleus collision is obtained by the convolution of the photon-nucleus cross section with the photon flux. There are two contributions that are added and the total cross section is obtained from the integration of both contributions, expressing the symmetry between the target nucleus and the nucleus which is the source of the photon.

The photon-nucleus cross section is given by the LO pQCD formula of the two-gluon exchange, with the phenomenological correction for other effects ζ_V:

$$\left.\frac{\mathrm{d}\sigma^{\gamma A\to VA}}{\mathrm{d}t}\right|_{t=0} = \zeta_V \frac{16\pi_3 \alpha_s^2 \Gamma_{ee}}{3\alpha M_V^5}[xg_A(x,Q^2)]^2 \tag{1.43}$$

at zero momentum transfer in the interaction vertex ($t = 0$, also called as the forward cross section).

The nuclear gluon distribution $xg_A(x,Q^2)$ is evaluated at the scale $Q^2 = (M_V/2)^2$, where M_V is the mass of the vector meson. The momentum fraction of the probed gluons is given by the mass and the photon-nucleus energy $W_{\gamma A}$ as $x = M_V^2/W_{\gamma A}^2$. Γ_{ee} is the width of electronic decay of the meson, α and α_s are the coupling constants of the electromagnetic and strong interactions respectively.

The gluon modification $R_g^A(x,Q^2)$ is the key element of the AB model. It relates the gluon distribution in the proton $g_p(x,Q^2)$ to the nuclear gluon distribution as

$$g_A(x,Q^2) = g_p(x,Q^2) \times R_g^A(x,Q^2). \tag{1.44}$$

With the experimentally known proton gluon distribution, the nuclear modification R_g^A contains all the information about the complex many-body effects in the nucleus and their influence on the observed gluon density.

The forward cross section in Eq. (1.43) extends to the general case of non-zero momentum transfer t with use of the nuclear form factor $F(t)$

$$\sigma^{\gamma A \to VA}(k) = \left. \frac{\mathrm{d}\sigma^{\gamma A \to VA}}{\mathrm{d}t} \right|_{t=0} \int_{t_{\min}(k)=(M_V^2/4k\gamma_L)^2}^{\infty} \mathrm{d}t |F(t)|^2, \tag{1.45}$$

where the form factor $F(t)$ is the Fourier transform of the Woods-Saxon nuclear density $\rho_A(r) = \rho_0/[1+e^{[(r-R_A)/d]}]$, where ρ_0 is the central density and d is the skin depth.

The integration in Eq. (1.45) begins at the minimal momentum transfer in the photon-nucleus vertex $t_{\min}(k)$, in which the γ_L is the Lorentz factor in the laboratory frame.

The rapidity y of the produced vector meson is given purely by the photon momentum via the relation $k = (M_V/2)\exp(y)$, allowing to construct the rapidity dependence of the cross section using the photon flux:

$$\frac{\mathrm{d}\sigma^{\gamma A \to VA}}{\mathrm{d}y} = k \frac{\mathrm{d}N}{\mathrm{d}k} \sigma^{\gamma A \to VA}(k). \tag{1.46}$$

Several sets of parametrizations for the nuclear modification R_g^A are incorporated in the AB model [48], as shown in Figure 1.15a for the case of the lead nucleus and the J/ψ.

The effect of shadowing occurs at low values of x at $x \lesssim 0.04$. The resulting depletion is manifested as $R_g^A < 1$, giving a gluon distribution in the nucleus smaller compared to the distribution in the proton.

The strongest shadowing is predicted by EPS08 [49], medium shadowing by EPS09 [50] and weak shadowing by HKN07 [51]. An special case is the parametrization MSTW08 [52], for which $R_G^A = 1$ for all values of x, treating thus the gluon in the nucleus as the sum of the gluon in each proton and neutron, assuming same gluon content in proton and neutron. The MSTW08 case serves as the cross-check distribution which neglects the nuclear effects to the gluon density.

The predicted cross section of coherent J/ψ photoproduction in Pb-Pb collisions, at the nominal LHC energy $\sqrt{s_{NN}} = 5.5$ TeV, is shown in Figure 1.15b for each parametrization of the nuclear modification.

The effect of the quadratic dependence on the gluon density in Eq. (1.43) is clearly visible in Figure 1.15b, as the cross section with the assumption of strongest shadowing in EPS08 is heavily suppressed in comparison to the cross section with absence of the nuclear effects in MSTW08. The predictions for EPS09 and HKN07 scale by the square of the amount of the shadowing.

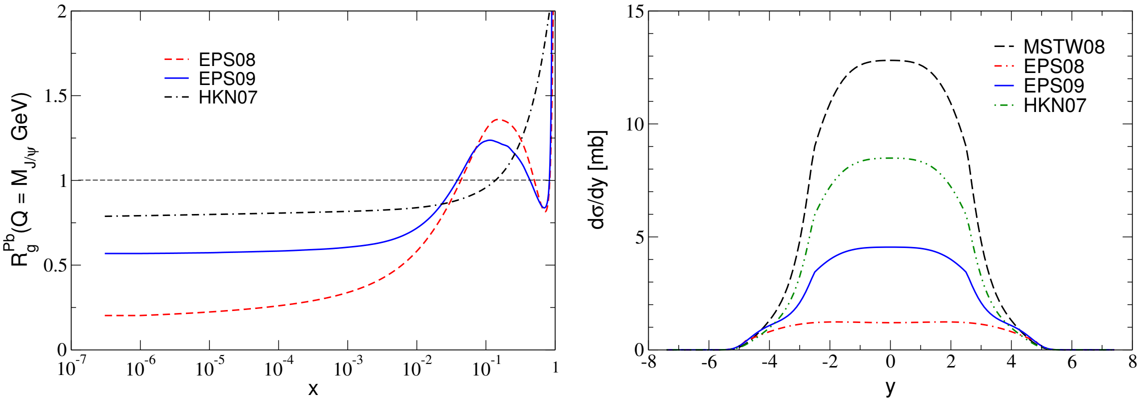

(a) (b)

Fig. 1.15 Nuclear gluon modifications (1.15a) and cross section predictions for the J/ψ (1.15b) in Pb-Pb [48].

In the opposite way, the measurement of the coherent cross section puts strong constrains on the amount of shadowing.

1.7.2 Model by V. Rebyakova, M. Strikman and M. Zhalov ("RSZ")

The RSZ model [53] is also based on the partonic formula in Eq. (1.14), where the nuclear gluon density is calculated by means of the leading twist theory [54, 55] of nuclear shadowing.

The flux of virtual photons is calculated in RSZ in the same way as it is done in STARLIGHT (section 1.5), the formula in Eq. (1.9) for the number of photons of a given energy at a given impact parameter is integrated over the impact parameter and modulated by the non-interaction probability of the strong interactions in the nucleus-nucleus collisions.

The partonic formula for the coherent cross section of the J/ψ photoproduction on the nucleus reads

$$\sigma_{\gamma A\to J/\psi A}(k) = \frac{\mathrm{d}\sigma_{\gamma p\to J/\psi p}(k,t_{\min})}{\mathrm{d}t}\left[\frac{g_A(x,\mu^2)}{Ag_p(x,\mu^2)}\right]^2 \Phi(t_{\min}), \tag{1.47}$$

where $\sigma_{\gamma p\to J/\psi p}$ is the cross section on the proton calculated within perturbative QCD, g_A and g_p are the gluon distributions in the nucleus and in the proton and $\phi(t_{\min})$ is the square of the nuclear form factor over the momentum transfer from the incoming to the outgoing nucleus, integrated from $-\infty$ up to the minimal momentum transfer $t_{\min}$.

The momentum fraction of the nucleus carried by the gluon, x, is kinematicaly constrained by the mass of the J/ψ $m_{J/\psi}$ and the interaction energy squared $s_{\gamma A}$ as $x = m^2_{J/\psi}/s_{\gamma A}$ and μ^2 is the scale at which the gluon density is evaluated.

The ratio g_A/Ag_p in the square brackets in Eq. (1.47) corresponds to the nuclear modification R_g^A introduced in Eq. (1.44).

In the RSZ model, the overall nuclear gluon density g_A/Ag_p is calculated by the Leading Twist Approximation (LTA) [54, 55] to nuclear shadowing.

Within the framework of the LTA, the interaction of the virtual photon is described by a series in the number of simultaneous interactions with the nucleons in the target nucleus (the multiple scattering series), as shown in Figure 1.16. In the final state there could be the J/ψ meson for the case of $\gamma A \to J/\psi A$ photoproduction.

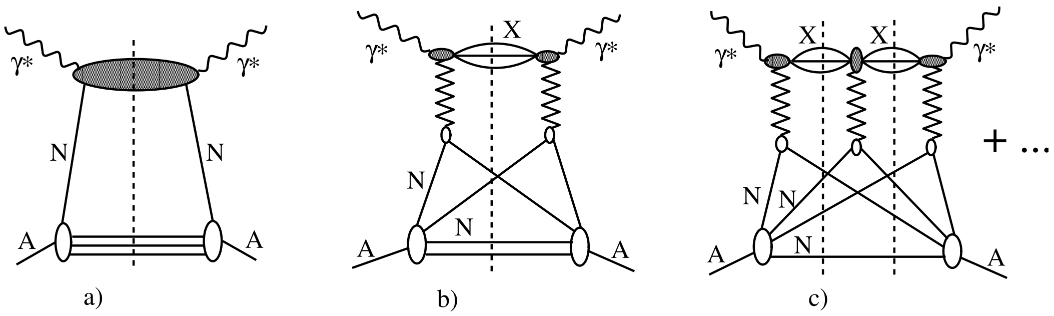

Fig. 1.16 The multiple scattering series of the LTA theory, interaction with a single nucleon (a), double scattering (b) and interaction with three nucleons (c) [55].

The photon fluctuates into a strongly interacting state, the lifetime of the fluctuation is the coherence length $l_c = 1/(2m_N x)$ where m_N is the mass of the nucleon. The interaction is considered coherent within the LTA when $l_c > 2R_A$, i.e. the length is larger than the diameter of the nucleus, allowing the virtual photon to interact with all nucleons of the nucleus.

The first graph (a) in Figure 1.16 corresponds to photoproduction on a single nucleon, giving the photonuclear cross section $\sigma_{\gamma A}$ as the photon-nucleon cross section $\sigma_{\gamma N}$ scaled by the number of nucleons, $\sigma_{\gamma A} = A\sigma_{\gamma N}$. This would be the only contribution to the cross section without the effect of the nuclear shadowing.

The second graph (b) in Figure 1.16 provides the leading contribution to shadowing, it describes the interaction with two nucleons of the nucleus.

The last graph (c) in Figure 1.16 describes the interaction with three and more nucleons of the target nucleus. This contribution becomes important at low values of x. In the general case of the interaction with N nucleons, the fluctuation of the photon scatters off two nucleons, then the intermediate state rescatters on the remaining $N-2$ nucleons.

Summation of the multiple scattering series (Figure 1.16) allows to express the nuclear gluon density in the square brackets in Eq. (1.47) as

$$\frac{g_A(x,\mu^2)}{Ag_p(x,\mu^2)} = 1 - \frac{\sigma_2}{\sigma_3} + \frac{\sigma_2}{\sigma_3}\frac{\sigma_3^A}{A\sigma_3}, \tag{1.48}$$

where $\sigma_2(x,\mu^2)$ is the cross section of graph (b) in Figure 1.16, σ_3 is the effective cross section of interaction with $N \geq 3$ nucleons and σ_3^A is the total hadron-nucleus cross section.

The leading contribution of graph (b) in Figure 1.16 is given by the diffractive gluon distribution in the proton g_p^{D3} constrained to the HERA data as

$$\sigma_2(x,\mu^2) = \frac{16\pi B_{\rm diff}}{(1+\eta^2)xg_p(x,\mu^2)} \int_x^{0.1} {\rm d}x_{\mathbb{P}}\beta\; g_p^{D3}(\beta,\mu^2,x_{\mathbb{P}}), \tag{1.49}$$

in which $B_{\rm diff}$ is the slope of the t-dependence in Eq. (1.15) of the cross section corresponding to the measurement of g_p^{D3}, η is the ratio of the real to the imaginary parts of the amplitude for the previously mentioned cross section.

The diffractive gluon proton distribution depends on the two momentum fractions, $x_{\mathbb{P}}$ is the nucleon momentum fraction (the zigzag line in Figure 1.16) and $\beta = x/x_{\mathbb{P}}$ is the momentum fraction of the active parton.

The cross section σ_3 is in the LTA modeled using the dipole formalism, the cross section σ_3^A is then obtained from σ_3 using the Glauber approach (Eq. (1.25)).

Input to the whole LTA framework is the gluon density in the proton $g_p(x,\mu^2)$ given in Eq. (1.49). The RSZ model uses the parametrization by the Durham-PNPI group [29] at the scale $\mu^2 = 2.5$ GeV^2.

The amount of shadowing in the prediction for coherent J/ψ photoproduction using the LTA depends on the selection of $g_p(x,\mu^2)$. In the description of the RSZ model [53] it is shown that another parametrization, or the Durham-PNPI proton gluon density evaluated at a larger scale would reduce the effect of shadowing.

The selection of the Durham-PNPI parametrization for the input proton gluon density at the given scale has been made in order to provide an upper limit to the shadowing effect within the LTA theory of nuclear shadowing.

1.7.3 Model by V. Guzey, M. Strikman and M. Zhalov ("GSZ")

The GSZ model [56] is based on the Leading Twist Approximation (LTA) [54, 55] of the nuclear shadowing, the formalism is described in the previous section 1.7.2. The model already takes into account ALICE data on coherent J/ψ photoproduction [1, 57].

The photon flux is calculated in the hard-sphere approximation, formula in Eq. (1.9) for the number of photons of a given energy at a given impact parameter is integrated in the impact parameter space starting at the sum of nuclear radii, $b > 2R_A$.

The main difference of GSZ compared to RSZ (Section 1.7.2) is in the parametrization for the proton gluon density $g_p(x,\mu^2)$ in Eq. (1.49). The CTEQ6L1 gluon parametrization [58] at the scale $\mu^2 = 3$ GeV^2 is used with GSZ, so the value of nuclear modification g_A/Ag_p in Eq. (1.47) calculated by the LTA allows the model to describe the ALICE cross section of coherent J/ψ photoproduction.

The LTA calculation of the coherent J/ψ photoproduction by the GSZ model, which is consistent with ALICE data, has been used to make predictions for the coherent photoproduction accompanied by neutron emission. This is the case when one or both nuclei are excited by additional photon exchange(s) and then de-excite while emitting one or more neutrons.

1.7.4 Model by V. P. Gonçalves and M. V. T. Machado ("GM")

The model [59] is based on the dipole formalism, as was introduced in Section 1.6.2. The interaction of the virtual photon with the hadron is described as a fluctuation of the photon into a color dipole, which then interacts with the hadron. After the interaction the dipole recombines into the final state.

As in the other models, the ultra-peripheral interaction of two nuclei is decomposed into the formation of the flux of virtual photons between the interacting nuclei and the interaction of the photon with the nucleus. In GM the photon flux is calculated using the hard sphere approximation in Eq. (1.10).

The amplitude of the photon-nucleus cross section in the dipole picture has the same form as in Eq. (1.32) used for the photon-proton interaction. The corresponding amplitude for the elemental interaction of the dipole with the nucleus is Eq. (1.34).

The photon-nucleus amplitude is corrected for the general case of non-forward wave functions the same way as it is done in Eq. (1.37). Both the virtual photon and the final state are described by the respective wave functions, which are implemented as the free particle wave functions. The free particle case implies zero momentum transfer by the projectile to the target, therefore in the general case of non-zero momentum transfer a correction has to be introduced.

The cross section of photon-nucleus interaction from the amplitude is calculated by Eq. (1.33) and is corrected for the ratio of real to imaginary parts of the amplitude.

The S-matrix element in the dipole scattering amplitude in Eq. (1.34) is the specific feature of the GM model. The element contains the dynamics of the dipole-nucleus interaction. According to [60], where the dipole model and Glauber-Gribov formalism was used to calculate the nuclear structure function, the element is

$$S(x,r,b) = \exp\left[-\frac{1}{2}AT_A(b)\sigma_{\mathrm{dip}}(x,r)\right], \tag{1.50}$$

where x is the momentum fraction carried by the harder gluon of the two gluons interacting with the dipole, r is the transverse size of the dipole and b is the impact parameter.

The nuclear profile function $T_A(b)$ in Eq. (1.50) is the integration of the nuclear density in the logitudinal direction. For the nuclear density the 3-parameter Fermi distribution was used.

The cross section of dipole-nucleon interaction $\sigma_{\mathrm{dip}}(x,r)$ in Eq. (1.50) is taken from the model by Iancu, Itakura, and Munier (IIM) [61], which is based on the Color Glass Condensate [62], an effective theory of strong interactions at high energies.

The IIM model of dipole-nucleon interaction has the same parameters as the GBW dipole-proton cross section.

The parameter σ_0 is in IIM related to the dimension of the proton. The initial conditions at low energy are fixed by x_0. The parameter λ describes the energy dependence of the saturation scale.

The predicted cross section for the coherent J/ψ photoproduction by the GM model with use of the IIM model of the dipole-nucleon cross section is ≈ 10 % larger compared to the implementation of the GBW as a model of the dipole-nucleon cross section.

1.7.5 Model by A. Cisek, W. Schäfer and A. Szczurek ("CSS")

The model [63] uses the dipole approach as described in Section 1.6.2, nuclear effects are modeled by multiple scattering of color dipoles on the nuclear target. The description of the flux of virtual photons incorporates the correction for the overlap of the colliding nuclei.

The amplitude for the cross section of the color dipole and the nucleus follows Eq. (1.34) with the nuclear S-matrix element having the form of Eq. (1.50).

To obtain the dipole-nucleus amplitude, the unintegrated nuclear gluon distribution in momentum space is used. The unintegrated distribution $\phi(\boldsymbol{b},x,\kappa)$ is defined by its relation to the dipole-proton cross section $\sigma(x,\boldsymbol{r})$ and the nuclear profile function normalized to the number of nucleons $T_A(\boldsymbol{b})$ as

$$1-\exp\left[-\frac{1}{2}T_A(\boldsymbol{b})\sigma(x,\boldsymbol{r})\right] = \int \mathrm{d}^2\kappa\left[1-e^{i\kappa\boldsymbol{r}}\right]\phi(\boldsymbol{b},x,\kappa), \tag{1.51}$$

where the integration runs over the transverse momenta κ of the gluons of the unintegrated gluon distribution.

The unintegrated nuclear gluon distribution is calculated using the theory for multiple scattering of color dipoles, as shown in Figure 1.17.

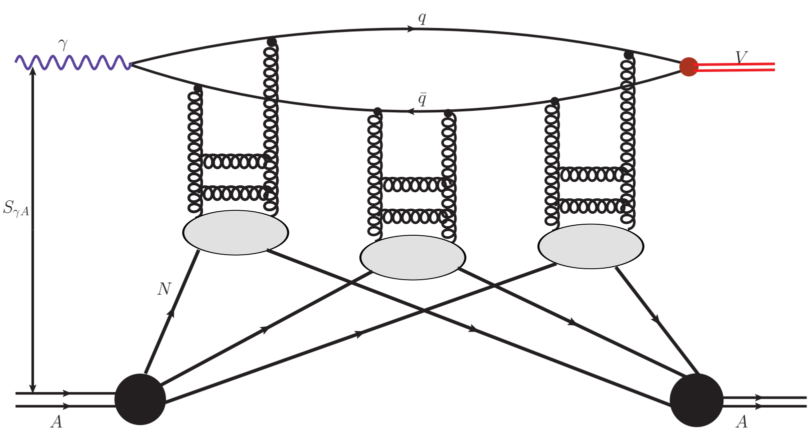

Fig. 1.17 Color dipole picture for vector meson photoproduction on nuclear target [63].

Summation of the multiple scattering series allows to construct an expansion for the unintegrated nuclear gluon density:

$$\phi(\boldsymbol{b},x,\kappa) = \sum_{j\geq 1} w_j(\boldsymbol{b}) f^{(j)}(x,\kappa), \tag{1.52}$$

where $f^{(j)}(x,\kappa)$ is the unintegrated gluon distribution of j nucleons, calculated as multiple convolutions of the proton unintegrated gluon distribution, and $w_j(\boldsymbol{b})$ is the probability of overlap of j nucleons at impact parameter $\boldsymbol{b}$.

At high energy (and small x), a correction is applied in order to account for the possible presence of a gluon in the dipole, the $q\bar{q}g$ state of the virtual photon instead of a simple quark-antiquark pair $q\bar{q}$.

The original gluon density $\phi(\boldsymbol{b},x,\kappa)$ is first evaluated at the higher $x = x_A = 0.1A^{-1/3} \sim 0.01$ in the case of the lead nucleus, and then evolved to the lower x using the Balitsky-Kovchegov equation [64, 65].

The gluon density corrected for the $q\bar{q}g$ contribution then reads

$$\phi(\boldsymbol{b},x,\kappa) = \phi(\boldsymbol{b},x_A,\kappa) + \ln\left(\frac{x_A}{x}\right) \left.\frac{\partial\phi(\boldsymbol{b},x,\kappa)}{\partial\ln(1/x)}\right|_{x=x_A}, \tag{1.53}$$

where $\partial\phi(\boldsymbol{b},x,\kappa)/\partial\ln(1/x)$ is calculated using the Balitsky-Kovchegov evolution equation.

1.7.6 Model by T. Lappi and H. Mäntysaari ("LM")

The model [66] is based on the dipole approach, where the reaction is described as a fluctuation of the virtual photon into the color dipole which then elastically scatters on the target nucleus, producing the final state. Basic ideas of the dipole picture are stated in Section 1.6.2.

The nucleus-nucleus interaction is factorized in the standard manner by convoluting the flux of virtual photons with the photon-nucleus cross section. The photon flux is calculated in the region of impact parameter $b > 2R_A$ with R_A the nuclear radius.

The dipole calculations are based on a phenomenological realistic formula for impact parameter dependent dipole-proton cross section, then the Glauber approach is used to calculate the coherent photon-nucleus cross section.

One of the two parametrizations for the dipole-proton cross section used by the LM model follows the IPsat model [67],

$$\frac{\mathrm{d}\sigma^p_{q\bar{q}}}{\mathrm{d}^2\boldsymbol{b}}(\boldsymbol{b},\boldsymbol{r},x) = 2[1-\exp(-r^2F(x,r)T_p(\boldsymbol{b}))], \tag{1.54}$$

where $\boldsymbol{b}$ is the impact parameter of the dipole-proton interaction, $\boldsymbol{r}$ is the transverse size of the dipole and x is the proton momentum fraction carried by the probed gluons.

The IPsat model provides the dipole-proton cross section using the proton profile function $T_p(\boldsymbol{b})$ in the Gaussian form of Eq. (1.42) and the function F, which is related to the proton gluon distribution as

$$F(x,r) = \frac{1}{2\pi B_p}\frac{\pi^2}{2N_c}\alpha_s\left(\mu_0^2+\frac{C}{r^2}\right)xg\left(x,\mu_0^2+\frac{C}{r^2}\right), \tag{1.55}$$

in which B_p is the width of the Gaussian proton profile, N_c is the number of colors. Values of B_p, the initial scale μ_0 and parameter C have been fixed using the HERA data.

The factorized approximation to the dipole-proton cross section in Eq. (1.54) is used with the LM model, denoted by the authors as "fIPsat":

$$\frac{\mathrm{d}\sigma^p_{q\bar{q}}}{\mathrm{d}^2\boldsymbol{b}}(\boldsymbol{b},\boldsymbol{r},x) \approx 2T_p(\boldsymbol{b})[1-\exp(-r^2F(x,r))]. \tag{1.56}$$

For the following we will introduce the imaginary part of the dipole-proton scattering amplitude as

$$\mathcal{N}(r,x) = [1-\exp(-r^2F(x,r))]. \tag{1.57}$$

The amplitude for the coherent photon-nucleus cross section takes the form of Eq. (1.37), which has the meaning of the Fourier transform of the dipole-nucleus cross section from the impact parameter to the momentum transfer at the photon-nucleus vertex. The non-forward corrections are neglected.

The dipole-nucleus cross section entering Eq. (1.37) is obtained using the Woods-Saxon nuclear density $T_A(b)$ and the dipole-proton amplitude in Eq. (1.57) as

$$\frac{\mathrm{d}\sigma^A_{q\bar{q}}}{\mathrm{d}^2\boldsymbol{b}} = 2[1-\exp(-2\pi B_p A T_A(b)\mathcal{N}(r,x))]. \tag{1.58}$$

The variable x now acquires the meaning of the momentum fraction of the probed gluons in the nucleus. The skewing effect, resulting from different momentum fractions of the two gluons interacting with the dipole, is corrected using the Shuvaev transform [21]. The correction for real part of the amplitude is also implemented.

The cross section of coherent J/ψ photoproduction is, within the framework of the LM model, calculated using a minimal set of initial assumptions, the dipole-proton cross section is fixed using the HERA data and the dipole-nucleus cross section is calculated using the nuclear geometry. The normalization of the cross section is given by the value of B_p and by the correction for the skewing effect and the real part of the amplitude, while the rapidity dependence of the cross section is provided by the structure of the dipole-target cross section.

1.8 Open issues and search for new physics using UPC

The amount of possibilities for novel methods and measurements in the field of physics of ultra-peripheral collisions is very large [3]. An outline of several examples relevant for the (near) future is given in this section.

Evidence for gluon saturation may be obtained also from the t-dependence of the photo-production cross section. Predictions in [68] suggest a specific pattern in the cross section as a function of t when saturation effects are included. This measurement has been performed at HERA, but in a kinematic range below the proposed effects.

In the case of coherent J/ψ photoproduction, current measurements suffer from ambiguity in value of Bjorken-x due to the source-target symmetry. Measurements with neutron tagging may allow to constrain the kinematics of the reaction [69].

Going to more exotic phenomena, recently the new prediction for light-by-light scattering $\gamma\gamma \to \gamma\gamma$ has been published [70], showing the possibility to measure this process already with existing LHC data.

Ultra-peripheral collisions have also potential for searches of new physics. In [71] graviton production in $\gamma\gamma$ fusion is discussed. These photons may be created as the Weizsäcker-Williams photons in UPC.

Chapter 2

The ALICE experiment at the LHC

2.1 The LHC machine

The Large Hadron Collider (LHC) is a hadron accelerator and collider constructed in the tunnel of 26.7 km circumference at CERN [72]. Beams to the LHC are injected from the accelerator complex by two transfer lines of 2.5 km. The design center-of-mass energy is 14 TeV for proton-proton collisions.

The collider is based on the synchrotron principle. The particles circulate within toroidal vacuum pipes, the orbit is held by a magnetic field oriented normal to the plane of circulation.

Acceleration to the final energy is performed once per orbit by a series of radio frequency (RF) cavities. As the energy of particles increases, the RF frequency and field B must synchronously increase with regard to larger velocity (RF) and momentum (B) of the particles.

At the design energy, the LHC magnetic field would be $B = 8.33$ T. Such a field is achieved by superconducting cryo-magnets. The design total beam current is 0.586 A, giving an energy stored in one beam of about 360 MJ.

The layout of the LHC is shown in Figure 2.1. The tunnel is not regularly circular, it consists of 8 arcs and 8 straight sections. There are two separate beams, denoted as Beam 1 rotating clockwise and Beam 2 rotating anticlockwise. The beams cross each other, and collide, at the sites of 4 experiments.

The RF systems are located in Octant 4, each beam has its independent RF system. The beam dump system in Octant 6 provides safe absorption of the energy stored in the beams at the end of a LHC run or in case of malfunction.

The beams are organized in bunches of accelerated particles, located at regular time slots around the orbit. The orbit is divided in 3564 slots per 25 ns. Each slot is sub-divided in 10 buckets per 2.5 ns. The beam is fully specified by the energy, number of filled slots, number of particles in each bunch and the configuration of filled slots around the orbit.

The particle bunch should be captured in the central bucket in the slot. Charges located outside the central bucket in the filled slot are denoted as satellite charges, charges present in slots which were not intentionally filled are called ghost charges.

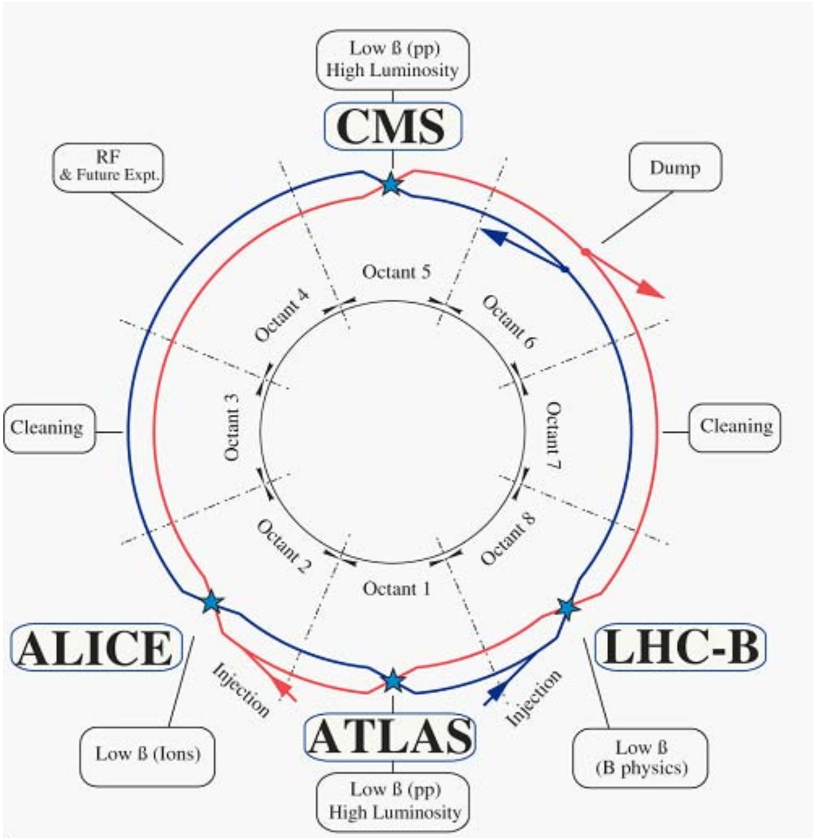

Fig. 2.1 Schematic layout of the LHC [72].

During the operation, the bunches are injected from the accelerator complex to the desired slots, the energy is continuously increased up to the final energy. Then the beams are squeezed to achieve the collisions at the experiment sites. After the operation has stabilized, the flag of stable beams is issued to allow the experiments to start collecting the data.

2.2 ALICE design considerations

ALICE (A Large Ion Collider Experiment) has been constructed as a heavy-ion detector at the CERN LHC, focused on the exploration of the physics of strongly-interacting hadronic matter and the quark-gluon plasma in nucleus-nucleus collisions at the highest values of energy density and temperature [73]. It has demonstrated an excellent performance in detecting various particle species at very high multiplicities of the collision products [74]. Moreover, the measurements of rare processes such as UPC collisions were successfully measured by ALICE. The physics program of the ALICE experiment include also proton-nucleus and proton-proton collisions.

The first proposal for a general-purpose heavy-ion detector took place in 1990, the experiment was approved in 1997 and the first collisions were detected in 2009.

The acceptance of ALICE is designed for 2 units of rapidity around mid-rapidity and 1.5

units of rapidity for the detection of forward muons. Physics considerations require tracking capabilities for a high multiplicity of charged particles of about $dN/d\eta$ = 4000, over large momentum range (up to 100 GeV/c), together with precise particle identification (PID). For PID, ALICE uses several techniques including the specific ionization energy loss dE/dx, time-of-flight and muon filters.

2.3 Detector layout

The layout of the ALICE experiment during Run 1 is shown in Figure 2.2. The central tracking detectors are placed inside a large solenoid magnet of $B = 0.5$ T. The forward muon spectrometer is located to the right of the solenoid magnet.

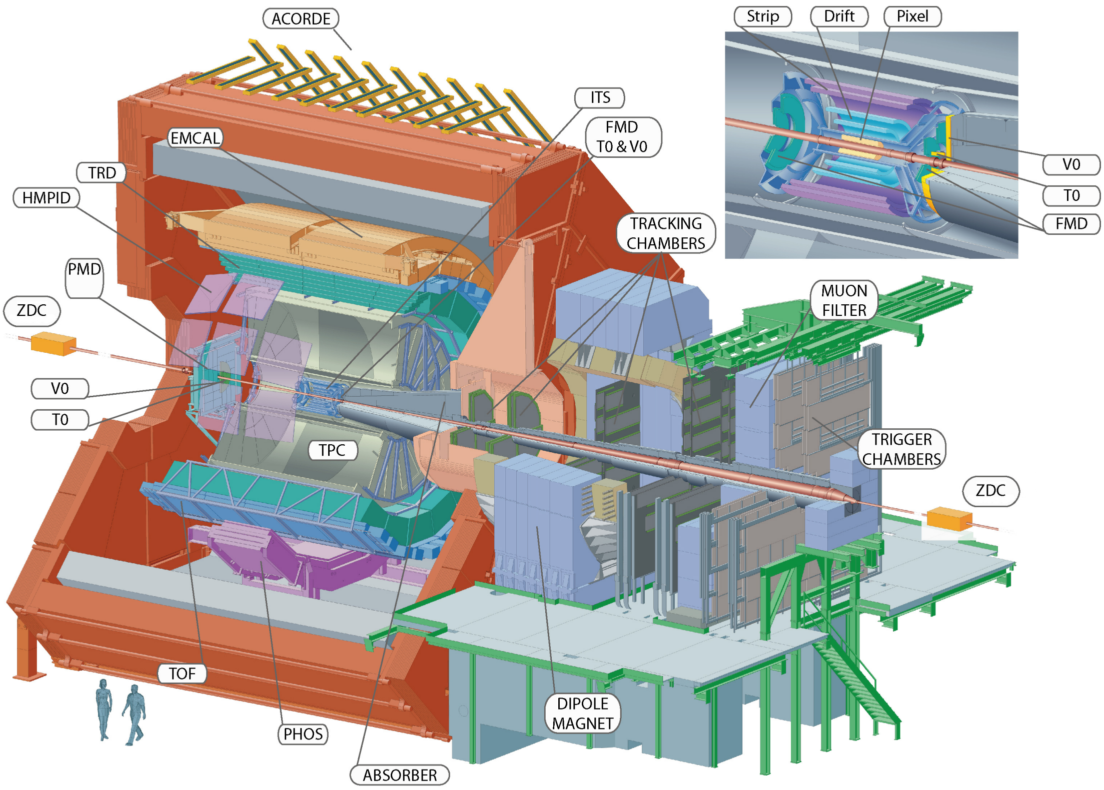

Fig. 2.2 Schematic layout of the ALICE experiment [73].

2.4 Inner Tracking System (ITS)

The Inner Tracking System (ITS) consists of six coaxial cylindrical layers of silicon position sensitive detectors with integrated pseudorapidity acceptance of $|\eta| < 0.9$. The main task of the ITS is to localize the primary vertex and the secondary vertices of hyperons and D and B mesons decays and to improve momentum and angular resolution of the tracks reconstructed in the Time Projection Chamber (TPC). The momentum resolution of the ITS is better than 2% for pions with transverse momentum p_T in the range of $0.1 < p_T < 3.0$ GeV/c.

The two innermost layers of the ITS, the Silicon Pixel Detector (SPD), have enlarged acceptance up to $|\eta| < 1.4$, they provide a trigger based on counting the fired fast-OR chips and also impose the exclusivity selection at the central rapidities in the UPC analyses. The SPD are able to reconstruct the primary vertex using tracklets, which are track fragments created from two reconstructed points in SPD, one in the inner layer and the second in the outer layer.

The SPD is made of a two-dimensional matrix of reverse-biased detector diodes, each sensor is made of 256×160 cells. The diodes are bump-bonded to the readout chips. Each cell gives binary readout if the signal, after pre-amplification and shaping, is higher than a threshold. The thickness of the sensor wafer is 200 μm. When a pixel cell detects a signal above threshold, a Fast-OR pulse is generated.

The Silicon Drift Detectors (SDD) are used as the two middle layers of the ITS. The SDD provide position information of the crossing particle and also a dE/dx signal. The acceptance of the SDD layers is $|\eta| < 0.9$.

The detection modules for the SDD are made of Neutron Transmutation Doped (NTD) silicon wafers 300 μm thick. The sensitive area of a module is split into two drift volumes with a negative HV bias applied to the central cathode. A drift electric field, parallel to the wafer surface, is generated by p+ cathode strips on both sides of the detector.

The two outermost layers of the ITS consist of the Silicon Strip Detectors (SSD). The SSD make a two-dimensional measurement of the track position, are important for matching the tracks from the TPC to the ITS and also provide a $\mathrm{d}E/\mathrm{d}x$ measurement. The detection modules of the SSD are based on 300 μm thick double sided silicon strip detectors. The rapidity acceptance of SSD is $|\eta| < 1.0$.

The main output of the ITS for physics analyses are the trigger inputs from SPD, the primary vertex reconstructed using SPD, number of SPD tracklets (multiplicity estimator at mid-rapidity), and the ITS points belonging to a given track to improve the track reconstruction precision.

2.5 Time Projection Chamber (TPC)

The Time Projection Chamber (TPC) is the main tracking detector at central rapidities. It is designed for charged-track momentum measurement, particle identification and vertex determination. The pseudorapidity acceptance of the TPC is $|\eta| < 0.9$ for tracks with its full radial length within the TPC and the possibility to match the ITS and TOF detectors. The acceptance extends up to $|\eta| \simeq 1.5$ for reduced track length. The azimuthal coverage is full. The range of track transverse momentum p_T accessible by the TPC starts at very low values, $0.1 < p_T < 100$ GeV/c with relative momentum precision of 0.7% at $p_T \simeq 0.5$ GeV/c.

The TPC is a cylindrical vessel of an inner radius of 85 cm and outer radius of 250 cm with length along the beam line of 500 cm. The volume is divided into two halves 250 cm long, filled with a gas mixture $Ne/CO_2/N_2$ (90/10/5), where the primary electrons are transported towards the end plates by the electric field parallel to the beam line. At the end plates there are the multi-wire proportional chambers with cathode pad readout.

The spacial points reconstructed within the TPC are matched to the tracks, fitted using a Kalman filter and together with the ITS reconstructed points provide track objects which can be accessed by the offline analysis. The track object carries information of the track momentum, charge, number of TPC clusters out of which it has been reconstructed and dE/dx identification.

2.6 Time-Of-Flight (TOF) detector

The Time-Of-Flight (TOF) detector is a large cylindrical area located beyond the TPC. It is designed to separate pions, kaons and protons according to particle velocities and to provide trigger inputs.

The coverage of TOF is $|\eta| < 0.9$ with full azimuthal coverage. The detector is mounted within a cylindrical vessel of inner and outer radii 370 cm and 399 cm respectively; the length of the active region of the cylinder is 741 cm.

The basic unit of the TOF structure is a strip of Multi-gap Resistive-Plate Chamber (MRPC) with 10 gaps of 250 μm. The gaps maintain a high and uniform electric field within the gas volume. Each strip has an active area of 120×7.4 cm^2, segmented into 96 pads of 3.5×2.5 cm^2. The pads are arranged on the strip into two rows per 48 pads.

For triggering purposes, the trigger pad is at the software level constructed as a logical OR of 96 pads in the two adjacent half-strips (48 pads in one half of the strip along the longer side of the strip) [75]. The area of the trigger pad is $\sim$1000 cm^2.

The trigger signal of TOF relevant for UPC physics is constructed using the number of fired trigger pads and a topology pattern of the trigger pads.

2.7 Muon spectrometer

The muon spectrometer measures the muons coming from dimuon decays of quarkonia and the dimuon continuum production. The acceptance is $-4.0 \leq \eta \leq -2.5$ in pseudorapidity and full in the azimuth. The muon spectrometer is able to compare the yields of different quarkonia species, measure the heavy flavour production via the semi-leptonic decays, and, in the case of the UPC it measures the J/ψ dimuon decays and the QED dimuon production. The resolution of the dimuon invariant mass is $\sim$ 73 MeV/c at the J/ψ peak in central Pb-Pb collisions [74].

The structure of the muon spectrometer is shown in Fig. 2.3. Closest to the nominal interaction point IP is the passive composite absorber, designed in order to absorb hadrons and photons from the interaction vertex. The tracking system consists of 10 detection planes of resistive-plate chambers (RPC). The detection planes are structured in 5 tracking stations ST1 - ST5. A dipole magnet of intergrated field of 3 T m enables the muon momentum measurement. Behind the tracking stations there is a passive muon-filter wall and four planes of trigger chambers.

During the offline analysis, the muon spectrometer provides the track object containing information on the reconstructed muon track momentum, charge, pseudorapidity and the radial position of the track at the entrance of the absorber.

The trigger system of the muon spectrometer provides the trigger inputs selecting at least one muon track with p_T above a programmable threshold or at least two unlike-sign muon tracks also satisfying (both of them or at least one) the p_T threshold.

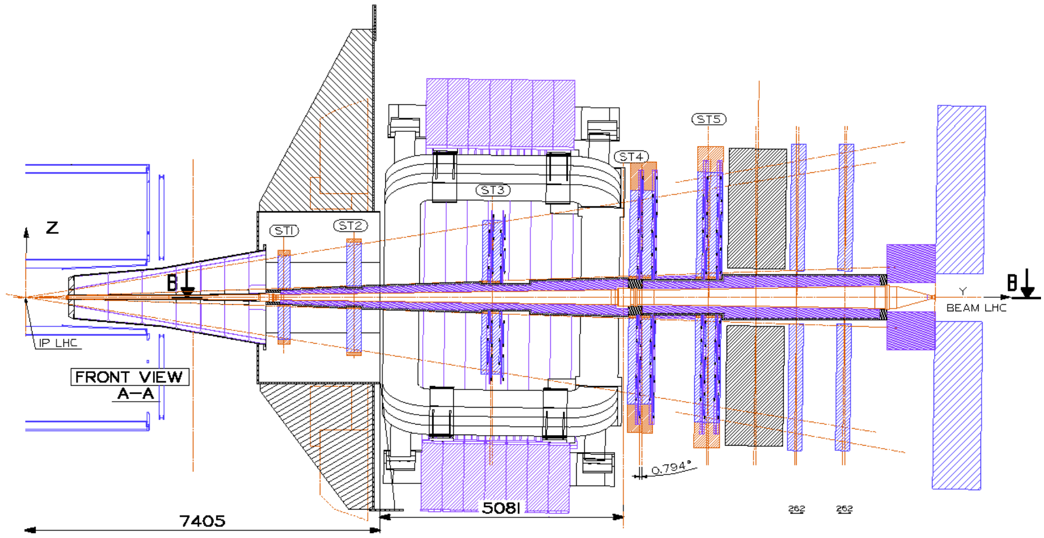

Fig. 2.3 The layout of the muon spectrometer [73].

2.8 Zero Degree Calorimeter (ZDC)

The main purpose of the ZDCs is to measure the energy carried by the spectator (non-interacting) nucleons in the very forward region in A-A collision. The calorimeter consists of two sets of hadronic sampling calorimeters (neutron and proton) placed on both sides of the ALICE experiment in the LHC tunnel at a distance of more than 100 meters from the nominal interaction point. The pseudorapidity acceptance of the ZDCs is $|\eta| > 8.8$ and $6.5 < |\eta| < 7.5$ for neutron and proton ZDC respectively, the azimuthal acceptance is full for the neutron ZDCs and $|\phi| < 10°$ for protons.

The neutron calorimeter (ZN) is located in between the LHC beam pipes at 0 degrees with respect to the beam direction. The proton calorimeter (ZP) is placed at the direction where the protons are deflected by the magnetic elements of the LHC, externally to the outgoing beam pipe. The location of one of the ZCDs is shown in Fig. 2.4.

The proton and neutron ZDCs are sampling calorimeters based on the detection of the shower produced by the incident particle in the passive absorber material. The generated shower is then detected using Cherenkov radiation produced in quartz fibres. The space restrictions are stronger for the neutron ZDCs and therefore a W-alloy is used as a passive material. The proton part of the ZDCs, which is placed outside the LHC beam pipes, is a larger device using a brass absorber.

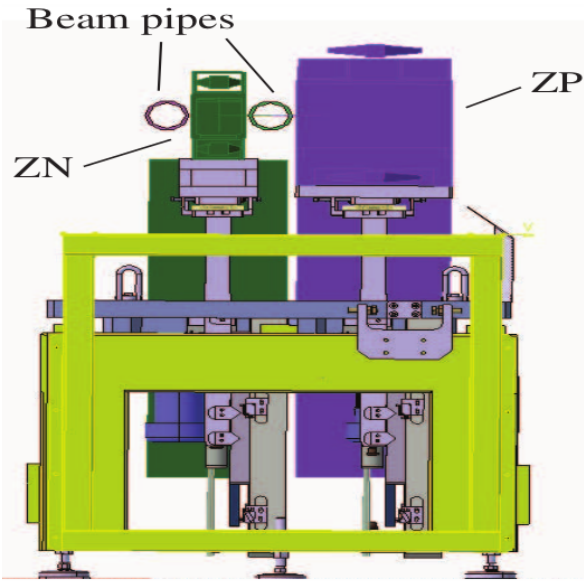

Fig. 2.4 Front view of one ZDC in the data taking position [73].

The output of the proton and neutron ZDCs usable for the physics analyses consists of the deposited energy in the proton and neutron parts, the position of the centroid of the spectator neutrons and the time of the signal occurrence in the neutron ZDC. The time sum and difference of the A-side and the C-side neutron ZDC can be used to reject the collisions where one of the Pb-ions is displaced from its nominal bunch by one or more RF buckets [74].

2.9 V0 detector

The V0 detector consists of two scintillator arrays placed on either side of the nominal interaction point, V0A and V0C. They cover pseudorapidity intervals $2.8 < \eta_{\mathrm{V0A}} < 5.1$ and $-3.7 < \eta_{\mathrm{V0C}} < -1.7$. The main task of V0 is to generate a minimum-bias trigger for the central barrel detectors, provide a centrality estimate at the trigger level for Pb-Pb collisions and reject beam-gas collisions. In the UPC analyses the V0 detectors serve mainly as a veto to hadronic contamination, but are also used as trigger detectors for the analysis based on forward J/ψ.

Each of the V0 detectors, V0A and V0C, is segmented into 32 individual counters made of BC104 scintillation material. The thickness is 2.5 and 2.0 cm for V0A and V0C respectively. The scintillating elements are read out by wave-length shifting fibers.

At the level of trigger and data analysis, the V0 detectors produce the number of fired cells in V0A and in V0C and the signal arrival time. The number of fired cells can be used then to impose the exclusivity selection in an UPC analysis and/or to trigger on the muons passing through the V0C (same side as the muon spectrometer). The arrival time of the signal is used to discriminate background events induced by the passing LHC beams.

2.10 Trigger and data acquisition

2.10.1 Trigger system

The purpose of the ALICE Central Trigger Processor (CTP) is to select the events of interest while following physics requirements and restrictions for appropriate use of the bandwidth of the Data AcQuisition System (DAQ), and the High Level Trigger (HLT). Using the trigger inputs coming from the triggering detectors, the CTP provides the decision whether the current event should be recorded.

The trigger is separated into three levels according to the time when the trigger detectors can provide their inputs. The fastest signal is called Level 0 (L0), the trigger decision reaches the detectors at 1.2 µs. The L0 is followed by the Level 1 (L1) at 6.5 µs, providing the remaining trigger inputs which are not so fast to be included in L0. The present triggers for UPC processes use only the L0 trigger. The final level of the trigger processing is Level 2 (L2) arriving at 88 µs.

The trigger inputs coming from trigger detectors are grouped into trigger classes. In total, there are 24 L0 inputs, 24 L1 inputs, 12 L2 inputs and 50 trigger classes. An input may be negated within the trigger class.

For the purposes of the UPC triggers, the trigger classes are formed out of the L0 inputs from SPD, TOF, V0 and the muon trigger.

Even though an event is recorded only by passing the L2 trigger, the number of events for each trigger class is recorded for every trigger level, L0, L1 and L2 (trigger scalers). Scalers are read at regular intervals and stored as technical data for each physics run. These numbers are essential for the luminosity measurement for a given trigger class.

To further optimize the recording bandwidth of DAQ, the trigger classes are separated into two groups, minimum bias and rare triggers. Due to the fact that the needed trigger rate for a given process may be different from the total event rate, introducing rare triggers prevents the DAQ to become saturated by triggers corresponding to minimum bias processes. All of the UPC processes belong to the group of rare triggers.

2.10.2 The Data Acquisition System (DAQ)

The DAQ project was designed in order to collect the data from all ALICE detectors and transport them to the CERN Tier-0 computing center. The bandwidth of the DAQ, the amount of data transported through the DAQ per unit of time, is optimized with regard to physic performance and with constraints given by technical limitations, cost and storage capacity.

The structure of the DAQ system is shown in Fig. 2.5. In the structure, the individual ALICE detectors are located in between the TTC and FERO modules.

The Timing, Trigger and Control (TTC) system acts as an interface to the Local Trigger Unit (LTU), which issues the trigger signal coming from the Central Trigger Processor (CTP) to the detector. The output data of the detector are transmitted by the Front-End Read-Out electronics (FERO) to the Detector Data Links (DDL). The protocol used by the DDLs is common for all ALICE detectors.

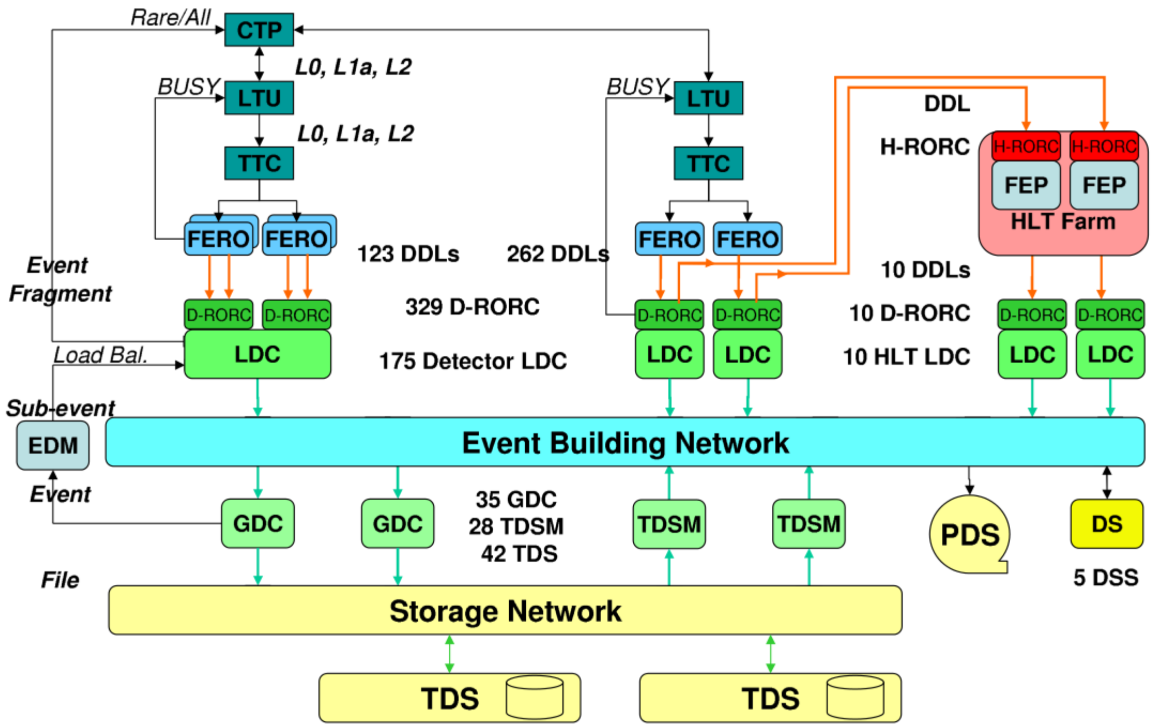

Fig. 2.5 Structure of the ALICE DAQ [73].

The event fragment issued by the detector to the DDL is received by the DAQ Readout Receiver Card (D-RORC). The D-RORCs are PCI-X modules hosted by the Local Data Concentrators (LDC), which are commodity PCs. Each LDC can handle more than one D-RORC. The D-RORCs write the data they receive to the memory of the LDC, the event fragments coming from each D-RORC are assembled within the LDC into sub-events.

The sub-events built within the LDCs are transported to the Global Data Collectors (GDC), which are also commodity PCs. In the GDCs the complete events are built and the event data are then transported to the Transient Data Storage (TDS). There is no direct communication between the LDCs, instead, the Event Destination Manager (EDM) informs the LDCs about the availability of the GDCs.

The High Level Trigger (HLT) acts, within the DAQ architecture, as an independent detector. The HLT receives all the relevant data via the DDLs through its HLT Readout Receiver Card (H-RORC) and Front-End Processors (FEP). The output data of the HLT and the decisions made by it are sent via the standard DDLs to the LDCs dedicated to the HLT.

Exporting ALICE data to the Permanent Data Storage (PDS) at the CERN computing center is driven by the TDS movers (TDSM). The data in the PDS finally become available for reconstruction and physics analysis.

2.10.3 Data taking during LHC collisions

Once the LHC machine declares stable beams, the data taking by the experiment may begin. When starting the data taking, the detectors, triggers and the data acquisition are turned to the ready state, able to detect the products of the LHC collisions and bring the data to the mechanisms of the DAQ.

The operation of the experiment is controlled by the Experiment Control System (ECS). The ECS, via system specific human interfaces, is the top level of controlling the operation of the detectors, individually or as a group of detectors, the trigger and the DAQ.

The "run" is the basic term describing the conditions of the data taking. The run can be defined as a period of operation of the experiment under constant conditions. When the data taking is to be started, the ECS issues commands to the detectors to perform the calibration routines and all other necessary procedures to bring themselves to the ready state. Once all of the detectors, the trigger and the DAQ declare readiness, the run may start and the data starts to be recorded.

The run is assigned a unique integer number. The number of the current run is the number of the previous run incremented by one. Not all of the runs contain data relevant for future physics analysis, since also calibration or other technical runs are assigned a number.

The run is maintained as long as the LHC is in stable operation. The reason to stop a run is either stopping of the LHC beams, a technical problem in the equipment or the need to change the configuration of the experiment.

After the run – the data taking – is stopped, all the relevant calibration informations are to be recorded and referenced to that run, since the next run will perform new calibrations at the beginning and the data taking will take place under different conditions.

The calibration information is important for the reconstruction of the data. The performance of the experiment, such as the momentum resolution and particle identification, depends on the quality of the calibration.

The calibration parameters are collected during the data taking or determined using dedicated calibration runs. At the end of the run, the parameters are collected using the corresponding system and stored as objects into the Offline Condition DataBase (OCDB). The parameters are e.g., geometric alignment of the detectors, pedestals and maps of the detector channels and response calibrations.

The reconstruction program, working with the raw data for a given run, can access the calibration parameters by retrieving the corresponding objects in the OCDB.

The parameters in the OCDB are also important for detector simulations, when the conditions of data taking are to be reproduced.

The runs are grouped into so called "periods" of data taking. The period is closed, and a new initiated, when the LHC energy, configuration of bunch distribution along the LHC or the beam particles are changed, or when a major modification to the detector configuration is performed, such as replacing trigger classes. The period is denoted by the last two digits of the year and a single letter incremented in alphabetical order. The periods relevant for the presented UPC analyses are LHC11h for Pb-Pb collisions and LHC13d, LHC13e and LHC13f for p-Pb collisions.

2.10.4 AliRoot framework

The ALICE offline framework, AliRoot, is an object-oriented environment based on the ROOT system [76], covering all activities related to the reconstruction, data analysis and simulations. The AliRoot is a collection of classes written in C++, while some parts are in FORTRAN, but these are accessed by virtual C++ classes.

The flow of the activities performed by AliRoot is shown in Fig. 2.6. At the level of the Monte Carlo simulations, the event generator of a given physics process provides the particles specified by their momenta and charges. The particles are transported through the detector, creating hits in the sensitive volumes in the detectors from the calculated energy deposition. The response function of readout electronics is applied to the hits, giving the digits. Taking of the real data, as described in Section 2.10.3, creates the raw data, which are equivalent to the simulated digits. The reconstruction chain is then the same for the real data reconstruction as well as for the simulations. Local reconstruction in each detector results in clusters, which are the spacial points associated with a given track of the measured or simulated particle. Typically, the cluster may be formed out of several neighboring hits by a dedicated algorithm. A Kalman filter is applied in order to get tracks out of the clusters. The final output of the reconstruction is the Event Summary Data (ESD) file. In the case of the MC simulations, the ESD contains also information about the generated particles.

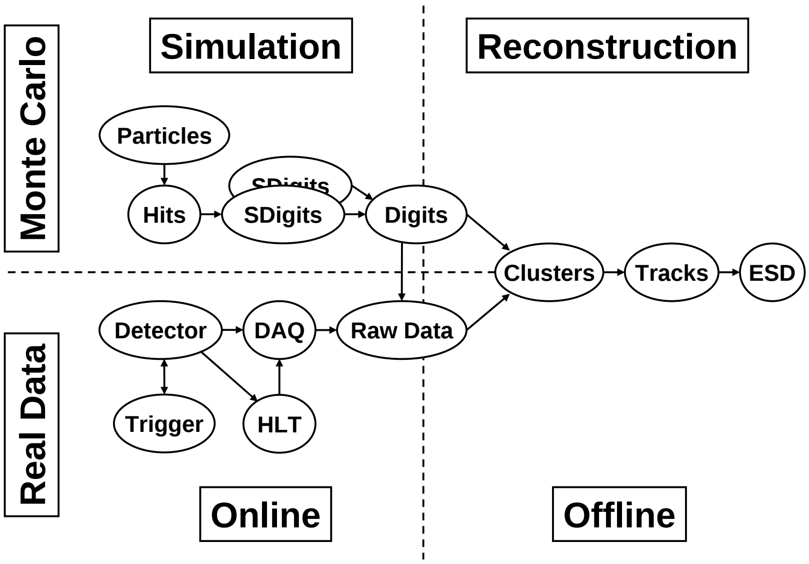

Fig. 2.6 Simulation and reconstruction activities managed by AliRoot [73].

The “event”, as it is used in the ESD acronym, is one collision of the beams recorded by the detector during the data taking, or one iteration of the event generator producing the particles belonging to the simulated interaction.

The simulation of the detector response is performed by transporting the generated particles through all the detector and construction material using the GEANT 3 [77] package. The full geometry of the ALICE detector is described using the ROOT geometry classes. The magnetic field is described by a detailed parameterization.

The events, either from real data or from MC simulations, are stored in objects in the ESD files. A more condensed format of the data, the Analysis Object Data AOD, can be derived from the ESD.

Physics analysis is performed by the analysis task, which runs over the ESD or AOD files and applies the algorithms to the event object. The algorithms typically process the reconstructed tracks in the event and evaluate other event observables such as energy deposition in the ZDCs, number of fired cells in the V0 detectors or multiplicity in the SPD.

A model of distributed computing [78] is used to cover the need for computing resources. The model [79] consists of a grid of computing Tier-0, Tier-1 and Tier-2 centers placed almost all around the world. Ordered, or scheduled, analyses run typically on Tier-1 centers, while unscheduled end-user analyses run on Tier-2 centers. Each physics analysis is divided into separate jobs, each job is assigned a set of data files to process. At the end, the outputs of all the jobs belonging to the given analysis are merged into the output file(s).

The MC simulations also use the Grid. Each simulation job performs the chain of tasks presented in Figure 2.6 for a unique set of generated events. The output of each job is then an ESD file. The grid jobs are driven using the Job Description Language JDL.

2.11 Organizational structure of the ALICE collaboration

The ALICE experiment is operated by the Collaboration of the member institutes. Members of the Collaboration are all physicists, engineers or graduate students belonging to one of the member institutes. The Collaboration is organized into task-specific boards and working groups.

The decision-making body is the Collaboration Board (CB), consisting of one representative from each institute. Each decision is accepted after consensus, or as the result of a voting procedure.

The second level of responsibility in the management structure of the Collaboration is the Management Board (MB). It is the body directing the experiment in scientific, technical, organizational and financial matters. The Spokesperson of the Management Board is the ALICE representative to the outside world and to the CERN organizational structure.

The Technical Board is directing the technical coordination. The board can take technical decisions, while the matters of more importance to the performance or costs are presented to the MB.

The costs and resources are managed by the Finance Board. Important decisions are presented to the CB for endorsement.

The Physics Board (PB) is responsible for the coordination of physics activities, such as simulations and physics performance of the experiment. Publications, conference contributions and internal notes are coordinated by the PB.

The Computing Board is responsible for the offline software framework and the Data Acquisition (DAQ). Proposals made by the board are presented to the MB.

The experimental work leading from the reconstructed LHC data to journal publications of physics importance is performed within the specific Physics Working Groups (PWG). Each PWG is chaired by two conveners, which are members of the PB.

The PWGs are grouped according to similar physics interests and further subdivided into Physics Analysis Groups PAG. The ultra-peripheral processes are studied within the UPC-PAG, which is part of the PWG-UD enclosing also studies of diffractive processes and cosmic-ray physics as well as measurements of the multiplicity distribution of produced particles in pp collisions.

Each physics analysis is first discussed within the PAG, progress is reported at the regular PAG meetings. When the analysis is becoming ready to provide the desired measurement, an internal analysis note is completed as a basis for the draft of a scientific publication.

The draft of the publication is reviewed by the Internal Review Committee (IRC). The mandate of the IRC is to perform a comprehensive review of the physics analysis, related documentation, text of the paper draft and answers to comments from the Collaboration and the journal referee.

The publication is accepted by the IRC after answering the comments from the IRC members and from the Collaboration and sent to the journal.

Chapter 3

General procedures towards the cross section measurement

3.1 ALICE measurements of J/ψ in UPC

We need to identify the J/ψ mesons and reconstruct their momenta. As the J/ψ is highly unstable, with a mean life time in order of 10^{-20} seconds, we may detect only its decay products and out of them reconstruct the original J/ψ.

Almost 90% of the decays of the J/ψ lead to a number of lighter hadrons, making it not feasible to detect every such secondary particle. Instead, the decays into pairs of electrons or muons are used for reconstruction. The dielectron or dimuon (dilepton) decays $J/\psi \to e^+e^-$ and $J/\psi \to \mu^+\mu^-$ have about 6% probability to occur [80].

Since the J/ψ is the only new particle produced in the ultra-peripheral process, the experimental signature is very clear, we expect just two tracks in an otherwise empty detector. See Figure 3.1 for a comparison of a hadronic collision and an UPC collision.

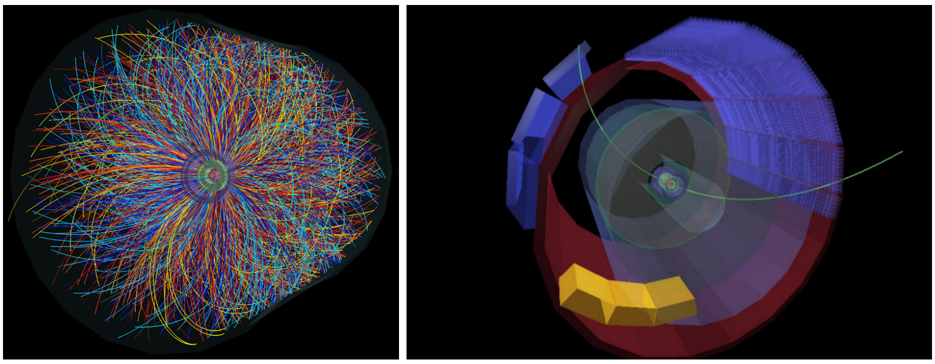

(a) Hadronic collision (b) Ultra-peripheral event

Fig. 3.1 Comparison of a typical hadronic Pb-Pb collision (a) and an UPC collision (b). We can see a large number of tracks in the detector coming from the hadronic interaction in contrast to the two tracks from the J/ψ decay in the UPC process.

Once the electrons or muons are detected, the J/ψ is reconstructed by summing-up their momentum 4-vectors. The interval of rapidity, as defined in Eq. (1.12), where the J/ψ can be measured, is determined by the acceptance and efficiency of the detector to measure the electrons or muons.

ALICE is able to reconstruct the J/ψ in the forward rapidity when the muons are detected in the muon spectrometer, in the semi-forward rapidity when one muon is detected in the muon spectrometer and the second one is detected in the central tracking detectors, and in the central rapidity when the electrons or muons are detected in the central tracking detectors.

3.2 Measured differential cross section

In a classical scattering experiment the cross section has a meaning of the transversal size of the target, while in a reaction where new particles are produced, the cross section characterizes the production mechanism. The validity of a theory prediction is tested by its ability to predict the value of the cross section.

The experimental determination of the cross section is based on counting the number of occurrences of the process in question with simultaneous knowledge of the efficiency to detect its occurrence and the parameters of the beams whose collisions produce the process.

The determination of the differential cross section for J/ψ production with respect to the rapidity y of the J/ψ follows the basic equation

$$\frac{\mathrm{d}\sigma}{\mathrm{d}y} = \frac{N}{\varepsilon \times \mathscr{B} \times \mathscr{L} \times \Delta y}, \tag{3.1}$$

where N is the number of measured events (the yield), ε is the total acceptance and efficiency correction and Δy is the width of the rapidity interval in which the process is measured. By the event we mean one measured occurrence of the process. The branching ratio $\mathscr{B}$ gives the probability of dilepton decay of the J/ψ.

The luminosity $\mathscr{L}$ describes the interacting beams. The instantaneous luminosity is the number of incoming particles in the overlap of the beams per unit time per unit area. By the luminosity $\mathscr{L}$ in Eq. (3.1) we will always mean the integrated luminosity over the data taking period.

3.3 Luminosity measurement

The luminosity at a collider experiment, like the LHC, is defined using the revolution frequency f_r of circulating bunches, the number of bunch crossings n_b at the interaction point, the average number of interactions in one bunch crossing μ and the total inelastic cross section σ_{inel} as [81]

$$L = \frac{\mu n_b f_r}{\sigma_{\mathrm{inel}}}. \tag{3.2}$$

In ALICE, a procedure to measure a visible cross section σ_{vis} is implemented. The advantage is that there is no need to know the total inelastic cross section. The visible cross section is the fraction of inelastic events which can be seen by a given trigger condition; it is denoted as a reference process. Once the σ_{vis} of the reference process is known, the luminosity is given by the measured rate of the reference process divided by the corresponding visible cross section. The knowledge of the fraction of σ_{vis} to σ_{inel} is not necessary.

The visible cross section of the reference process is measured using the van der Meer scan (vdM) technique [82, 83]. The two colliding beams are displaced with respect to each other along the transverse directions x and y, the rate of the reference trigger is collected for each displacement, giving the effective beam widths h_x and h_y.

The luminosity for a head-on collision (no beam displacement) of a pair of bunches containing particle intensities N_1 and N_2 is given by

$$L = \frac{N_1 N_2 f_r}{h_x h_y}. \tag{3.3}$$

Using the value of the rate of head-on collisions f^{00}, the visible cross section for the reference process is

$$\sigma_{\mathrm{vis}} = f^{00}/L. \tag{3.4}$$

The integrated luminosity $\mathscr{L}$ of a given UPC trigger, appearing in Eq. (3.1), is then given as

$$\mathscr{L} \equiv \int L\mathrm{d}t = \frac{N^{\mathrm{ref}} P^{\mathrm{ref}}}{\sigma_{\mathrm{vis}}} \cdot R, \tag{3.5}$$

where N^{ref} is the number of reference triggers, σ_{vis} is the visible cross section of the reference process measured in the vdM scan using Eq. (3.4) and Eq. (3.3), P^{ref} is the pile-up correction and R is the trigger lifetime.

The pile-up correction P^{ref} accounts for the possibility of several collisions firing the reference trigger in the same bunch crossing. Using Poisson statistics, it is given by

$$P^{\mathrm{ref}} = \frac{\mu}{1 - e^{-\mu}}. \tag{3.6}$$

The average number of interactions per bunch crossing μ is

$$\mu = \ln\left(1 - \frac{f^{\mathrm{ref}}}{f_r n_b}\right), \tag{3.7}$$

where f^{ref} is the rate of the reference process. The value of μ may be time-dependent as the beam intensities evolve.

The trigger lifetime R is the fraction of time where the signals of the UPC trigger are accepted by the trigger electronics. Counters for all trigger classes are recorded during the run at all levels of the trigger logic and then stored in the OCDB. The L0b level is the number of triggered events and L2a is the number of triggers passing all possible vetoes within the trigger logic.

The value of the trigger lifetime is then

$$R = \frac{N_{L2a}^{\mathrm{UPC}}}{N_{L0b}^{\mathrm{UPC}}}, \tag{3.8}$$

where N^{UPC} is the number of times the trigger set for the UPC process was fired at the given level of the trigger logic.

3.4 Corrections for acceptance and efficiency

The acceptance and efficiency ε in the cross section Eq. (3.1) is the probability that the J/ψ created in the collision is successfully reconstructed in the detector.

The correction can be determined using Monte Carlo (MC) simulations, where the events of the process in question are generated by a software generator of the process, then folded by a detailed detector simulation (see Section 2.10.4 for details), and finally analyzed applying the same requirements as were the basis for the determination of the number of measured events (N in Eq. (3.1)).

The analysis of the simulation provide the number of successfully reconstructed events, n_{rec} and the number of events which were generated as the input to the simulation, n_{gen}. Both numbers should be taken in a defined phase space. The least requirement is the interval $y_{\mathrm{min}} < y < y_{\mathrm{max}}$ in rapidity y of the J/ψ.

The correction is then the ratio of these two numbers,

$$\varepsilon = \frac{n_{\mathrm{rec}}(y_{\mathrm{min}} < y < y_{\mathrm{max}})}{n_{\mathrm{gen}}(y_{\mathrm{min}} < y < y_{\mathrm{max}})}, \tag{3.9}$$

dividing the number of reconstructed J/ψ in a given rapidity interval by the number of J/ψ generated in the same interval.

In order to account for time-varying conditions of the data taking in the simulations, the full simulation is split into a set of simulations running at the conditions specific for each run of the data sample used in getting the number of measured events. The conditions are loaded from the Offline Condition DataBase (OCDB), see Section 2.10.3 for details.

Each run is provided a unique set of input events. The efficiencies are calculated separately for each run according to Eq. (3.9), the final efficiency entering Eq. (3.1) is calculated as the average of the partial efficiencies weighted by the luminosities of the runs.

The efficiency from the simulation may be further corrected for phenomena not accurately covered within the simulation framework, such as the efficiency of one particular trigger element or the correction to the original generator setup.

The STARLIGHT event generator [34, 36], Section 1.5, was used as the event generator in UPC simulations. At the time when the analyses described in this work have been conducted, STARLIGHT was not embedded into AliRoot. Therefore, the specific data output of STARLIGHT was converted to the data format which can be recognized by AliRoot, and then inserted as an input to the simulation.

In order to save computing time and the data space occupied by the simulation output files, the events generated by STARLIGHT are preselected for rapidity y within the fiducial region, $y_{\mathrm{min,fid}} < y < y_{\mathrm{max,fid}}$. The preselection is made as an intermediate step prior to converting the STARLIGHT output to the data format suitable for AliRoot.

Besides STARLIGHT, the JPSILIGHT [53, 84] generator was used in the analysis of coherent J/ψ production in Pb-Pb UPC. The simulation using this generator served as a cross-check of the analysis and for the assessment of the systematic error coming from the choice of the generator.

MC productions related to the measurement of exclusive J/ψ photoproduction in p-Pb UPC, fully managed by the author, cover almost 50 million simulated events. The model of distributed computing, as described in Section 2.10.4, is generally used also for the simulations. Each run in each production was split into 400 jobs, giving almost 10 million of computation jobs running throughout the simulation campaign. The amount of time to finish all the jobs is about one thousand years.

3.5 Signal extraction

The number of measured events N in Eq. (3.1) is obtained from data by applying the selection criteria tuned for the process in question. Even then, a variety of other phenomena may be present in the selected sample of events. Treatment of such contributions is mainly specific for each analysis.

What is common for both analyses presented in this work is the feed-down from ψ', the higher bound state of the $c\bar{c}$ pair. The ψ' can be created in the protoproduction reaction in analogy with J/ψ production and can decay with the J/ψ in the final state as $\psi' \to J/\psi + X$ with X for the other particles coming from the decay (mainly pions). The J/ψ from the decay thus may contribute to the signal if the other decay products are for some reason not observed in the detector.

The correction for feed-down f_D is calculated using the efficiencies ε of the J/ψ produced directly and for those coming from the decay of ψ', which we will denote as J/ψ^x:

$$f_D = \frac{\sigma_{\mathrm{SL},y}(\psi') * \mathscr{B}(\psi' \to J/\psi + X) * \mathscr{B}(J/\psi \to l^+l^-) * \varepsilon(J/\psi^x)}{\sigma_{\mathrm{SL},y}(J/\psi) * \mathscr{B}(J/\psi \to l^+l^-) * \varepsilon(J/\psi)}, \tag{3.10}$$

where $\sigma_{\mathrm{SL},y}$ is the STARLIGHT theoretical cross section for a given rapidity interval and $\mathscr{B}$ is the branching ratio of the given decay. Both efficiencies are obtained using the MC simulations.

The branching ratios of the leptonic decay of the J/ψ cancel out, so we are left with

$$f_D = \frac{\sigma_{\mathrm{SL},y}(\psi') * \mathscr{B}(\psi' \to J/\psi + X) * \varepsilon(J/\psi^x)}{\sigma_{\mathrm{SL},y}(J/\psi) * \varepsilon(J/\psi)}. \tag{3.11}$$

The theoretical cross section $\sigma_{\mathrm{SL},y}$ is obtained using the total cross section σ_{SL} and the ratio R_y of the number of events generated into the given rapidity interval to all generated events corresponding to σ_{SL}:

$$\sigma_{\mathrm{SL},y} = \sigma_{\mathrm{SL}} * R_y. \tag{3.12}$$

The feed-down correction is applied to the number of measured events. If we denote N_{raw} the uncorrected number, then the corrected number of events N_{corr} is calculated as

$$N_{\mathrm{corr}} = \frac{N_{\mathrm{raw}}}{1 + f_d}. \tag{3.13}$$

The final list of corrections which are applied to the number of measured events, as well as the method of obtaining the yield, is specific to each analysis.

3.6 Experimental cross section of photon-proton interactions

Equation (3.1) provides the production cross section from the two beams of colliding particles. However, in p-Pb collisions, the main objective is the cross section for the interaction of photons on the proton target, $\sigma(\gamma\text{+p})$.

The cross sections are related via the spectrum of virtual photons of the Pb ion. The spectrum (also called the photon flux) is the distribution of photons carrying the momentum k, dN_γ/dk. The relation is

$$\frac{\mathrm{d}\sigma}{\mathrm{d}y}(\text{p+Pb} \to \text{p+Pb} + J/\psi) = k\frac{dN_\gamma}{dk}\sigma(\gamma\text{+p} \to J/\psi\text{+p}). \tag{3.14}$$

The photon flux can be calculated using STARLIGHT as described in Section 1.5.1.

Chapter 4

Measurement of coherent J/ψ photoproduction in forward Pb-Pb UPC

4.1 Physics impact

Coherent photoproduction of J/ψ, occurring when the photon couples to the whole nucleus, is sensitive to the nuclear gluon distribution. A brief introduction to the mechanism of coherent photoproduction is given in Section 1.3.2.

The current knowledge of the nuclear gluon modification, R_g^A, defined by Eq. (1.44) as a relation of the free proton gluon distribution $g_p(x,Q^2)$ to the nuclear gluon distribution $g_A(x,Q^2)$ as $g_A(x,Q^2) = g_p(x,Q^2) \times R_g^A(x,Q^2)$, is not as well constrained by the DIS and Drell–Yan processes as the similar coefficient is for quarks. Especially at small values of momentum fraction x and intermediate scales Q^2 there are considerable theoretical uncertainties in determining the R_g^A.

The situation is shown in Figure 4.1 for the lead nucleus and $Q^2 = 1.69$ GeV^2 [85]. At small values of x, $x \lesssim 0.04$, the effect of gluon shadowing occurs (see Section 1.4.2), partially depleting the gluon density with respect to that of the free protons, $R_g^A < 1$ here. Enhancement of the gluon density, $R_g^A > 1$, takes place in the middle interval $0.04 \lesssim x \lesssim 0.3$, the phenomenon is known as antishadowing. The EMC effect [86] causes the depletion in the interval $0.3 \lesssim x \lesssim 0.8$, the mechanism is different to that of shadowing. The region of Fermi motion for large momentum transfer $x \gtrsim 0.8$ creates another enhancement in the nuclear gluon density. As we can see from Figure 4.1, large uncertainties are present especially in the shadowing region.

Coherent photoproduction of vector mesons, on the other hand, is a good probe of the gluon distribution at low Bjorken-x, because the cross section is proportional to the square of the nuclear gluon distribution.

Previous experimental data on coherent photoproduction have been obtained at RHIC. Coherent photoproduction of ρ^0 mesons was measured by STAR collaboration [87–89] and coherent photoproduction of J/ψ by PHENIX [32]. However, the scale imposed by the rest mass of light ρ^0 is not suitable to use pQCD, and the measurement by PHENIX provide no definite physics conclusions, mainly due to lack of statistics.

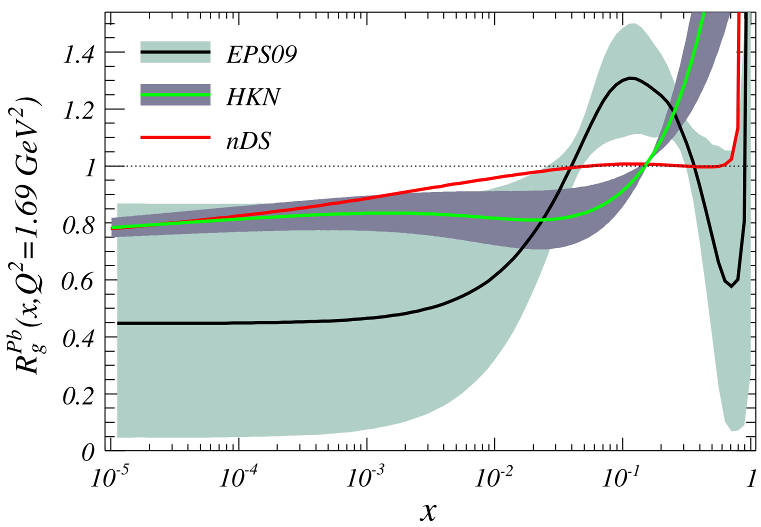

Fig. 4.1 Gluon nuclear modification for the lead nucleus. [85]

In ALICE, at the forward rapidity reached by the muon spectrometer (see Section 2.7), the measurement of coherent J/ψ photoproduction was performed in the rapidity interval $-3.6 < y < -2.6$ in Pb-Pb collisions at $\sqrt{s_{\mathrm{NN}}} = 2.76$ TeV[1].

The momentum fraction of the probed gluons is given by Eq. (1.17), which states that $x = (M_{J/\psi}/\sqrt{s_{NN}})\exp(\pm y)$. The ambiguity introduced here by the $\pm$ sign of the rapidity refers to the possibility of each of the lead nuclei to act as a source or a target of the virtual photons. In our case the x takes values of $\approx 10^{-2}$ and $\approx 10^{-5}$. The photon flux corresponding to the larger x values amounts to about 96% of the cross section, so this process probes mainly the gluon distribution at $x \sim 10^{-2}$.

The scale of the measurement is determined by the mass of the J/ψ as $Q^2 \approx M^2_{J/\psi}/4$, neglecting the virtuality of the photons in the approximation.

These values of x and Q^2 put the measurement at the beginning of the shadowing region, the cross section of coherent J/ψ photoproduction constraints the amount of nuclear shadowing in this region.

A wide variety of model predictions of the coherent cross section have preceded the LHC measurement. Refer to Section 1.7 for a description of methods and assumptions that the models use. The models use a variety of approaches both to the photon-nucleus interactions and to the nuclear effects.

The measurement of the coherent cross section presented in [1] is the first LHC photoproduction measurement and opened this field of study at the LHC. Nowadays, ALICE, LHCb and CMS have published results in this field.

4.2 Experimental procedure to measure the coherent J/ψ photoproduction cross section

This section describes all the analysis steps towards the measurement of the cross section for the coherent photoproduction of J/ψ in the forward rapidity $-3.6 < y < -2.6$. The procedures described in Section 3 have been followed.

4.2.1 Characterization of coherent events

In the data we expect the tracks of the J/ψ dimuon decay $J/\psi \to \mu^+\mu^-$ in the forward rapidity and no other activity in the detector.

The J/ψ is expected to have a very low transverse momentum $p_T \lesssim 0.3$ GeV due to the coherence of the process.

In the ZDC (Section 2.8) we may expect a signal of up to few neutrons from nuclear break-up, taking place after additional photon exchange between the nuclei. Such interaction does not spoil the coherence of the photoproduction.

Other detectors used in the analysis are V0 (Section 2.9) and the pixel detectors of the ITS (Section 2.4).

4.2.2 Trigger configuration

A dedicated trigger class was used to get candidate coherent events, see Section 2.10.1 about the ALICE trigger system. The trigger class is CMUP1-B-NOPF-ALLNOTRD (in the following it will be referred to just as CMUP1).

The CMUP1 class is defined via its L0 trigger inputs as

CMUP1 = 0MSL & 0VBC & !0VBA

with the inputs working as

0MSL: single muon with $p_T > 1$ GeV,

0VBC: at least one V0C cell fired in beam-beam time window,

0VBA: at least one V0A cell fired in beam-beam time window.

Thus the trigger selects the events with at least one muon track candidate (the muon trigger system is separated of muon tracking), minimal detectable signal in V0C and no signal in V0A, both during the expected time of the beam-beam interaction.

The rapidity coverage of the V0C detector overlaps most of the coverage of the muon arm ($-3.7 < \eta_{\mathrm{V0C}} < -1.7$ and $-4.0 < \eta_{\mathrm{muon}} < -2.5$). Requiring some activity in V0C suppresses beam-gas events from firing of the muon trigger (the vacuum in ALICE during 2011 was not optimal).

The total veto in the V0A detector, located on the opposite side the the muon spectrometer, removes hadronic events.

4.2.3 Definition of the cross section

The formula for the cross section originates from the general Eq. (3.1). The cross section of the J/ψ coherent photoproduction, $\mathrm{d}\sigma^{\mathrm{coh}}_{J/\psi}/\mathrm{d}y$, is

$$\frac{\mathrm{d}\sigma^{\mathrm{coh}}_{J/\psi}}{\mathrm{d}y} = \frac{N^{\mathrm{coh}}_{J/\psi}}{\mathscr{B}\cdot\varepsilon_{J/\psi}\cdot\mathscr{L}}\cdot\frac{1}{\Delta y}, \tag{4.1}$$

where $N^{\mathrm{coh}}_{J/\psi}$ is the number of measured coherently produced J/ψ, $\mathscr{B}$ is the branching ratio of the J/ψ to decay to the pair of muons, $\mathscr{B}(J/\psi\to\mu^+\mu^-) = 0.0593\pm0.0006$ [80]. $\mathscr{L}$ is the luminosity of the data sample in which the $N^{\mathrm{coh}}_{J/\psi}$ was measured. The factor $\varepsilon_{J/\psi}$ accounts for all inefficiencies and the acceptance of the detector. Δy is the width of the rapidity interval where the cross section was measured.

The total acceptance and efficiency correction $\varepsilon_{J/\psi}$ covers the detector acceptance, efficiencies and effects of the applied selection criteria. During the data taking, the threshold of the V0 was set to about ≈ 1.15 minimum ionizing particles. Such value was motivated by the use of V0 to trigger Pb-Pb collisions according to their centrality. As a consequence to the UPC events (there are just two muons), some inefficiency of the 0VBC trigger input is introduced.

For the following, we factorize the total efficiency correction as

$$\varepsilon_{J/\psi} = \varepsilon_{\mathrm{V0}}\cdot(\mathrm{Acc}\times\varepsilon)_{J/\psi}, \tag{4.2}$$

in which $\varepsilon_{\mathrm{V0}}$ is the efficiency of the 0VBC trigger input, issued by the V0C detector, and the rest, the $(\mathrm{Acc}\times\varepsilon)_{J/\psi}$, represents the correction to the remaining acceptance and efficiencies of the detector.

Determination of $\varepsilon_{\mathrm{V0}}$ from the MC simulation is not feasible due to large fluctuations of the deposited energy in the two-muon UPC events. The MC would need to perfectly reproduce the signal distribution in a relatively thin scintillator out of which the V0 detector is made. An alternative trigger class suitable for a data-driven estimate of $\varepsilon_{\mathrm{V0}}$ was not present during the data taking.

Therefore the decision was made to get the $\varepsilon_{\mathrm{V0}}$ efficiency using the reference QED process of two-photon production of dimuon pairs (see Section 1.3.3). The theoretical cross section $\sigma_{\gamma\gamma}$ of $\gamma\gamma\to\mu^+\mu^-$ is known up to a 20% accuracy. The CMUP1 trigger was also sensitive to such events.

The V0 efficiency can be written as

$$\varepsilon_{\mathrm{V0}} = \frac{N_{\gamma\gamma}}{(\mathrm{Acc}\times\varepsilon)_{\gamma\gamma}\cdot\mathrm{d}\sigma_{\gamma\gamma}/\mathrm{d}y\cdot\mathscr{L}}\cdot\frac{1}{\Delta y}, \tag{4.3}$$

where $N_{\gamma\gamma}$ is the number of dimuon events measured in a given interval of the $\mu^+\mu^-$ invariant mass and $(\mathrm{Acc}\times\varepsilon)_{\gamma\gamma}$ is the corresponding acceptance and efficiency correction.

Putting Eq. (4.3) into Eq. (4.2) and using it in Eq. (4.1), we end up with the final formula for the coherent cross section:

$$\frac{\mathrm{d}\sigma^{\mathrm{coh}}_{J/\psi}}{\mathrm{d}y} = \frac{1}{\mathscr{B}} \cdot \frac{N^{\mathrm{coh}}_{J/\psi}}{N_{\gamma\gamma}} \cdot \frac{(\mathrm{Acc}\times\varepsilon)_{\gamma\gamma}}{(\mathrm{Acc}\times\varepsilon)_{J/\psi}} \cdot \frac{\sigma_{\gamma\gamma}}{\Delta y}, \tag{4.4}$$

in which the theoretical value for the two-photon cross section $\sigma_{\gamma\gamma}$ is needed to be supplied for the current rapidity interval and the interval in the dimuon invariant mass where the $N_{\gamma\gamma}$ was measured.

4.3 Data sample

The measurement was performed on the data sample collected during the 2011 Pb-Pb data taking. The relevant period of the data taking is LHC11h, a sample of 130 runs was selected for the data analysis (see Section 2.10.3 for the definition of "period" and "run").

The selection of runs took into account availability and good shape of all systems relevant for the analysis, which are the muon spectrometer, SPD and V0. The selection included the standard QA procedure performed by muon spectrometer experts. It was also required for runs to be marked as good when the run was finished during the data taking.

The list of selected runs is given in Appendix A.1.

In the grid analysis of the data (flow of the data processing is covered in Section 2.10.4), 97.01% of all collected CMUP1 events was analyzed, showing high efficiency in the reconstruction and data processing.

4.4 Luminosity of the data sample

Calculation of the luminosity follows the form of Eq. (3.5) in Section 3.3. Neglecting the pile-up for these data and using the VLN trigger for the reference cross section (a trigger for the most central hadronic Pb–Pb collisions based on the V0A and V0C coincidence [90]), the luminosity of CMUP1 trigger is defined as

$$\mathscr{L} = \frac{N^{\mathrm{CMUP1}}_{\mathrm{L2a}}}{N^{\mathrm{CMUP1}}_{\mathrm{L0b}}} \frac{f_{\mathrm{found}} N_{\mathrm{VLN}}}{\sigma_{\mathrm{VLN}}}, \tag{4.5}$$

where f_{found} is the fraction of collected triggers used in the analysis (attributed to the grid efficiency). The trigger lifetime is given by the ratio of number of CMUP1 triggers at L2a level to the number at the L0a level.

The total luminosity of the data sample is $\mathscr{L} = 55.87 \pm 0.013\%\ (stat)\ \mu\mathrm{b}^{-1}$.

4.5 MC samples

Three main samples were produced for $\gamma\gamma \to \mu^+\mu^-$, coherent J/ψ and incoherent J/ψ. The simulations were assigned the tags LHC12a8a, LHC12a8b and LHC12a8c, under which they are referred to in the ALICE data structures.

The events for these processes were generated using the STARLIGHT [34, 36] MC and folded by detector simulation, as is described in Section 2.10.4. A separate simulation was performed for each run in the list of runs selected for the data analysis, in order to account for time variations in the detector performance. Refer to Section 3.4 for a more detailed description. An amount of 10 000 events of each of the processes was simulated for each run.

The generated events were preselected for rapidity y of the J/ψ in $-5.0 < y < -1.5$ and for pseudorapidity of both muons in the two-photon production $\gamma\gamma \to \mu^+\mu^-$ in $-5.0 < \eta_{1,2} < -1.5$. The motivation behind is to speed-up the simulation process and to reduce the amount of data produced by the simulation. The more strict preselection for the $\gamma\gamma \to \mu^+\mu^-$ production was a result of the expected lower efficiency for these events.

Other J/ψ samples were created to study a possible dependence of the efficiency on the generated spectra.

Coherent production of the J/ψ was also simulated using the JPSILIGHT [53, 84] event generator. Preselection for the rapidity was the same as for the main coherent simulation, $-5.0 < y < -1.5$, a sample of 60 000 events was simulated for one typical run: 167813.

To other J/ψ samples were simulated with a flat distribution in transverse momentum p_T and rapidity y in the intervals $0 < p_T < 0.3$ GeV/c and $-5.0 < y < -1.5$ assuming either no polarization of the J/ψ or transverse polarization. 24 000 events were simulated for the case of no polarization and 60 000 events for transverse polarization.

A group of simulations of the ψ' was created to determine the feed-down correction (see Section 3.5). The ψ' were generated using STARLIGHT, then the decays $\psi' \to J/\psi + X$ were simulated under assumptions for the extremal polarization scenarios for the J/ψ: no polarization, full longitudinal and transverse polarization. Samples of 10 000 events were created for the case of no polarization and 20 000 events were simulated for the longitudinal and transverse scenarios. All the ψ' simulations were produced under the conditions of one typical run: 167813.

4.6 Event selection criteria

Each event out of the collected data sample had to fulfill the following requirements.

- General requirements:

  R1 The event belongs to any of the selected runs.

  R2 The event was triggered by the CMUP1 trigger class.

- Requirements against the background:

  R3 The energy in each of the neutron ZDCs (both sides of the interaction point, A and C) had to be less than 6 TeV.

  The value of maximal energy corresponds to the emission of 4 or fewer neutrons. The requirement rejects very peripheral hadronic interactions.

R4 The V0 offline decision had to be EMPTY on the A-side and BEAMBEAM at the C-side, the side of the muon spectrometer.

The offline decisions are evaluated using the timing information on the expected beam-beam interactions. The requirement thus removes any interaction between the beam and residual gas in the beam pipe. The trigger CMUP1 already contains similar requirements, build-up using the fast trigger inputs, but the offline decisions take into account the final response of the detector.

R5 The number of SPD tracklets had to be less than 2.

The small residual activity was compatible with the MC where no generated particles were directing towards the central SPD detector.

- Requirements for the tracks in the muon spectrometer:

R6 The radial position of the track at the end of the absorber R_{abs} should fall into the interval $17.5 < R_{\text{abs}} < 89.5$ cm.

The commonly-used values for the R_{abs} interval ensure that the track passed through the homogeneous part of the absorber.

R7 Pseudorapidity of the track η should pass $-3.7 < \eta < -2.5$.

The requirement selects the tracks withing overlap in the acceptance of the muon spectrometer and the V0C detector.

R8 The track fulfilled the $p \times$ DCA requirement.

The distribution of the DCA (distance between vertex and the track extrapolated to the vertex transverse plane) of the tracks belonging the the interaction vertex follows a Gaussian distribution of width proportional to $1/p$ with p the 3-momentum of the track. In the case of the muon spectrometer with the absorber in front of it, the width depends on the absorber material due to multiple scattering. The beam induced background does not follow such a specific trend and is removed by requiring the $p \times$ DCA condition. The condition is formulated inside the implementation of a muon selection class. It is also calibrated for time variations in the detector response.

- Requirements for dimuons. The dimuon is the sum of 4-vectors of both tracks reconstructed in the muon spectrometer. The 4-vectors of the individual muon tracks were created assuming the rest mass of a muon.

R9 There was only one dimuon candidate in the event.

Any additional activity in the muon spectrometer is rejected by the requirement. Only two muons from the decay of the J/ψ are expected for the UPC event.

R10 The two tracks had opposite sign of the electric charge.

The requirement selected the dimuon decays of the J/ψ and events of two-photon production of dimuon pairs, $\gamma\gamma \rightarrow \mu^+\mu^-$.

R11 At least one of the two muon tracks was matched to a trigger track.

The requirement selects the dimuon events where at least one of the tracks is matched to a trigger track recorded in the triggering part of the muon spectrometer.

R12 The dimuon had transverse momentum $p_T < 300$ MeV/c.

Coherent events are expected to have low momenta. The requirement provided a coherent-enriched sample containing only a small incoherent contribution. The incoherent J/ψs have higher values of transverse momenta.

R13 The dimuon rapidity fit into the range $-3.6 < y < -2.6$.

By this requirement the phase space of the measurement is defined. The numerical values of the interval select the region of well-defined acceptance for the trigger and the involved detectors.

4.7 Acceptance and efficiency correction for coherent J/ψ

Determination of the correction follows the ideas stated in Section 3.4. The corresponding MC sample was analyzed by applying the same selection criteria as for the data (Section 3.4) to the events reconstructed in the MC.

The obtained number of reconstructed and accepted events n_{rec} was divided by the number of events n_{gen} generated into the rapidity interval $-3.6 < y < -2.6$ imposed by the requirement **R13**.

Separate ratios $n_{\mathrm{rec}}/n_{\mathrm{gen}}$ were obtained for each of the simulated runs, weighted by the luminosity of the run and summed over all runs, providing the final value of the efficiency correction $(\mathrm{Acc} \times \varepsilon)_{J/\psi}$.

The combined acceptance and efficiency is 16.6% for coherent J/ψ.

The time dependence of the correction, expressed as the acceptance and efficiency as a function of run number, is shown in Figure B.1a in Appendix B.1.

4.8 The yield of J/ψ candidates

The yield $N_{J/\psi}$ was obtained by fitting the distribution of the invariant mass of selected dimuon candidates in the range between 2.2 and 4.6 GeV/c^2. The distribution was modeled with and exponential function to describe the two-photon dimuon production and a Crystal Ball function [91] to account for the J/ψ.

The fit was performed using an extended binned likehood method which is implemented in the RooFit package [92]. The tail parameters of the Crystal Ball α_{CB} and n were fixed using the MC of the coherent J/ψ.

The fit is shown in Figure 4.2. The yield extracted from the fit is $N_{J/\psi} = 96 \pm 12$.

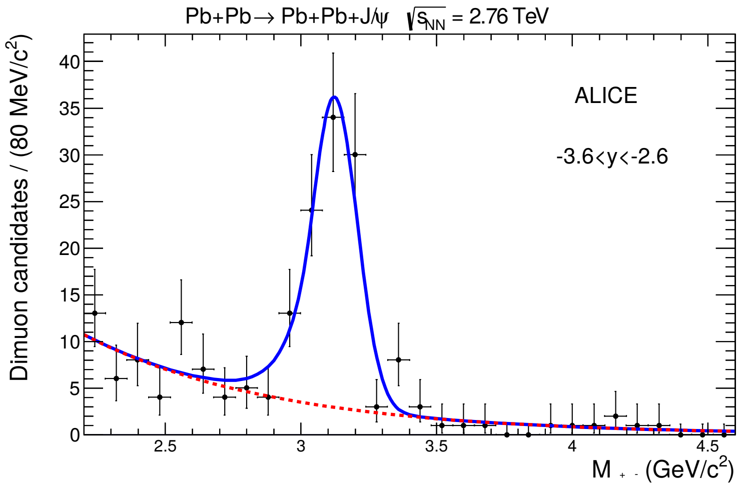

Fig. 4.2 Invariant mass distribution for events selected by the criteria listed in Section 4.6 [1].

4.9 Correction for feed-down from ψ'

The correction takes account of the contribution of the J/ψ from the decays $\psi' \to J/\psi + X$ to the signal of coherent J/ψ. The calculation of the correction follows Section 3.5.

Equation (3.11) for the feed-down reads

$$f_D = \frac{\sigma_{\mathrm{SL},y}(\psi') \cdot \mathscr{B}(\psi' \to J/\psi + X) \cdot (\mathrm{Acc} \times \varepsilon)^{P}_{J/\psi}}{\sigma_{\mathrm{SL},y}(J/\psi) \cdot (\mathrm{Acc} \times \varepsilon)_{J/\psi}}, \tag{4.6}$$

where $\sigma_{\mathrm{SL},y}(\psi') = 4.4 \times 0.068$ mb and $\sigma_{\mathrm{SL},y}(J/\psi) = 23.1 \times 0.067$ mb. According to Eq. (3.12) the first number is the total STARLIGHT cross section and the second is the fraction of events generated into $-3.6 < y < -2.6$. The branching ratio is $\mathscr{B}(\psi' \to J/\psi + X) = 0.595 \pm 0.008$ [80].

The efficiency of coherent J/ψ is $(\mathrm{Acc} \times \varepsilon)_{J/\psi} = 0.166$, as stated above in Section 4.7. The efficiency for the J/ψ from the ψ' decays, $(\mathrm{Acc} \times \varepsilon)^{P}_{J/\psi}$ was obtained using the same procedure applied to the MC samples of ψ'. Depending on the polarization P of the J/ψ from ψ', the efficiencies are 0.170, 0.133 and 0.244 for no, transverse and longitudinal polarization respectively. The corresponding values of the feed-down are $f_D = 0.119$, 0.093 and 0.168.

4.10 Contribution from incoherent photoproduction

Despite the fact that the incoherent production of the J/ψ occurs at larger values of transverse momentum compared to coherent production, the coherent-enriched sample, created by requirement **R12** by asking for $p_T < 300$ MeV/c, still contains a contribution of incoherent J/ψ.

The correction for this incoherent contribution f_I is

$$f_I = \frac{\sigma^{\mathrm{inc}}_{J/\psi}}{\sigma^{\mathrm{coh}}_{J/\psi}} \cdot \frac{(\mathrm{Acc}\times\varepsilon)^{\mathrm{inc}}_{J/\psi}}{(\mathrm{Acc}\times\varepsilon)^{\mathrm{coh}}_{J/\psi}}. \tag{4.7}$$

The cross sections for incoherent and coherent productions $\sigma^{\mathrm{inc}}_{J/\psi}$ and $\sigma^{\mathrm{coh}}_{J/\psi}$ are the STARLIGHT cross sections corresponding to rapidity $-3.6 < y < -2.6$ and transverse momentum $p_T < 300$ MeV/c. Numerical values are 255 μb and 1.85 mb for incoherent and coherent processes respectively.

The acceptance and efficiencies of incoherent and coherent J/ψ are in this order $(\mathrm{Acc}\times\varepsilon)^{\mathrm{inc}}_{J/\psi} = 0.143$ and $(\mathrm{Acc}\times\varepsilon)^{\mathrm{coh}}_{J/\psi} = 0.166$. The time dependence of both efficiencies is shown in Figures B.1b and B.1a (incoherent and coherent, respectively).

The resulting incoherent contribution is $f_I = 0.12$. Using the JPSILIGHT for the ratio of the cross sections in Eq. (4.7) it is $f_I = 0.08$.

An alternative method based on the description of the transverse momentum of the J/ψ candidates was used to determine the incoherent contribution. A special selection was applied to the data narrowing the interval of the mass of dimuon candidates around the peak of the J/ψ (Figure 4.2) to $2.8 < m_{\mu^+\mu^-} < 3.4$ GeV/c^2 and extending the transverse momentum range to $p_T < 0.8$ GeV/c. MC templates of contributing processes were used to build-up a model to fit the p_T distribution of the J/ψ candidates from the data.

The inputs to the templates were obtained using the STARLIGHT MC simulations of coherent and incoherent J/ψ, J/ψ from ψ' decays and two-photon production of dimuon pairs.

The contribution of J/ψ from ψ' was fixed using the value of the feed-down (Section 4.9) and the contribution of $\gamma\gamma \to \mu^+\mu^-$ was fixed using the fit to the mass distribution (Figure 4.2). The contributions from coherent and incoherent photoproduction of the J/ψ were left free.

The fit to the data using the templates is shown in Figure 4.3. The incoherent contribution estimated from the fit is $f_I = 0.26 \pm 0.05$.

In the fit, the incoherent contribution is constrained mainly in the region $0.5 < p_T < 0.8$ GeV/c where also the hadronic contamination is most likely to occur. Therefore the result for the f_I from the fit was considered as an upper bound for the incoherent contribution.

The middle value of the two model calculations and the fit was selected as the final value of the incoherent contribution while the two other results provide lower and upper limits, giving:

$$f_I = 0.12^{+0.14}_{-0.04}. \tag{4.8}$$

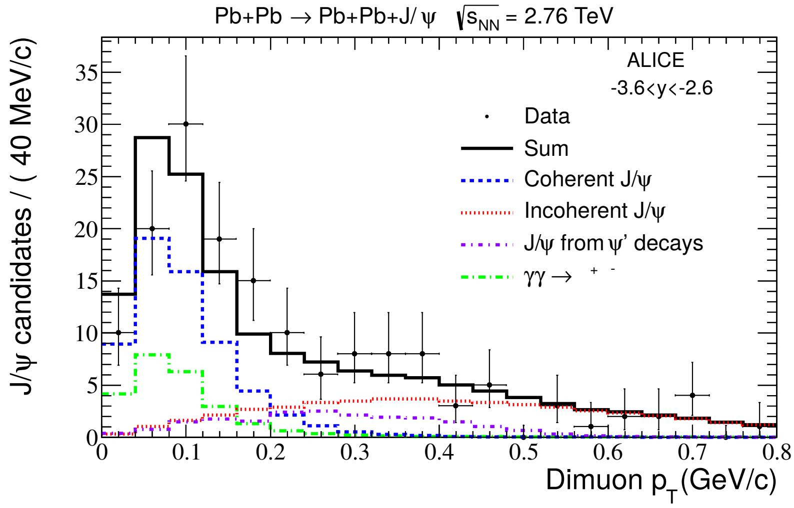

Fig. 4.3 Distribution of transverse momentum of the J/ψ candidates and fit to the data points by summing four different MC templates: coherent J/ψ (dashed – blue), incoherent J/ψ (dotted – red), J/ψ from ψ' (dash-dotted – violet) and $\gamma\gamma \to \mu^+\mu^-$ (dash-dotted – green) [1].

4.11 Cross section of coherent J/ψ photoproduction

The experimental cross section of coherent J/ψ photoproduction is given by Eq. (4.4) which reads

$$\frac{\mathrm{d}\sigma^{\mathrm{coh}}_{J/\psi}}{\mathrm{d}y} = \frac{1}{\mathscr{B}} \cdot \frac{N^{\mathrm{coh}}_{J/\psi}}{N_{\gamma\gamma}} \cdot \frac{(\mathrm{Acc} \times \varepsilon)_{\gamma\gamma}}{(\mathrm{Acc} \times \varepsilon)_{J/\psi}} \cdot \frac{\sigma_{\gamma\gamma}}{\Delta y}. \tag{4.9}$$

The number of coherently produced J/ψ is obtained from the yield $N_{J/\psi}$ by applying the correction for the feed-down f_D and for the incoherent contribution f_I as

$$N^{\mathrm{coh}}_{J/\psi} = \frac{N_{J/\psi}}{1 + f_D + f_I}. \tag{4.10}$$

The number of dimuon events $N_{\gamma\gamma}$, corresponding efficiency $(\mathrm{Acc} \times \varepsilon)_{\gamma\gamma}$ and the cross section $\sigma_{\gamma\gamma}$ were obtained in two intervals of the dimuon invariant mass, below and above the J/ψ mass peak, to avoid contamination by dimuons coming from the decay of the J/ψ.

In the intervals $2.2 < m_{\mu^+\mu^-} < 2.6$ GeV/c^2 (low mass region) and $3.5 < m_{\mu^+\mu^-} <$ 6.0 GeV/c^2 (high mass region) the $N_{\gamma\gamma}$ was obtained by counting the events satisfying all the selection criteria **R1** - **R13** and pass the given mass interval. In the low mass region there is 43 such events and in the high mass region there is 15 events, giving $N_{\gamma\gamma} = 58 \pm 7.6(\mathrm{stat})$.

The theoretical cross section $\sigma_{\gamma\gamma}$ of $\gamma\gamma \to \mu^+\mu^-$ was calculated using STARLIGHT for the rapidity of the dimuon restricted by **R13**, transverse momentum by **R12** and pseudorapidity of both muons satisfying **R7**. For the two mass intervals, low and high, it is

$$\begin{aligned}(\sigma_{\gamma\gamma})_{\text{low}} &= 13.6\ \mu\text{b}\\ (\sigma_{\gamma\gamma})_{\text{high}} &= 3.7\ \mu\text{b},\end{aligned} \tag{4.11}$$

providing for both regions $\sigma_{\gamma\gamma} = 13.6 + 3.7 = 17.3$ μb.

The efficiency $(\text{Acc} \times \varepsilon)_{\gamma\gamma}$ was obtained using the MC of $\gamma\gamma \to \mu^+\mu^-$ in a way similar to that of the J/ψ. The generated rapidity of the muons was restricted to the interval $-3.7 < \eta < -2.5$ given by **R7**. Separate efficiencies were calculated in both mass regions, giving the efficiency of 0.379 for the low mass region and 0.575 for the high mass region. The time dependence of $(\text{Acc} \times \varepsilon)_{\gamma\gamma}$ is shown in Figure B.2 in both mass regions.

The efficiencies in the intervals were then weighted by the theoretical cross sections corresponding to both intervals which are given by Eq. (4.11), producing the final efficiency value:

$$(\text{Acc} \times \varepsilon)_{\gamma\gamma} = \frac{(0.379 \cdot 13.6) + (0.575 \cdot 3.7)}{13.6 + 3.7} = 0.421. \tag{4.12}$$

Putting all the numbers into Eq. (4.9), we obtain

$$\frac{\mathrm{d}\sigma^{\text{coh}}_{J/\psi}}{\mathrm{d}y} = 1.00 \pm 0.18(\text{stat})^{+0.14}_{-0.26}(\text{syst})\ \text{mb}. \tag{4.13}$$

The systematical error in Eq. (4.13) contains contributions from the theoretical uncertainty in $\sigma_{\gamma\gamma}$, the uncertainty on the signal extraction, uncertainties on the reconstruction and muon trigger efficiencies, the uncertainty on the acceptance calculation, the pile-up from $\gamma\gamma \to e^+e^-$ and the uncertainty from the knowledge of the branching ratio.

Chapter 5

Discussion of physics results on coherent J/ψ photoproduction in Pb-Pb UPC

The physics impact of the experimental results are discussed in this chapter. The measured cross section of coherent J/ψ photoproduction is compared to theoretical models and an attempt to extract the amount of nuclear gluon shadowing is summarized. Also the results provided by the CMS experiment are shown.

The measured cross section at the forward rapidity $-3.6 < y < -2.6$ is in Eq. (4.13), the value reads as $\mathrm{d}\sigma^{\mathrm{coh}}_{J/\psi}/\mathrm{d}y = 1.00 \pm 0.18(\mathrm{stat})^{+0.14}_{-0.26}(\mathrm{syst})$ mb. Another measurement by the ALICE experiment at mid-rapidity provided the coherent cross section at $-0.9 < y < 0.9$ [57], the value is $\mathrm{d}\sigma^{\mathrm{coh}}_{J/\psi}/\mathrm{d}y = 2.38^{+0.34}_{-0.24}(\mathrm{stat}) + (\mathrm{syst})$ mb. Both measurements are shown in Figure 5.1.

The value of Bjorken-x of the probed gluons is given by Eq. (1.16). With the symmetrical system of Pb-Pb, at forward rapidity there is two-fold ambiguity in the value of x, because each Pb-ion can serve as a photon source or target. This results in two possible center-of-mass energies of photon-lead nucleus system and hence two values of x. At the current kinematics, the two possible values are $x = 5\times10^{-5}$ and $x = 2\times10^{-2}$ for higher and lower energy respectively when the J/ψ is produced at rapidity $y = 3$. According to STARLIGHT the contribution of low energy events amounts to 95% of the cross section, therefore the coherent photoproduction at forward rapidity is mainly sensitive to the gluons with $x = 2\times10^{-2}$.

The Bjorken-x at mid-rapidity is in the range $x = 5\times10^{-4}$ and $x = 3\times10^{-3}$, given by the width of the interval. As the interval is symmetrical around $y = 0$, the range of x at mid-rapidity is free of ambiguities.

Model predictions of coherent J/ψ photoproduction are also shown in Figure 5.1. An overview of the models is presented in Section 1.7.

The models with the largest deviation from the forward measurements are STARLIGHT and AB-MSTW08. The reason is neglected nuclear effects in these two models. The STARLIGHT model uses experimental data on photon-proton interactions and Glauber approach to calculate the photon-nucleus cross section. The AB-MSTW08 was created as a cross check where the nuclear effects were intentionally omitted by using a proton gluon distri-

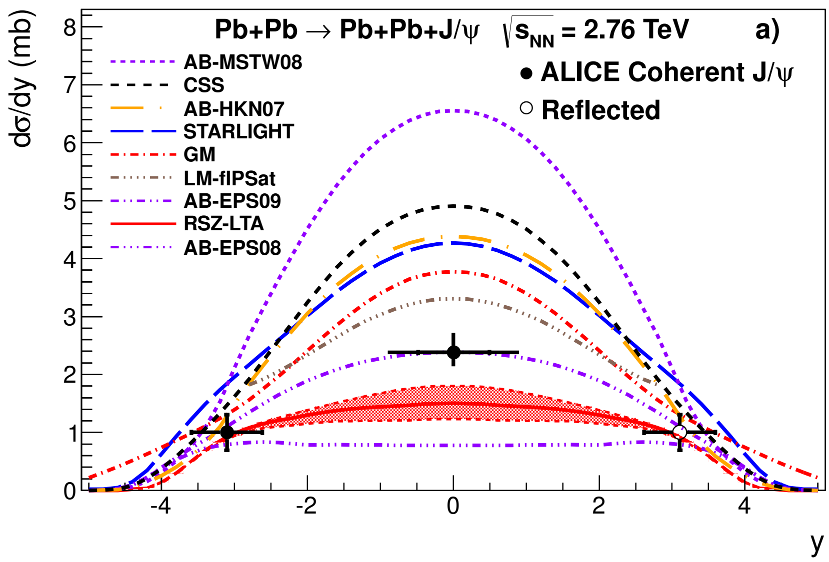

Fig. 5.1 Measured differential cross section of coherent J/ψ photoproduction in ultra-peripheral Pb-Pb collisions at $\sqrt{s_{\mathrm{NN}}}$ = 2.76 TeV [1, 57].

bution for the calculation of the photon-nucleus interaction. Both the models overestimate the measured cross section by more than 3 standard deviations.

The other models which overestimate the mid-rapidity measurement are GM, CSS and LM, also based on the Glauber approach, and partonic model AB-HKN07, in which the used parametrization of the nuclear gluon distribution predicts weaker gluon shadowing than is observed in the data.

The models which underestimate the mid-rapidity measurement are AB-EPS08 and RSZ-LTA. The amount of nuclear gluon shadowing in AB-EPS08, given by the respective parametrization to the nuclear gluon density, is too strong compared to data, the deviation is about 5 standard deviations. The model RSZ-LTA, based on a partonic approach and leading twist theory of nuclear shadowing, also provided a prediction significantly below the data.

The models consistent with the forward measurement within one standard deviation are RSZ-LTA, AB-EPS09, and AB-EPS08. The model consistent also with the mid-rapidity measurement is AB-EPS09 for which the nuclear gluon density given by the EPS09 parameterization predicts medium nuclear shadowing, consistent with the amount of nuclear shadowing seen in the data.

An attempt to extract the amount of nuclear gluon shadowing from the measured data in a model-independent way has been made by making the ratio of the measured cross section to the calculation in the impulse approximation [93].

The nuclear suppression factor $S(W_{\gamma\mathrm{p}})$ was defined as the ratio of the experimental photon-lead coherent cross section to the calculation in the impulse approximation (IA), both as a function of energy $W_{\gamma\mathrm{p}}$:

$$S(W_{\gamma\mathrm{p}}) = \left[\frac{\sigma^{\mathrm{exp}}_{\gamma\,\mathrm{Pb}\to J/\psi\,\mathrm{Pb}}(W_{\gamma\mathrm{p}})}{\sigma^{\mathrm{IA}}_{\gamma\,\mathrm{Pb}\to J/\psi\,\mathrm{Pb}}(W_{\gamma\mathrm{p}})}\right]^{1/2}. \tag{5.1}$$

The cross section in the impulse approximation in Eq. (5.1) has been calculated using measured data on the photon-proton cross section $\sigma(\gamma\mathrm{p} \to J/\psi\,\mathrm{p})$ and experimental data on the nuclear density distribution.

The photon-nucleus cross section in Eq. (5.1) was obtained from the two ALICE measurements of coherent photoproduction using the flux of virtual photons. The energy corresponding to the forward measurement at $-3.6 < y < -2.6$ is $W_{\gamma\mathrm{p}} = 19.6$ GeV and the energy for the mid-rapidity measurement in $-0.9 < y < 0.9$ is $W_{\gamma\mathrm{p}} = 92.4$ GeV.

The obtained values of the nuclear suppression factor are

$$\begin{aligned} S(W_{\gamma\mathrm{p}} = 19.6\ \mathrm{GeV}) &= 0.74^{+0.11}_{-0.12} \\ S(W_{\gamma\mathrm{p}} = 92.4\ \mathrm{GeV}) &= 0.61^{+0.05}_{-0.04}. \end{aligned} \tag{5.2}$$

The uncertainties are predominantly given by the experimental errors.

The extracted nuclear suppression in Eq. (5.2) is then compared to the theoretical predictions. The predictions based on VDM and Glauber model overestimate the values of S, which is not surprising since such models also overestimate the measured coherent cross sections.

The pQCD prediction for S, based at the leading order (LO) on Eq. (1.43) and Eq. (1.45), gives the nuclear suppression directly in terms of the gluon distribution in a proton g_p and in a nucleus g_A as

$$S = \frac{g_p(x,Q^2)}{A g_A(x,Q^2)}, \tag{5.3}$$

which is at the same time the definition of the nuclear modification R_A. In the LO pQCD picture the gluon shadowing is described as a partial depletion of the nuclear gluon field with respect to that of the free proton.

The experimental values of S are compared to several parameterizations of the x-dependence of the nuclear gluon shadowing in the lead nuclei in Figure 5.2. The parameterizations are evaluated at the scale given by the mass of the J/ψ as $Q^2 = M^2_{J/\psi}/4 = 2.4\ \mathrm{GeV}^2$.

A good agreement is achieved with the parametrization in the HIJING 2.0 generator which include the impact parameter dependence of shadowing [94].

Among the nuclear parton distribution functions, shown in the middle part of Figure 5.2, the EPS09 LO is in agreement with the data (as was successful in the models for the coherent cross section), but there are large uncertainties going to lower values of x.

In comparison to calculations using the leading twist theory of nuclear gluon shadowing (applied also in the RSZ model), the calculation with MSTW08LO nucleon gluon density is close to the experimental data, as shown in the bottom part of Figure 5.2.

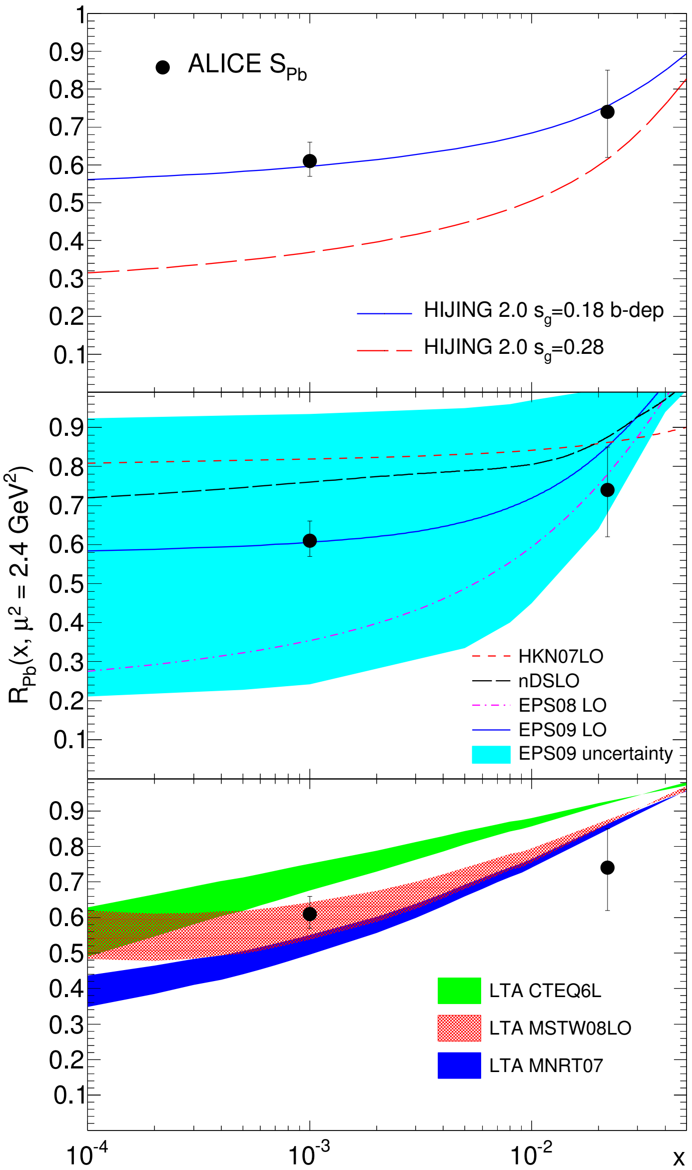

Fig. 5.2 Comparison of the nuclear suppression factor extracted from ALICE data on coherent J/ψ photoproduction to predictions for nuclear gluon shadowing, top: HIJING, middle: nuclear distribution functions, bottom: leading twist theory [93].

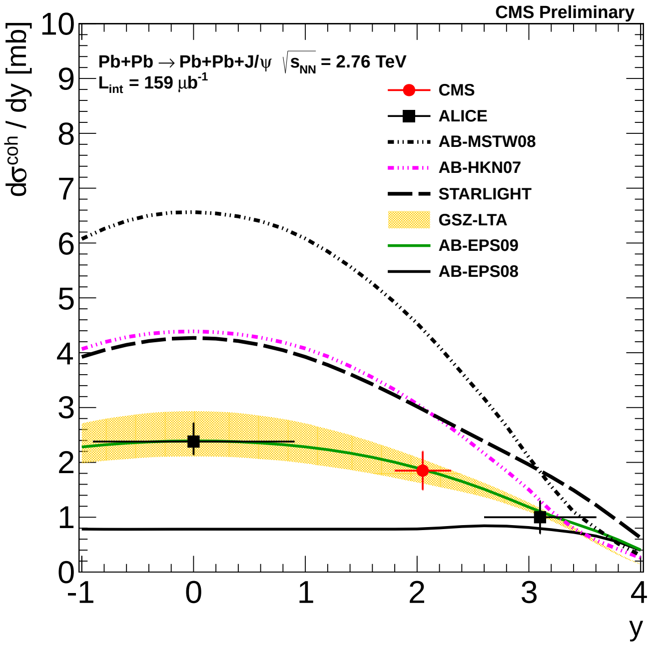

Fig. 5.3 CMS coherent cross section [95].

The CMS experiment published their preliminary results on coherent J/ψ photoproduction at $\sqrt{s_{\mathrm{NN}}}$ = 2.76 TeV in the rapidity interval $1.8 < |y| < 2.3$. The J/ψ have been reconstructed in the dimuon channel $J/\psi \to \mu^+\mu^-$ [95].

Due to triggering reasons, the CMS measurement was performed with associated neutron emission by the interacting lead nuclei. The neutrons have been detected in the Zero Degree Calorimeters ($\mathrm{ZDC_C}$) of the CMS experiment.

The cross section was first evaluated in the breakup mode X_n0_n with at least one neutron in one of the $\mathrm{ZDC_C}$ and no signal in the $\mathrm{ZDC_C}$ on the opposite side, and then scaled using STARLIGHT to the mode without nuclear breakup.

The scaling to no breakup allows comparison to the ALICE results, which were obtained with no neutron emission. However, the cross section is not corrected for the feed-down from ψ' as it was done for ALICE data.

The measurement of coherent J/ψ photoproduction by the CMS experiment is shown in Figure 5.3 together with ALICE results and model predictions. The cross section measured by CMS is consistent with the rapidity dependence of the cross section established by ALICE measurements.

In addition to the models shown in Figure 5.1, the GSZ model is shown and is compatible with the measurement by the CMS. The model is based on the leading twist approximation, the ALICE data were used to describe the coherent cross section with no neutron emission.

In summary, measurements of coherent J/ψ photoproduction in ultra-peripheral Pb-Pb collisions at $\sqrt{s_{\mathrm{NN}}}$ = 2.76 TeV provide evidence for medium gluon shadowing at low values of the Bjorken-x. Theoretical models which neglect nuclear effects, as well as those predicting strong nuclear shadowing, are disfavored by the measurement. Models which include nuclear effects and medium amount of shadowing are consistent with the data.

Chapter 6

Measurement of exclusive J/ψ photoproduction in p-Pb UPC

The purpose of this chapter is to present the physics motivation for the measurement and to describe the analysis. The level of detail provided in the description of the analysis is biased by the author's personal contribution to the results. Part of the results which are shown here are published [2] and part is in the final stages of the paper preparation.

6.1 Physics impact

By studying exclusive photoproduction of J/ψ in photon-proton interactions we can probe the gluon distribution of the proton. The process of $\gamma\mathrm{p} \rightarrow J/\psi\mathrm{p}$ is initiated by the quasi-virtual photon interacting on the proton target, producing a J/ψ as a free particle while the proton remains intact. An introductory description of photoproduction in photon-proton interactions is given in Section 1.3.1.

The mass of the J/ψ provides a hard scale, which allows to describe the process in terms of perturbative QCD (pQCD) [17]. The cross section of $\gamma\mathrm{p} \rightarrow J/\psi\mathrm{p}$ is then related to the square of the gluon distribution according to Eq. (1.14).

At high energies of the photon-proton system, $W_{\gamma\mathrm{p}}$, we probe gluons carrying a very small fraction x of the proton momentum. According to Eq. (1.16), the momentum fraction is proportional to the inverse square of the energy, $x = (M_{J/\psi}/W_{\gamma\mathrm{p}})^2$.

The process of high energy exclusive photoproduction off protons was extensively studied at HERA in the energy range of $20 < W_{\gamma\mathrm{p}} < 305$ GeV, see Section 1.4.1. It was found that the cross section of $\gamma\mathrm{p} \rightarrow J/\psi\mathrm{p}$ is growing with the energy as $\sigma \propto W_{\gamma\mathrm{p}}^{\delta}$, where the slope parameter δ is constant.

The growth of the cross section indicates a rapid increase in the gluon density with decreasing x, meaning more and more gluons at smaller momentum fractions. To meet the unitarity requirement, the basic assumptions of perturbative field theories, the growth of the cross section should be tamed in the limit of very high energies, and hence the gluon density cannot increase arbitrarily at small values of x.

The proposed mechanism to slow down the increase in the gluon density is gluon saturation [13, 96]. As the gluons can interact with each other, the mutual recombination should become dominant below some very small x, when the gluons start to overlap. Finding the onset of the saturation is one of the most important challenges nowadays in QCD.

An illustration of gluon saturation is shown in Figure 6.1 [97], which is the partonic analogy to the phase diagrams used in thermodynamics. The color rings represent the gluon field of the proton.

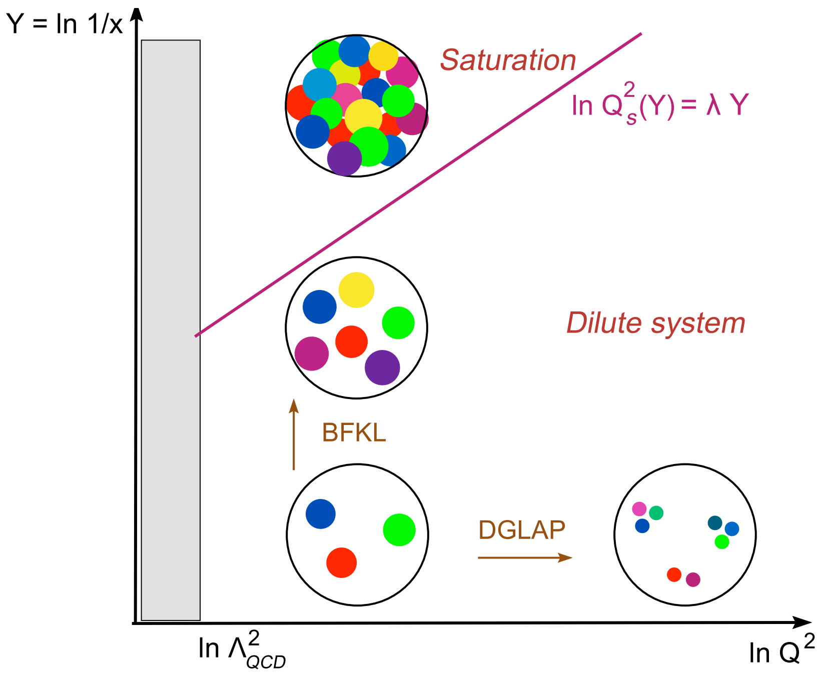

Fig. 6.1 The diagram for parton evolution in QCD [97].

Along the horizontal axis, the gluon distribution is seen more dilute with increasing scale Q^2; it is realized by probing the distribution with heavier objects. Evolution along this scale is described by DGLAP equations [44–46], as is used with the b-Sat model (Section 1.6.2).

A measure of the smallness of x along the vertical axis is $Y = \ln 1/x$. Evolution towards higher Y (and smaller x) is driven by the BFKL equation (abbreviation for Balitsky, Fadin, Kuraev, and Lipatov) [98–100]. The equation describes the exponential increase in the gluon density by radiating new gluons, which do not interact with each other.

The non-linear effects of saturation are introduced by the saturation momentum Q_s. In a simple approach, the saturation line $\ln Q_s^2(Y) = \lambda Y$ in Figure 6.1 separates the non-interacting dilute gluons and saturated dense gluons.

Experimental evidence for gluon saturation will provide the absolute scale for the vertical axis of Figure 6.1.

ALICE has measured the process of exclusive J/ψ photoproduction off protons in ultra-peripheral p-Pb collisions at $\sqrt{s_{\rm NN}}$ = 5.02 TeV. Using the forward muon spectrometer and central tracking detectors, ALICE can measure the energy evolution of the cross section of $\gamma \mathrm{p} \rightarrow J/\psi\, \mathrm{p}$ over the energy range of $21 < W_{\gamma\mathrm{p}} < 952$ GeV, thereby increasing the energy range of the previous HERA measurements by more than a factor of two. The interval of Bjorken-x of the probed gluons corresponding to this energy range is 10^{-2} down to 10^{-5}.

The physics of gluon saturation is also an important part of experimental programs for future facilities which want to study QCD in electron-hadron collisions [47, 101, 102].

6.2 Experimental setup for the photoproduction measurements in p-Pb UPC

6.2.1 Measurement of J/ψ photoproduction off protons

The measurement is performed in p-Pb collisions at $\sqrt{s_{\mathrm{NN}}}$ = 5.02 TeV collected during the 2013 LHC p-Pb run, the J/ψs are reconstructed via the leptonic decays as $J/\psi \to e^+e^-(\mu^+\mu^-)$ in a given rapidity interval. There should be no other signal in the detector.

The energy of the photon-proton system is given by Eq. (1.13) as

$$W_{\gamma\mathrm{p}} = 2E_p M_{J/\psi} \exp(-y), \tag{6.1}$$

where $E_p = 4$ TeV is the energy of the proton beam in the laboratory frame, $M_{J/\psi}$ is the mass of the J/ψ and y is the laboratory rapidity of the J/ψ. Computing the energy from the rapidity is possible thanks to the asymmetrical p-Pb system. The lead ion is predominant (at $\sim$95%) the source of the virtual photons.

The rapidity y of the J/ψ in Eq. (6.1) is measured in the laboratory frame with respect to the proton beam direction. If the J/ψ is produced at non-zero rapidity in the same direction as the proton, the rapidity is positive. When the J/ψ has the same absolute value of the rapidity, but it is produced opposite to the direction of the proton, the rapidity is negative and the energy $W_{\gamma\mathrm{p}}$ from Eq. (6.1) is higher with respect to the case of positive rapidity.

The acceptance of the ALICE detector is given in units of laboratory pseudorapidity η. The forward muon spectrometer (Section 2.7) is located at $\eta < 0$. For the J/ψs detected there, the rapidity is positive if the proton beam is directed towards the muon spectrometer, and negative for the opposite direction.

6.2.2 LHC configurations for p-Pb and Pb-p

The LHC switched the direction of the beams approximately in the middle of the p-Pb run. In the first part, denoted as **p-Pb**, the proton beam was oriented towards the muon spectrometer, producing J/ψs at positive forward rapidity, lower energies $W_{\gamma\mathrm{p}}$ are reached there.

For the second part of the run, the directions were reversed. The proton beam was directed opposite to the muon spectrometer, the lead beam was now oriented towards the muon spectrometer. Outside mid-rapidity the J/ψs were produced at negative backward rapidities, leading to higher photon-proton energies $W_{\gamma\mathrm{p}}$ according to Eq. (6.1). The configuration is denoted as **Pb-p**.

In the following, the p-Pb alone stands for for both parts of the run, p-Pb + Pb-p together.

6.2.3 Measurement at forward rapidity

The forward rapidity is reached when both muons of the J/ψ dimuon decay $J/\psi \to \mu^+\mu^-$ are detected in the forward muon spectrometer. This situation is illustrated in Figure 6.2.

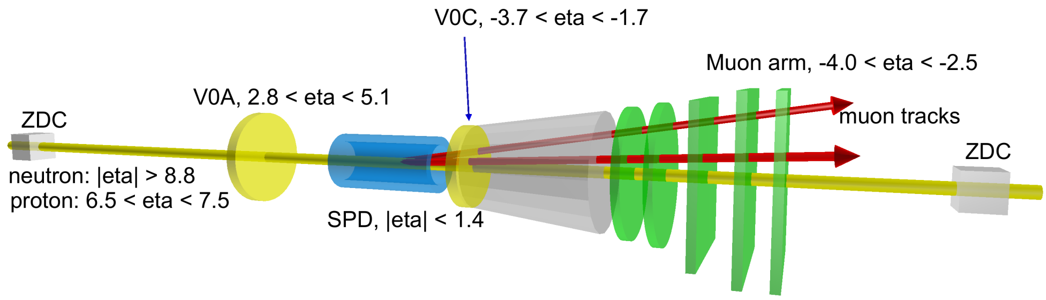

Fig. 6.2 Analysis strategy at forward rapidity. Both muons are detected in the muon spectrometer. The individual detectors are not in scale.

The selection of such events is aimed for two muons of unlike sign detected in the muon spectrometer, a signal in V0C compatible with the two muons and no signal in the central pixel detectors SPD, V0A on the side opposite to the muon spectrometer and no signal in both zero degree calorimeters ZDC.

The rapidity of the J/ψ is $2.5 < y < 4.0$ for p-Pb and $-3.6 < y < -2.6$ for Pb-p, giving energy ranges $21 < W_{\gamma p} < 45$ GeV for p-Pb and $577 < W_{\gamma p} < 952$ GeV for Pb-p. These are the limiting values of energy reached by the ALICE experiment.

6.2.4 Measurement at semi-forward rapidity

One of the decaying muons is again detected in the muon spectrometer while the second one is detected in the central tracking detectors ITS and TPC. The semi-forward configuration is shown in Figure 6.3.

The events are selected having one track in the forward muon spectrometer, one in the central tracking detectors. The signal in V0C and SPD should be compatible with one crossing track and no activity should be present in V0A nor in any of the ZDCs

The rapidity interval for the semi-forward measurement is $1.2 < y < 2.7$ for p-Pb and $-2.5 < y < -1.2$ for Pb-p. The extended acceptance for the central track is $|\eta| < 1.1$ and the acceptance for the track in the muon spectrometer is $-4.0 < \eta < -2.5$, so the actual rapidity interval for the J/ψ covers the range of space where there are no tracking detectors.

The corresponding energies are within the range set by the forward analysis, $41 < W_{\gamma p} < 86$ GeV for p-Pb and $287 < W_{\gamma p} < 549$ GeV for Pb-p. It is worth noting that the Pb-p energies are also beyond the range explored at HERA.

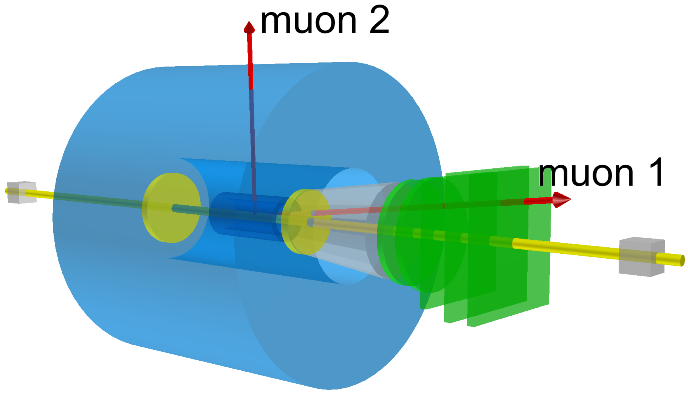

Fig. 6.3 Analysis strategy at semi-forward rapidity. One muon is detected in the muon spectrometer and the second one in the central tracking detectors. The individual detectors are not in scale.

6.2.5 Measurement at mid-rapidity

At mid-rapidity, both tracks are measured in the central tracking detectors. These allow to measure both leptonic decay modes of the J/ψ, dielectrons e^+e^- and dimuons $\mu^+\mu^-$.

Just two tracks are expected in the central detectors and no activity in V0A nor in V0C nor in ZDCs.

The interval in rapidity is $|y| < 0.8$ as a result of the overall acceptance of the central detectors. There is only one interval because of the symmetry around $y = 0$ for the p-Pb and Pb-p cases.

The data from p-Pb and Pb-p were analyzed as a one common sample. In Pb-p, the positive direction along the proton beam is the same as the positive η in the ALICE laboratory frame, while in p-Pb the directions are opposite. Therefore the data taken during the p-Pb part of the run were added to the common sample with reversed sign of the rapidity while the data from Pb-p remained unchanged. This way all the events in the common p-Pb + Pb-p sample had the sign of laboratory rapidity defined along the direction of the proton beam.

The energy reached at mid-rapidity is $100 < W_{\gamma\mathrm{p}} < 246$ GeV, providing the central part for the total energy range defined by the forward rapidity and connecting the semi-forward p-Pb and Pb-p data.

6.2.6 Definition of the cross section

The experimental cross section is determined according the ideas given in Section 3.2 by Eq. (3.1). The differential cross section for exclusive photoproduction in the p-Pb system,

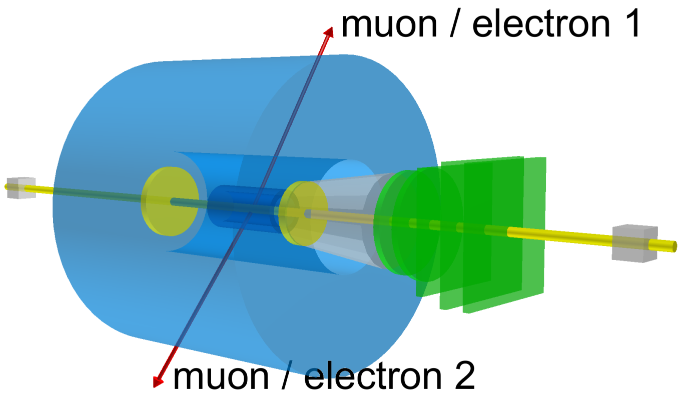

Fig. 6.4 Analysis strategy for mid-rapidity. Both the tracks, electrons or muons, are detected in the central tracking detectors. The individual detectors are not in scale.

$\mathrm{d}\sigma/\mathrm{d}y$, is given by the number of J/ψ produced in the γp interactions $N^{\mathrm{exc}}_{J/\psi}$ divided by the luminosity of the data sample $\mathscr{L}$ and the total acceptance and efficiency correction $\varepsilon_{J/\psi}$ as

$$\frac{\mathrm{d}\sigma}{\mathrm{d}y}(\mathrm{p{+}Pb} \rightarrow \mathrm{p{+}Pb} + J/\psi) = \frac{N^{\mathrm{exc}}_{J/\psi}}{\varepsilon_{J/\psi} \cdot \mathscr{B} \cdot \mathscr{L}} \cdot \frac{1}{\Delta y}, \tag{6.2}$$

where $\mathscr{B}$ is the branching ratio of one of the leptonic decays $J/\psi \rightarrow e^+e^-$ or $J/\psi \rightarrow \mu^+\mu^-$ and Δy is the width of the rapidity bin where the measurement was performed.

6.2.7 Triggers for the p-Pb measurements

The mechanism of triggering is described in Section 2.10.1. The triggering detectors provide the binary (fired / not fired) trigger inputs, out of which a relevant trigger class is formed by requiring a particular state of each of the inputs.

For triggering of the J/ψ in UPC during the 2013 p-Pb run, 10 different trigger inputs were used for 7 trigger classes.

The trigger inputs and their definitions providing the signals at forward and backward rapidities are:

0MSL: single muon with $p_T > 0.5$ GeV,

0MUL: dimuon in the muon spectrometer with the muons of opposite sign and each of them having $p_T > 0.5$ GeV,

0VBA: at least one V0A cell fired in the beam-beam time window,

0VBC: at least one V0C cell fired in the beam-beam time window,

0VC5: at least 5 V0C cells fired in the beam-beam window,

0VGA: VGA & VBC - a hit in the beam-gas time window in V0A accompanied by at least one hit in the beam-beam window in V0C.

The inputs 0MSL and 0MUL are issued by the triggering part of the muon spectrometer, they require one or two muon candidates satisfying the lower threshold of transverse momenta. The rest of the forward inputs (0VBA, 0VBC, 0VC5 and 0VGA) are provided by V0A and V0C. The amount of deposited signal is defined in terms of the number of fired cells. The timing of the hits in the individual cells is compared with the timing of bunches of the LHC beams.

The trigger inputs working at central rapidities are:

0SMB: at least one SPD trigger chip fired (inner or outer layer),

0SH1: at least 7 hits fired in the SPD outer chip layer,

0STP: back-to-back topology in SPD,

0OMU: back-to-back topology in TOF and fired TOF sectors n_{TOF}: $2 < n_{\mathrm{TOF}} < 6$.

The SPD inputs 0SMB and 0SH1 concern the number of fired Fast-Or triggering chips of SPD.

The SPD topology trigger input 0STP selects events with two hits in the inner layer and two hits in the outer layer, which are arranged in a back-to-back pattern. The selection is performed as a 4-fold coincidence in SPD inner and outer layer with opening angle of $\geq 150°$. The back-to-back topology is expected for two body decays of J/ψ at transverse momenta much lower than is the rest mass.

The TOF trigger input 0OMU selects the events with a number of fired trigger pads $2 < n_{\mathrm{TOF}} < 6$, which are arranged in a back-to-back pattern $150° \leq \Delta\phi \leq 180°$, where ϕ is the azimuthal angle of the track at the TOF radius.

All of the trigger inputs listed belong to the fastest Level 0, the trigger signals should reach the detectors in 1.2 μs.

The trigger classes are specific for each rapidity interval of the measurement. The classes consist of simultaneous requirements on the inputs.

The triggering classes for the forward measurement are:

CMUP3-B defined as: 0MUL & !0VBA & 0VBC,

CMUP6-B defined as: 0MUL & !0VBA,

CMUP8-B defined as: 0MUL & !0VBA & 0VBC & !0VGA.

Only when all inputs are fired and inputs preceded by the exclamation mark (!) are not fired, the entire trigger class is fired and the event is accepted for further processing. An event is lost when the trigger class is not fired.

The trigger class CMUP6-B was used for p-Pb data taking. It requires a dimuon candidate and no signal in V0A. In Pb-p, the triggers CMUP3-B and CMUP8-B were used. The purity of the trigger (rejection of triggered background events) was improved by suppressing the beam-induced background because 0VBC require the presence of a signal in V0C in the time expected for beam-beam interaction. Events of collisions of a beam with the residual gas are further suppressed by !0VGA.

For the semi-forward measurement, the list of trigger classes is as follows:

CMUP5 defined as: 0MSL & !0VBA & !0VC5 & !0SH1 & 0SMB & 0VBC,

CMUP7 defined as: 0MSL & !0VBA & !0VC5 & !0SH1 & 0SMB,

CMUP9 defined as: 0MSL & !0VBA & !0VC5 & !0SH1 & 0SMB & 0VBC & !0VGA.

The trigger class CMUP7 was used for the p-Pb part of the run and classes CMUP5 and CMUP9 were used for Pb-p. The muon track candidate is selected by 0MSL and minimal amount of central activity corresponding to one crossing track is achieved by 0SH1 for some non-zero activity and by asking not to fire 0SH1 to suppress higher activity.

For semi-forward Pb-p, the purity was again improved by requiring a minimal signal in V0C in the time interval expected for interacting beams.

At mid-rapidity there was one trigger class both for p-Pb and Pb-p:

CCUP7 defined as: 0STP & !0SH1 & 0OMU & !0VBA & !0VBC,

which requires two back-to-back oriented track candidates, small amount activity in the pixel detectors and no activity in V0A nor in V0C.

6.2.8 Data sample

The data are collected during the runs of the experiment, groups of runs are gathered into the data taking periods according to conditions of the experiment and the LHC machine. See section 2.10.3 for definitions.

The periods relevant for the p-Pb part are LHC13d and LHC13e. For Pb-p the relevant period is LHC13f.

Selection of runs for the analysis took into account the availability and good conditions of all relevant systems, the muon spectrometer, V0, ITS, TPC, TOF and ZDC. The run should be marked as good in the respective documentation of conditions during the data taking and accepted by the standard quality assurance of each detector. Further it was required that at least one of the trigger classes listed in the previous section 6.2.7 was active.

The list of runs selected for the analysis in each rapidity interval (forward, semi-forward and mid-rapidity) is given in Appendix A.2.

6.3 Luminosity of the data sample

The procedure to compute the luminosity is described in general terms in Section 3.3. Using the cross section of the reference process σ_{ref}, it is possible to get the integrated luminosity

$\mathscr{L}$ of a given UPC trigger class using the number of recorded triggers at different levels of the trigger logic $N_{\mathrm{L2a}}^{\mathrm{UPC}}$ and $N_{\mathrm{L0b}}^{\mathrm{UPC}}$ as

$$\mathscr{L} = \frac{N^{\mathrm{ref}}}{\sigma_{\mathrm{ref}}} \cdot \frac{\mu}{1-e^{-\mu}} \cdot \frac{N_{\mathrm{L2a}}^{\mathrm{UPC}}}{N_{\mathrm{L0b}}^{\mathrm{UPC}}}, \tag{6.3}$$

where N^{ref} is the number of recorded triggers for the reference process and μ is the average number of reference triggers per one bunch crossing.

The middle term in Eq. (6.3) depending on μ is the probability of having several interactions per one collision bunch crossing (the pile-up), which corrects the number of reference triggers N^{ref}.

Equation (6.3) was used to calculate the integrated luminosity $\mathscr{L}$ of all trigger classes listed in Section 6.2.7.

6.4 MC samples

The STARLIGHT event generator was used to simulate the J/ψ and ψ' production in photon-proton interactions $\gamma\,\mathrm{p} \to J/\psi(\psi')\,\mathrm{p}$, coherent photoproduction of J/ψ in photon-lead interactions $\gamma\,\mathrm{Pb} \to J/\psi\,\mathrm{Pb}$ and two-photon production of lepton pairs $\gamma\gamma \to l^+l^-$ with l^+l^- standing either for e^+e^- or $\mu^+\mu^-$. Simulations of ψ' were used to determine the feed-down correction from its decays into J/ψ. The collision energy in the generator was set to $\sqrt{s_{\mathrm{NN}}}$ = 5.02 TeV p-Pb and Pb-p.

The vector mesons J/ψ and ψ' were produced by the generator already after the leptonic decays to the e^+e^- or $\mu^+\mu^-$ pairs, assuming transversal polarization of the original meson.

Inputs to productions of lepton pairs were created for invariant masses of $1.0 < m_{l^+l^-} < 10.0$ GeV/c^2.

The generated events were preselected to match the expected intervals of rapidity of the J/ψ. The kinematics of the J/ψ was retrieved from the generator output by adding the 4-momenta of the e^+e^- or $\mu^+\mu^-$ pairs. Other preselections for pseudorapidity of the decay leptons or the invariant mass of lepton pairs in the two-photon simulations were preformed in several cases.

At the time when the simulations were prepared, STARLIGHT was not part of the ALICE offline software project AliRoot. The events were produced by a data format specific for the generator, then private code was used to make all the preselections, still working with the data in the STARLIGHT format.

The preselected data in the STARLIGHT format were then converted to the object format specific for AliRoot and used as an input to the full detector simulations.

In the case of the ψ' simulations for the feed-down, the aim was to obtain the J/ψs produced as a decay product of the ψ'. The initial sample of ψ' was generated using STARLIGHT, the decays of $\psi' \to J/\psi + X$ to the J/ψ and the rest of the final state X were simulated using PYTHIA [103], and finally polarized leptonic decays $J/\psi \to l^+l^-$ of the J/ψ from ψ' were generated for a particular polarization state using a dedicated AliRoot class. The input to the ψ' simulations was then the leptons of the polarized decay of the

J/ψ and the remaining products X of the decay of original ψ'.

6.4.1 Main MC samples

The large-scale samples were used as a baseline for the determination of correction factors and the description of data in the process of signal extraction. For each particular simulation, 20 000 events were simulated under the specific conditions of each run selected for the analysis in order to account for time-dependent effects in the detector response. Given the number of selected runs (Section 6.2.8), the total number of events in one production amounts to several hundred thousands of generated events.

Most of the main simulations were performed using the official framework of the ALICE experiment. The test simulations were performed as private simulations on the computing grid, where technical issues and potential problems were fixed. Once approved for large-scale productions, the codes and input data for the simulation were provided to the central management of the official productions.

Each of the official productions was assigned a tag, which provides a unique identifier of the productions in the directory structure of the data on the ALICE computing grid. Each tag consists of 'LHC' followed by the two digits specifying the year the production was performed and an incremental letter-and-digit sequence further specifying the production.

Simulations for the analysis in the forward rapidity are listed in Table 6.1. The first column gives the tag of the simulation, *Process* is the reaction which was simulated, *System* is the beam configuration (orientation for p-Pb or Pb-p) and *Period* is the LHC period corresponding to the selected runs used to anchor the simulation. The number of events simulated in each production for the p-Pb configuration is 900 000, the number of events for each Pb-p production is 1 280 000.

Simulation	Process	System	Period
LHC13c2	$\gamma \mathrm{p} \to J/\psi \mathrm{p}$	p-Pb	LHC13d+e
LHC13c3	$\gamma\gamma \to \mu^+\mu^-$	p-Pb	LHC13d+e
LHC13c4	$\gamma \mathrm{p} \to J/\psi \mathrm{p}$	Pb-p	LHC13f
LHC13c5	$\gamma\gamma \to \mu^+\mu^-$	Pb-p	LHC13f
LHC13c8	$\gamma\,\mathrm{Pb} \to J/\psi\,\mathrm{Pb}$	p-Pb	LHC13d+e
LHC13c9	$\gamma\,\mathrm{Pb} \to J/\psi\,\mathrm{Pb}$	Pb-p	LHC13f

Table 6.1 Overview of official STARLIGHT simulations for the analysis in the forward rapidity.

The J/ψs and dimuons in $\gamma\gamma \to \mu^+\mu^-$ in the forward simulations listed in Table 6.1 were preselected for rapidity in $2.0 < |y| < 4.5$, slightly larger than the coverage of the forward muon spectrometer.

Simulations of ψ' for the forward analysis were performed as a smaller private simulation on the grid. A sample of generated ψ' with consecutive decay $\psi' \to J/\psi + X$ was preselected for the J/ψ in the rapidity interval $2.0 < |y| < 4.5$ as for the large-scale official simulations.

Dimuon decays of the J/ψ from ψ' were simulated assuming (i) full transverse polarization, (ii) full longitudinal polarization and (iii) no polarization. The simulations were anchored to one typical run of p-Pb, 195682 and to one typical run of Pb-p, 196474. An amount of 50 000 events was simulated for each production. In total, there were six productions of ψ' for the forward analysis for three extremal polarization states and two beam configurations.

The simulations used for the semi-forward analysis are presented in Table 6.2. The rapidity of the J/ψ in the semi-forward simulations was preselected to be within $1.0 < |y| < 3.0$ which corresponds to the expected interval determined using smaller-scale test simulations and the first analysis of data. As a cross-check, some of the test simulations were created using the JPSILIGHT event generator [53, 84].

The number of events simulated in each semi-forward p-Pb production in Table 6.2 is 780 000 and the number of events in each Pb-p production is 1 240 000.

Simulation	Process	System	Period
LHC13e6a	$\gamma\mathrm{p} \to J/\psi\,\mathrm{p}$	p-Pb	LHC13d+e
LHC13e6b	$\gamma\,\mathrm{Pb} \to J/\psi\,\mathrm{Pb}$	p-Pb	LHC13d+e
LHC13e6f	$\gamma\gamma \to \mu^+\mu^-$	p-Pb	LHC13d+e
LHC13f1a	$\gamma\mathrm{p} \to J/\psi\,\mathrm{p}$	Pb-p	LHC13f
LHC13f1b	$\gamma\,\mathrm{Pb} \to J/\psi\,\mathrm{Pb}$	Pb-p	LHC13f
LHC13f1f	$\gamma\gamma \to \mu^+\mu^-$	Pb-p	LHC13f
LHC13e6c	$\psi' \to J/\psi^{\perp} + X$	p-Pb	LHC13d+e
LHC13e6d	$\psi' \to J/\psi^{\parallel} + X$	p-Pb	LHC13d+e
LHC13e6e	$\psi' \to J/\psi^{0} + X$	p-Pb	LHC13d+e
LHC13f1c	$\psi' \to J/\psi^{\perp} + X$	Pb-p	LHC13f
LHC13f1d	$\psi' \to J/\psi^{\parallel} + X$	Pb-p	LHC13f
LHC13f1e	$\psi' \to J/\psi^{0} + X$	Pb-p	LHC13f

Table 6.2 Official STARLIGHT simulations for the semi-forward analysis. The polarization state of the J/ψ from ψ' decay is denoted by one of upper indices '$\perp$', '$\parallel$' and '0' for transversal, longitudinal and no polarization, respectively.

The semi-forward two-photon productions of $\gamma\gamma \to \mu^+\mu^-$ were preselected for dimuon rapidity in $1.0 < |y| < 3.0$, same as for the J/ψ. The interval of invariant mass of the $\mu^+\mu^-$ pairs was further preselected to be within $1.5 < m_{\mu^+\mu^-} < 10.0$ GeV/c^2.

To increase statistics of reconstructed events in the semi-forward two-photon productions, an additional filter for the pseudorapidity of the generated muons was applied. The pseudorapidity filter requirements were (i) one muon in $-4.5 < \eta < -2.0$ and (ii) the second muon in $-1.5 < \eta < 1.5$. As a result, the additional filter preselected the two-photon events with one muon generated towards the muon spectrometer and one muon generated within the acceptance of central detectors.

The simulations created for the mid-rapidity analysis are shown in Tables 6.3 and 6.4. The field *Channel* is the decay channel of the simulated J/ψ, the other fields have the same meaning as described in Table 6.1.

The number of events simulated in each mid-rapidity production in Tables 6.3 and 6.4 for p-Pb is 580 000 and the number of events in each Pb-p production for mid-rapidity is 1 560 000.

Simulation	Process	Channel	System	Period
LHC13e6g	$\gamma \mathrm{p} \to J/\psi \mathrm{p}$	$\mu^+\mu^-$	p-Pb	LHC13e
LHC13e6h	$\gamma \mathrm{p} \to J/\psi \mathrm{p}$	e^+e^-	p-Pb	LHC13e
LHC13f1g	$\gamma \mathrm{p} \to J/\psi \mathrm{p}$	$\mu^+\mu^-$	Pb-p	LHC13f
LHC13f1h	$\gamma \mathrm{p} \to J/\psi \mathrm{p}$	e^+e^-	Pb-p	LHC13f
LHC13e6i	$\gamma\,\mathrm{Pb} \to J/\psi\,\mathrm{Pb}$	$\mu^+\mu^-$	p-Pb	LHC13e
LHC13e6j	$\gamma\,\mathrm{Pb} \to J/\psi\,\mathrm{Pb}$	e^+e^-	p-Pb	LHC13e
LHC13f1i	$\gamma\,\mathrm{Pb} \to J/\psi\,\mathrm{Pb}$	$\mu^+\mu^-$	Pb-p	LHC13f
LHC13f1j	$\gamma\,\mathrm{Pb} \to J/\psi\,\mathrm{Pb}$	e^+e^-	Pb-p	LHC13f
LHC13e6q	$\gamma\gamma \to \mu^+\mu^-$	-	p-Pb	LHC13e
LHC13e6r	$\gamma\gamma \to e^+e^-$	-	p-Pb	LHC13e
LHC13f1q	$\gamma\gamma \to \mu^+\mu^-$	-	Pb-p	LHC13f
LHC13f1r	$\gamma\gamma \to e^+e^-$	-	Pb-p	LHC13f

Table 6.3 Official STARLIGHT simulations of J/ψ and two-photon processes for the mid-rapidity analysis.

The J/ψ for mid-rapidity simulations were preselected in the rapidity range $-1.0 < y < 1.0$, corresponding to the coverage of the central tracking detectors.

The dileptons in the two-photon productions were also preselected for e^+e^- and $\mu^+\mu^-$ pairs in $-1.0 < y < 1.0$, invariant mass of the pairs was required to be within $1.5 < m_{l^+l^-} < 10.0$ GeV/c^2. The pseudorapidity of the dileptons was further preselected to be in the range $-1.0 < \eta < 1.0$ to speed-up the simulation.

6.4.2 Auxiliary MC samples

Other MC simulations were created to achieve a correct description of the transverse momentum of the J/ψ candidates in the process of extraction the yield of the $\gamma \mathrm{p} \to J/\psi \mathrm{p}$ process or to test kinematic properties of the trigger selection.

Simulation	Process	Channel	System	Period
LHC13e6k	$\psi' \to J/\psi^{\perp} + X$	$\mu^+\mu^-$	p-Pb	LHC13e
LHC13e6l	$\psi' \to J/\psi^{\parallel} + X$	$\mu^+\mu^-$	p-Pb	LHC13e
LHC13e6m	$\psi' \to J/\psi^{0} + X$	$\mu^+\mu^-$	p-Pb	LHC13e
LHC13e6n	$\psi' \to J/\psi^{\perp} + X$	e^+e^-	p-Pb	LHC13e
LHC13e6o	$\psi' \to J/\psi^{\parallel} + X$	e^+e^-	p-Pb	LHC13e
LHC13e6p	$\psi' \to J/\psi^{0} + X$	e^+e^-	p-Pb	LHC13e
LHC13f1k	$\psi' \to J/\psi^{\perp} + X$	$\mu^+\mu^-$	Pb-p	LHC13f
LHC13f1l	$\psi' \to J/\psi^{\parallel} + X$	$\mu^+\mu^-$	Pb-p	LHC13f
LHC13f1m	$\psi' \to J/\psi^{0} + X$	$\mu^+\mu^-$	Pb-p	LHC13f
LHC13f1n	$\psi' \to J/\psi^{\perp} + X$	e^+e^-	Pb-p	LHC13f
LHC13f1o	$\psi' \to J/\psi^{\parallel} + X$	e^+e^-	Pb-p	LHC13f
LHC13f1p	$\psi' \to J/\psi^{0} + X$	e^+e^-	Pb-p	LHC13f

Table 6.4 Official STARLIGHT simulations of ψ' for the mid-rapidity analysis. Polarization indices have the same meaning as is given in Table 6.2.

Simulations of J/ψ in photon-proton interactions with modified p_T distribution

During the signal extraction of $\gamma\mathrm{p} \to J/\psi\mathrm{p}$ and the determination of the yield, an accurate description of the shape of the transverse momentum distribution of the J/ψ from $\gamma\mathrm{p} \to J/\psi\mathrm{p}$ is needed. The shape is provided by the large-scale STARLIGHT simulations of the process, as listed in Section 6.4.1.

In STARLIGHT the distribution of the transverse momentum p_T of the J/ψ in photon-proton interactions takes the form

$$\frac{\mathrm{d}N}{\mathrm{d}p_T} = A \cdot p_T \cdot \exp\left(-b \cdot p_T^2\right), \tag{6.4}$$

where A is the normalization constant and the slope parameter b is a constant in the standard STARLIGHT program, but according to measurements performed at HERA it depends on the photon-proton energy $W_{\gamma\mathrm{p}}$ as [27]

$$b(W_{\gamma\mathrm{p}}) = b_0 + 4\alpha' \ln(W_{\gamma\mathrm{p}}/W_0). \tag{6.5}$$

The parameters of Eq. (6.5) are $b_0 = 4.630\ \mathrm{GeV}^{-2}$, $\alpha' = 0.164$ and W_0 was arbitrarily set to $W_0 = 90$ GeV [27].

Because the value of α' is positive, the distribution in Eq. (6.4) is softer at higher energies. The rapidity of the J/ψ is related to the energy $W_{\gamma\mathrm{p}}$, therefore a specific value of b should be used with a given rapidity interval.

STARLIGHT uses a constant value of $b = 4.0\ \mathrm{GeV}^{-2}$, which is good enough at lower energies. However, at the energies reached at mid-rapidity, semi-forward Pb-p and forward

Pb-p, fine tuning of the slope parameter was needed.

Following discussion with one of the authors of STARLIGHT [104], the value of b was changed in the generator resulting in a sample of J/ψ generated with a modified transverse momentum distribution in Eq. (6.4).

Values of the slope parameter b used for rapidities where high energies are reached are shown in Table 6.5.

Rapidity interval	$W_{\gamma p}$(GeV)	$\langle W_{\gamma p}\rangle$(GeV)	b (GeV^{-2})
Mid-rapidity	[106, 235]	161	5.0
Semi-forward Pb-p	[287, 550]	391	5.6
Forward Pb-p	[577, 952]	706	6.7

Table 6.5 Values of the exponential slope parameter for the distribution in Eq. (6.4) calculated for mean values of the energy $\langle W_{\gamma p}\rangle$ from Eq. (6.5). Energy ranges and mean values are given for rapidity intervals where high energies are reached.

A more detailed study has been done for the behavior of the distribution in Eq. (6.4) for the mid-rapidity and semi-forward Pb-p analyses. The normalized distributions corresponding to the modified exponential slope parameter b are shown together with the distribution using the default $b = 4.0$ GeV^{-2} in Figure 6.5, the softening of the distribution at higher energies is visible.

The generated events were preselected and put into the full detector simulation following the same procedures as for the official large-scale simulations described in Section 6.4.1.

The simulation for the analysis in the forward rapidity was performed with a sample of events of $\gamma\text{p} \rightarrow J/\psi\text{p}$ generated with the assumption $b = 6.7$ GeV^{-2} according to Table 6.5. The events were preselected such that the rapidity of the J/ψ is in $-3.6 < y < -2.6$. The simulation was anchored to 5 runs of LHC13f, 196477, 197388, 197386, 197098 and 197089. 20000 events were simulated for each run, giving the total statistics of the simulation of 100000 events.

For the simulation in the semi-forward rapidity, the J/ψ produced in the photon-proton interactions were generated at $b = 5.6$ GeV^{-2} (Table 6.5). The generated events were preselected for $-3.0 < y < -1.0$, as was done for the official large-scale productions. The rapidity is negative in Pb-p. The simulation was performed corresponding to the conditions of six runs of LHC13f covering the data taking period, 196535, 196601, 196876, 197138, 197256 and 197348. Again 20000 events were simulated for each run, giving the total amount of 120000 events.

At mid-rapidity, the simulation of J/ψ in photon-proton interactions used the value of $b = 5.0$ GeV^{-2} as was summarized in Table 6.5. The J/ψ were preselected for central rapidity $-1.0 < y < 1.0$. The simulation was anchored to two runs of LHC13e, 196085 and 196310 and to four runs belonging to LHC13f, 196601, 196876, 197138 and 197348. For each run there were 20000 generated events, giving total statistics of 120000 events. Two separate simulations were performed for each J/ψ dilepton decay channel, $J/\psi \rightarrow e^+e^-$

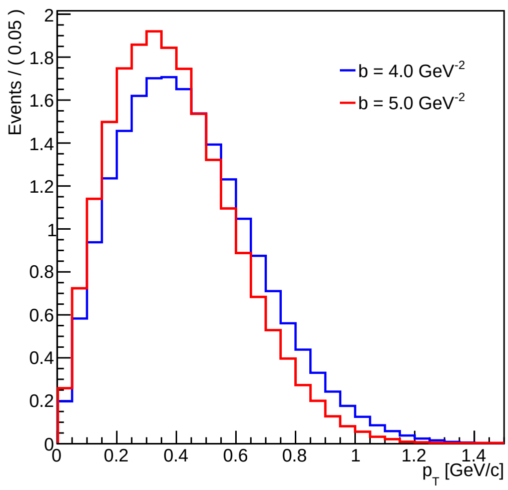

(a)

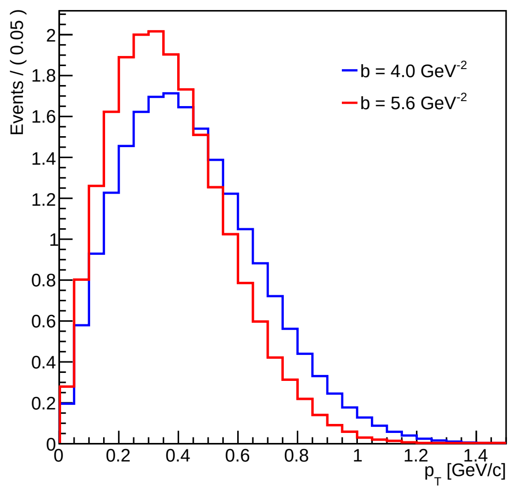

(b)

Fig. 6.5 Comparison of distribution in Eq. (6.4) between the default value $b = 4.0$ GeV^{-2} used in STARLIGHT and the value corresponding to mid-rapidity $b = 5.0$ GeV^{-2} (a) and the value $b = 5.6$ GeV^{-2} for energy at semi-forward Pb-p (b). The distribution is softer when the energy is increased.

and $J/\psi \to \mu^+\mu^-$.

Simulation of J/ψ with uniform p_T distribution

Another set of special simulations have been set up using the J/ψ generated with a uniform p_T distribution at mid-rapidity. The purpose was the need to evaluate the effect of the trigger on the dependence of the detection efficiency as a function of the p_T of the J/ψ.

The standardized generator of flat distributions embedded in AliRoot produced the di-electrons and the dimuons with the mass of the J/ψ, uniform p_T within $0 < p_T < 4$ GeV, uniform azimuthal angle and uniform dilepton rapidity $|y| < 1.5$. The distribution of the daughter leptons polar angle in the rest frame of the J/ψ corresponded to transverse polarization of the J/ψ.

Simulations of two-photon processes using the LPAIR event generator

Simulations of elastic and proton-dissociative production of two-photon production of di-muon pairs, $\gamma\gamma \to \mu^+\mu^-$ have been carried out using the LPAIR event generator [105] for the forward p-Pb analysis.

The aim of measuring the cross section of $\gamma\gamma \to \mu^+\mu^-$, for which the simulations were used, was to understand the background to the J/ψ from this process and to make cross checks of several steps in the analysis.

The LPAIR simulations were supplementary to the STARLIGHT simulation of elastic two-photon production in p-Pb listed in Table 6.1.

The generator was set to the kinematics of p-Pb, the generated events were preselected for the forward rapidity of the dimuon pair in $2.0 < y < 4.5$ and invariant mass $m_{\mu^+\mu^-} > 1.0$ GeV/c^2. Then the events were converted into the object format used by AliRoot and put to the full detector simulation. Both simulations, elastic and proton dissociative, were performed as a private simulation on the ALICE computing grid.

The simulation of elastic $\gamma\gamma \to \mu^+\mu^-$ was anchored to runs 195682, 195724, 195725, 195783, 195826 and 195872, the number of events generated for each run was 20 000, giving 120 000 events in total.

The simulation of $\gamma\gamma \to \mu^+\mu^-$ with proton dissociation was performed for runs 195682, 195724, 195725, 195783, 195826, 195872 and 195873. Again 20 000 events were generated for each run, giving for 7 runs the final statistics of 140 000 events.

The demands on the computing time for this simulation proved to be very high, due to the transport of the boosted dissociation products through the detector and construction material.

6.5 Event selection

The selection criteria described in this section have been applied during the offline analysis of the data collected by the UPC triggers listed in Section 6.2.7.

The criteria have been tuned to get as cleaner a sample of exclusive J/ψ as possible, by selecting only events having two tracks and no other signal in the detectors.

Besides the exclusivity selection, additional requirements regarding the quality of the reconstruction have been required, to select only the events of well defined properties.

This section is divided into the general requirements common to the rapidity intervals where the J/ψ was measured and to further requirements specific to each interval.

In the end, the statistics of selected events after each analysis step is given and the basic properties of the selected J/ψ candidates is shown, comparing the data and results to the corresponding STARLIGHT simulations.

6.5.1 General requirements

The requirements common to events reconstructed in all rapidity intervals are denoted as **GR** (for General Requirement) followed by the number of the requirement.

The general requirements also include criteria on the tracks reconstructed in the forward muon spectrometer and central tracking detectors which are shared among the intervals which use the muon spectrometer or central tracking.

The general requirements are:

- General requirements at the event scope.

  GR-1 The event belonged to any of the selected runs for a given rapidity interval.

This requirement ensures that the different detector systems were well understood by the experts and could be used in the analysis.

GR-2 The V0A offline decision had to be in the empty state.

This requirement rejected beam-gas and peripheral hadronic events. Although the triggers required a similar configuration, this criterion was needed, because the signals from the trigger are different from the offline signals which take into account the final response of all the V0 cells to build the offline V0 decision state. The requirement on the state of V0C depends on the presence of the muon track(s), crossing the V0C, and will be discussed for each rapidity interval separately.

GR-3 The neutron ZDC had to be compatible with no neutrons.

This selection rejected events with extra activity, which was not expected in the desired UPC events. The selection has been implemented, following the advice of the experts, by requiring empty timing information in the neutron ZDCs on both sides, A and C.

- General requirements for the muon track.

GR-4 The radial position of the track at the end of the absorber R_{abs} should be in the interval of $17.5 < R_{\mathrm{abs}} < 89.5$ cm.

This requirement ensured that the track went through the homogeneous part of the absorber.

GR-5 Pseudorapidity of the track η should fulfill $-4.0 < \eta < -2.5$ for p-Pb and $-3.7 < \eta < -2.5$ for Pb-p.

This requirement ensured that the track was within the acceptance of the muon spectrometer and also of the V0-C in the Pb-p case, where the trigger required presence of the signal in V0C.

GR-6 The track fulfills the $p \times \mathrm{DCA}$ requirement.

Due to the multiple scattering in the front absorber, the DCA (distance between the vertex and the track extrapolated to the vertex transverse plane) distribution of the tracks coming from the interaction vertex is described by a Gaussian function whose width depends on the absorber material and is proportional to $1/p$, where p is the 3–momentum of the track. The beam induced background does not follow this trend and is removed by the $p \times \mathrm{DCA}$ condition. The selection is formulated inside the implementation of a muon selection class in AliRoot.

GR-7 It was matched to a trigger track.

This requirement selected the track matching a trigger track recorded in the spectrometer trigger chambers.

- General requirements for a track in the central detectors.

GR-8 The track had tracking flags from ITS and TPC.

This requirement ensured that the track was reconstructed by ITS and TPC.

GR-9 At least one space point associated to the track was from SPD.

This requirement provided the past-future protection for the central track. The read-out time of SPD is fast enough to assure that a track with a point in SPD belongs to the time interval of the current event. Tracks belonging to one of the previous events were rejected by this requirement.

GR-10 Number of TPC space points was at least 50.

The requirement suppressed tracks passing a small fraction of the TPC active volume. Such track would have ill defined kinematics properties.

GR-11 Reduced χ^2 of the track in TPC was $\chi^2/\mathrm{NDF} < 4$.

Selection for the quality of the fit to the reconstructed space points of the track.

- Requirements for dileptons. (A dilepton is built as the vectorial sum of the four momenta of the two accepted tracks in the central barrel, where the four momentum of the track was computed assuming the mass of an electron or a muon).

GR-12 There was only one dilepton candidate.

This requirement rejected events with extra activity in the tracking detectors. This activity is not expected for the UPC we are interested in.

GR-13 The two tracks had opposite electric charges.

This requirement selected the expected cases for both J/ψ and two-photon dilepton production. The opposite requirement, that the tracks had the same electric charge, was used to estimate the remaining background from random coincidences.

6.5.2 Selection criteria at forward rapidity

At forward rapidity, there should be two tracks reconstructed in the forward muon spectrometer and no other signals. The selection strategy is shown in Figure 6.2.

Each event should fulfill the general requirements and the requirements specific for the forward rapidity. The requirements are denoted as **FR** for Forward Requirement.

The requirements for the forward analysis are:

- Requirements for the event.

  FR-1 The event should pass **GR-1 – GR-3**.

  FR-2 The event was triggered by one of CMUP3-B, CMUP6-B or CMUP8-B trigger classes.

  This requirement selected only those events of interest.

  FR-3 The proton ZDC should be compatible with no protons.

  FR-4 The offline decision of V0C should be in the empty or beam-beam state for p-Pb and in the beam-beam state in Pb-p.

  Possible activity corresponds to the crossing muons. In the case of Pb-p, the trigger required online activity in the V0C which is followed by the offline requirement. The beam-beam state means non-zero activity at the time within the interval expected for particles produced in the collision of the crossing beams.

  FR-5 The number of SPD tracklets had to be zero. Tracklets are track segments formed by two hits at each SPD layer.

  The requirement implied no activity in the central rapidity region.

- Requirements for tracks in the muon spectrometer.

  FR-6 Each track should fulfill the general requirements **GR-4 – GR-7**.

- Requirements for dimuons.

  FR-7 The dimuon should pass the general requirements **GR-12** and **GR-13**.

  FR-8 The rapidity of the dimuon was in the range $2.5 < y < 4.0$ for p-Pb and $-3.6 < y < -2.6$ for Pb-p.

  This requirement defined the phase space for the measurement and ensured that the measurement was carried out in a region of good acceptance for the trigger and the different detectors.

6.5.3 Selection criteria at semi-forward rapidity

The J/ψ at semi-forward rapidity is reconstructed using one track in the forward muon spectrometer and one track in the central tracking detectors. The analysis strategy is illustrated in Figure 6.3.

Each event should pass the general requirements and the current specific requirements, which are denoted as **SR** for Semi-forward Requirement.

Requirements for the semi-forward analysis are:

- Requirements for the event.

SR-1 The event should pass **GR-1 – GR-3**.

SR-2 The event was triggered by one of CMUP5-B, CMUP7-B or CMUP9-B trigger classes.

This requirement selected only those events of interest.

SR-3 The number of SPD tracklets had to be zero or one. Tracklets are track segments formed by two hits at each SPD layer.

This requirement is consistent with the assumption of one track crossing the SPD.

SR-4 The offline decision of V0C should be in the empty or beam-beam state in p-Pb and in the beam-beam state in Pb-p.

Possible activity corresponds to the crossing muon. In the case of Pb-p, the trigger required online activity in the V0C which is followed by the offline requirement. The beam-beam state means non-zero activity at the time within the interval expected for particles produced in the collision of the crossing beams.

SR-5 The number of offline hits in V0C had to be zero or one.

The requirement allowed at most one active cell of V0C, which is consistent with one crossing muon. Events with additional activity are removed.

- Requirements for a track in the muon spectrometer.

SR-6 The track should fulfill the general requirements **GR-4 – GR-7**.

- Requirements for a track in the central detectors.

SR-7 The track should fulfill the general requirements **GR-8 – GR-11**.

SR-8 Pseudorapidity η of the track had to be within $-1.1 < \eta < 1.1$.

This requirement ensured that the track was within the acceptance of SPD and extended acceptance of TPC. The track is not restricted to pass the full volume of TPC to gain more statistics.

SR-9 The DCA of the track to the nominal interaction point at the coordinates (0,0,0) along the beam direction, DCA_z, is constrained to be within $-15 < DCA_z <$ 15 cm.

This selection should suppress particles from secondary hadronic interactions or from conversions in the material, the value is chosen to keep as much statistics as possible.

- Requirements for dimuons.

SR-10 The dimuon should pass the general requirements **GR-12** and **GR-13**.

SR-11 The energy loss in the TPC for the central track which forms the dimuon candidate is consistent with muon expectation from the Bethe-Bloch parametrization within 4 standard deviations.

SR-12 The rapidity of the dimuon was in the range $1.2 < y < 2.7$ for p-Pb and $-2.5 < y < -1.2$ for Pb-p.

This requirement defined the phase space for the measurement and ensured that the measurement was carried out in a region of good acceptance for the trigger and the different detectors.

6.5.4 Selection criteria at mid-rapidity

The J/ψ at mid-rapidity is reconstructed from the two tracks in the central tracking detectors. Both leptonic decay channels, dielectron and dimuon are measured in this interval. The selection scheme is shown in Figure 6.4.

Each event should pass the general requirement and the criteria below, here denoted as **MR** for Mid-rapidity Requirement.

Requirements at mid-rapidity are:

- Requirements for the event.

MR-1 The event should pass **GR-1 – GR-3**.

MR-2 The event was triggered by the CCUP7-B trigger class.

This requirement selected only those events of interest.

MR-3 The number of SPD tracklets had to be ≤ 2. Tracklets are track segments formed by two hits at each SPD layer.

This requirement is consistent with the assumption of two tracks crossing the SPD.

MR-4 The V0C offline decision had to be in the empty state.

No activity is expected on the C-side.

- Requirements for the primary vertex.

MR-5 The vertex had at least two contributors.

MR-6 The reconstructed position of the vertex along the beam direction was $|\mathrm{vtx}_z| <$ 15 cm.

- Requirements for the tracks.

MR-7 Each track should fulfill the general requirements **GR-8 – GR-11**.

MR-8 The pseudorapidity η of the track had to be within $-0.9 < \eta < 0.9$.

This requirement ensured that each track was within the acceptance of SPD and TPC.

MR-9 The track is not a kink candidate.

The kink is a result of a weak decay of the particle while passing through the tracking detectors. Part of the total energy is carried away by the neutrino, which is observed as a sudden change in the particle momentum.

MR-10 The DCA of the track to the primary vertex along the beam direction DCA_z had to pass $|\mathrm{DCA}_z| < 2$ cm and the DCA in the transversal plane DCA_{xy} should fulfill the parametrization $|\mathrm{DCA}_{xy}| < 0.0182 + 0.0350/p_T^{1.01}$, where the p_T of the track is in GeV.

- Requirements for dileptons.

MR-11 The dilepton should pass the general requirements **GR-12** and **GR-13**.

MR-12 The dilepton is identified as a dielectron or a dimuon by the specific energy loss in the TPC.

The energy loss in the TPC had to be consistent with the Bethe-Bloch expectations for electrons or muons within four standard deviations. Normalized deviation from the Bethe-Bloch expectation $\Delta\sigma_+$ and $\Delta\sigma_-$ of the positive and negative track should fall into the circle within the 4σ interval, $\Delta\sigma_+^2 + \Delta\sigma_-^2 < 4^2$.

MR-13 Rapidity of the dilepton was in the range $-0.8 < y < 0.8$.

This requirement defined the phase space for the measurement and ensured that the measurement was carried out in a region of good acceptance for the trigger and the different detectors.

6.5.5 Event displays

The figures show events displays of events passing the selection criteria described in the previous Section 6.5. The events have been selected to have the mass of the dilepton in the range expected for the J/ψ.

A forward event is shown in Figure 6.6, a semi-forward event is shown in Figure 6.7 and an event at mid-rapidity is shown in Figure 6.8.

6.5.6 Selection for background samples

The signal extraction requires a sample of non-exclusive J/ψ and of $\gamma\gamma \to e^+e^-(\mu^+\mu^-)$, which correspond to proton dissociation. The sample for each rapidity interval was obtained from data by modifying some of the selection criteria.

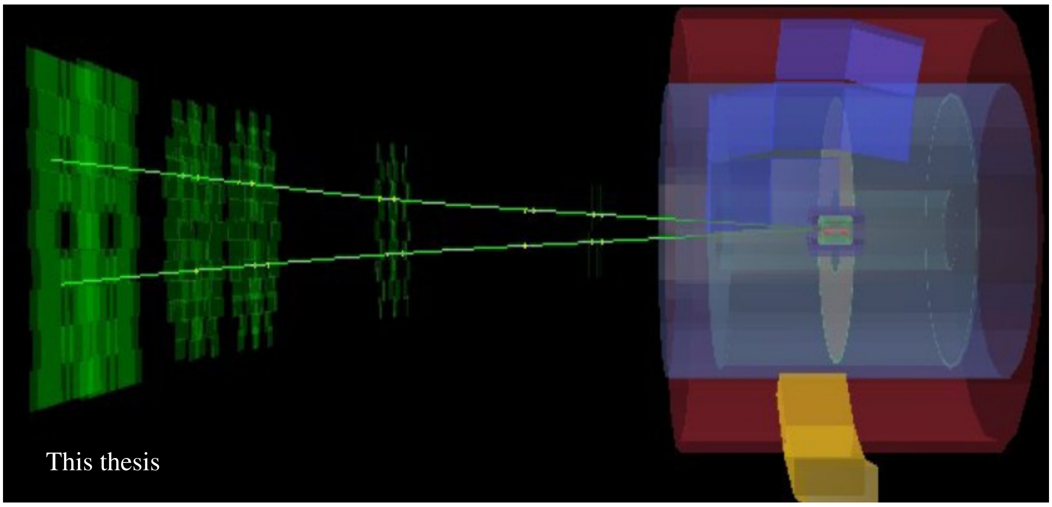

Fig. 6.6 Event display for a J/ψ candidate at forward rapidity. Both muons of the dimuon decay $J/\psi \rightarrow \mu^{+}\mu^{-}$ are detected in the forward muon spectrometer.

In the forward rapidity, the non-exclusive background was found to be present in p-Pb, but very negligible in Pb-p, where the protons were moving toward the V0A, which was used as a veto at a trigger level. The forward sample of non-exclusive events was obtained from data using the same selection criteria as listed in Section 6.5, but requiring more than two hits in V0C. Another sample for systematic checks was created by removing the requirements **GR-3** and **FR-3** for no signal in the neutron and the proton ZDCs.

At semi-forward rapidity and at mid-rapidity, some amount of non-exclusive background was found to be present both in p-Pb and Pb-p. A unified method for obtaining the sample of non-exclusive events based on the ZDCs was used. The requirement **GR-3** for no signal in both neutron ZDCs was modified for non-zero signal in the ZDC in the direction of the proton beam (A-side for Pb-p and C-side for p-Pb) while there should be no signal in the ZDC on the opposite side. The presence of a signal in the respective ZDC was ensured by requiring non-zero timing information in that ZDC. Dileptons of both signs were allowed in order to account also for the like-sign background, the sample was a mixture of unlike-sign and like-sign events.

6.5.7 Statistics of selected events

An overview of the number of events triggered for each rapidity interval and the number of events passing the offline selection criteria is given in this section. The events passing the criteria are then used for the signal extraction.

At forward rapidity, the number of events triggered by the p-Pb class CMUP6-B is 329 626 and the number of events of CMUP3-B and CMUP8-B Pb-p classes is 1 920 367. In p-Pb there are 682 events passing the criteria and having the dimuon mass in the range expected for the J/ψ, $2.8 < m_{\mu^{+}\mu^{-}} < 3.4$ GeV/c^{2}, in Pb-p there are 105 such events.

For the semi-forward and mid-rapidity intervals, the effect of the individual levels of

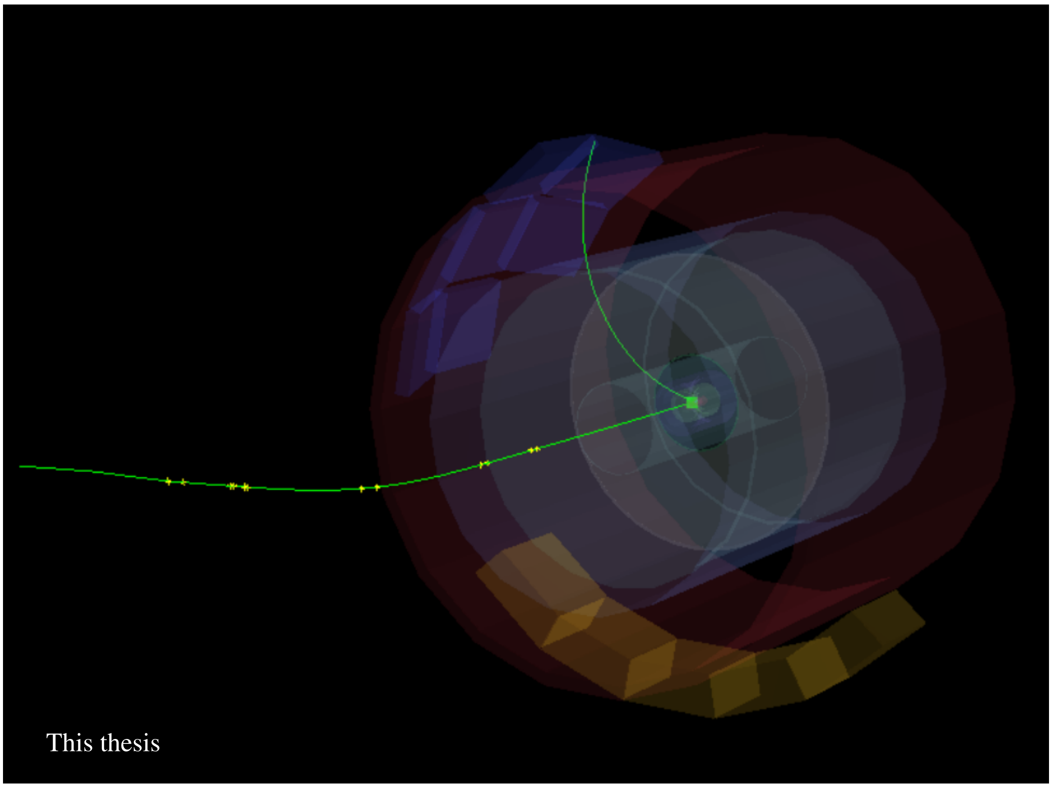

Fig. 6.7 Event display for a semi-forward J/ψ candidate. The dimuon decay is reconstructed with one muon in the muon spectrometer and the other one in the central detectors.

selection criteria to the statistics is shown in Tables 6.6 and 6.7. The top of both of the tables begins with the number of analyzed triggers for each rapidity interval (Section 6.2.6). Then the number of events remaining after each selection requirement is given, going down towards the final sample of the J/ψ candidates to be used for signal extraction. The last line of both tables refers to the final sample of dileptons within a given rapidity interval and mass expected for the J/ψ in the interval of $2.9 < m_{\mu^+\mu^-} < 3.2$ GeV/c^2 at semi-forward rapidity and intervals of dielectron and dimuon masses $2.9 < m_{e^+e^-} < 3.2$ GeV/c^2 and $3.0 < m_{\mu^+\mu^-} < 3.2$ GeV/c^2 respectively at mid-rapidity.

At the level of ZDC, the selection splits up to the sample of standard selection for the signal, and to the selection for the non-exclusive background sample according to Section 6.5.6.

6.5.8 Properties of the selected candidates

Kinematics and technical properties of the semi-forward and mid-rapidity J/ψ candidates are shown in this section by making distributions of the related quantities accompanied by the distribution of the same quantity from the MC simulation. All the figures are shown in Appendix C.

The MC distributions are created for a given quantity as was reconstructed after the full

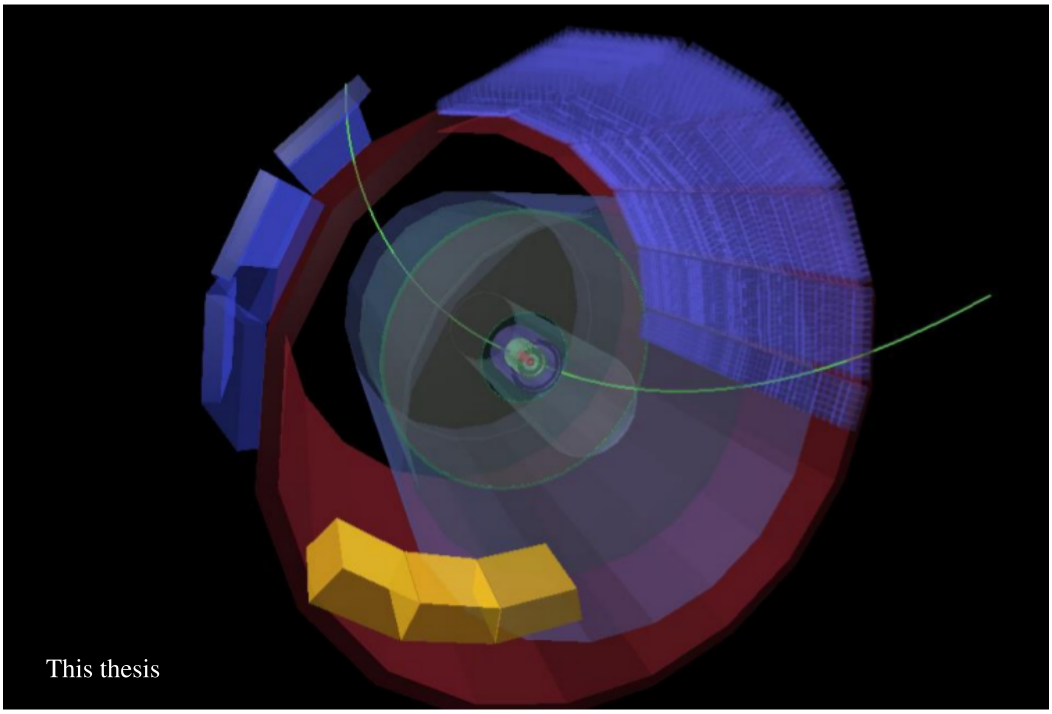

Fig. 6.8 Event display for a J/ψ candidate at mid-rapidity. Both tracks are reconstructed in the central detectors.

detector simulation. The normalization of each MC distribution is scaled to that of data.

The properties of the semi-forward J/ψ candidates are shown in Figures C.1 – C.10. The mass of the dimuon is restricted to the range of the J/ψ as indicated in the legend in each plot, together with the interval of rapidity. The large-scale simulations LHC13e6a and LHC13f1a (Table 6.2) are used for semi-forward p-Pb and Pb-p respectively.

The properties of the J/ψ candidates selected at mid-rapidity are shown in Figures C.11 – C.19. The ranges of invariant masses selecting the J/ψ are indicated in the legend of each plot. The simulations LHC13e6g, LHC13e6h, LHC13f1g, LHC13f1h (Table 6.3) are used for the scaled MC distributions in the mid-rapidity plots.

The distributions of reconstructed quantities from data and results of the full MC simulations presented in Appendix C indicate a good ability of the simulations to describe the data.

System	p-Pb		Pb-p	
SR-2, triggered events	495 653		894 653	
SR-3, SPD tracklets	396 813		839 499	
GR-2+SR-4,5, V0	168 633		157 774	
ZDC selection	signal	background	signal	background
GR-3, ZDC	108 740	36 234	125 223	6445
GR-12, two tracks	2366	2130	390	102
SR-11, TPC identification	2214	1888	365	98
GR-13, unlike sign	1775	-	314	-
Rapidity and J/ψ mass	382	255	105	45

Table 6.6 Events passing selected levels of the offline selection criteria at semi-forward rapidity. The reference to a given requirement with a short description is given in the left column and the number of remaining events is shown in the right part for p-Pb and Pb-p.

MR-2, triggered events	1 486 605			
MR-3, SPD tracklets	466 339			
GR-2+MR-4, V0	396 856			
ZDC selection	signal		background	
GR-3, ZDC	210 165		73 691	
MR-5,6,vertex	195 806		70 935	
GR-12, two tracks	61 567		25 732	
Identification selection	electrons	muons	electrons	muons
MR-12, identification in TPC	2072	52 781	685	21 793
GR-13, unlike sign	1888	44 447	-	-
J/ψ mass and $\|y\| < 0.8$	304	538	105	183

Table 6.7 Events at mid-rapidity passing selected levels of the offline selection criteria. The reference to a given requirement with a short description is given in the left column and the number of remaining events is shown in the right part.

6.6 Correction factors for acceptance and efficiency

The total acceptance and efficiency correction $\varepsilon_{J/\psi}$ for the cross section in Eq. (6.2) takes into account all detector acceptance effects and inefficiencies. The basic ideas to determine the correction are outlined in Section 3.4.

The overall acceptance and efficiency was determined using the MC simulations of the process in question, $\gamma \mathrm{p} \to J/\psi \mathrm{p}$. Specific contributions resulting from the trigger requirements were calculated separately. The total correction $\varepsilon_{J/\psi}$ is then product of all factors.

6.6.1 Acceptance and efficiency using MC simulations

The product of detector acceptance and efficiency $(\mathrm{Acc} \times \varepsilon)_{J/\psi}$ was determined using the large-scale MC simulations of J/ψ production in photon-proton interactions $\gamma \mathrm{p} \to J/\psi \mathrm{p}$. Tags of the simulations are given in Section 6.4.1 in Tables 6.1, 6.2 and 6.3 for all the three rapidity intervals.

The acceptance and efficiency $(\mathrm{Acc} \times \varepsilon)_{J/\psi}$ provides the overall correction to the case when one or both electrons or muons from the decay of the J/ψ point outside the detector coverage (acceptance), or to the case when they were not properly registered (efficiency).

The calculation of $(\mathrm{Acc} \times \varepsilon)_{J/\psi}$ was done as the ratio of events reconstructed in the MC to the number of generated events, both in a given interval of rapidity of the J/ψ.

The same selection criteria as for the data (Section 6.5) were applied to events reconstructed in MC, and an additional requirement on the reconstructed mass was used to correct for events reconstructed outside the fiducial range around the mass of the J/ψ. Counting the events surviving all the criteria provided the number of reconstructed events n_{rec}.

By reading the generator input in the MC data, the number of J/ψ which were generated into a given rapidity interval was counted, providing the number of generated events n_{gen}.

The acceptance and efficiency is then the probability of a generated event to pass all selections, $n_{\mathrm{rec}}/n_{\mathrm{gen}}$.

To account for time variations in the detector response, separate ratios of $n_{\mathrm{rec}}/n_{\mathrm{gen}}$ were made for each run. The final $(\mathrm{Acc} \times \varepsilon)_{J/\psi}$ was obtained as the average of individual ratios weighted by the luminosity collected in each run.

The correction varies from 3% to 31%, depending on the decay channel and interval of rapidity (forward, semi-forward and mid-rapidity).

The time dependence of the acceptance and efficiency is shown in Figure B.4 for semi-forward rapidity and in Figure B.5 for mid-rapidity. The dependence is provided as the efficiency as a function of run number.

The rapidity dependence of $(\mathrm{Acc} \times \varepsilon)_{J/\psi}$ is shown in Figure 6.9 for the semi-forward rapidity interval and in Figure 6.10 for mid-rapidity.

The plots of the rapidity dependence are created by dividing the distribution of reconstructed rapidity of the J/ψ with the distribution of generated rapidity. The full set of trigger inputs was used to get the reconstructed sample for the plots.

We can see that the efficiency is peaked in the middle of the interval and smoothly falls to the edges of the acceptance.

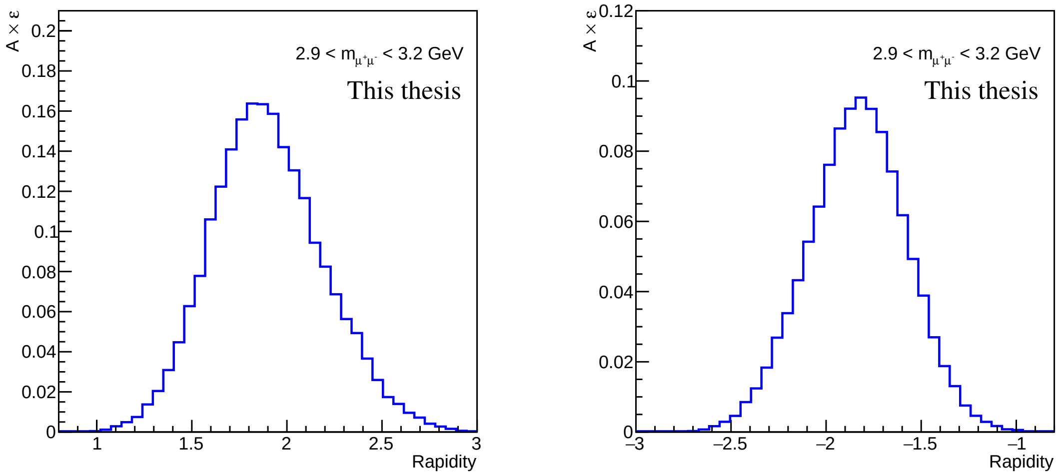

Fig. 6.9 Acceptance and efficiency $(\mathrm{Acc} \times \varepsilon)_{J/\psi}$ as a function of rapidity of the J/ψ for semi-forward p-Pb (left) and Pb-p (right). The fiducial mass interval, which was required for the reconstructed dimuon, is shown in the legend.

6.6.2 Efficiency of the V0C trigger input

The trigger classes for the Pb-p measurements in the forward and semi-forward rapidity intervals required the presence of a signal in the V0C in the direction of the forward muon spectrometer. The requirement was imposed by asking for the 0VBC input in the fired state (Section 6.2.7). The input required at least one scintillator cell of V0C to be fired within the time interval expected for particles coming from the interaction of the two colliding beams.

It was not possible to obtain the efficiency of the 0VBC trigger from MC simulations. The energy deposition by one (semi-forward) or two (forward) muons in a relative thin scintillator is subject to large fluctuations, the MC simulation would need perfect reproduction of the signal deposition.

The issue was also encountered in the analysis of coherent J/ψ photoproduction in Pb-Pb collisions, as described in Section 4.2.3. A procedure based on the reference QED cross section of $\gamma\gamma \rightarrow \mu^+\mu^-$ was used to eliminate the 0VBC efficiency from the calculation of the coherent cross section.

In the present analyses, data driven methods were proposed, profiting from the larger statistics of the selected events.

Efficiency of V0C trigger input at forward rapidity

Assuming that one muon crossing the V0C can fire at most one V0C cell, the efficiency of the 0VBC trigger input $\varepsilon_{0\mathrm{VBC}}$ was calculated by counting the events with one and two cells fired.

For the data of Pb-p, the requirement of at most two offline hits in V0C and transverse momentum of the dimuon $p_T < 1$ GeV/c was added to the forward selection criteria (Sec-

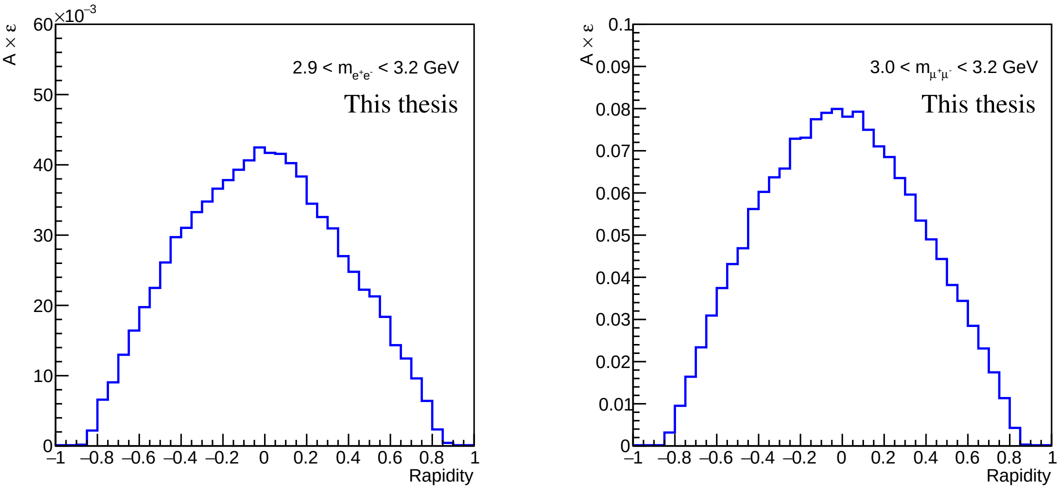

Fig. 6.10 Acceptance and efficiency $(\mathrm{Acc}\times\varepsilon)_{J/\psi}$ as a function of rapidity of the J/ψ at mid-rapidity in the dielectron channel (left) and dimuon channel (right). Fiducial mass intervals, which were required for the reconstructed dileptons, are shown in the legend.

tion 6.5) to get a clean sample.

The events were counted according to the number of V0C fired cells, giving n_0 events with no fired cells, n_1 events with one cell fired and n_2 events having two fired cells. The number of all selected events is then

$$n = n_0 + n_1 + n_2. \tag{6.6}$$

The desired efficiency of 0VBC to select the events with at least one cell fired is

$$\varepsilon_{0\mathrm{VBC}} = \frac{n-n_0}{n} = \frac{n_1+n_2}{n}. \tag{6.7}$$

As the trigger in Pb-p required at least one cell fired, it is only possible to get n_1 and n_2 from the data, therefore we need to formulate Eq. (6.7) in terms of n_1 and n_2.

For this purpose we introduce the efficiency to detect a single muon ε_1 as

$$\frac{n_1}{n} = 2\varepsilon_1(1-\varepsilon_1) \tag{6.8}$$

$$\frac{n_2}{n} = \varepsilon_1^2. \tag{6.9}$$

By dividing the above equations, we will get the single muon efficiency determined by the ratio r of events with one and two cells fired:

$$r \equiv \frac{n_1}{n_2} = \frac{2(1-\varepsilon_1)}{\varepsilon_1}. \tag{6.10}$$

The ratio r can be measured from the Pb-p counts of n_1 and n_2, giving the data driven estimates for the single muon efficiency and the final efficiency of the 0VBC trigger to select the dimuons:

$$\varepsilon_1 = \frac{2}{r+2} \tag{6.11}$$

$$\varepsilon_{0\mathrm{VBC}} = 1 - (1-\varepsilon_1)^2. \tag{6.12}$$

The 0VBC trigger input was used with the two forward trigger classes, CMUP3-B and CMUP8-B, giving two values of $\varepsilon_{0\mathrm{VBC}}$ for each of these:

$$(\varepsilon_{0\mathrm{VBC}})_{\mathrm{CMUP3}} = 0.868 \pm 0.030 \tag{6.13}$$

$$(\varepsilon_{0\mathrm{VBC}})_{\mathrm{CMUP8}} = 0.795 \pm 0.046. \tag{6.14}$$

The errors were calculated with the assumption of binomial statistics for the counts n_1 and n_2.

The procedure was tested with the p-Pb forward data, where the trigger did not required the 0VBC input, and was possible to count events without any hits in V0C, giving the n_0 counts. The true efficiency in Eq. (6.7) was compared with the estimate in Eq. (6.12). A very good agreement was found.

Efficiency of the V0C trigger input at semi-forward rapidity

The above procedure is not applicable for the semi-forward Pb-p analysis, where there is only one muon crossing the V0C detector. The efficiency of the 0VBC trigger input was obtained using the p-Pb semi-forward data. This trigger input was not part of the relevant trigger class.

The selection criteria for the p-Pb data sample have been modified in what respects the pseudorapidity of the muon track and the rapidity of dimuons so that they have the same limits as in Pb-p (overlap of muon and V0C acceptance, $-3.7 < \eta < -2.5$ and $1.2 < y < 2.5$). In this way only p-Pb events with the muon track passing within the V0C acceptance were selected.

The neutron ZDC on the A-side was not restricted, dimuons of both signs were allowed, both in order to gain more statistics in the sample.

The efficiency of the 0VBC trigger input, $\varepsilon_{0\mathrm{VBC}}$, was calculated as the ratio of events having the 0VBC trigger input fired to the number of all selected events.

The interval of dimuon mass of the events used to calculate the $\varepsilon_{0\mathrm{VBC}}$ was continuously varied from $2.9 < m_{\mu^+\mu^-} < 3.2$ GeV/c^2 to $2.0 < m_{\mu^+\mu^-} < 5.0$ GeV/c^2. The maximal difference between the efficiencies obtained for individual mass intervals was found to be 2%, giving the systematic error to the 0VBC efficiency.

Using the largest mass interval, $2.0 < m_{\mu^+\mu^-} < 5.0$ GeV/c^2, the efficiency is

$$\varepsilon_{0\mathrm{VBC}} = 0.585 \pm 0.016(\mathrm{stat}) \pm 0.012(\mathrm{syst}). \tag{6.15}$$

When the errors are added in quadrature, we have

$$\varepsilon_{0\mathrm{VBC}} = 0.585 \pm 0.020. \tag{6.16}$$

6.6.3 Cross-check of the 0VBC efficiency at semi-forward rapidity

Results on the efficiency of the 0VBC trigger at forward rapidity have been used to make a cross-check for the efficiency in the semi-forward rapidity.

Using the final values and errors for the dimuon efficiency ε_2 (Eq. (6.13)), the single muon efficiency ε_1 can be retrieved from Eq. (6.12) for the dimuon efficiency as

$$\begin{aligned} \varepsilon_1 &= 1 - \sqrt{1-\varepsilon_2} \\ \sigma_{\varepsilon_1} &= \sigma_{\varepsilon_2} \frac{1}{\sqrt{1-\varepsilon_2}} \end{aligned} \tag{6.17}$$

In the semi-forward rapidity, the efficiency for single muons is directly the efficiency of the 0VBC trigger input. We may identify the cross check of the efficiency with ε_1 from Eq. (6.17) as $\varepsilon_{0\mathrm{VBC}}^{\mathrm{x-check}} \equiv \varepsilon_1$.

The semi-forward trigger classes for Pb-p, CMUP5-B and CMUP9-B, were active at the same time as the forward CMUP3-B and CMUP8-B classes, therefore the single muon efficiency for semi-forward data $\varepsilon_{0\mathrm{VBC}}^{\mathrm{x-check}}$ is given by the luminosity-weighted average of the single muon efficiencies ε_1 from Eq. (6.17) for the forward triggers CMUP3-B and CMUP8-B:

$$\varepsilon_{0\mathrm{VBC}}^{\mathrm{x-check}} = \frac{\mathscr{L}_{\mathrm{CMUP5}} \times \varepsilon_{1\mathrm{CMUP3}} + \mathscr{L}_{\mathrm{CMUP9}} \times \varepsilon_{1\mathrm{CMUP8}}}{\mathscr{L}_{\mathrm{CMUP5}} + \mathscr{L}_{\mathrm{CMUP9}}} = 0.592 \pm 0.066. \tag{6.18}$$

The result is in good agreement with the semi-forward 0VBC efficiency obtained in the previous Section 6.6.2 ($\varepsilon_{0\mathrm{VBC}} = 0.585 \pm 0.020$).

6.6.4 Correction for the shape of the generated p_T distribution

The global efficiency at mid-rapidity is decreasing with increasing transverse momentum of the J/ψ. The effect is mostly a result of the topology trigger 0STP requiring the hits in SPD to be oriented in a back-to-back pattern. For the J/ψ produced at a higher p_T it is more difficult to pass the topology selection.

As a consequence, the efficiency becomes at some extent dependent on the initial shape of the p_T distribution from the event generator.

The dependence of the efficiency on p_T at mid-rapidity was studied using the MC productions with an initial flat distribution of p_T, LHC15a1a and LHC15a1b (described in Section 6.4.2). The two productions are needed, one for each decay channel of the J/ψ.

In the study, the efficiency as a function of p_T was constructed as a ratio of reconstructed and accepted events to the number of generated events, both in a given rapidity interval and a given bin in p_T. The reconstructed event should satisfy the standard offline selection and on top of that also the predefined trigger configuration for individual trigger inputs or the full set for mid-rapidity class CCUP7-B.

Results of the study, showing the substantial contribution of SPD topology trigger to the final trend of the efficiency at mid-rapidity is shown in Figures 6.11 and 6.12.

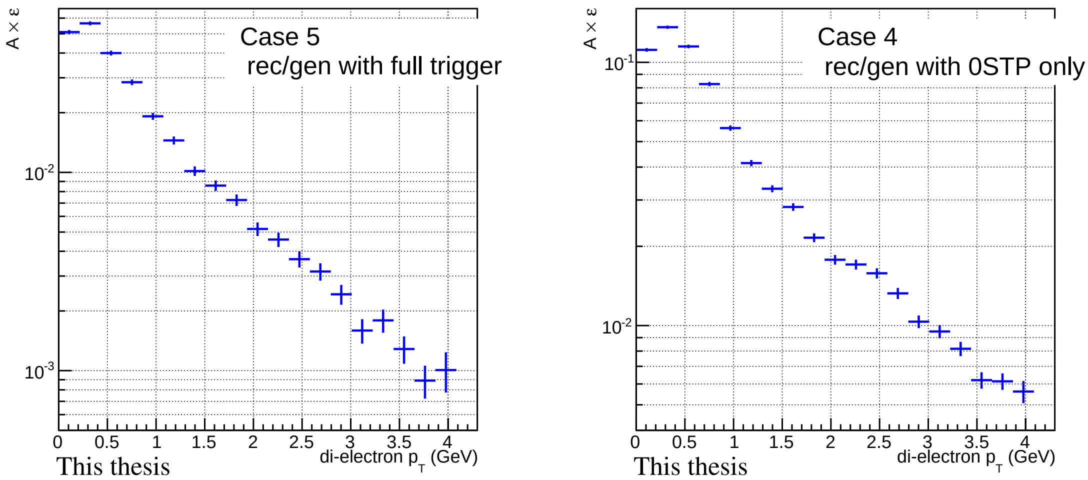

Fig. 6.11 Results of the study showing the contribution of separate trigger inputs to the overall efficiency in the dielectron channel. The initially flat distribution of p_T was subjected to a full detector simulation, reconstructed events were analyzed by the same selection criteria as for the data. On the left there is the final dependence of the efficiency on p_T which include all trigger inputs of the CCUP7-B class, for the right plot only the 0STP input was required. The trend of the final efficiency is dominated by the trend of 0STP.

At semi-forward rapidity, the efficiency slightly increases with p_T, but the effect is not so dramatic as it is at mid-rapidity.

In the STARLIGHT event generator, which was used for all main simulations, including the photon-proton production $\gamma\mathrm{p} \to J/\psi\mathrm{p}$, the initial p_T distribution is given by Eq. (6.4), which gives the distribution in terms of two constants A and b as $\mathrm{d}N/\mathrm{d}p_T = A \cdot p_T \cdot \exp(-bp_T^2)$.

In Section 6.4.2 it was shown that the exponential parameter b, and thus the shape of the initial distribution, depends on the center-of-mass energy of the photon-proton system $W_{\gamma\mathrm{p}}$.

While in STARLIGHT there is default value of $b = 4.0$ GeV^{-2}, the exponential parameter at mid-rapidity is $b = 5.0$ GeV^{-2} and the value corresponding to semi-forward Pb-p is $b = 5.6$ GeV^{-2}.

Such variations in the exponential parameter b indicate a softening of the distribution at higher energies. As a result, the true efficiency at mid-rapidity should be higher than the estimate of the default STARLIGHT, because more generated events in the region of

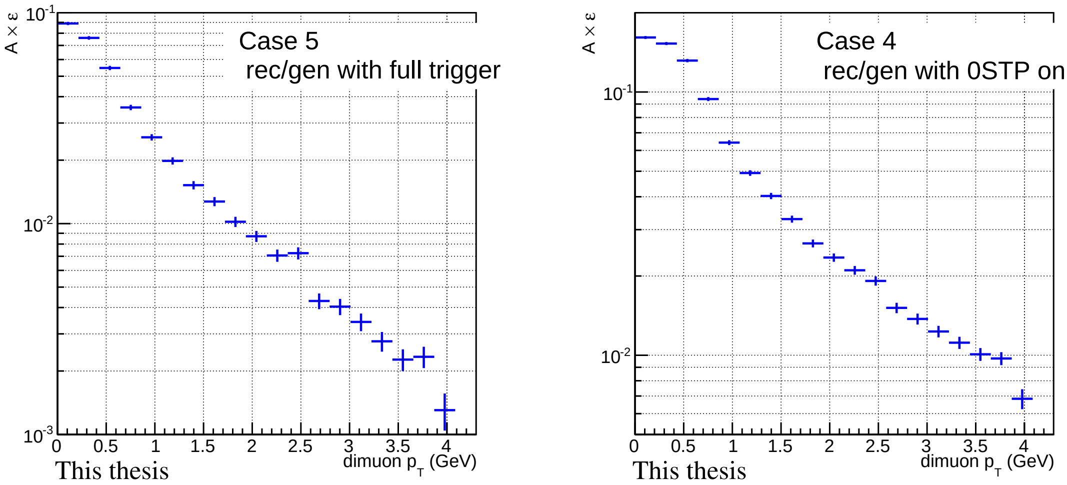

Fig. 6.12 Study of the efficiency dependence on p_T in the dimuon channel. See details in the caption of Figure 6.11. Like in the dielectron channel, the trend of the final efficiency is dominated by the trend of 0STP.

higher efficiency will increase the global efficiency. The efficiency in semi-forward Pb-p then should be slightly lower.

The acceptance and efficiency $(\mathrm{Acc} \times \varepsilon)_{J/\psi}$ from the large-scale STARLIGHT simulations performed with inputs from the default STARLIGHT was corrected for its dependence on the shape of the p_T distribution by the b-dependence correction factor f_b.

The correction f_b was calculated as the ratio of the efficiency obtained from one of the auxiliary samples with modified b to the efficiency from the main large-scale production which used the default b in STARLIGHT. The efficiency from the main sample was restricted to runs used with the corresponding auxiliary sample.

Numerical values of the correction are $f_b = 1.137$ and 1.158 for the dielectron and dimuon channels at mid-rapidity and $f_b = 0.956$ for semi-forward Pb-p.

As expected, the efficiency is enhanced at mid-rapidity and decreased in semi-forward rapidity in Pb-p.

6.6.5 Implementing the correction factors

The efficiency of the V0C trigger input 0VBC $\varepsilon_{\mathrm{0VBC}}$ and the correction to the shape of the generated p_T distribution f_b, presented in Sections 6.6.2 and 6.6.4, are multiplicative to the global acceptance and efficiency $(\mathrm{Acc} \times \varepsilon)_{J/\psi}$ calculated from the main MC samples.

The former is relevant for forward Pb-p, the latter is relevant for mid-rapidity and both of them apply for semi-forward Pb-p.

In the forward and semi-forward intervals in Pb-p, the $(\mathrm{Acc} \times \varepsilon)_{J/\psi}$ is calculated without requiring the 0VBC input to be fired in the data reconstructed from the MC, the separate efficiency $\varepsilon_{\mathrm{0VBC}}$ is used instead.

The total acceptance and efficiency correction $\varepsilon_{J/\psi}$ entering the experimental cross section in Eq. (6.2) is calculated as

$$\begin{aligned}
\varepsilon_{J/\psi} &= (\mathrm{Acc}\times\varepsilon)_{J/\psi}\times\varepsilon_{0\mathrm{VBC}} && \text{(forward Pb-p)}\\
\varepsilon_{J/\psi} &= (\mathrm{Acc}\times\varepsilon)_{J/\psi}\times\varepsilon_{0\mathrm{VBC}}\times f_b && \text{(semi-forward Pb-p)}\\
\varepsilon_{J/\psi} &= (\mathrm{Acc}\times\varepsilon)_{J/\psi}\times f_b && \text{(mid-rapidity).}
\end{aligned} \tag{6.19}$$

In the other intervals not specified in Eq. (6.19) (forward and semi-forward p-Pb), no special corrections are needed, the total acceptance and efficiency is completely described by the MC. We may identify it as

$$\varepsilon_{J/\psi} = (\mathrm{Acc}\times\varepsilon)_{J/\psi} \quad \text{(all other cases).} \tag{6.20}$$

6.7 Signal extraction

The selection criteria listed in Section 6.5 are aimed to get the two-track events with no other signals throughout the detector coverage. However, these events are still a mixture of the J/ψ and $\gamma\gamma\to l^+l^-$ produced in elastic or non-exclusive photon-proton interactions. The process of getting the number of J/ψ produced in $\gamma\mathrm{p}\to J/\psi\,\mathrm{p}$ out of the selected two-track events is described in this section.

6.7.1 Signal extraction at forward rapidity

The invariant mass of dimuons selected at forward rapidity is shown in Figure 6.13a. The positive rapidity y of the J/ψ shown in the legend corresponds to p-Pb and the negative rapidity to opposite beam directions in Pb-p. A clear signal of the J/ψ is visible above the background from two-photon production of dimuon pairs $\gamma\gamma\to\mu^+\mu^-$.

The peak from the J/ψ is described by a Crystal Ball function [91], the continuum of $\gamma\gamma\to\mu^+\mu^-$ is described by an exponential function.

The Crystal Ball function is a composition of a Gaussian of mean $\bar{m}$ and standard deviation σ_m and a power law tail towards lower masses with power n. Both functions are continuously (value and the first derivative) joined at a point m_1. The line shape of reconstructed dimuon masses m is

$$\mathrm{CB}(m) = \begin{cases} \exp\left[-(\bar{m}-m)^2/(2\sigma_m)^2\right] & ,\ m\geq m_1 \\ \\ A\left[\sigma_m/(m'-m)\right]^n & ,\ m<m_1, \end{cases} \tag{6.21}$$

where the parameters m_1, A and m' are fixed by the continuity requirement:

$$\begin{aligned}
m_1 &= \bar{m}-\alpha\sigma_m\\
A &= (n/\alpha)^n\cdot\exp\left(-\alpha^2/2\right)\\
m' &= \bar{m}+\sigma_m\left(n/\alpha-\alpha\right).
\end{aligned} \tag{6.22}$$

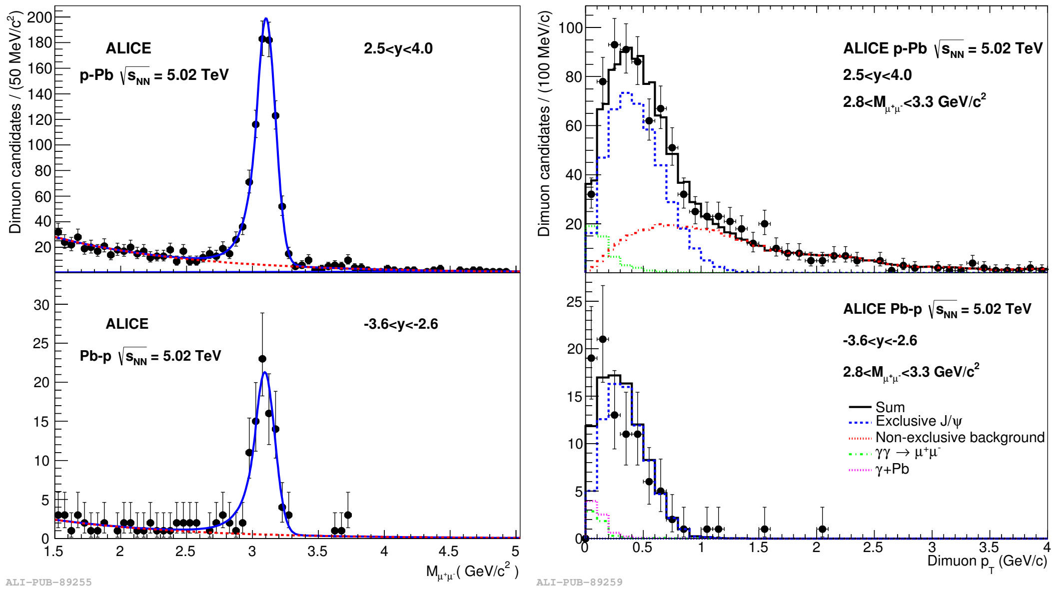

(a) (b)

Fig. 6.13 Invariant mass distribution of events selected in the forward rapidity (a), upper panels correspond to p-Pb, lower to Pb-p. In the right part (b), the transverse momentum of dimuons is shown for an interval of masses in the range of the J/ψ mass peak [2].

The Crystal Ball function in Eq. (6.21) is then fully determined by the 4 parameters, mean and width of the Gaussian $\bar{m}$ and σ_m and tail parameters α and n.

The exponential function describing the mass distribution of dimuon pairs from the two-photon production $\gamma\gamma \to \mu^+\mu^-$ was used in a simple form

$$\mathrm{E}(m) = \exp(\lambda m). \tag{6.23}$$

The invariant mass of the selected two-track candidates is described by a maximum likelihood fit to an unbinned set of reconstructed masses using the ROOFIT package [92].

The shapes of the Crystal Ball and exponential functions, represented by the relevant ROOFIT classes, have been used to create a composite distribution for the fit, including the normalization parameters for both functions. The parameters $\bar{m}$ and σ_m of the Gaussian part of the CB function and the exponential parameter λ have been left free for the fit, while the tail parameters α and n of the CB have been fixed using the same composite fit to the MC simulation of $\gamma\mathrm{p} \to J/\psi\,\mathrm{p}$ where all the parameters were determined from the fit.

The tail parameters α and n were strongly correlated. Had they have been left free for the fit to data, a risk of ambiguity in the fit results would have occurred. The risk was prevented by fixing them using the MC.

The observed width of the J/ψ mass peak in Figure 6.13a was used to select events for a further stage of the signal extraction procedure. Events within the J/ψ peak were selected requiring their mass to be within $2.8 < m_{\mu^+\mu^-} < 3.3$ GeV/c^2.

The J/ψ within the mass peak still may be produced by several processes. The de-

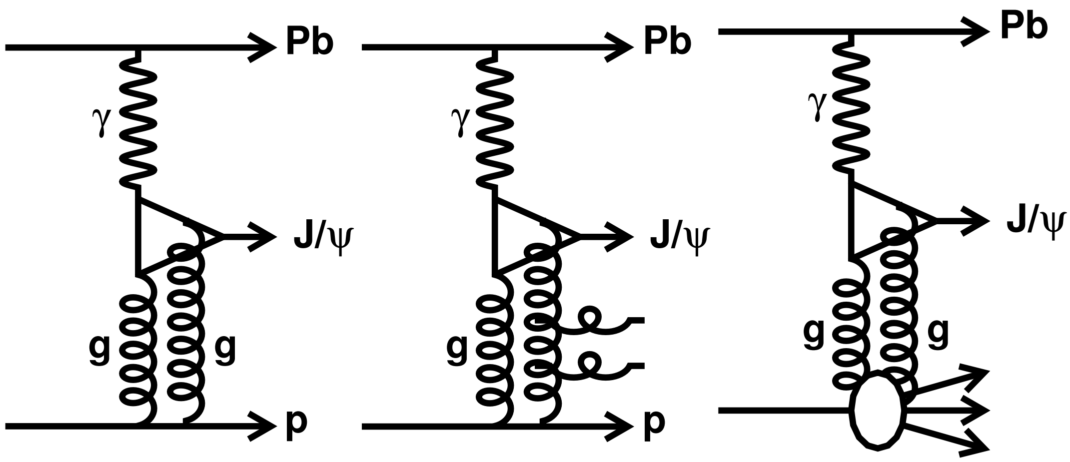

(a) Exclusive (b) Inelastic (c) Proton dissociative

Fig. 6.14 Production modes of J/ψ in photon-proton interactions.

sired exclusive photoproduction in Figure 6.14a is accompanied by inelastic photoproduction where gluon radiation produces other particles (Figure 6.14b) and by photoproduction with proton dissociation, shown in Figure 6.14c.

Dimuon pairs from two-photon production $\gamma\gamma \to \mu^+\mu^-$ also present within the J/ψ mass interval $2.8 < m_{\mu^+\mu^-} < 3.3$ GeV/c^2, may be produced elastically or with proton dissociation.

All of the above mentioned processes contribute to the distribution of transverse momentum of dimuon pairs. The elastic production of $\gamma\gamma \to \mu^+\mu^-$ is expected to occur at low values of p_T, inelastic and dissociative production of J/ψ and $\gamma\gamma \to \mu^+\mu^-$ occur at higher transverse momenta, while the exclusive production $\gamma\mathrm{p} \to J/\psi\,\mathrm{p}$ occurs at middle values of p_T.

The differences in the p_T distributions serve as a baseline for the determination of the number of exclusive J/ψ. The distribution of the p_T of the events within the J/ψ mass peak ($2.8 < m_{\mu^+\mu^-} < 3.3$ GeV/c^2) is described by templates of exclusive J/ψ, elastic $\gamma\gamma \to \mu^+\mu^-$ and non-exclusive background of inelastic and dissociative J/ψ and $\gamma\gamma \to \mu^+\mu^-$.

A binned maximum likelihood fit to the p_T distribution is performed using the model composed of separate distributions from the templates. Again the ROOFIT package was used. The fit in the forward rapidity is shown in Figure 6.13b.

The templates for exclusive J/ψ in $\gamma\mathrm{p} \to J/\psi\,\mathrm{p}$ and elastic $\gamma\gamma \to \mu^+\mu^-$ have been created using the MC productions of the relevant processes. For the forward p-Pb, the corresponding production for the J/ψ is LHC13c2 and for p-Pb and Pb-p $\gamma\gamma \to \mu^+\mu^-$ the productions are LHC13c3 and LHC13c5.

For the template of exclusive J/ψ in Pb-p, the auxiliary MC production was used. The shape of the generated p_T distribution was tuned for the photon-proton energies $W_{\gamma\mathrm{p}}$ reached in the forward Pb-p. The production is described in Section 6.4.2.

The events reconstructed in the MC were subject to the same selection criteria as for the data, including the full set of the forward triggers (Section 6.2.7). Finally the requirement on the J/ψ mass ($2.8 < m_{\mu^+\mu^-} < 3.3$ GeV/c^2) was applied.

The template for the non-exclusive background was obtained from data according to Section 6.5.6. Events with an increased activity in V0C were selected to form the non-exclusive template.

The relative normalization of the components in the p-Pb fit was left free, only the upper limit for the template of elastic $\gamma\gamma \to \mu^+\mu^-$ was set by integrating the exponential function in the mass fit in the range of the J/ψ mass peak $2.8 < m_{\mu^+\mu^-} < 3.3$ GeV/c^2. The actual limit was set as a result of the integration plus two times the standard deviation of the result.

The fit to the p_T distribution produces the number of exclusive J/ψ candidates $N_{J/\psi}$ as the number of events corresponding to the template of exclusive J/ψ. At forward p-Pb rapidity, the fit shown in Figure 6.13b yilded $N_{J/\psi} = 447 \pm 30$.

The fit for forward Pb-p in Figure 6.13b also include a contribution of coherent J/ψ photoproduction in photon-nucleus interactions. The template was created using the large-scale MC simulation of coherent photoproduction in Pb-p.

The number of events corresponding to the component of coherent J/ψ was fixed using the measured coherent cross section in Pb-Pb at $\sqrt{s_{\mathrm{NN}}}$ = 2.76 TeV in the forward rapidity [1].

The number of J/ψ in coherent γ-Pb, $N_{\gamma\mathrm{Pb}}$, is calculated using the coherent cross section $\sigma^{\mathrm{coh}}_{J/\psi}$ in Pb-p as

$$N_{\gamma\mathrm{Pb}} = (1 + f_D) \times \sigma^{\mathrm{coh}}_{J/\psi} \times \varepsilon_{J/\psi} \times \mathscr{B} \times \mathscr{L}. \tag{6.24}$$

The f_D is the feed-down correction, $\varepsilon_{J/\psi}$ is the acceptance and efficiency for the coherent J/ψ in Pb-p, $\mathscr{B}$ is the branching ratio of dimuon decay of the J/ψ and $\mathscr{L}$ is the luminosity of the Pb-p data sample.

The coherent cross section in Pb-p was obtained using the total STARLIGHT cross section in Pb-p σ_{SL}, restricted to the forward rapidity by fraction of events R_y generated into the forward rapidity and scaled to the measured coherent cross section in Pb-Pb by the ratio r:

$$\sigma^{\mathrm{coh}}_{J/\psi} = \sigma_{\mathrm{SL}} \times R_y \times r. \tag{6.25}$$

The ratio r is the ratio of the measured cross section to the STARLIGHT cross section in Pb-Pb in the forward rapidity interval $-3.6 < y < -2.6$.

Constraining the template of the coherent J/ψ to a number of events $N_{\gamma\mathrm{Pb}} = 7 \pm 2$ into the fit for Pb-p (bottom part of Figure 6.13b), the fit then gives us $N_{J/\psi} = 74 \pm 9$.

However, to get the yield in the forward Pb-p, the procedure of event counting was used (the fit to p_T was left as a cross check to the resulting number). Starting with all events within the J/ψ mass peak $N = 93 \pm 10$, the $N_{\gamma\mathrm{Pb}}$ was subtracted as the number of expected γ-Pb interactions, 5 ± 1 events was subtracted as the expected number of $\gamma\gamma \to \mu^+\mu^-$ events and two higher p_T events with $p_T > 1.5$ GeV were subtracted as background.

After subtraction of the components, the yield of the J/ψ in the forward Pb-p is $N_{J/\psi} = 79 \pm 10$.

6.7.2 Signal extraction at semi-forward rapidity

Templates for the same mechanisms as described in the previous Section 6.7.1 were used to extract the signal at semi-forward rapidity.

The distribution of the invariant masses of the selected dimuon candidates is described by the Crystal Ball function in Eq. (6.21) and the exponential function in Eq. (6.23). The distributions of the p-Pb and Pb-p semiforward data samples are shown in Figure 6.15. The two functions provide an accurate fit to data, showing the peak of the J/ψ above a continuum from the two-photon process $\gamma\gamma \to \mu^+\mu^-$.

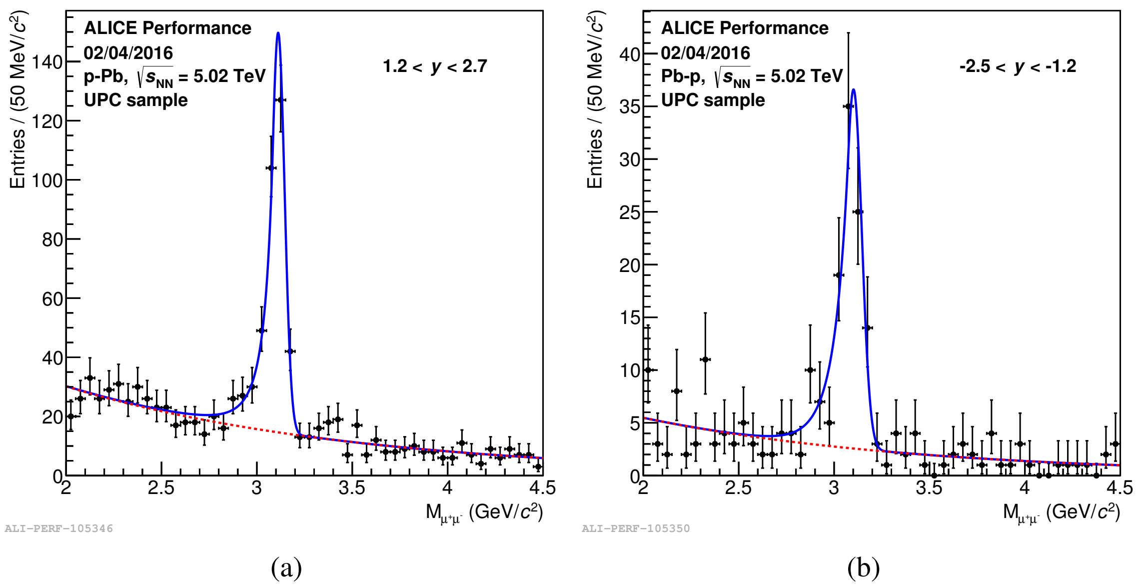

Fig. 6.15 Invariant mass distribution of events selected in the semi-forward rapidity, (a) for p-Pb sample and (b) for Pb-p sample.

The parameters of the fits in Figure 6.15 are shown in Table 6.8.

Again the events within the J/ψ mass peak may come from elastic, inelastic and proton dissociative production of the J/ψ and $\gamma\gamma \to \mu^+\mu^-$, as illustrated in Figure 6.14.

The yield of the J/ψ from elastic photon-proton interactions was separated by fitting the p_T distribution of J/ψ candidates by templates of the contributing processes.

Profiting from the better mass resolution at semi-forward rapidity, the J/ψ candidates intended for the fit were selected as dimuons with invariant mass in $2.9 < m_{\mu^+\mu^-} < 3.2$ GeV/c^2. The interval is long enough to encompass most of the peak of the J/ψ present in Figure 6.15.

Templates for elastic $\gamma\gamma \to \mu^+\mu^-$ interactions and $\gamma p \to J/\psi p$ production in p-Pb were obtained using the STARLIGHT MC productions listed in Table 6.2.

The template of $\gamma p \to J/\psi p$ in Pb-p was created from the special production with a tuned shape for the initial p_T distribution (Section 6.4.2). The value of the exponential slope parameter in Eq. (6.4) was set according to Table 6.5 to $b = 5.6$ GeV^{-2}.

Figure	6.15a		6.15b	
Rapidity	$1.2 < y < 2.7$		$-2.5 < y < -1.2$	
Parameter	Value	Constraint	Value	Constraint
$\bar{m}$ (GeV)	3.112 ± 0.003	-	3.101 ± 0.007	-
σ_m (MeV)	34 ± 3	-	45 ± 6	-
α	0.786	$=0.786$	0.602	$=0.602$
n	3.147	$=3.147$	11.046	$=11.046$
λ (GeV^{-1})	-0.727 ± 0.049	-	-0.621 ± 0.150	-
χ^2/NDF	0.509	-	0.495	-

Table 6.8 Parameters of the Crystal Ball and exponential function and reduced χ^2 of the fits in Figure 6.15. The tail parameters of the Crystal Ball have been constrained to a fixed value according to the MC of semi-forward J/ψ in $\gamma\mathrm{p} \to J/\psi\mathrm{p}$.

The templates for non-exclusive J/ψ and $\gamma\gamma \to \mu^+\mu^-$ were obtained from data using the selection for the background sample (Section 6.5.6). Activity was required in the ZDC in the direction of the proton beam. Dimuons of both sign combinations, unlike and like sign were accepted for the template to account for some amount of like-sign events present in the standard selection (there is about ~10% level of like-sign background within the range $2.9 < m_{\mu^+\mu^-} < 3.2$ GeV/c^2 in p-Pb and ~3% in Pb-p).

Because of the statistics in the background selection is limited (Table 6.6, only tens of events), the binned distribution of the sample would be subject to large statistical fluctuations.

To eliminate the fluctuations, a toy Monte Carlo [92] was adopted to smoothly describe the data in the background sample (the same was also done for the forward rapidity). Distributions of transverse momenta of dimuons passing the background selection are shown in Figure 6.16 along with the toy MC description.

The data selected as non-exclusive background were first smoothened using the procedure presented by J. Friedman in [106] (implemented in ROOT). Then a large statistics toy MC distribution was generated out of the resulting smooth distribution by ROOFIT.

Fits to the p_T distribution of J/ψ candidates at semi-forward rapidity are shown in Figure 6.17, results of the fits are given in Table 6.9.

The upper limit to the contribution of $\gamma\gamma \to \mu^+\mu^-$ was set from the fit to the mass distribution (Figure 6.15). The value of the limit was taken by the integration of the exponential function within the range of the J/ψ peak ($2.9 < m_{\mu^+\mu^-} < 3.2$ GeV/c^2) and an addition of two times the error of the integration. The limit was practically not reached in the p_T fit.

The normalization was left free for the remaining templates, $\gamma\mathrm{p} \to J/\psi\mathrm{p}$ and non-exclusive background.

The fit provided the yield of $N_{J/\psi} = 170 \pm 23$ for p-Pb and $N_{J/\psi} = 78 \pm 11$ for Pb-p.

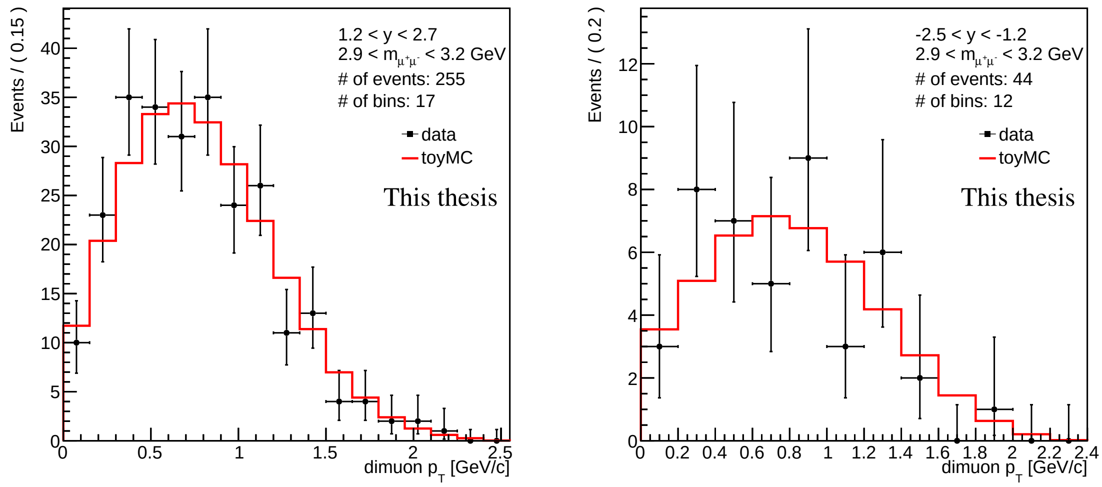

(a) (b)

Fig. 6.16 Non-exclusive background and its representation by toy MC, (a) for the p-Pb sample and (b) for the Pb-p sample.

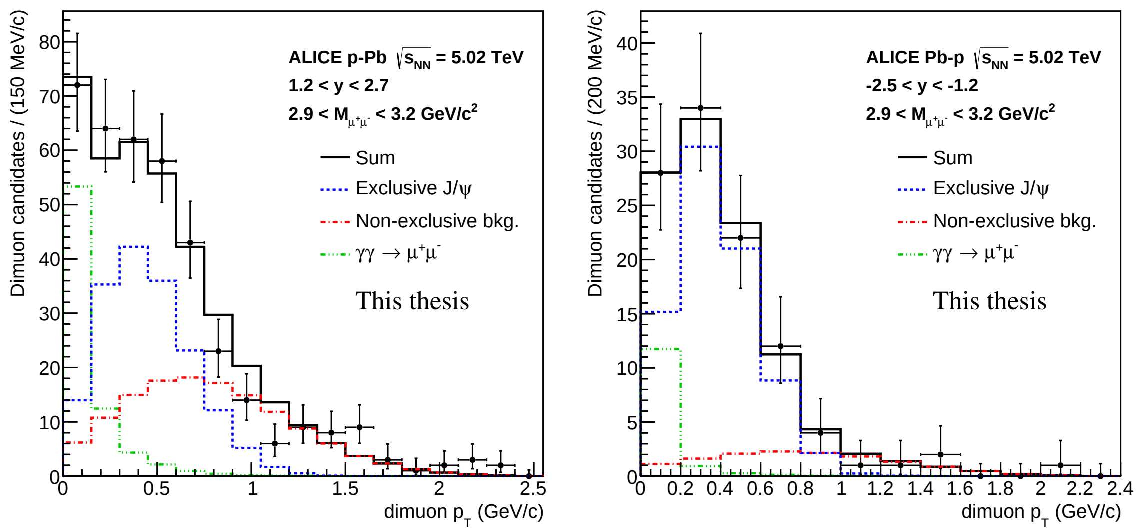

(a) (b)

Fig. 6.17 Transverse momentum distribution of J/ψ candidates in the semi-forward rapidity and fit by templates of contributing processes, (a) for the p-Pb sample and (b) for the Pb-p sample.

Figure	6.17a		6.17b	
Rapidity	$1.2 < y < 2.7$		$-2.5 < y < -1.2$	
Tempate	Value	Constraint	Value	Constraint
Exclusive J/ψ	170 ± 23	-	78 ± 11	-
Non-exclusive bkg.	135 ± 19	-	14 ± 6	-
$\gamma\gamma \to \mu^+\mu^-$	74 ± 12	≤ 100	13 ± 6	≤ 18
χ^2/NDF	1.374	-	0.405	-

Table 6.9 Contributions of the individual templates to the model in Figure 6.17 and reduced χ^2 of the fit.

6.7.3 Signal extraction at mid-rapidity

The situation regarding the production mechanisms of the J/ψ at mid-rapidity is similar to the cases of forward and semi-forward rapidity intervals, resulting in the use of previously established procedures.

The data samples of p-Pb and Pb-p were analyzed simultaneously (symmetry about $y = 0$, described in Section 6.2.5). The common sample is referred to as p-Pb.

The J/ψ at mid-rapidity was measured both in the dielectron channel $J/\psi \to e^+e^-$ and in the dimuon decay channel $J/\psi \to \mu^+\mu^-$, therefore all the procedures are performed separately on data from both channels.

The invariant mass of dielectron and dimuon candidates selected at mid-rapidity is in Figure 6.18 together with the fit using the Crystal Ball in Eq. (6.21) and the exponential function in Eq. (6.23). The inclination of the CB shape to the exponential in the dielectron channel (Figure 6.18a) is not as perfect, it is fine for the dimuon channel (Figure 6.18a).

The parameters of the mass fits in Figure 6.18 are given in Table 6.10.

Before the fits to the p_T distribution of J/ψ candidates were employed to separate contributions of elastic, inelastic and dissociative productions of the J/ψ and $\gamma\gamma \to e^+e^-$ or $\gamma\gamma \to \mu^+\mu^-$ (diagrams in Figure 6.14), the feasibility of the procedure was examined.

A fit by templates relies on differences in the mean and the width of individual templates, starting with soft two-photon processes $\gamma\gamma \to l^+l^-$ up to hard non-exclusive production of the J/ψ and $\gamma\gamma \to l^+l^-$.

At mid-rapidity, the efficiency rapidly decreases with transverse momentum of dielectron and dimuon pairs, as shown in Figure 6.11 and 6.12. As a result, a J/ψ or pairs from $\gamma\gamma \to l^+l^-$ produced at higher p_T have much smaller probability to be detected than those produced at lower transverse momentum.

If the shape of non-exclusive background was strongly modified towards lower values of p_T, while the shape of $\gamma\mathrm{p} \to J/\psi\,\mathrm{p}$ was modified only by a small amount, both shapes may overlap of each other.

An overlap of templates of $\gamma\mathrm{p} \to J/\psi\,\mathrm{p}$ and non-exclusive background would leave their ratio unconstrained by the fit to the p_T of J/ψ candidates, which would spoil the feasibility

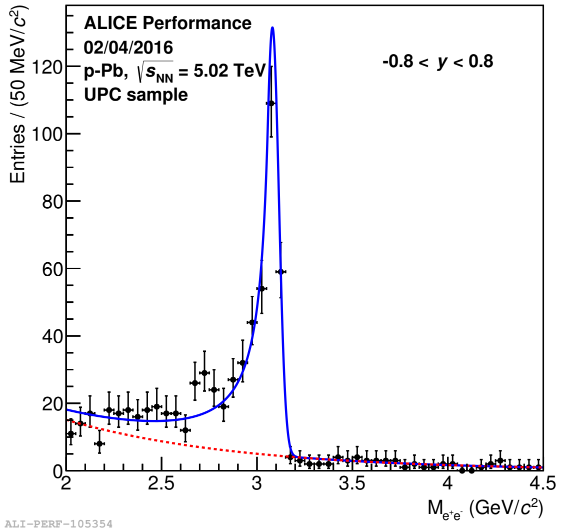

(a) (b)

Fig. 6.18 Invariant mass distribution of events selected at mid-rapidity in (a) dielectron channel and (b) dimuon channel.

of making the fit.

To check whether the shapes of $\gamma p \to J/\psi p$ and non-exclusive background are enough separated from each other, the templates were fitted using the parametric form in Eq. (6.4) for the distribution of the transverse momenta,

$$f(p_T) = A \cdot p_T \cdot \exp\left(-b \cdot p_T^2\right), \tag{6.26}$$

and noting the resulting value of exponential parameter b for the template of exclusive J/ψ in γp and non-exclusive J/ψ.

For the formulas in Eq. (6.4) or Eq. (6.26), a smaller value of b will produce a harder distribution and vice versa. Parametric fits to templates of $\gamma p \to J/\psi p$ and non-exclusive background should yield high and low b respectively. In the opposite case of similar b for both of the templates, the templates would overlap and the signal extraction using a template fit to p_T distribution of J/ψ candidates would not be possible.

As the template of exclusive J/ψ in $\gamma p \to J/\psi p$ the special MC of modified slope parameter was used (Section 6.4.2). The exponential slope of the shape of generated p_T distribution in Eq. (6.4) was set to $b = 5.0$ GeV^{-2}, as indicated in Table 6.5.

The template of non-exclusive background was obtained from the data by requiring activity in ZDC in the direction of the proton beam. Dileptons of both sign were allowed. The description of selections used for the template is given in Section 6.5.6.

A parametric unbinned fit by Eq. (6.26) to the templates of the simulation of exclusive J/ψ and the data-driven template of non-exclusive background is presented in Figure 6.19.

The fit to the template of $\gamma p \to J/\psi p$ in Figure 6.19a yields $b = 6.399 \pm 0.114$ GeV^{-2}, while the fit to the non-exclusive sample gives $b = 2.695 \pm 0.264$ GeV^{-2}. The slope pa-

Figure Channel	6.18a Dielectron		6.18b Dimuon	
Parameter	Value	Constraint	Value	Constraint
$\bar{m}$ (GeV)	3.082 ± 0.004	-	3.098 ± 0.001	-
σ_m (MeV)	32 ± 3	-	24 ± 1	-
α	0.710	$=0.710$	2.744	$=2.744$
n	1.157	$=1.157$	3.500	$=3.500$
λ (GeV^{-1})	-1.310 ± 0.112	-	-1.714 ± 0.062	-
χ^2/NDF	0.513	-	0.799	-

Table 6.10 Parameters of the Crystal Ball and exponential function and reduced χ^2 of the fits in Figure 6.18. Tail parameters of the Crystal Ball have been constrained to fixed value according to the MC of mid-rapidity J/ψ in γp $\rightarrow J/\psi$p.

rameter of non-exclusive sample is thus about 57% lower than that of exclusive J/ψ in γp, proving that the shapes of both templates are well separated from each other.

Similar results were obtained in the dimuon channel, where the difference in b between result from the fit to MC of exclusive J/ψ and the non-exclusive sample is 68%. Corresponding fits are shown in Appendix D in Figure D.1.

We may conclude here that despite the rapid decrease in efficiency with p_T, the shapes of the templates from MC for γp $\rightarrow J/\psi$p and data-driven non-exclusive sample do not overlap, but instead the non-exclusive sample is much harder. The procedure of signal extraction using a template fit to the p_T of the selected dielectron and dimuon candidates is feasible.

However, it is worth noting that the template of exclusive J/ψ was originally generated at $b = 5.0$ GeV^{-2}, but the parametric fit by the same functional form of Eq. (6.26) yields $b =$ 6.399 GeV^{-2}. The effect of the detector response is clearly apparent, the drop in efficiency makes the folded distribution softer than what was originally generated.

Fits to the p_T distribution of selected J/ψ candidates are shown in Figure 6.20. Similar to the previous analyses at forward rapidity (Section 6.7.1) and at semi-forward rapidity (Section 6.7.2), the p_T distribution is described by the templates for $\gamma\gamma \rightarrow e^+e^-$ or $\gamma\gamma \rightarrow \mu^+\mu^-$ (depending on the decay channel), template for exclusive J/ψ in γp $\rightarrow J/\psi$p, non-exclusive background and coherent J/ψ in γ-Pb. The parameters of the fits are given in Table 6.11.

The J/ψ candidates selected for the fit have been obtained according to the width of the J/ψ mass peak in the invariant mass distributions (Figure 6.18). The intervals are $2.9 < m_{e^+e^-} < 3.2$ GeV/c^2 for the dielectron channel and $3.0 < m_{\mu^+\mu^-} < 3.2$ GeV/c^2 in the dimuon channel, profiting from the good mass resolution.

Templates for $\gamma\gamma \rightarrow e^+e^-(\mu^+\mu^-)$ have been obtained from the relevant MC productions listed in Table 6.4, the template for exclusive J/ψ was created using the special MC pro-

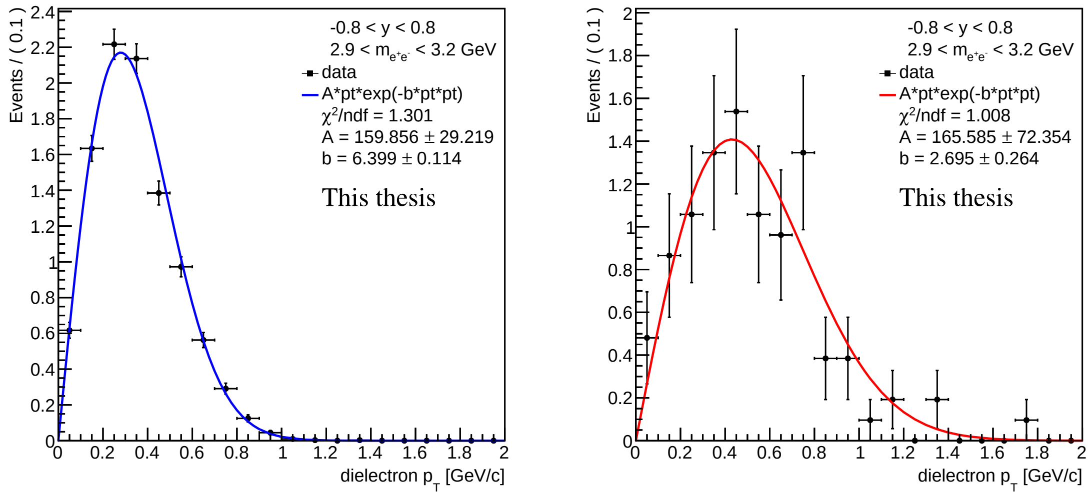

(a) (b)

Fig. 6.19 Unbinned maximum likelihood fit by the parametrization in Eq. (6.26) to (a) the MC simulation of exclusive J/ψ and (b) non-exclusive data sample. Both fits are for the dielectron channel.

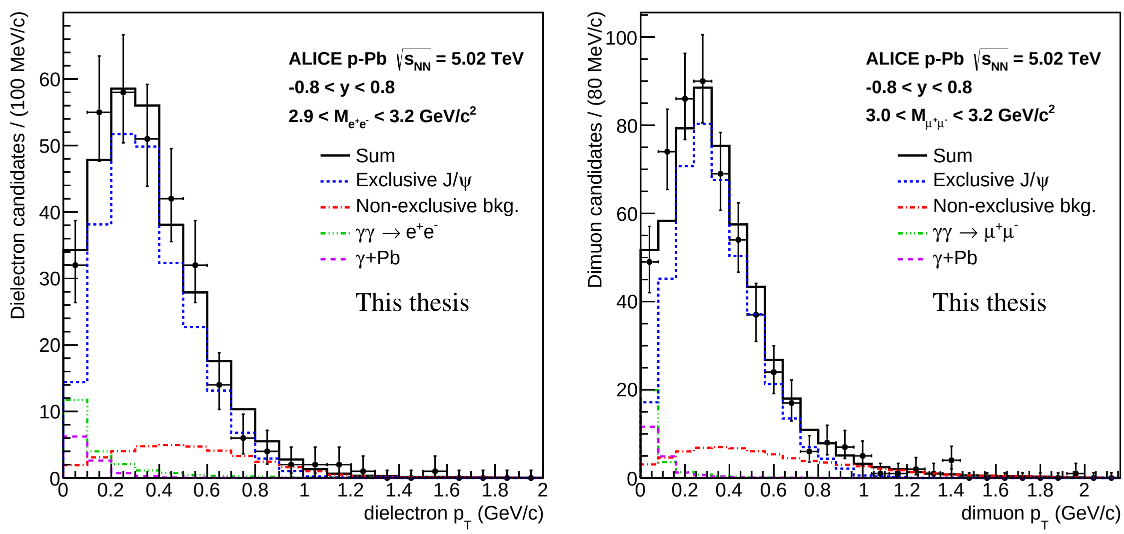

(a) (b)

Fig. 6.20 Distribution of transverse momentum of J/ψ candidates at mid-rapidity and fit by templates of contributing processes, (a) in the dielectron channel and (b) in the dimuon channel.

Figure Channel	6.20a Dielectron		6.20b Dimuon	
Tempate	Value	Constraint	Value	Constraint
Exclusive J/ψ	233 ± 22	-	417 ± 27	-
Non-exclusive bkg.	37 ± 15	-	72 ± 18	-
$\gamma\gamma \to e^+e^-(\mu^+\mu^-)$	21 ± 9	≤ 39	27 ± 10	≤ 92
γ+Pb	10 ± 1	[8, 10]	19 ± 4	[15, 19]
χ^2/NDF	0.705	-	0.838	-

Table 6.11 Contributions of the individual templates to the model in Figure 6.20 and reduced χ^2 of the fit.

duction tuned for the energy at mid-rapidity, as described in Section 6.4.2. The events have had to pass the same selection criteria as for data, including intervals of invariant masses for the J/ψ candidates.

The normalization was left free for the template of exclusive J/ψ, while the upper limits to events belonging to templates of $\gamma\gamma \to e^+e^-(\mu^+\mu^-)$ was set according to the integration of the exponential function in the invariant mass fits (Figure 6.18) within the ranges of events selected for the p_T fit. These upper limits provided a failsafe check of the fit, in practice they were never reached.

The template of non-exclusive production of $\gamma\gamma \to e^+e^-(\mu^+\mu^-)$ and J/ψ was obtained following Section 6.5.6. Events with activity in the neutron ZDC in the direction of the proton beam have been selected with other selection criteria unchanged. Dileptons of both signs have been allowed, so the sample contains unlike-sign and like-sign dilepton events together. The same procedure was applied also for the semi-forward analysis. The normalization of the template by the fit was left free.

A toy MC was used to incorporate the non-exclusive sample into the p_T fits, a procedure similar to that described in Section 6.7.2 was used. Also here the main reason for the use of a toy MC is the relatively small number of events selected for the non-exclusive samples (see Table 6.7). Plots of the p_T distributions of events selected in the non-exclusive sample in both decay channels and their representation by the toy MC are shown in Figure D.2 in Appendix D.

The number of events corresponding to the contribution of coherent J/ψ in γ-Pb was for the p_T fits calculated with Eq. (6.24) and Eq. (6.25) using the measured coherent cross section in Pb-Pb at $\sqrt{s_{\mathrm{NN}}}$ = 2.76 TeV at mid-rapidity [57]. The ratio r of the measured cross section to the STARLIGHT coherent cross section in Eq. (6.25) is $r = 0.57^{+0.08}_{-0.06}$, where the errors correspond to errors in the measured cross section. The value of feed-down of coherent J/ψ in Pb-Pb in Eq. (6.24) is $f_D = 0.1$. The resulting contribution of coherent J/ψ is $N_{\gamma\mathrm{Pb}} = 9 \pm 1$ in the dielectron channel and $N_{\gamma\mathrm{Pb}} = 17 \pm 2$ in the dimuon channel. Corresponding templates in the fit in Figure 6.20 have been confined to limits given by the values and errors of $N_{\gamma\mathrm{Pb}}$.

The final yield of exclusive J/ψ in $\gamma\mathrm{p} \to J/\psi\mathrm{p}$ interactions determined by the fit to the p_T distributions in Figure 6.20 is $N_{J/\psi} = 233 \pm 22$ in the dielectron channel and $N_{J/\psi} = 417 \pm 27$ in the dimuon decay channel.

6.7.4 Correction for feed-down from ψ'

Contribution of J/ψ from decays $\psi' \to J/\psi + X$ (the feed-down) is corrected by the feed-down factor f_D. The procedure is in general terms described in Section 3.5.

The feed-down formula in Eq. (3.11) can be written as

$$f_D = \frac{\sigma_{\mathrm{SL},y}(\psi')}{\sigma_{\mathrm{SL},y}(J/\psi)} \cdot \mathscr{B}(\psi' \to J/\psi + X) \cdot \frac{(\mathrm{Acc} \times \varepsilon)^P_{J/\psi}}{(\mathrm{Acc} \times \varepsilon)_{J/\psi}}, \tag{6.27}$$

where the first term is the ratio of STARLIGHT cross sections $\sigma_{\mathrm{SL},y}$ of J/ψ and ψ' photoproduction into a given rapidity interval, the middle term is the branching ratio of ψ' decays into the J/ψ and other products X and the last term is the ratio of efficiencies of direct J/ψ $(\mathrm{Acc} \times \varepsilon)_{J/\psi}$ and of J/ψ from ψ' $(\mathrm{Acc} \times \varepsilon)^P_{J/\psi}$ with a given assumption for the polarization P.

Cross sections for a given rapidity $\sigma_{\mathrm{SL},y}$ are calculated using the total STARLIGHT cross section σ_{SL} and fractions of events generated into a given rapidity R_y:

$$\sigma_{\mathrm{SL},y} = \sigma_{\mathrm{SL}} \cdot R_y. \tag{6.28}$$

The total cross sections are $\sigma_{\mathrm{SL}}(\psi') = 11.25$ µb and $\sigma_{\mathrm{SL}}(J/\psi) = 69.06$ µb. Factors R_y were calculated using a large sample of generated events as a ratio of events generated into a given rapidity interval to all generated events corresponding to the total cross sections.

The efficiencies $(\mathrm{Acc} \times \varepsilon)_{J/\psi}$ and $(\mathrm{Acc} \times \varepsilon)^P_{J/\psi}$ have been obtained using the respective simulations of $\gamma\mathrm{p} \to J/\psi\mathrm{p}$ and $\psi' \to J/\psi^P + X$ described in Section 6.4.1 following the same steps as outlined in Section 6.6.1, but here with effects of all trigger inputs determined from the simulation to describe properly the ratio of acceptances to events of direct J/ψ and J/ψ from ψ'.

For the polarization P of the J/ψ from decays of ψ' the assumptions were made for full transverse polarization ($\perp$), full longitudinal ($\|$) and for no polarization (0). The feed-down correction is then the average of calculations from Eq. (6.27) when assuming one particular polarization state:

$$f_D = \frac{f_D^{\perp} + f_D^{\|} + f_D^{0}}{3}. \tag{6.29}$$

The numerical values of the correction range from $f_D = 0.021$ to $f_D = 0.110$, depending on the rapidity interval.

The yield of J/ψ from fits to the p_T distribution $N_{J/\psi}$ is corrected by f_D to get the number $N^{\mathrm{exc}}_{J/\psi}$ of exclusive J/ψ as

$$N^{\mathrm{exc}}_{J/\psi} = \frac{N_{J/\psi}}{1+f_D}. \tag{6.30}$$

The number $N^{\mathrm{exc}}_{J/\psi}$ is used in the cross section in Eq. (6.2) to calculate the differential cross section of J/ψ photoproduction in p-Pb collisions.

6.7.5 Continuum production of dilepton pairs

The two-photon production of dilepton pairs, $\gamma\gamma \to e^+e^-$ or $\gamma\gamma \to \mu^+\mu^-$ is at high energies driven by perturbative QED, which is at present understood at sufficient accuracy (see Section 1.3.3). The measurement of the respective cross section $\sigma_{\gamma\gamma}$ and its comparison to the theoretical calculation provides a test to background subtraction using data-driven templates as was described in the previous sections on signal extraction for the J/ψ. In this analysis, a comparison will be made with STARLIGHT prediction of the two-photon cross section (Section 1.5.3).

In semi-forward rapidity $1.2 < y < 2.7$ the cross section of $\gamma\gamma \to \mu^+\mu^-$ was measured in two intervals of dimuon masses. One below the region of the J/ψ in $1.8 < m_{\mu^+\mu^-} < 2.5$ GeV/c^2 and one at masses above the J/ψ in the interval of $3.5 < m_{\mu^+\mu^-} < 6.0$ GeV/c^2.

The experimental cross section of the two-photon production is

$$\sigma_{\gamma\gamma} = \frac{N_{\gamma\gamma}}{\varepsilon_{\gamma\gamma} \cdot R_\eta \cdot \mathscr{L}}, \tag{6.31}$$

in which the $N_{\gamma\gamma}$ is the number of elastic $\gamma\gamma \to \mu^+\mu^-$ events extracted from the data, $\varepsilon_{\gamma\gamma}$ is the total acceptance and efficiency correction for the two-photon events, the factor R_η corrects for preselections on generated pseudorapidity of the muons which was done for simulations of the two-photon processes (Section 6.4.1) and $\mathscr{L}$ is the luminosity of the data sample.

The number $N_{\gamma\gamma}$ was obtained by fitting the p_T distribution of dimuon pairs within the semi-forward rapidity and respective mass intervals by templates of elastic $\gamma\gamma \to \mu^+\mu^-$ and non-exclusive background. Fits for the two mass intervals are shown in Figure 6.21. Results of the fits are given in Table 6.12.

The template for elastic $\gamma\gamma \to \mu^+\mu^-$ was obtained from MC production LHC13e6f (details in Section 6.4.1), the template for the non-exclusive sample was obtained from data using the same method as was previously used in the p_T fits to extract the signal of the J/ψ. The data driven method for obtaining the sample is described in Section 6.5.6.

The total acceptance and efficiency $\varepsilon_{\gamma\gamma}$ was obtained from the MC production LHC13e6f of $\gamma\gamma \to \mu^+\mu^-$ as the ratio of events reconstructed within the semi-forward rapidity and the respective mass intervals to events generated into the same rapidity and mass intervals. Separate ratios were made for each run, the final efficiency was obtained as luminosity-weighted average. More details about the procedure are given in Section 6.6.1.

The preselection factor R_η follows from the generator input to semi-forward simulations of $\gamma\gamma \to \mu^+\mu^-$ (Section 6.4.1). The events had to be in the basic interval of invariant masses

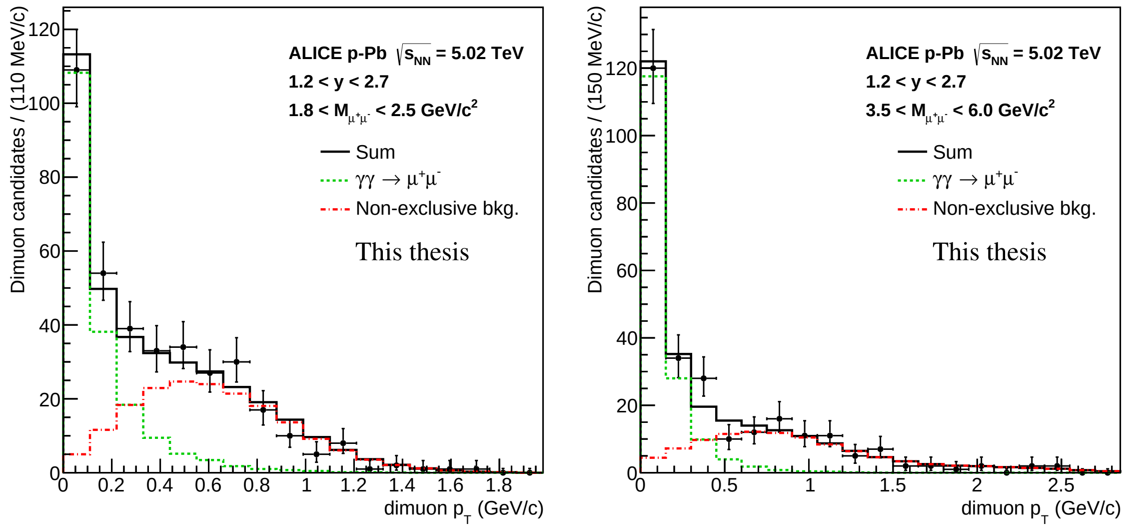

(a) (b)

Fig. 6.21 Fit by templates to the p_T distribution of dimuons at semi-forward rapidity for invariant masses below the J/ψ (a) and above the J/ψ (b).

and in the wider semi-forward rapidity interval and also there should be one generated muon with pseudorapidity in $-4.5 < \eta < -2.0$ and the other muon in $-1.5 < \eta < 1.5$. The factor R_η was obtained using a large sample of generated $\gamma\gamma \rightarrow \mu^+\mu^-$ events within the rapidity and mass ranges for the measurement of the $\sigma_{\gamma\gamma}$ cross section as a fraction of events out of this sample which also satisfy the previously defined pseudorapidity requirements.

The calculation of the two-photon cross section $\sigma_{\gamma\gamma}$ at semi-forward rapidity and the comparison to the STARLIGHT prediction is shown in Table 6.13. The experimental cross section $\sigma_{\gamma\gamma}$ is calculated using Eq. (6.31), the errors are statistical errors from $N_{\gamma\gamma}$ as was determined by the fit to the p_T distribution.

The factor R_{ym} is the selection ratio for a given invariant mass and rapidity interval, made as the ratio of STARLIGHT generated events passing into a given mass and rapidity interval to the total number of generated events and $\sigma_{\gamma\gamma}^{\mathrm{SL}}$ = 14.002 μb is the STARLIGHT cross section over the full generator rapidity and dimuon mass $1.5 < m_{\mu^+\mu^-} < 10$ GeV/c^2. The cross section $\sigma_{\gamma\gamma}^{\mathrm{SL}}$ corresponds to the data sample out of which the R_{ym} and R_η factors are calculated.

The comparison data/STARLIGHT in the last line of Table 6.13 is the ratio of the measured cross section $\sigma_{\gamma\gamma}$ to the prediction $\sigma_{\gamma\gamma}^{\mathrm{SL}} \cdot R_{ym}$. As we can see, even with statistical errors only the experimental cross section is compatible with theoretical calculation at about one standard deviation, which is a good agreement.

At mid-rapidity ($|y| < 0.8$), the two-photon cross section was measured for both final states, $\gamma\gamma \rightarrow e^+e^-$ and $\gamma\gamma \rightarrow \mu^+\mu^-$ in the interval of masses $3.3 < m_{l^+l^-} < 4.3$ GeV/c^2 with exception of $[3.64, 3.75]$ GeV/c^2 in the dimuon channel due to the presence of the ψ'. The experimental cross section was also calculated using Eq. (6.31).

Figure	6.21a	6.21b
Dimuon mass (GeV)	[1.8, 2.5]	[3.5, 6.0]
Tempate	Value	
$\gamma\gamma \to \mu^+\mu^-$	188 ± 16	163 ± 14
Non-exclusive bkg.	184 ± 16	102 ± 12
χ^2/NDF	0.609	0.564

Table 6.12 Contributions of the individual templates to the model in the two-photon production $\gamma\gamma \to \mu^+\mu^-$ in Figure 6.21 and reduced χ^2 of the fits.

Dimuon mass (GeV)	[1.8, 2.5]	[3.5, 6.0]
$N_{\gamma\gamma}$	188 ± 16	163 ± 14
$\varepsilon_{\gamma\gamma}$	0.086	0.260
R_η	0.5991978	0.4985074
$\mathscr{L}$ (μb^{-1})	3147	3147
$\sigma_{\gamma\gamma}$ (μb)	1.159 ± 0.099	0.400 ± 0.034
$\sigma_{\gamma\gamma}^{\mathrm{SL}}$ (μb)	14.002	14.002
R_{ym}	0.0754138	0.0252920
$\sigma_{\gamma\gamma}^{\mathrm{SL}} \cdot R_{ym}$ (μb)	1.056	0.354
data/STARLIGHT	1.10 ± 0.09	1.13 ± 0.10

Table 6.13 Cross section of two-photon production $\sigma_{\gamma\gamma}(\gamma\gamma \to \mu^+\mu^-)$ in the semi-forward rapidity $1.2 < y < 2.7$.

The fit to the p_T distribution of dilepton candidates in a given mass range was not possible, because the non-exclusive background (created according to Section 6.5.6) was not well constrained. Only a few events were present for the non-exclusive template, which made the p_T fit for $\gamma\gamma \to l^+l^-$ unfeasible.

Instead, a method based on counting the events of low dilepton transverse momentum $p_T < p_{T,\max}$ was applied to get the $N_{\gamma\gamma}$. Events passing the standard selection criteria for mid rapidity were further selected for a given mass range, and then the condition on $p_{T,\max}$ was applied. The number of surviving events was then interpreted as the yield $N_{\gamma\gamma}$ of elastic $\gamma\gamma \to l^+l^-$ events.

The upper limit $p_{T,\max}$ was set to 0.2 GeV in the dielectron channel and 0.07 GeV in the dimuon channel, giving comparable statistics in both samples.

The efficiency $\varepsilon_{\gamma\gamma}$ at mid-rapidity was obtained using simulations of two-photon processes from Table 6.3 as a luminosity weighted average over all runs (see Section 6.6.1). Both generated and reconstructed samples have had to be in the rapidity interval for mid-rapidity, $|y| < 0.8$, and the previously specified interval of dilepton invariant masses. The reconstructed events were required to pass the standard selection and on top of that also the requirement for maximum transverse momentum, $p_T < p_{T,\max}$.

The results of the measurement of the two-photon cross section $\sigma_{\gamma\gamma}$ for $\gamma\gamma \to e^+e^-$ and $\gamma\gamma \to \mu^+\mu^-$ at mid-rapidity are given in Table 6.14. The meaning of all symbols is the same as in the semi-forward analysis.

	Dielectrons	Dimuons
$p_{T,\max}$, GeV	0.2	0.07
Dilepton mass, GeV	[3.3, 4.3]	[3.3, 4.3] - [3.64, 3.75]
$N_{\gamma\gamma}$	20 ± 4	23 ± 5
$\varepsilon_{\gamma\gamma}$	0.070	0.098
R_η	0.0413905	0.1146991
$\mathscr{L}$ (μb^{-1})	6915	6915
$\sigma_{\gamma\gamma}$ (μb)	0.998 ± 0.200	0.296 ± 0.064
$\sigma_{\gamma\gamma}^{\text{SL}}$ (μb)	43.127	14.002
R_{ym}	0.0152027	0.0151898
$\sigma_{\gamma\gamma}^{\text{SL}} \cdot R_{ym}$ (μb)	0.656	0.213
data/STARLIGHT	1.52 ± 0.30	1.39 ± 0.30

Table 6.14 Cross section of two-photon processes $\gamma\gamma \to e^+e^-$ and $\gamma\gamma \to \mu^+\mu^-$ at mid-rapidity $|y| < 0.8$.

The selection factors R_{ym} and R_η were calculated using a large sample of generated STARLIGHT events corresponding to $\sigma_{\gamma\gamma}^{\text{SL}}$. The R_{ym} is the fraction of events generated into the mid-rapidity interval $|y| < 0.8$ and into a given mass interval. The preselection factor R_η is the fraction of events in the sample of correct rapidity and mass, which also have both tracks generated into the pseudorapidity interval $-1.0 < \eta < 1.0$. This interval in pseudorapidity was used for MC productions of two-photon processes at mid-rapidity.

The comparison data/STARLIGHT at mid-rapidity is the ratio of the measured cross section $\sigma_{\gamma\gamma}$ to the prediction $\sigma_{\gamma\gamma}^{\text{SL}} \cdot R_{ym}$.

As we can see from Table 6.14, the experimental $\gamma\gamma \to l^+l^-$ cross section is in agreement with STARLIGHT well within two standard deviations, which is, given the quite non-sophisticated method, an acceptable result. The measurement at mid-rapidity shows that the region of low transverse momenta is populated by elastic $\gamma\gamma \to l^+l^-$ production, which is one of the assumptions of the fits to the p_T distribution for getting the signal of the J/ψ.

At forward rapidity $2.5 < y < 4.0$, the cross section of $\gamma\gamma \to \mu^+\mu^-$ was measured in the invariant mass range of $1.5 < m_{\mu^+\mu^-} < 2.5$ GeV/c^2 also by fitting the p_T distribution of dimuon candidates. The resulting cross section was $\sigma_{\gamma\gamma}(\gamma\gamma \to \mu^+\mu^-) = 1.76 \pm 0.12$ (stat) $^{+0.16}_{-0.15}$ (syst) μb in a given kinematic range. The corresponding STARLIGHT prediction is $\sigma_{\gamma\gamma}^{\mathrm{SL}} = 1.8$ μb, which is in a good agreement with the measurement.

6.8 Results

Now everything is ready to come back to the equation for the differential cross section of J/ψ photoproduction in p-Pb collisions in Eq. (6.2) and put all the numbers. The equation, together with the yield by Eq. (6.30), reads as

$$\frac{\mathrm{d}\sigma}{\mathrm{d}y}(\text{p+Pb} \rightarrow \text{p+Pb} + J/\psi) = \frac{N_{J/\psi}^{\mathrm{exc}}}{\varepsilon_{J/\psi} \cdot \mathscr{B} \cdot \mathscr{L}} \cdot \frac{1}{\Delta y} \quad \text{and} \quad N_{J/\psi}^{\mathrm{exc}} = \frac{N_{J/\psi}}{1+f_D}. \tag{6.32}$$

The process of signal extraction which provides the number of J/ψ candidates $N_{J/\psi}$ and the correction for feed-down f_D from decays of ψ' is described in Section 6.7. The total acceptance and efficiency correction $\varepsilon_{J/\psi}$ is given by one of variants of Eq. (6.19) or by Eq. (6.20), according to the specific rapidity and beam configuration. The process of calculation of the efficiency is described in Section 6.6. The branching ratio $\mathscr{B}$ of dimuon decays $J/\psi \rightarrow \mu^+\mu^-$ was for the published analysis in the forward rapidity taken from [107], while for the later performed analyses in the semi-forward and mid-rapidity intervals, the updated document [80] was used for $\mathscr{B}$ of dilepton decays $J/\psi \rightarrow e^+e^-$ or $J/\psi \rightarrow \mu^+\mu^-$. The description of the method to obtain the luminosity $\mathscr{L}$ of the data sample is given in Section 6.3. The width of the rapidity bin Δy is given by the actual interval where the J/ψ has been measured.

6.8.1 Photon-proton cross section

The differential cross section in Eq. (6.32) is related to the photon-proton cross section $\sigma(\gamma\text{p} \rightarrow J/\psi\,\text{p})$ using the flux of virtual photons, as was outlined in Section 3.6. The cross section of J/ψ production in photon-proton interactions is found by

$$\frac{\mathrm{d}\sigma}{\mathrm{d}y}(\text{p+Pb} \rightarrow \text{p+Pb} + J/\psi) = k\frac{\mathrm{d}N_\gamma}{\mathrm{d}k}\sigma(\gamma + \text{p} \rightarrow J/\psi + \text{p}), \tag{6.33}$$

where the flux of virtual photons $k(\mathrm{d}N_\gamma/\mathrm{d}k)$ was calculated using STARLIGHT in the impact parameter space (Section 1.5.1).

The differential cross section $\mathrm{d}\sigma/\mathrm{d}y$ is measured in a specific interval in rapidity y of the J/ψ for which there is the mean energy of the photon-proton system $\langle W_{\gamma\text{p}} \rangle$, corresponding to the photon-proton cross section $\sigma(\gamma + \text{p})$. The energy of the J/ψ produced at the rapidity y with respect to the direction of the proton beam is given by Eq. (6.1), the mean energy $\langle W_{\gamma\text{p}} \rangle$ in a given interval of the rapidity has been calculated using STARLIGHT.

6.8.2 Cross section at forward rapidity

The photon-proton cross section $\sigma(\gamma+\mathrm{p})$ has been measured at forward rapidity in p-Pb in $2.5 < y < 4.0$ and in Pb-p in the interval of $-3.6 < y < -2.6$. The corresponding energies are $21 < W_{\gamma\mathrm{p}} < 45$ GeV and $577 < W_{\gamma\mathrm{p}} < 952$ GeV for p-Pb and Pb-p respectively. The full p-Pb rapidity interval has been subdivided into three bins of rapidity of $(2.5, 3.0)$, $(3.0, 3.5)$ and $(3.5, 4.0)$. The results from the forward rapidity analysis are published in [2].

The results in the forward rapidity are summarized in Table 6.15. The feed-down f_D has been calculated using Eq. (6.29) with inputs from simulations described in Section 6.4.1. The number of J/ψ candidates $N_{J/\psi}$ was obtained by the fit to the p_T distribution in Figure 6.13b. The luminosity $\mathscr{L}$ corresponds to the trigger class CMUP6-B in p-Pb and classes CMUP3-B and CMUP8-B in Pb-p. The total acceptance and efficiency correction $\varepsilon_{J/\psi}$ was in p-Pb obtained using Eq. (6.20), while for Pb-p Eq. (6.19) was used (the version for forward Pb-p).

System	p-Pb				Pb-p
Rapidity	$(2.5, 4.0)$	$(3.5, 4.0)$	$(3.0, 3.5)$	$(2.5, 3.0)$	$(-3.6, -2.6)$
$f_D^{\perp}$	0.060	0.082	0.058	0.044	0.082
f_D^{0}	0.074	0.102	0.070	0.057	0.102
$f_D^{\parallel}$	0.103	0.143	0.096	0.083	0.146
f_D	0.079	0.109	0.075	0.061	0.110
$\Delta f_D^{-} = \lvert f_D - f_D^{\perp}\rvert$	0.019	0.027	0.017	0.017	0.028
$\Delta f_D^{+} = \lvert f_D - f_D^{\parallel}\rvert$	0.024	0.034	0.021	0.021	0.036
$N_{J/\psi}$	447 ± 30	99 ± 13	259 ± 23	97 ± 14	79 ± 10
$N_{J/\psi}^{\mathrm{exc}} = N_{J/\psi}/(1+f_D)$	414 ± 28	89 ± 12	241 ± 21	91 ± 13	71 ± 9
$\mathscr{B}$	0.0593	0.0593	0.0593	0.0593	0.0593
$\mathscr{L}$ (μb^{-1})	3922	3922	3922	3922	4505
Δy	1.5	0.5	0.5	0.5	1.0
$\varepsilon_{J/\psi}$	0.185	0.133	0.309	0.115	0.108
$\varepsilon_{0\mathrm{VBC}}$	-	-	-	-	0.840
$\mathrm{d}\sigma/\mathrm{d}y$ (μb)	6.42	5.77	6.71	6.83	2.46
$\Delta(\mathrm{d}\sigma/\mathrm{d}y)$ (μb)	0.43	0.76	0.60	1.00	0.31
$k(\mathrm{d}N_{\gamma}/\mathrm{d}k)$	193.3	208.9	193.3	177.6	8.7
$W_{\gamma\mathrm{p}}$ (GeV)	(21, 45)	(21, 27)	(27, 35)	(35, 45)	(577, 952)
$\langle W_{\gamma\mathrm{p}}\rangle$ (GeV)	32.3	24.1	30.9	39.6	706
$\sigma(\gamma+\mathrm{p})$ (nb)	33.2	27.6	34.7	38.5	284
$\Delta\sigma(\gamma+\mathrm{p})$ (nb)	2.2	3.6	3.1	5.6	36

Table 6.15 Details for the calculation of the cross section at forward rapidity.

The differential cross section $\mathrm{d}\sigma/\mathrm{d}y$ was calculated using Eq. (6.32), the photon-proton cross section was obtained from Eq. (6.33). The errors quoted in Table 6.15 are statistical errors from the number of candidates $N_{J/\psi}$.

All the calculations have been performed separately in the bins of rapidity in p-Pb.

6.8.3 Cross section at semi-forward rapidity

The measurement at semi-forward rapidity was done in the intervals $1.2 < y < 2.7$ and $-2.5 < y < -1.2$ for p-Pb and Pb-p respectively. The relevant energies are $40.8 < W_{\gamma\mathrm{p}} < 86.4$ GeV and $287 < W_{\gamma\mathrm{p}} < 550$ GeV (p-Pb and Pb-p). Thanks to better statistics in p-Pb, the full interval was divided into the two bins, $(1.2, 1.9)$ and $(1.9, 2.7)$.

The results are given in Table 6.16. The feed-down f_D was calculated from Eq. (6.29), for which all the efficiencies have been obtained using simulations listed in Table 6.2. The number of candidates $N_{J/\psi}$ was taken by fitting the p_T distribution, as shown in Figure 6.17. Similar fits to obtain the $N_{J/\psi}$ in the bins of rapidity in semi-forward p-Pb are shown in Figure D.4 in Appendix D.3 (together with toy MC representation of non-exclusive template in Figure D.3). The luminosity $\mathscr{L}$ stands in this case for the semi-forward trigger classes CMUP7 for p-Pb and CMUP5 and CMUP9 for Pb-p. The correction for acceptance and efficiency $\varepsilon_{J/\psi}$ was calculated by Eq. (6.20) for p-Pb and for Pb-p by Eq. (6.19) in the version for the semi-forward Pb-p.

The differential cross section $\mathrm{d}\sigma/\mathrm{d}y$ of J/ψ photoproduction in p-Pb was obtained by Eq. (6.32), the corresponding photon-proton cross section was calculated by Eq. (6.33). The errors shown in semi-forward Table 6.16 are statistical errors given by errors in the number of candidates $N_{J/\psi}$.

Separate calculations have been performed in all intervals of rapidity. In the case of p-Pb, the full interval was subdivided into the two intervals, as indicated in the second line of Table 6.16.

6.8.4 Cross section at mid-rapidity

At mid-rapidity, the measurement was performed in the interval $(-0.8, 0.8)$, which was, thanks to enough statistics, separeted into the two symmetrical bins of $(-0.8, 0.0)$ and $(0.0, 0.8)$. The range of energy of the photon-proton system probed at mid-rapidity is $105.5 < W_{\gamma\mathrm{p}} < 234.9$ GeV.

The cross section was first measured separately in the dielectron and dimuon decay channels of the J/ψ. Then both of the cross sections have been combined to the final results at mid-rapidity.

The measurements at mid-rapidity are presented in Tables 6.17 and 6.18 in the dielectron and dimuon channel respectively. The feed-down f_D at mid-rapidity was again obtained from Eq. (6.29), in this case using simulations given in Tables 6.3 and 6.4. The number of candidates $N_{J/\psi}$ was taken from the fit to the p_T distribution in Figure 6.20. Fits in bins of rapidity are shown in Figure D.6 in Appendix D.3, the toy MC representation of non-exclusive background is given in Figure D.5. The luminosity $\mathscr{L}$ of the data sample was

System	p-Pb			Pb-p
Rapidity	$(1.2, 2.7)$	$(1.2, 1.9)$	$(1.9, 2.7)$	$(-2.5, -1.2)$
$f_D^{\perp}$	0.032	0.033	0.033	0.029
$f_D^{\parallel}$	0.009	0.010	0.007	0.010
f_D^{0}	0.025	0.026	0.024	0.023
f_D	0.022	0.023	0.021	0.021
$\Delta f_D^{-} = \lvert f_D - f_D^{\perp}\rvert$	0.013	0.013	0.014	0.011
$\Delta f_D^{+} = \lvert f_D - f_D^{\parallel}\rvert$	0.010	0.010	0.012	0.008
$N_{J/\psi}$	170 ± 23	100 ± 17	75 ± 15	78 ± 11
$N_{J/\psi}^{\mathrm{exc}} = N_{J/\psi}/(1+f_D)$	166 ± 23	98 ± 17	73 ± 15	76 ± 11
$\mathscr{B}$	0.05961	0.05961	0.05961	0.05961
$\mathscr{L}$ (μb^{-1})	3147	3147	3147	3743
Δy	1.5	0.7	0.8	1.3
$\varepsilon_{J/\psi}$	0.078	0.086	0.071	0.039
$\varepsilon_{\mathrm{0VBC}}$	-	-	-	0.585
f_b	-	-	-	0.956
$\mathrm{d}\sigma/\mathrm{d}y$ (μb)	7.56	8.68	6.85	7.03
$\Delta(\mathrm{d}\sigma/\mathrm{d}y)$ (μb)	1.05	1.51	1.41	1.02
$k(\mathrm{d}N_\gamma/\mathrm{d}k)$	152.6	140.2	163.6	36.5
$W_{\gamma\mathrm{p}}$ (GeV)	(40.8, 86.4)	(60.9, 86.4)	(40.8, 60.9)	(287, 550)
$\langle W_{\gamma\mathrm{p}}\rangle$ (GeV)	61.5	73.1	50.4	391.2
$\sigma(\gamma+\mathrm{p})$ (nb)	49.54	61.91	41.87	192.60
$\Delta\sigma(\gamma+\mathrm{p})$ (nb)	6.88	10.77	8.62	27.95

Table 6.16 Details for the cross section calculation at semi-forward rapidity.

calculated for the mid-rapidity trigger CCUP7 (same for p-Pb and Pb-p). The acceptance and efficiency correction was calculated using Eq. (6.19) in the variant for mid-rapidity.

As in the previous cases, the differential cross section $\mathrm{d}\sigma/\mathrm{d}y$ was calculated using the formula in Eq. (6.32), the photon-proton cross section $\sigma(\gamma+\mathrm{p})$ then from Eq. (6.33). The errors given in Tables 6.17 and 6.18 come from statistical errors on the number of J/ψ candidates $N_{J/\psi}$. Separate calculations have been performed in the full rapidity interval and in the two bins of rapidity.

The differential cross sections $\mathrm{d}\sigma/\mathrm{d}y$ and photon-proton cross sections $\sigma(\gamma+\mathrm{p})$ obtained in each decay channel have been combined using the weighted averages of the results presented in Tables 6.17 and 6.18. As a weighting factor, the inverse square of the statistical error of each particular decay channel was used. When we denote the weights as w_i, these are calculated from the statistical errors σ_i as $w_i = 1/\sigma_i^2$, where i stands for the dielectron

Rapidity	$(-0.8, 0.8)$	$(-0.8, 0.0)$	$(0.0, 0.8)$
$f_D^{\perp}$	0.040	0.038	0.042
$f_D^{\parallel}$	0.051	0.052	0.053
f_D^0	0.044	0.042	0.046
f_D	0.045	0.044	0.047
$\Delta f_D^- = \lvert f_D - f_D^{\perp}\rvert$	0.005	0.006	0.005
$\Delta f_D^+ = \lvert f_D - f_D^{\parallel}\rvert$	0.006	0.008	0.006
$N_{J/\psi}$	233 ± 22	122 ± 14	111 ± 17
$N_{J/\psi}^{\mathrm{exc}} = N_{J/\psi}/(1+f_D)$	223 ± 21	117 ± 13	106 ± 16
$\mathscr{B}(J/\psi \to e^+e^-)$	0.05971	0.05971	0.05971
$\mathscr{L}$ (μb^{-1})	6915	6915	6915
Δy	1.6	0.8	0.8
$\varepsilon_{J/\psi}$	0.031	0.033	0.029
f_b	1.137	1.165	1.107
$\mathrm{d}\sigma/\mathrm{d}y$ (μb)	10.89 ± 1.07	10.73 ± 1.28	11.07 ± 1.77
$k(\mathrm{d}N_\gamma/\mathrm{d}k)$	91.9	79.4	104.3
$W_{\gamma\mathrm{p}}$ (GeV)	(105.5, 234.9)	(157.4, 234.9)	(105.5, 157.4)
$\langle W_{\gamma\mathrm{p}}\rangle$ (GeV)	161.4	193.3	129.9
$\sigma(\gamma+\mathrm{p})$ (nb)	118.50 ± 11.64	135.14 ± 16.12	106.14 ± 16.97

Table 6.17 Calculation of the cross section at mid-rapidity in the dielectron channel.

or dimuon channel.

The combined cross sections $\mathrm{d}\sigma/\mathrm{d}y$ and $\sigma(\gamma+\mathrm{p})$ are given in Table 6.19 in the full interval at mid-rapidity and in the bins of rapidity.

Rapidity	$(-0.8, 0.8)$	$(-0.8, 0.0)$	$(0.0, 0.8)$
$f_D^{\perp}$	0.043	0.041	0.043
$f_D^{\parallel}$	0.055	0.054	0.055
f_D^{0}	0.047	0.045	0.049
f_D	0.048	0.047	0.049
$\Delta f_D^{-} = \lvert f_D - f_D^{\perp} \rvert$	0.005	0.006	0.006
$\Delta f_D^{+} = \lvert f_D - f_D^{\parallel} \rvert$	0.007	0.007	0.006
$N_{J/\psi}$	417 ± 27	208 ± 21	206 ± 18
$N_{J/\psi}^{\mathrm{exc}} = N_{J/\psi}/(1+f_D)$	398 ± 26	199 ± 20	196 ± 17
$\mathscr{B}(J/\psi \to \mu^+\mu^-)$	0.05961	0.05961	0.05961
$\mathscr{L}$ (μb^{-1})	6915	6915	6915
Δy	1.6	0.8	0.8
$\varepsilon_{J/\psi}$	0.060	0.063	0.057
f_b	1.158	1.165	1.150
$\mathrm{d}\sigma/\mathrm{d}y$ (μb)	10.06 ± 0.68	9.58 ± 1.01	10.43 ± 0.96
$k(\mathrm{d}N_\gamma/\mathrm{d}k)$	91.9	79.4	104.3
$W_{\gamma\mathrm{p}}$ (GeV)	(105.5, 234.9)	(157.4, 234.9)	(105.5, 157.4)
$\langle W_{\gamma\mathrm{p}} \rangle$ (GeV)	161.4	193.3	129.9
$\sigma(\gamma+\mathrm{p})$ (nb)	109.47 ± 7.40	120.65 ± 12.72	100.00 ± 9.20

Table 6.18 Calculation of the cross section at mid-rapidity in the dimuon channel.

Rapidity	$(-0.8, 0.8)$	$(-0.8, 0.0)$	$(0.0, 0.8)$
$\langle W_{\gamma\mathrm{p}} \rangle$ (GeV)	161.4	193.3	129.9
$\mathrm{d}\sigma/\mathrm{d}y$ (μb)	10.30 ± 0.57	10.02 ± 0.79	10.58 ± 0.84
$\sigma(\gamma+\mathrm{p})$ (nb)	112.07 ± 6.24	126.21 ± 9.99	101.39 ± 8.09

Table 6.19 Weighted average of dielectron and dimuon cross sections at mid-rapidity.

6.9 Evaluation of systematic errors

6.9.1 Systematic errors in the forward analysis

Sources and values of systematic errors considered in the analysis at forward rapidity are given in Table 6.20.

Source	p-Pb	Pb-p
Signal extraction	6%	$^{+0.0}_{-6.0}$%
Luminosity	3.3%	3.0%
Tracking efficiency	4%	6%
Muon trigger efficiency	2.8%	3.2%
Matching	1%	1%
V0C efficiency	-	3.5%
Total uncorrelated	8.5%	$^{+8.3}_{-10.2}$%
Luminosity	1.6%	1.6%
Branching ratio	1%	1%
V0A veto efficiency	$^{+2.0}_{-0.0}$%	$^{+2.0}_{-0.0}$%
Feed-down	$^{-2.2}_{+1.8}$%	$^{+2.6}_{-3.1}$%
J/ψ acceptance	3%	3%
Total	±9.6%	$^{+9.6}_{-11.3}$%

Table 6.20 Systematic errors for the measurement of the cross section at forward rapidity [2].

Another source of systematic error is the uncertainty in the determination of the flux of virtual photons $k(\mathrm{d}N_\gamma/\mathrm{d}k)$, which appears in Eq. (6.33). The error affects only the photon-proton cross section $\sigma(\gamma+\mathrm{p})$.

The flux of virtual photons is in STARLIGHT calculated in impact space with requirement of no hadronic interactions (Section 1.5.1). The related uncertainty was estimated by increasing or decreasing the radius of the Pb-ion by ±0.5 fm, which corresponds to the nuclear skin thickness.

The uncertainty in the photon flux ranges from 2% at low energy (forward p-Pb) up to 9% at the highest energies (forward Pb-p) [2]. The flux at high energy is dominated by small impact parameters and is then more sensitive to the rejection of hadronic interactions close to surface of the Pb nucleus.

6.9.2 Systematic errors in the semi-forward analysis

Sources of systematic uncertainties considered in the analysis at semi-forward rapidity and their evaluation are described in this section. The summary Table 6.21 is given at the end of the section.

TPC track selection

The minimal number of TPC space points imposed by requirement **GR-10** was gradually increased from 70 up to 90 (the default is 50) by steps of 10. All other selection criteria remained unchanged. The ratio of events surviving the selection was made for events from the data to events in the MC of J/ψ in γp $\rightarrow J/\psi$p. Both samples were selected within more strict range of invariant mass around the J/ψ and for lower values of p_T corresponding to a cleaner sample.

The error was calculated as the RMS of ratio for the default selection minus ratios with modified requirement for the space points.

The error is 3.4% for full p-Pb rapidity and 3.3% for Pb-p.

Roughly same results were achieved when the number of crossed TPC rows was varied from 80 to 100 by steps of 10 (so the minimal values 80, 90 and 100 were required). The selection criteria remained unchanged, just the requirement on minimal TPC crossed rows was added. The related errors are 2.5% for p-Pb and 2.8% for Pb-p. Since the number of TPC crossed rows is correlated with the number of TPC clusters, the results obtained by varying the TPC clusters will be used further.

It is worth noting that the requirement on minimal number of TPC clusters or number of crossed rows affects the acceptance of the central track. When using the highest value for clusters or crossed rows (90 clusters or 100 rows), the observed range of pseudorapidity of the central track reduces to $|\eta| < 0.9$ (the default requirement is $|\eta| < 1.1$).

Signal extraction

The parameters of fits to the p_T distribution (Section 6.7.2), range of the fit or width of the bins were varied within $\sim$10%. The cross section was evaluated with the yield from the modified p_T fit, replacing thus $N_{J/\psi}$ in Table 6.16. The error was calculated as the RMS of default cross section minus cross section with modified p_T fit.

In the Pb-p fit the assumption of the slope parameter was also changed. According to Section 6.4.2, the slope parameter corresponding to the semi-forward Pb-p energy is $b = 5.6$ GeV^{-2}. A MC sample at this value of b is used to describe the signal in Pb-p fit. Additional p_T fits using $b = 5.0$ and $b = 6.0$ GeV^{-2} were made in addition to the variations stated above.

Muon trigger efficiency, matching and tracking efficiency

The systematic error on the tracking efficiency of a single muon track is described in [108], the error is 2% for p-Pb and 3% for Pb-p. An additional contribution from matching of the track to the trigger information is 0.5%.

The systematic uncertainty on the muon trigger chambers is evaluated in [109]. The systematic uncertainty related to the trigger chamber efficiency is 1%.

The second source of trigger systematic uncertainty comes from the behavior of the trigger around the threshold. The contribution was evaluated for the present analysis as a small discrepancy between the trigger response in the data and in MC. The trigger response function was obtained as the ratio of muon tracks matching the trigger to all muon tracks, as a function of p_T of the muon track. This contribution is 1.7% for p-Pb and 1.3% for Pb-p.

Both contributions for muon triggering have been added in quadratures, giving 2.0% for p-Pb and 1.6% for Pb-p.

V0C efficiency

The related systematic error is described in Section 6.6.2, given in Eq. (6.16). The error is 3.4%.

V0 offline veto

A possible mismatch between V0 online requirements implemented in the trigger and offline requirements in the event selection was studied by modifying the selection requirements **GR-2** (V0A) and **SR-4** (V0C).

For p-Pb the offline decisions of V0A and V0C were removed and counting of the hits in V0C for requirement **SR-5** was changed from offline to online.

In the case of Pb-p, the activity in V0C was part of the trigger as is described in Section 6.2.7. Only the offline veto in V0A was removed in Pb-p.

The related errors are well below 3% for all rapidity intervals.

Branching ratio

The error is 0.6% according to [80].

Feed-down

The errors on feed-down resulting from different polarization assumptions, as they are listed in Table 6.16, have been propagated to the cross section. The contribution is below 1.4% in all rapidity intervals.

Luminosity

The error is based on the forward analysis [2] because the procedure to get the luminosity is exactly the same here. The errors quoted in the forward analysis are 3.3% for p-Pb and 3.0% in Pb-p and 1.6% correlated between p-Pb and Pb-p.

Because of the p-Pb and Pb-p samples are analyzed separately, same as was done for the forward analysis, in the current case of semi-forward analysis the forward values will be quoted.

Table of systematic errors at semi-forward rapidity

Table 6.21 shows the sources and values of systematic uncertainties at the semi-forward rapidity.

System	p-Pb			Pb-p
Rapidity	$(1.2, 2.7)$	$(1.2, 1.9)$	$(1.9, 2.7)$	$(-2.5, -1.2)$
TPC track selection, %	3.4	1.2	5.7	3.3
Signal extraction, %	2.6	2.2	3.6	3.0
Muon tracking efficiency, %	2.0	2.0	2.0	3.0
Muon matching, %	0.5	0.5	0.5	0.5
Muon trigger efficiency, %	2.0	2.0	2.0	1.6
V0C efficiency, %	-	-	-	3.4
V0 offline veto, %	3.1	3.5	2.7	1.2
Branching ratio, %	0.6	0.6	0.6	0.6
Feed down, %	$^{+0.5}_{-1.2}$	$^{+1.0}_{-1.0}$	$^{+0.0}_{-1.3}$	$^{+0.0}_{-1.4}$
Luminosity, %	3.3	3.3	3.3	3.0
Luminosity correlated, %	1.6			

Table 6.21 Systematic errors for the measurement of the cross section at semi-forward rapidity.

Flux of virtual photons

The procedure is inherited from the forward analysis (Section 6.9.1), the contribution is within the interval for the forward rapidity.

6.9.3 Systematic errors in the mid-rapidity analysis

The evaluation of systematic uncertainties at mid-rapidity is presented in the current section, Table 6.22 gives the list of the uncertainties and their values.

TPC track selection

The requirement on the minimal number of TPC clusters, **GR-10**, was gradually increased from 70 to 90 by steps of 10, i.e. values of 70, 80 and 90 were used instead of the nominal value of 50. All other selection criteria remained unchanged. The ratio of events surviving the selection was made for events from data to events in the MC of J/ψ in $\gamma\mathrm{p} \rightarrow J/\psi\mathrm{p}$. Both samples were selected within a more strict range of invariant mass around the J/ψ and for lower values of p_T corresponding to a cleaner sample.

The error was calculated as the RMS of the ratio for the default selection minus the ratios with modified requirement for the space points.

The related systematic error amounts to 1.4% for the full rapidity and 1.4% (1.7%) for the lower (higher) bin, which is in agreement with the semi-forward analysis.

Signal extraction

The parameters of fits to the p_T distribution (Section 6.7.3), the range of the fit or the width of the bins were varied within $\sim$10%. The cross section was evaluated with the yield from the modified p_T replacing thus $N_{J/\psi}$ in Tables 6.17 and 6.17. The error was calculated as the RMS of the default cross section minus the cross section with the modified p_T fits.

The assumption on the slope parameter was also changed. According to Section 6.4.2, the slope parameter corresponding to mid-rapidity is $b = 5.0$ GeV^{-2}. A sample at this value of b is used to describe the signal in the fits. Additional p_T fits using $b = 4.5$ and $b = 5.6$ GeV^{-2} were made in addition to the variations stated above.

Trigger efficiency

The trigger required the tracks to have a difference in azimuthal angle $\Delta\phi > 150°$ reflecting a back-to-back topology. The requirement is implemented by the trigger input 0STP (Section 6.2.7). The efficiency of the 0STP trigger input from the MC was checked using the unbiased trigger CTRUE-B.

The efficiency of 0STP was for this purpose defined as the number of events having the two reconstructed tracks with a separation in azimuthal angle as $\Delta\phi > 150°$ and the 0STP trigger input fired to all events with $\Delta\phi > 150°$.

The efficiency was first extracted from the MC samples LHC13e6g and LHC13f1g (p-Pb and Pb-p, Table 6.3) and then from the CTRUE-B data.

As the control trigger CTRUE-B was largely downscaled, the selection criteria were reduced to get the sample of two-track events at $\Delta\phi > 150°$. Therefore the requirements on SPD, V0, ZDC were removed, tracks of both signs were allowed.

Analyzing the CTRUE-B two-track events sample, 119 events were found to satisfy $\Delta\phi > 150°$, out of which 64 events had the 0STP trigger input fired, giving the 0STP efficiency of 0.538 ± 0.046.

The same procedure was applied to the MC providing 412 184 events in $\Delta\phi > 150°$, out of which 211 693 events had the 0STP trigger, giving the efficiency as 0.514.

Using the ratio of these efficiencies as related systematics, we have a 4.5% systematic error from the trigger efficiency. The same value is implemented for the full rapidity and for the bins.

Statistics in the CTRUE-B sample is very limited, but it was the only MC-independent test of the trigger.

V0 offline veto

A possible mismatch between the online V0 veto implemented in the CCUP7 trigger and offline veto implemented in the analysis by requirements **GR-2** and **MR-4** was studied by removing both of these requirements while keeping the rest of the selection criteria unchanged.

The error was obtained as a relative difference between the number of events selected by the default criteria and number of events selected without the offline V0 veto.

The contribution is up to 4.2% in the higher rapidity bin.

Particle identification

An alternative method for electron/muon separation (requirement **MR-12**) was used to get the sample of electron and muon candidates. The other selection criteria remained unchanged.

The TPC $\mathrm{d}E/\mathrm{d}x$ signal of the positive track was put against the signal of the negative track, as shown in Fig. 6.22. The separation was performed using the parametrization $\mathrm{d}E/\mathrm{d}x^{\mathrm{TPC}}(l^+) + \mathrm{d}E/\mathrm{d}x^{\mathrm{TPC}}(l^-) = 150$ (a.u.). The specific form of the parametrization was tuned using the MC. Events with higher ionization than the parametrization were interpreted as electrons, events with lower ionization as muons.

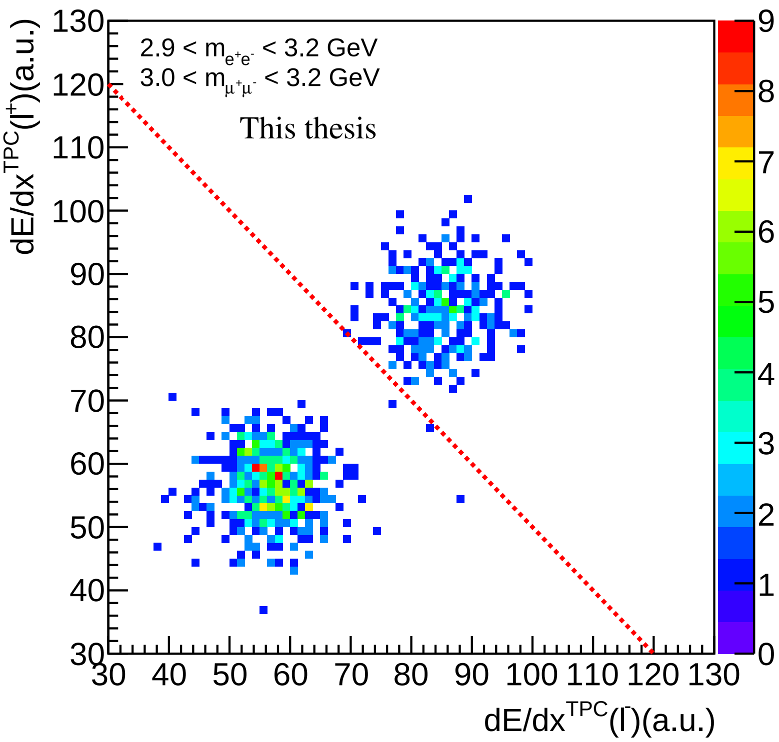

Fig. 6.22 Ionization signal from the TPC for the positive track relative to the signal for the negative track. The events above the red dashed line are interpretted as dielectrons, the events below are treated as dimuons. The line is described by the parametrization $\mathrm{d}E/\mathrm{d}x^{\mathrm{TPC}}(l^+) + \mathrm{d}E/\mathrm{d}x^{\mathrm{TPC}}(l^-) = 150$ (a.u.). Both samples, dielectrons and dimuons are shown for masses within the J/ψ mass peak, as indicated in the legend.

Ratios of events selected as electrons or muons for each of the methods (default and alternative) between the data and MC were compared. The number of events around the mass of the J/ψ and at lower p_T was counted for the default method and then for the alternative, the ratio was made. These ratios were compared between data and MC.

The error is 1.8% in full mid-rapidity interval and 1.2% and 2.5% in the lower and higher bin respectively.

Branching ratio

The error is 0.5% according to [80]. The errors in the dielectron and dimuon channels were weighted among the channels.

Feed-down

Possible errors come from the different polarization assumptions for the J/ψ coming from the ψ' decays. The f_D factors in Tables 6.17 and 6.18 produced the mean f_D and upper and lower errors on the f_D. These errors were propagated to the cross section yielding the related systematics.

Luminosity

The error is based on the forward analysis [2] because the procedure to get the luminosity is exactly the same here. The errors quoted in the forward analysis are 3.3% for p-Pb and 3.0% in Pb-p.

Since the data are analyzed as a common sample of p-Pb and Pb-p events triggered by the mid-rapidity class CCUP7, the errors from the forward analysis are weighted by the CCUP7 luminosity in p-Pb and Pb-p, giving 3.1% systematic error for the luminosity of CCUP7. The contribution correlated between p-Pb and Pb-p is 1.6%.

Table of systematic errors

Systematic uncertainties and their values at mid-rapidity are listed in Table 6.22.

Rapidity	$(-0.8, 0.8)$	$(-0.8, 0.0)$	$(0.0, 0.8)$
TPC track selection, %	1.4	1.4	1.7
Signal extraction, %	2.6	3.6	4.1
Trigger efficiency, %	4.5	4.5	4.5
V0 offline veto, %	4.1	3.9	4.2
Particle identification, %	1.8	1.2	2.5
Branching ratio, %	0.5	0.5	0.5
Feed down, %	$^{+0.7}_{-0.5}$	$^{+1}_{-0.6}$	$^{+0.6}_{-1}$
Luminosity, %	3.1	3.1	3.1
Luminosity correlated, %		1.6	

Table 6.22 Systematic errors for the measurement of the cross section at mid-rapidity.

Flux of virtual photons

The determination of the error was done using the same approach as at forward rapidity in Section 6.9.1.

Chapter 7

Discussion of physics results in p-Pb UPC

The measurement of exclusive J/ψ photoproduction off protons by the ALICE experiment, presented in the preceding sections, is discussed here for its physics implications. The cross section of exclusive J/ψ photoproduction $\sigma(\gamma + \mathrm{p} \to J/\psi + \mathrm{p})$ obtained in each rapidity interval is given in Table 7.1 in order of increasing energy $W_{\gamma\mathrm{p}}$. Errors in each measurement are given as statistical from the number of exclusive J/ψ candidates, systematical of the measurement, and theoretical from the uncertainty in the flux of virtual photons. The results of the measurements at forward rapidity are already published [2], results from the semi-forward rapidity and mid-rapidity are in the final stages of paper preparation in the ALICE collaboration.

Rapidity	$\langle W_{\gamma\mathrm{p}} \rangle$(GeV)	$\sigma(\gamma + \mathrm{p} \to J/\psi + \mathrm{p})$ (nb)	Reference
(3.5, 4.0)	24.1	$27.6 \pm 3.6(\mathrm{stat}) \pm 2.8(\mathrm{syst}) \pm 0.6(\mathrm{theor})$	[2]
(3.0, 3.5)	30.9	$34.7 \pm 3.1(\mathrm{stat}) \pm 2.9(\mathrm{syst}) \pm 0.7(\mathrm{theor})$	[2]
(2.5, 3.0)	39.6	$38.5 \pm 5.6(\mathrm{stat}) \pm 4.2(\mathrm{syst}) \pm 0.8(\mathrm{theor})$	[2]
(1.9, 2.7)	50.4	$41.9 \pm 8.6(\mathrm{stat}) \pm 3.6(\mathrm{syst}) \pm 0.4(\mathrm{theor})$	This thesis
(1.2, 1.9)	73.1	$61.9 \pm 10.8(\mathrm{stat}) \pm 3.8(\mathrm{syst}) \pm 0.7(\mathrm{theor})$	This thesis
(0.0, 0.8)	129.9	$101.4 \pm 8.1(\mathrm{stat}) \pm 8.9(\mathrm{syst}) \pm 1.4(\mathrm{theor})$	This thesis
(-0.8, 0.0)	193.3	$126.2 \pm 10.0(\mathrm{stat}) \pm 10.2(\mathrm{syst}) \pm 2.4(\mathrm{theor})$	This thesis
(-2.5, -1.2)	391.2	$192.6 \pm 28.0(\mathrm{stat}) \pm 13.8(\mathrm{syst}) \pm 7.4(\mathrm{theor})$	This thesis
(-3.6, -2.6)	706	$284 \pm 36(\mathrm{stat})^{+27}_{-32}(\mathrm{syst}) \pm 26(\mathrm{theor})$	[2]

Table 7.1 Measured cross section of exclusive J/ψ photoproduction off protons.

The energy dependence of the photoproduction cross section is show in Figure 7.1. The data given in Table 7.1 are plotted as a function of the energy. Errors in the plot are given as a quadrature sum of statistical and systematical uncertainties. The upper horizontal axis is marked in values of the Bjorken-x, which is, using Eq. (1.16), given as $x = (M_{J/\psi}/W_{\gamma\mathrm{p}})^2$. The measurement corresponds to the range in x from $\sim 2 \times 10^{-2}$ down to $\sim 2 \times 10^{-5}$.

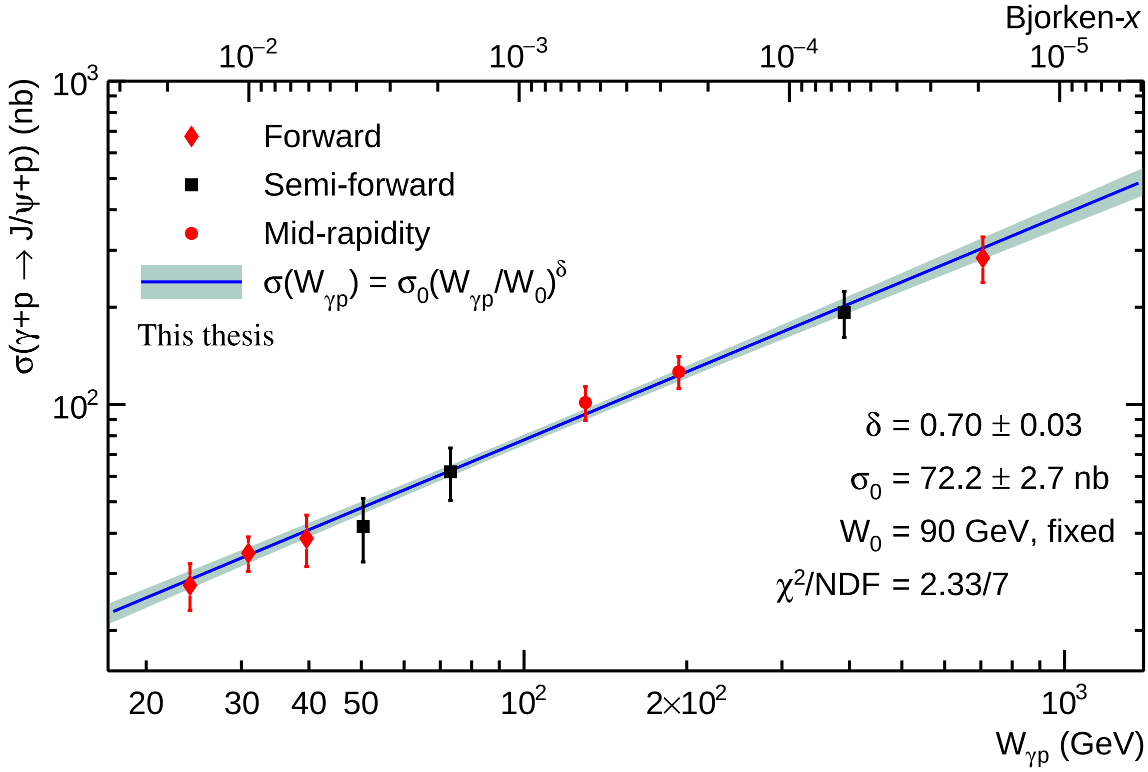

Fig. 7.1 Cross section of exclusive J/ψ photoproduction off protons as measured by the ALICE experiment. Data from Table 7.1 are shown using separate symbols for each rapidity interval. A fit to a power-law dependence is also shown.

Similar to the analysis of HERA data (Section 1.4.1), a χ^2 fit to the photoproduction cross section is done using a power law as in Eq. (1.21). A fit to the power law formula

$$\sigma(W_{\gamma p}) = \sigma_0 \left(\frac{W_{\gamma p}}{W_0} \right)^{\delta} . \tag{7.1}$$

is included in Figure 7.1. The fit considered statistical errors of the measurement, results of the fit are shown in the legend.

The fit to the ALICE data yields the slope of $\delta_{\mathrm{ALICE}} = 0.70 \pm 0.03$, the same fit to the forward data reported in [2] gives $\delta_{\mathrm{PRL}} = 0.68 \pm 0.06$. As we can see, the addition of semi-forward and mid-rapidity data improves the precision of the measurement, the error gets two times reduced.

ALICE results on the energy dependence can be directly compared with HERA (Section 1.4.1), experiments H1 and ZEUS found $\delta_{\mathrm{H1}} = 0.67 \pm 0.03$ and $\delta_{\mathrm{ZEUS}} = 0.69 \pm 0.04$. The current measurement at energies up to $W_{\gamma p} \sim 700$ GeV is consistent with a power law proportionality determined by HERA experiments at energies $W_{\gamma p} \lesssim 300$ GeV.

Figure 7.2 gives a comparison of the ALICE measurement with HERA data on the photon-proton cross section, theoretical models and the solutions by LHCb. As introduced in Section 1.4.1, the measurement by LHCb was performed with symmetrical proton-proton collisions. For each differential cross section the two solution of photon-proton cross section have been extracted assuming higher energy (W+) or lower energy (W-).

Measurements of ALICE within the energy range covered by HERA are consistent with H1 and ZEUS results, the two ALICE points beyond the range of HERA, semi-forward Pb-p and forward Pb-p are in agreement with the trend set by H1 and ZEUS data.

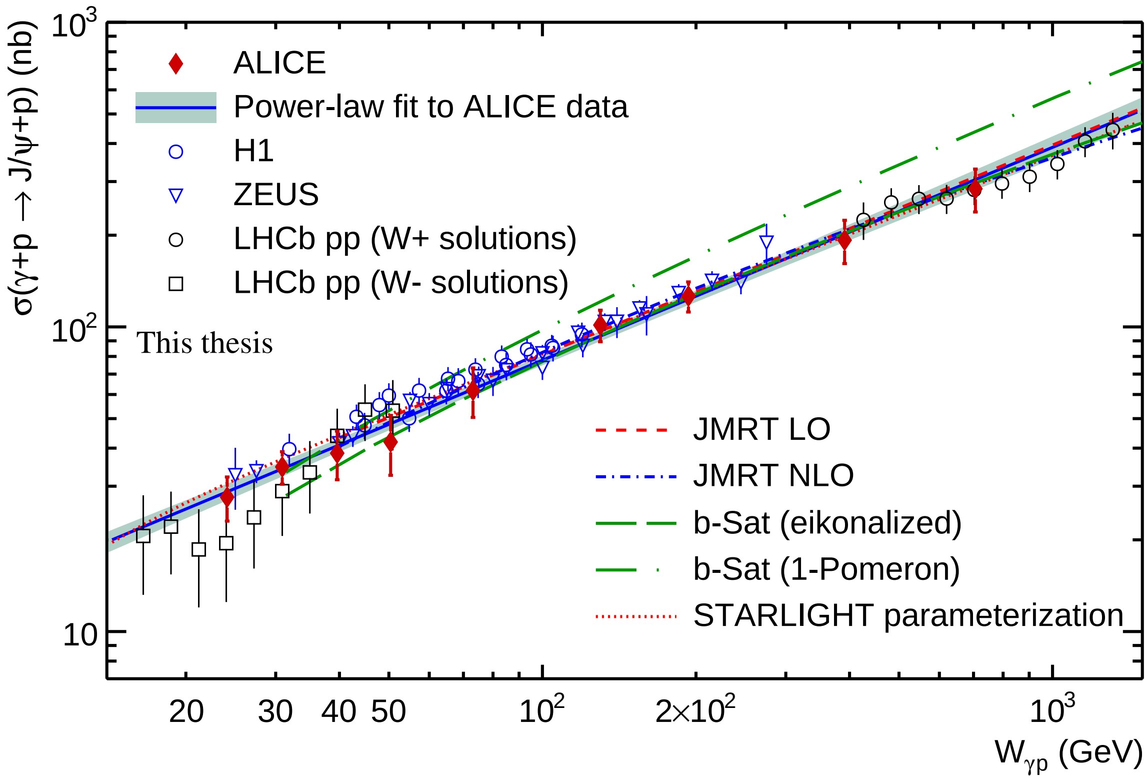

Fig. 7.2 ALICE data on exclusive J/ψ photoproduction off protons together with the previous measurements and theoretical calculations.

The theoretical models shown in Figure 7.2 are described in Section 1.6. Calculations by the JMRT group, which use the partonic description of the photoproduction process at the LO and includes some dominant effects of NLO are consistent with ALICE data up to the highest energies corresponding to $x \sim 2 \times 10^{-5}$ in the parametrization for the gluon distribution in the model. The b-Sat model, based on the dipole approach and color glass condensate, describes the ALICE data. The 1-Pomeron version of the b-Sat model, which neglects the saturation effects, is consistent with low energy ALICE data, but is about 4 standard deviations above the measurement at higher energies. The STARLIGHT parametrization for the photon-proton cross sections is based on a direct fit to the experimental data.

The models, except non-saturation 1-Pomeron b-Sat, describe well ALICE data. However, both JMRT and b-Sat calculations use parameterizations for the gluon distribution determined by the experimental data.

Another test of the validity of the power law proportionality up to the higher energies may be set up. The ALICE measurement covers a wide range of energy, wider than any experiment before, including two measurements beyond energies of previous measurements. In the test, the fit by the power law in Eq. (7.1) is made only to ALICE data within the energy range of HERA, and the two high energy points are compared to the fit.

It is expected that effects of gluon saturation will tame the growth of the cross section beyond some energy $W_{\gamma p}$. The parameter δ in Eq. (7.1) should not be a universal constant. Instead, the value of δ should start decreasing when the energy $W_{\gamma p}$ for onset of saturation will be reached.

The power law fit to ALICE data within HERA energies $20 \lesssim W_{\gamma p} \lesssim 300$ GeV is shown in Figure 7.3, the two high energy points in $390 \lesssim W_{\gamma p} \lesssim 700$ GeV are compared to the fit. To reduce the statistical errors as much as possible measurements in full rapidity intervals in the forward p-Pb and semi-forward p-Pb have been considered, the upper two points in the low energy data are measurements in the two bins of rapidity at mid-rapidity. The fit used the sum of statistical and systematical errors in quadratures, treating the systematical errors as uncorrelated. The actual errors are an upper bound for the true errors.

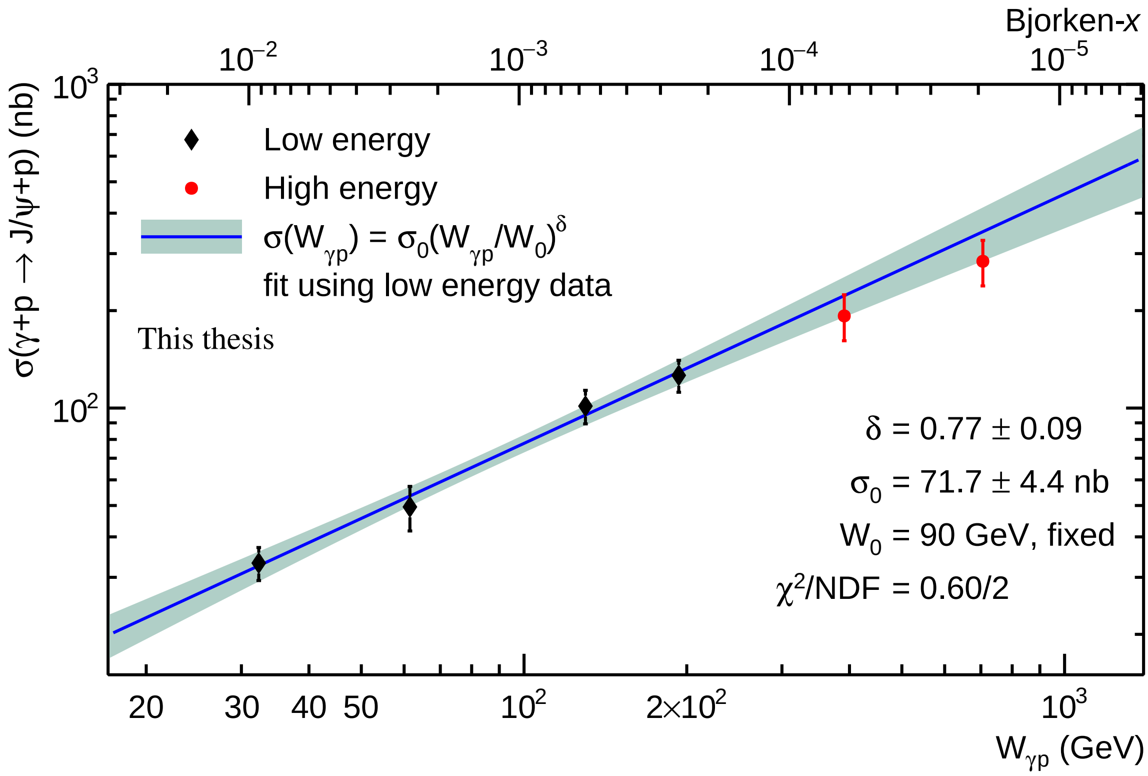

Fig. 7.3 Power law fit to ALICE data at lower energies and comparison with the data points at the higher energies.

The high energy ALICE points are consistent with the fit but both are at the lower edge. Result of the fit in Figure 7.3, $\delta_{\text{low}} = 0.77 \pm 0.09$, is in agreement with measurements at HERA (and with the global fit to ALICE data in Figure 7.1).

From the consistency in the slope of the power law dependence of the photoproduction cross section between experiments at HERA and ALICE we may conclude that no change in gluon behavior has been observed up to $W_{\gamma p} \sim 700$ GeV, which probes the gluon distribution at $x \sim 2 \times 10^{-5}$. When ALICE data at the highest energies are compared with a power law fit to the data at lower energies, the high energy data show slight decrease in growth of the cross section with $W_{\gamma p}$ but both the data points are perfectly consistent with the fit at one standard deviation. Only new precise data can provide more conclusive statements.

Chapter 8

Conclusions

The ALICE experiment was originally designed to measure thousands of particles per unit of rapidity produced by processes in a molten phase of deconfined quarks and gluons. In analyses presented in this Ph.D. thesis, events with only two tracks detected in the entire detector have been used.

The author has contributed to the results on coherent J/ψ photoproduction in the forward rapidity by providing correction factors for acceptance and efficiency of coherent and incoherent J/ψ and $\gamma\gamma \rightarrow \mu^+\mu^-$ using the official simulations and by preparing special simulations of ψ' production for the feed-down correction and by determining the correction. In the analysis of exclusive J/ψ photoproduction off protons the author was in charge of all official MC production for all three rapidity intervals and created the specific auxiliary MC productions, except the J/ψ with uniform p_T distribution. For the analysis in the forward rapidity the author has determined the acceptance and efficiency correction using the official simulations and determined the feed-down correction. At semi-forward rapidity and at mid-rapidity, the author actively performed both analyses. This work has been reported in the publications listed in Appendix E.

These measurements provided important information on the gluon structure of protons and lead nuclei. The first direct evidence for moderate gluon shadowing was obtained by measuring the cross section of coherent J/ψ photoproduction off lead nuclei. Exclusive J/ψ photoproduction probed the gluon distribution in protons over three orders of magnitude in Bjorken-x to the smallest values of $x \sim 2 \times 10^{-5}$ in the search for gluon saturation.

Using the experience gained by performing these analyses and improvements in the capabilities of ALICE, this research program will be continued during Run 2 at the LHC. Since 2015, ALICE is equipped by the two very forward scintillators, ADA and ADC, which provide cleaner signal thanks to a stronger veto to non-UPC events. The new data for coherent J/ψ photoproduction from Pb-Pb collisions at $\sqrt{s_{\mathrm{NN}}}$ = 5.02 TeV are being analysed, current results are very encouraging. Increased luminosity and larger production cross section provide larger statistics than what was available for the very first measurements at the LHC reported in this thesis.

At the end of this year, 2016, a new p-Pb run is planned. In the case of energy $\sqrt{s_{\mathrm{NN}}}$ = 8 TeV, a precision measurement over 30 GeV $\lesssim W_{\gamma\mathrm{p}} \lesssim$ 1300 GeV will be possible. The top $W_{\gamma\mathrm{p}}$ energy is almost two times higher than for measurements presented in this thesis, and may allow a first experimental glimpse of gluon saturation in the proton. ALICE is also planning to perform these measurements for Run 3 and also to explore lighter ρ and heavier Υ mesons, as well as more exotic processes like light-by-light scattering.

New horizons of deeper kinematic regimes and a larger variety of final states are ready to be explored.

References

[1] **ALICE** Collaboration, B. Abelev *et al.*, “Coherent J/ψ photoproduction in ultra-peripheral Pb-Pb collisions at $\sqrt{s_{\mathrm{NN}}} = 2.76$ TeV,” *Physics Letters B* **718** no. 4–5, (2013) 1273 – 1283. http://www.sciencedirect.com/science/article/pii/S0370269312012257.

[2] **ALICE** Collaboration, B. Abelev *et al.*, “Exclusive J/ψ photoproduction off protons in ultra-peripheral p-Pb collisions at $\sqrt{s_{\mathrm{NN}}} = 5.02$ TeV,” *Phys. Rev. Lett.* **113** (Dec, 2014) 232504. http://link.aps.org/doi/10.1103/PhysRevLett.113.232504.

[3] C. A. Bertulani, S. R. Klein, and J. Nystrand, “Physics of ultra-peripheral nuclear collisions,” *Ann.Rev.Nucl.Part.Sci.* **55** (2005) 271–310, `arXiv:nucl-ex/0502005 [nucl-ex]`.

[4] A. Baltz *et al.*, “The Physics of Ultraperipheral Collisions at the LHC,” *Phys.Rept.* **458** (2008) 1–171, `arXiv:0706.3356 [nucl-ex]`.

[5] G. Baur, K. Hencken, D. Trautmann, S. Sadovsky, and Y. Kharlov, “Coherent $\gamma\gamma$ and γA interactions in very peripheral collisions at relativistic ion colliders,” *Phys.Rept.* **364** (2002) 359–450, `arXiv:hep-ph/0112211 [hep-ph]`.

[6] J. G. Contreras and J. D. Tapia Takaki, “Ultra-peripheral heavy-ion collisions at the LHC,” *Int. J. Mod. Phys.* **A30** (2015) 1542012.

[7] E. Fermi, “On the Theory of the impact between atoms and electrically charged particles,” *Z.Phys.* **29** (1924) 315–327.

[8] C. von Weizsacker, “Radiation emitted in collisions of very fast electrons,” *Z.Phys.* **88** (1934) 612–625.

[9] E. Williams, “Nature of the high-energy particles of penetrating radiation and status of ionization and radiation formulae,” *Phys.Rev.* **45** (1934) 729–730.

[10] J. Blumlein, “The Theory of Deeply Inelastic Scattering,” *Prog. Part. Nucl. Phys.* **69** (2013) 28–84, `arXiv:1208.6087 [hep-ph]`.

[11] **ZEUS, H1** Collaboration, F. D. Aaron *et al.*, “Combined measurement and QCD analysis of the inclusive $e^{\pm}p$ scattering cross sections at HERA,” *JHEP* **01** (2010) 109, `arXiv:0911.0884 [hep-ex]`.

[12] **ZEUS, H1** Collaboration, H. Abramowicz *et al.*, "Combination of measurements of inclusive deep inelastic $e^{\pm}p$ scattering cross sections and QCD analysis of HERA data," *Eur. Phys. J.* **C75** no. 12, (2015) 580, `arXiv:1506.06042 [hep-ex]`.

[13] L. Gribov, E. Levin, and M. Ryskin, "Semihard Processes in QCD," *Phys.Rept.* **100** (1983) 1–150.

[14] G. A. Schuler and T. Sjostrand, "Towards a complete description of high-energy photoproduction," *Nucl. Phys.* **B407** (1993) 539–605.

[15] J. J. Sakurai, "Theory of strong interactions," *Annals Phys.* **11** (1960) 1–48.

[16] J. J. Sakurai and D. Schildknecht, "Generalized vector dominance and inelastic electron-proton scattering," *Phys. Lett.* **B40** (1972) 121–126.

[17] M. Ryskin, "Diffractive J/ψ electroproduction in LLA QCD," *Z.Phys.* **C57** (1993) 89–92.

[18] C. A. Bertulani and G. Baur, "Electromagnetic Processes in Relativistic Heavy Ion Collisions," *Phys.Rept.* **163** (1988) 299.

[19] P. Faccioli, C. Lourenco, J. Seixas, and H. K. Wohri, "Towards the experimental clarification of quarkonium polarization," *Eur. Phys. J.* **C69** (2010) 657–673, `arXiv:1006.2738 [hep-ph]`.

[20] L. Frankfurt, W. Koepf, and M. Strikman, "Diffractive heavy quarkonium photoproduction and electroproduction in QCD," *Phys.Rev.* **D57** (1998) 512–526, `arXiv:hep-ph/9702216 [hep-ph]`.

[21] A. Shuvaev, K. J. Golec-Biernat, A. D. Martin, and M. Ryskin, "Off diagonal distributions fixed by diagonal partons at small x and ξ," *Phys.Rev.* **D60** (1999) 014015, `arXiv:hep-ph/9902410 [hep-ph]`.

[22] L. J. Lanzerotti *et al.*, "High-energy photoproduction of neutral rho mesons," *Phys. Rev. Lett.* **15** (Aug, 1965) 210–213. http://link.aps.org/doi/10.1103/PhysRevLett.15.210.

[23] T. Bauer, R. Spital, D. Yennie, and F. Pipkin, "The Hadronic Properties of the Photon in High-Energy Interactions," *Rev.Mod.Phys.* **50** (1978) 261.

[24] M. E. Binkley *et al.*, "J/ψ Photoproduction from 60 to 300 GeV$/c$," *Phys.Rev.Lett.* **48** (1982) 73.

[25] B. H. Denby *et al.*, "Inelastic and Elastic Photoproduction of J/ψ (3097)," *Phys.Rev.Lett.* **52** (1984) 795–798.

[26] **ZEUS** Collaboration, S. Chekanov *et al.*, "Exclusive photoproduction of J/ψ mesons at HERA," *Eur.Phys.J.* **C24** (2002) 345–360, `arXiv:hep-ex/0201043 [hep-ex]`.

[27] **H1** Collaboration, A. Aktas *et al.*, "Elastic J/ψ production at HERA," *Eur.Phys.J.* **C46** (2006) 585–603, `arXiv:hep-ex/0510016 [hep-ex]`.

[28] **H1** Collaboration, C. Alexa *et al.*, "Elastic and Proton-Dissociative Photoproduction of J/ψ Mesons at HERA," *Eur.Phys.J.* **C73** no. 6, (2013) 2466, `arXiv:1304.5162 [hep-ex]`.

[29] A. D. Martin, C. Nockles, M. G. Ryskin, and T. Teubner, "Small x gluon from exclusive J/ψ production," *Phys. Lett.* **B662** (2008) 252–258, `arXiv:0709.4406 [hep-ph]`.

[30] **LHCb** Collaboration, R. Aaij *et al.*, "Updated measurements of exclusive J/ψ and $\psi(2S)$ production cross-sections in pp collisions at $\sqrt{s} = 7$ TeV," *J.Phys.* **G41** (2014) 055002, `arXiv:1401.3288 [hep-ex]`.

[31] **CDF** Collaboration, T. Aaltonen *et al.*, "Observation of exclusive charmonium production and $\gamma\gamma \to \mu^+\mu^-$ in $p\bar{p}$ collisions at $\sqrt{s} = 1.96$ TeV," *Phys.Rev.Lett.* **102** (2009) 242001, `arXiv:0902.1271 [hep-ex]`.

[32] **PHENIX** Collaboration, S. Afanasiev *et al.*, "Photoproduction of J/ψ and of high mass e^+e^- in ultra-peripheral Au+Au collisions at $\sqrt{s_{NN}} = 200$ GeV," *Phys.Lett.* **B679** (2009) 321–329, `arXiv:0903.2041 [nucl-ex]`.

[33] N. Armesto, "Nuclear shadowing," *J. Phys.* **G32** (2006) R367–R394, `arXiv:hep-ph/0604108 [hep-ph]`.

[34] S. Klein and J. Nystrand, "Exclusive vector meson production in relativistic heavy ion collisions," *Phys.Rev.* **C60** (1999) 014903, `arXiv:hep-ph/9902259 [hep-ph]`. https://starlight.hepforge.org.

[35] R. Glauber, "Cross-sections in deuterium at high-energies," *Phys.Rev.* **100** (1955) 242–248.

[36] A. J. Baltz, Y. Gorbunov, S. R. Klein, and J. Nystrand, "Two-Photon Interactions with Nuclear Breakup in Relativistic Heavy Ion Collisions," *Phys.Rev.* **C80** (2009) 044902, `arXiv:0907.1214 [nucl-ex]`.

[37] A. H. Mueller, "Soft gluons in the infinite momentum wave function and the BFKL pomeron," *Nucl. Phys.* **B415** (1994) 373–385.

[38] N. N. Nikolaev and B. G. Zakharov, "Color transparency and scaling properties of nuclear shadowing in deep inelastic scattering," *Z. Phys.* **C49** (1991) 607–618.

[39] H. Kowalski, L. Motyka, and G. Watt, "Exclusive diffractive processes at HERA within the dipole picture," *Phys.Rev.* **D74** (2006) 074016, `arXiv:hep-ph/0606272 [hep-ph]`.

[40] S. Jones, A. Martin, M. Ryskin, and T. Teubner, "Probes of the small x gluon via exclusive J/ψ and Υ production at HERA and the LHC," *JHEP* **1311** (2013) 085, `arXiv:1307.7099`.

[41] J. Bartels, K. J. Golec-Biernat, and K. Peters, "On the dipole picture in the nonforward direction," *Acta Phys. Polon.* **B34** (2003) 3051–3068, `arXiv:hep-ph/0301192 [hep-ph]`.

[42] K. J. Golec-Biernat and M. Wusthoff, "Saturation effects in deep inelastic scattering at low Q^2 and its implications on diffraction," *Phys.Rev.* **D59** (1998) 014017, `arXiv:hep-ph/9807513 [hep-ph]`.

[43] K. J. Golec-Biernat and M. Wusthoff, "Saturation in diffractive deep inelastic scattering," *Phys.Rev.* **D60** (1999) 114023, `arXiv:hep-ph/9903358 [hep-ph]`.

[44] V. N. Gribov and L. N. Lipatov, "Deep inelastic e p scattering in perturbation theory," *Sov. J. Nucl. Phys.* **15** (1972) 438–450. [Yad. Fiz.15,781(1972)].

[45] Y. L. Dokshitzer, "Calculation of the Structure Functions for Deep Inelastic Scattering and e+ e- Annihilation by Perturbation Theory in Quantum Chromodynamics.," *Sov. Phys. JETP* **46** (1977) 641–653. [Zh. Eksp. Teor. Fiz.73,1216(1977)].

[46] G. Altarelli and G. Parisi, "Asymptotic Freedom in Parton Language," *Nucl. Phys.* **B126** (1977) 298.

[47] J. Abelleira Fernandez *et al.*, "A Large Hadron Electron Collider at CERN," `arXiv:1211.4831 [hep-ex]`.

[48] A. Adeluyi and C. Bertulani, "Constraining Gluon Shadowing Using Photoproduction in Ultraperipheral *pA* and *AA* Collisions," *Phys.Rev.* **C85** (2012) 044904, `arXiv:1201.0146 [nucl-th]`.

[49] K. J. Eskola, H. Paukkunen, and C. A. Salgado, "An Improved global analysis of nuclear parton distribution functions including RHIC data," *JHEP* **0807** (2008) 102, `arXiv:0802.0139 [hep-ph]`.

[50] K. Eskola, H. Paukkunen, and C. Salgado, "EPS09: A New Generation of NLO and LO Nuclear Parton Distribution Functions," *JHEP* **0904** (2009) 065, `arXiv:0902.4154 [hep-ph]`.

[51] M. Hirai, S. Kumano, and T.-H. Nagai, "Determination of nuclear parton distribution functions and their uncertainties in next-to-leading order," *Phys.Rev.* **C76** (2007) 065207, `arXiv:0709.3038 [hep-ph]`.

[52] A. Martin, W. Stirling, R. Thorne, and G. Watt, "Parton distributions for the LHC," *Eur.Phys.J.* **C63** (2009) 189–285, `arXiv:0901.0002 [hep-ph]`.

[53] V. Rebyakova, M. Strikman, and M. Zhalov, "Coherent ρ and J/ψ photoproduction in ultraperipheral processes with electromagnetic dissociation of heavy ions at RHIC and LHC," *Phys.Lett.* **B710** (2012) 647–653, `arXiv:1109.0737 [hep-ph]`.

[54] L. Frankfurt and M. Strikman, "Diffraction at HERA, color opacity and nuclear shadowing," *Eur. Phys. J.* **A5** (1999) 293–306, `arXiv:hep-ph/9812322 [hep-ph]`.

[55] L. Frankfurt, V. Guzey, and M. Strikman, "Leading Twist Nuclear Shadowing Phenomena in Hard Processes with Nuclei," *Phys. Rept.* **512** (2012) 255–393, `arXiv:1106.2091 [hep-ph]`.

[56] V. Guzey, M. Strikman, and M. Zhalov, "Disentangling coherent and incoherent quasielastic J/ψ photoproduction on nuclei by neutron tagging in ultraperipheral ion collisions at the LHC," *Eur.Phys.J.* **C74** no. 7, (2014) 2942, `arXiv:1312.6486 [hep-ph]`.

[57] **ALICE** Collaboration, E. Abbas *et al.*, "Charmonium and e^+e^- pair photoproduction at mid-rapidity in ultra-peripheral Pb-Pb collisions at $\sqrt{s_{\rm NN}}$=2.76 TeV," *Eur.Phys.J.* **C73** no. 11, (2013) 2617, `arXiv:1305.1467 [nucl-ex]`.

[58] J. Pumplin *et al.*, "New generation of parton distributions with uncertainties from global QCD analysis," *JHEP* **07** (2002) 012, `arXiv:hep-ph/0201195 [hep-ph]`.

[59] V. Goncalves and M. Machado, "Vector Meson Production in Coherent Hadronic Interactions: An update on predictions for RHIC and LHC," *Phys.Rev.* **C84** (2011) 011902, `arXiv:1106.3036 [hep-ph]`.

[60] N. Armesto, "A Simple model for nuclear structure functions at small x in the dipole picture," *Eur.Phys.J.* **C26** (2002) 35–43, `arXiv:hep-ph/0206017 [hep-ph]`.

[61] E. Iancu, K. Itakura, and S. Munier, "Saturation and BFKL dynamics in the HERA data at small x," *Phys.Lett.* **B590** (2004) 199–208, `arXiv:hep-ph/0310338 [hep-ph]`.

[62] R. Venugopalan, "The Color glass condensate: A Summary of key ideas and recent developments," in *INFN Eloisatron Project 44th Workshop on QCD at Cosmic Energies: The Highest Energy Cosmic Rays and QCD Erice, Italy, August 29-September 5, 2004.* 2004. `arXiv:hep-ph/0412396 [hep-ph]`.

[63] A. Cisek, W. Schafer, and A. Szczurek, "Exclusive coherent production of heavy vector mesons in nucleus-nucleus collisions at LHC," *Phys.Rev.* **C86** (2012) 014905, `arXiv:1204.5381 [hep-ph]`.

[64] I. Balitsky, "Operator expansion for high-energy scattering," *Nucl. Phys.* **B463** (1996) 99–160, `arXiv:hep-ph/9509348 [hep-ph]`.

[65] Y. V. Kovchegov, "Small-x F_2 structure function of a nucleus including multiple pomeron exchanges," *Phys. Rev.* **D60** (1999) 034008, `arXiv:hep-ph/9901281 [hep-ph]`.

[66] T. Lappi and H. Mantysaari, "J/ψ production in ultraperipheral Pb+Pb and p+Pb collisions at energies available at the CERN Large Hadron Collider," *Phys.Rev.* **C87** no. 3, (2013) 032201, `arXiv:1301.4095 [hep-ph]`.

[67] H. Kowalski and D. Teaney, "An Impact parameter dipole saturation model," *Phys.Rev.* **D68** (2003) 114005, `arXiv:hep-ph/0304189 [hep-ph]`.

[68] N. Armesto and A. H. Rezaeian, "Exclusive vector meson production at high energies and gluon saturation," *Phys.Rev.* **D90** no. 5, (2014) 054003, `arXiv:1402.4831 [hep-ph]`.

[69] V. Guzey, E. Kryshen, and M. Zhalov, "Coherent photoproduction of vector mesons in heavy ion ultraperipheral collisions: update for Run 2 at the LHC," `arXiv:1602.01456 [nucl-th]`.

[70] M. Klusek-Gawenda, P. Lebiedowicz, and A. Szczurek, "Light-by-light scattering in ultraperipheral PbPb collisions at the Large Hadron Collider," *Phys. Rev.* **C93** no. 4, (2016) 044907, `arXiv:1601.07001 [nucl-th]`.

[71] S. C. Ahern, J. W. Norbury, and W. J. Poyser, "Graviton production in relativistic heavy ion collisions," *Phys. Rev.* **D62** (2000) 116001, `arXiv:gr-qc/0009059 [gr-qc]`.

[72] L. Evans and P. Bryant, "LHC Machine," *JINST* **3** (2008) S08001.

[73] **ALICE** Collaboration, K. Aamodt *et al.*, "The ALICE experiment at the CERN LHC," *JINST* **3** (2008) S08002.

[74] **ALICE** Collaboration, B. B. Abelev *et al.*, "Performance of the ALICE Experiment at the CERN LHC," *Int.J.Mod.Phys.* **A29** (2014) 1430044, `arXiv:1402.4476 [nucl-ex]`.

[75] A. Akindinov *et al.*, "A topological trigger based on the time-of-flight detector for the ALICE experiment," *Nuclear Instruments and Methods in Physics Research Section A: Accelerators, Spectrometers, Detectors and Associated Equipment* **602** no. 2, (2009) 372 – 376. http://www.sciencedirect.com/science/article/pii/S0168900208018093.

[76] R. Brun and F. Rademakers, "ROOT: An object oriented data analysis framework," *Nucl. Instrum. Meth.* **A389** (1997) 81–86. http://root.cern.ch/.

[77] R. Brun *et al.*, *GEANT: detector description and simulation tool; March 1994*. CERN Program Library. CERN, Geneva, 1993. http://cds.cern.ch/record/1073159. Long Writeup W5013.

[78] I. Foster and C. Kesselman, *The Grid 2: Blueprint for a New Computing Infrastructure*. Morgan Kaufmann Publishers Inc., San Francisco, CA, USA, 2003.

[79] **ALICE** Collaboration, P. Cortese, F. Carminati, C. W. Fabjan, L. Riccati, and H. de Groot, *ALICE computing: Technical Design Report*. Technical Design Report ALICE. CERN, Geneva, 2005. http://cds.cern.ch/record/832753. Submitted on 15 Jun 2005.

[80] **Particle Data Group** Collaboration, K. Olive *et al.*, "Review of Particle Physics," *Chin.Phys.* **C38** (2014) 090001.

[81] L. Aphecetche *et al.*, "Luminosity determination for the $J/\psi \to \mu^+\mu^-$ analysis in p+p interactions at $\sqrt{s}$=7 TeV,". https://cds.cern.ch/record/1388921.

[82] S. van der Meer, "Calibration of the effective beam height in the ISR," Tech. Rep. CERN-ISR-PO-68-31. ISR-PO-68-31, CERN, Geneva, 1968. https://cds.cern.ch/record/296752.

[83] **ALICE** Collaboration, B. B. Abelev *et al.*, "Measurement of visible cross sections in proton-lead collisions at $\sqrt{s_{\rm NN}}$ = 5.02 TeV in van der Meer scans with the ALICE detector," *JINST* **9** no. 11, (2014) P11003, `arXiv:1405.1849 [nucl-ex]`.

[84] L. Frankfurt, V. Guzey, M. Strikman, and M. Zhalov, "Onset of perturbative color opacity at small x and Υ coherent photoproduction off heavy nuclei at LHC," *JHEP* **0308** (2003) 043, `arXiv:hep-ph/0304218 [hep-ph]`.

[85] C. A. Salgado *et al.*, "Proton-Nucleus Collisions at the LHC: Scientific Opportunities and Requirements," *J. Phys.* **G39** (2012) 015010, `arXiv:1105.3919 [hep-ph]`.

[86] **European Muon** Collaboration, J. J. Aubert *et al.*, "The ratio of the nucleon structure functions F_2^N for iron and deuterium," *Phys. Lett.* **B123** (1983) 275.

[87] **STAR** Collaboration, B. I. Abelev *et al.*, "ρ_0 photoproduction in ultraperipheral relativistic heavy ion collisions at $\sqrt{s_{\rm NN}}$=200 GeV," *Phys. Rev.* **C77** (2008) 034910, `arXiv:0712.3320 [nucl-ex]`.

[88] **STAR** Collaboration, C. Adler *et al.*, "Coherent ρ_0 production in ultraperipheral heavy ion collisions," *Phys. Rev. Lett.* **89** (2002) 272302, `arXiv:nucl-ex/0206004 [nucl-ex]`.

[89] **STAR** Collaboration, G. Agakishiev *et al.*, "ρ^0 Photoproduction in AuAu Collisions at $\sqrt{s_{NN}}$ = 62.4 GeV measured with the STAR detector," *Phys. Rev.* **C85** (2012) 014910, `arXiv:1107.4630 [nucl-ex]`.

[90] **ALICE** Collaboration, K. Oyama, "Reference cross section measurements with ALICE in pp and Pb-Pb collisions at LHC," in *LHC Lumi Days 2012 Geneva,*

Switzerland, February 29-March 1, 2012. 2013. arXiv:1305.7044 [nucl-ex]. http://inspirehep.net/record/1236193/files/arXiv:1305.7044.pdf.

[91] J. Gaiser, *Charmonium Spectroscopy From Radiative Decays of the J/ψ and ψ'*. PhD thesis, SLAC, 1982. www.slac.stanford.edu/cgi-wrap/getdoc/slac-r-255.pdf.

[92] W. Verkerke and D. P. Kirkby, "The RooFit toolkit for data modeling," *eConf* **C0303241** (2003) MOLT007, arXiv:physics/0306116 [physics].

[93] V. Guzey, E. Kryshen, M. Strikman, and M. Zhalov, "Evidence for nuclear gluon shadowing from the ALICE measurements of PbPb ultraperipheral exclusive J/ψ production," *Phys.Lett.* **B726** (2013) 290–295, arXiv:1305.1724 [hep-ph].

[94] W.-T. Deng, X.-N. Wang, and R. Xu, "Gluon shadowing and hadron production in heavy-ion collisions at LHC," *Phys. Lett.* **B701** (2011) 133–136, arXiv:1011.5907 [nucl-th].

[95] **CMS** Collaboration, "Photoproduction of the coherent J/ψ accompanied by the forward neutron emission in ultra-peripheral PbPb collisions at 2.76 TeV," Tech. Rep. CMS-PAS-HIN-12-009, CERN, Geneva, 2014. http://cds.cern.ch/record/1971267.

[96] A. H. Mueller, "Small-x Behavior and Parton Saturation: A QCD Model," *Nucl.Phys.* **B335** (1990) 115.

[97] E. Iancu, "QCD in heavy ion collisions," in *Proceedings, 2011 European School of High-Energy Physics (ESHEP 2011)*, pp. 197–266. 2014. arXiv:1205.0579 [hep-ph]. http://inspirehep.net/record/1113441/files/arXiv:1205.0579.pdf.

[98] L. N. Lipatov, "Reggeization of the Vector Meson and the Vacuum Singularity in Nonabelian Gauge Theories," *Sov. J. Nucl. Phys.* **23** (1976) 338–345. [Yad. Fiz.23,642(1976)].

[99] E. A. Kuraev, L. N. Lipatov, and V. S. Fadin, "The Pomeranchuk Singularity in Nonabelian Gauge Theories," *Sov. Phys. JETP* **45** (1977) 199–204. [Zh. Eksp. Teor. Fiz.72,377(1977)].

[100] I. I. Balitsky and L. N. Lipatov, "The Pomeranchuk Singularity in Quantum Chromodynamics," *Sov. J. Nucl. Phys.* **28** (1978) 822–829. [Yad. Fiz.28,1597(1978)].

[101] A. Accardi *et al.*, "Electron Ion Collider: The Next QCD Frontier - Understanding the glue that binds us all," arXiv:1212.1701 [nucl-ex].

[102] A. Dainese *et al.*, "Heavy ions at the Future Circular Collider," arXiv:1605.01389 [hep-ph].

[103] T. Sjostrand, "High-energy physics event generation with PYTHIA 5.7 and JETSET 7.4," *Comput. Phys. Commun.* **82** (1994) 74–90.

[104] J. Nystrand. Personal communication.

[105] S. P. Baranov, O. Duenger, H. Shooshtari, and J. A. M. Vermaseren, "LPAIR: A generator for lepton pair production," in *In *Hamburg 1991, Proceedings, Physics at HERA, vol. 3* 1478-1482. (see HIGH ENERGY PHYSICS INDEX 30 (1992) No. 12988)*. 1991.

[106] *1974 CERN School of Computing, Godoysund, Norway, 11-24 Aug 1974: Proceedings*. 1974. http://www.slac.stanford.edu/spires/find/books/www?cl=QA76:C2:1974.

[107] **Particle Data Group** Collaboration, J. Beringer *et al.*, "Review of Particle Physics (RPP)," *Phys. Rev.* **D86** (2012) 010001.

[108] **ALICE** Collaboration, K. Aamodt *et al.*, "Rapidity and transverse momentum dependence of inclusive J/ψ production in pp collisions at $\sqrt{s} = 7$ TeV," *Phys. Lett.* **B704** (2011) 442–455, `arXiv:1105.0380 [hep-ex]`. [Erratum: Phys. Lett.B718,692(2012)].

[109] **ALICE** Collaboration, B. B. Abelev *et al.*, "J/ψ production and nuclear effects in p-Pb collisions at $\sqrt{S_{NN}}$ = 5.02 TeV," *JHEP* **02** (2014) 073, `arXiv:1308.6726 [nucl-ex]`.

Appendix A

Lists of runs

Numbers of runs used in the presented analyses are given in this Appendix.

A.1 List of runs for coherent J/ψ in the forward Pb-Pb UPC

The list of runs selected in LHC11h period is following: (130 runs)

170593, 170572, 170390, 170389, 170388, 170387, 170313, 170312, 170311, 170309, 170308, 170306, 170270, 170269, 170268, 170230, 170228, 170207, 170204, 170203, 170193, 170163, 170159, 170155, 170091, 170089, 170088, 170085, 170084, 170083, 170081, 170040, 170036, 170027, 169969, 169965, 169859, 169858, 169855, 169846, 169838, 169837, 169835, 169590, 169588, 169587, 169586, 169557, 169555, 169554, 169553, 169550, 169515, 169512, 169506, 169504, 169498, 169475, 169420, 169419, 169418, 169417, 169415, 169411, 169238, 169236, 169167, 169160, 169156, 169148, 169145, 169144, 169138, 169099, 169094, 169091, 169045, 169044, 169040, 169035, 168992, 168826, 168777, 168514, 168512, 168511, 168467, 168464, 168461, 168460, 168458, 168362, 168361, 168342, 168341, 168325, 168322, 168318, 168311, 168310, 168213, 168212, 168208, 168207, 168206, 168205, 168203, 168181, 168175, 168173, 168172, 168115, 168108, 168107, 168076, 168069, 168066, 167988, 167987, 167986, 167985, 167921, 167920, 167915, 167818, 167814, 167813, 167808, 167807, 167806.

A.2 Lists of runs for exclusive J/ψ in p-Pb UPC

A.2.1 Runs selected at forward rapidity

Runs selected for LHC13d period are: (20 runs)

195873, 195872, 195871, 195869, 195867, 195831, 195830, 195829, 195827, 195826, 195787, 195783, 195767, 195765, 195760, 195727, 195726, 195725, 195724, 195682.

Runs selected for LHC13e period are: (25 runs)

196310, 196309, 196308, 196214, 196201, 196200, 196199, 196194, 196187, 196185, 196107, 196105, 196091, 196090, 196089, 196085, 196006, 196000, 195994, 195989, 195958, 195955, 195954, 195950, 195949.

Runs selected for LHC13f period are: (64 runs)

197089, 197011, 197003, 196974, 196973, 196972, 196965, 196876, 196869, 196774, 196773, 196772, 196722, 196721, 196720, 196702, 196701, 196648, 196646, 196608, 196605, 196601, 196568, 196566, 196564, 196563, 196535, 196528, 196477, 196475, 196474, 197388, 197387, 197386, 197349, 197348, 197342, 197341, 197302, 197299, 197298, 197258, 197256, 197255, 197254, 197247, 197189, 197184, 197153, 197152, 197150, 197148, 197147, 197145, 197144, 197143, 197142, 197139, 197138, 197099, 197098, 197092, 197091, 197089.

A.2.2 Runs selected at semi-forward rapidity

Runs selected for LHC13d period are: (15 runs)

195760, 195765, 195767, 195783, 195787, 195826, 195827, 195829, 195830, 195831, 195867, 195869, 195871, 195872, 195873.

Runs selected for LHC13e period are: (24 runs)

195949, 195950, 195954, 195955, 195958, 195994, 196000, 196006, 196085, 196089, 196090, 196091, 196105, 196107, 196185, 196187, 196194, 196199, 196200, 196201, 196214, 196308, 196309, 196310.

Runs selected for LHC13f period are: (62 runs)

196474, 196475, 196477, 196528, 196535, 196563, 196564, 196566, 196568, 196601, 196605, 196608, 196646, 196648, 196701, 196702, 196720, 196721, 196722, 196772, 196773, 196774, 196869, 196876, 196965, 196972, 196973, 196974, 197003, 197011, 197089, 197091, 197092, 197098, 197099, 197138, 197139, 197142, 197143, 197144, 197145, 197147, 197148, 197150, 197152, 197153, 197184, 197189, 197247, 197254, 197255, 197256, 197258, 197298, 197299, 197302, 197341, 197342, 197348, 197386, 197387, 197388.

A.2.3 Runs selected at mid-rapidity

Runs selected for LHC13e period are: (29 runs)

195935, 195949, 195950, 195954, 195955, 195958, 195994, 196000, 196006, 196085, 196089, 196090, 196091, 196099, 196105, 196107, 196185, 196187, 196194, 196197, 196199, 196200, 196201, 196203, 196208, 196214, 196308, 196309, 196310.

Runs selected for LHC13f period are: (78 runs)

196474, 196475, 196477, 196528, 196535, 196563, 196564, 196566, 196568, 196601, 196605, 196608, 196646, 196648, 196701, 196702, 196706, 196714, 196720, 196721, 196722, 196772, 196773, 196774, 196869, 196870, 196874, 196876, 196965, 196967, 196972, 196973, 196974, 197003, 197011, 197012, 197015, 197027, 197031, 197089, 197091, 197092, 197094, 197098, 197099, 197138, 197139, 197142, 197143, 197144, 197145, 197147, 197148, 197149, 197150, 197152, 197153, 197184, 197189, 197247, 197254, 197255, 197256, 197258, 197260, 197296, 197297, 197298, 197299, 197300, 197302, 197341, 197342, 197348, 197351, 197386, 197387, 197388.

Appendix B

Plots of time dependence of efficiency

Aim of this appendix is to give the plots of efficiency as a function of run number, which is a measure of the actual efficiency over the period of the data taking. The stability of operation of the detector is manifested by the flatness of the dependency.

B.1 Efficiency of coherent and incoherent J/ψ and $\gamma\gamma \rightarrow \mu^+\mu^-$ in Pb-Pb

The run-by-run efficiency of coherent and incoherent J/ψ, $(\mathrm{Acc} \times \varepsilon)_{J/\psi}$ and $(\mathrm{Acc} \times \varepsilon)^{\mathrm{inc}}_{J/\psi}$, and two-photon production $(\mathrm{Acc} \times \varepsilon)_{\gamma\gamma}$ is shown in this section.

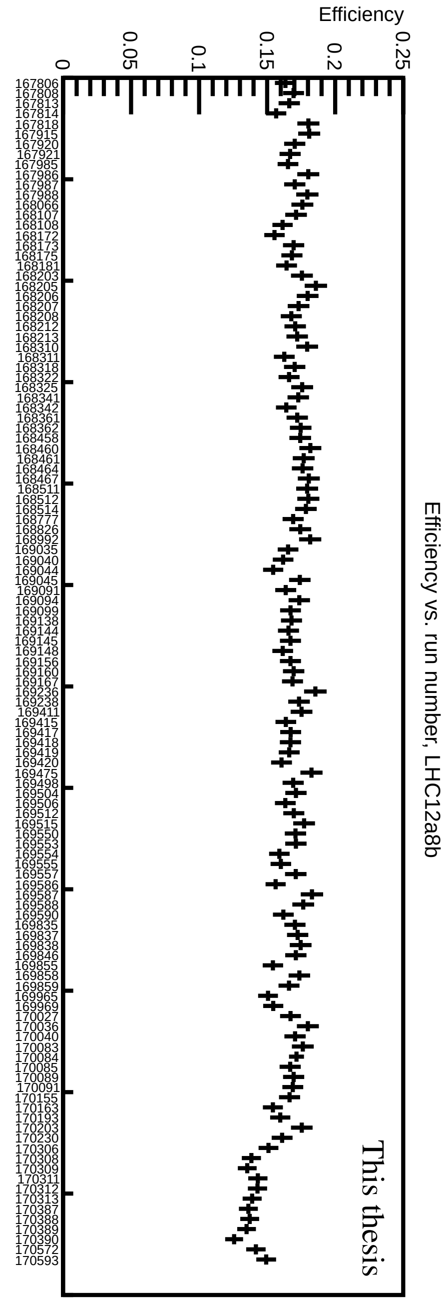

(a)

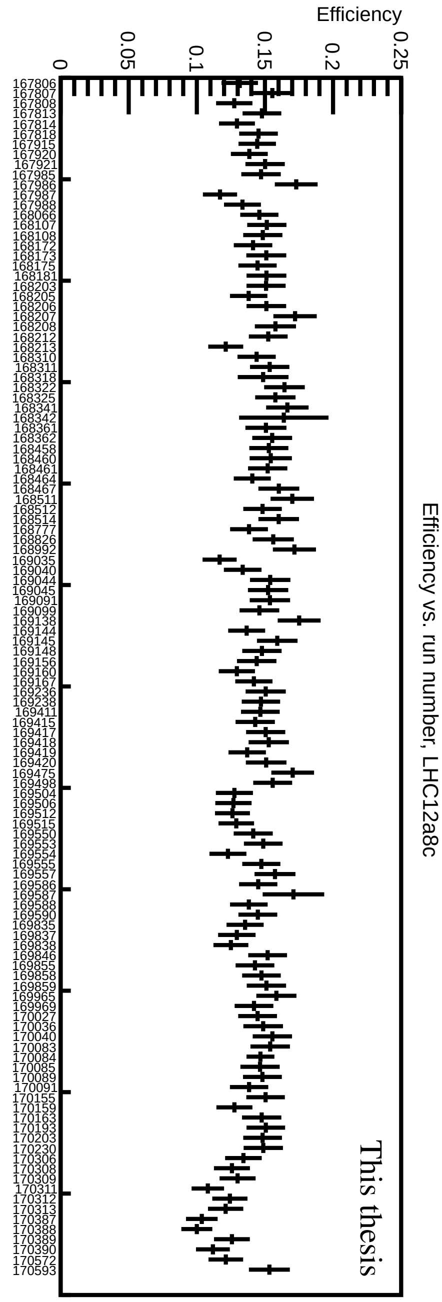

(b)

Fig. B.1 Acceptance and efficiency of coherent J/ψ (a) and incoherent J/ψ (b) as a function of run number.

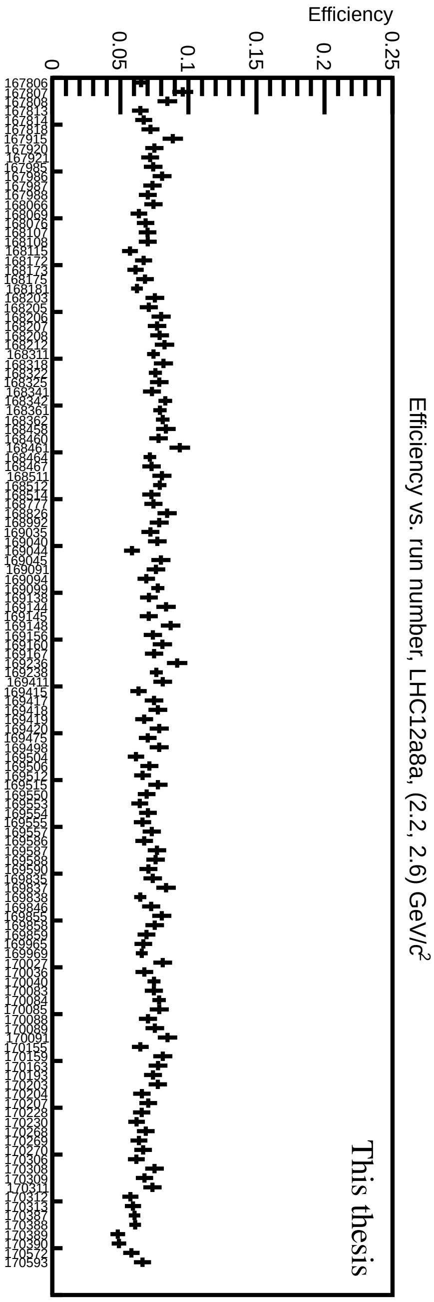

(a)

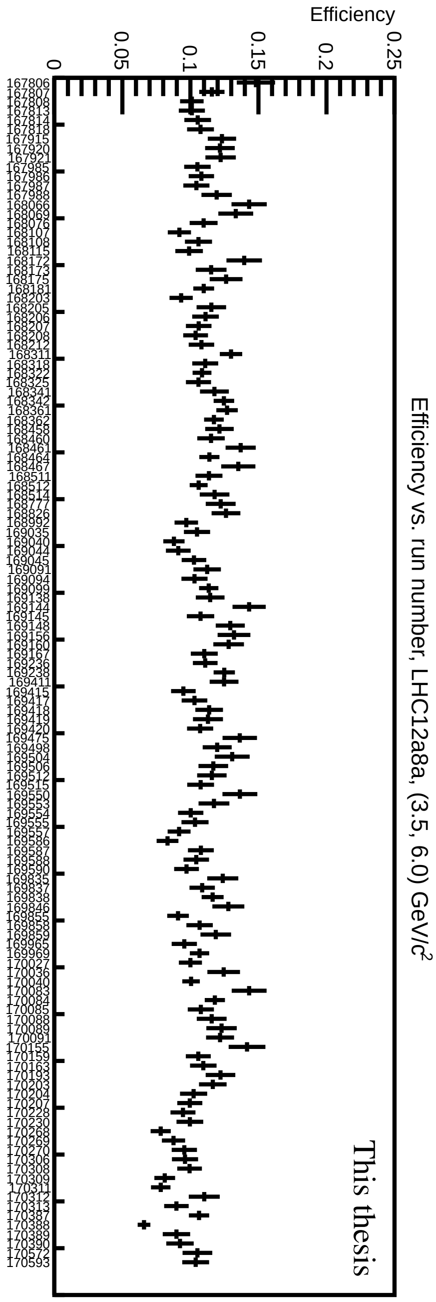

(b)

Fig. B.2 Acceptance and efficiency of $\gamma\gamma \to \mu^+\mu^-$ in the lower mass interval (a) and the higher mass interval (b).

B.2 Efficiency of exclusive J/ψ in p-Pb

This section gives plots of acceptance and efficiency $(\mathrm{Acc} \times \varepsilon)_{J/\psi}$ vs. run number of exclusive J/ψ in $\gamma\mathrm{p} \rightarrow J/\psi\,\mathrm{p}$ at forward rapidity, semi-forward rapidity and at mid-rapidity.

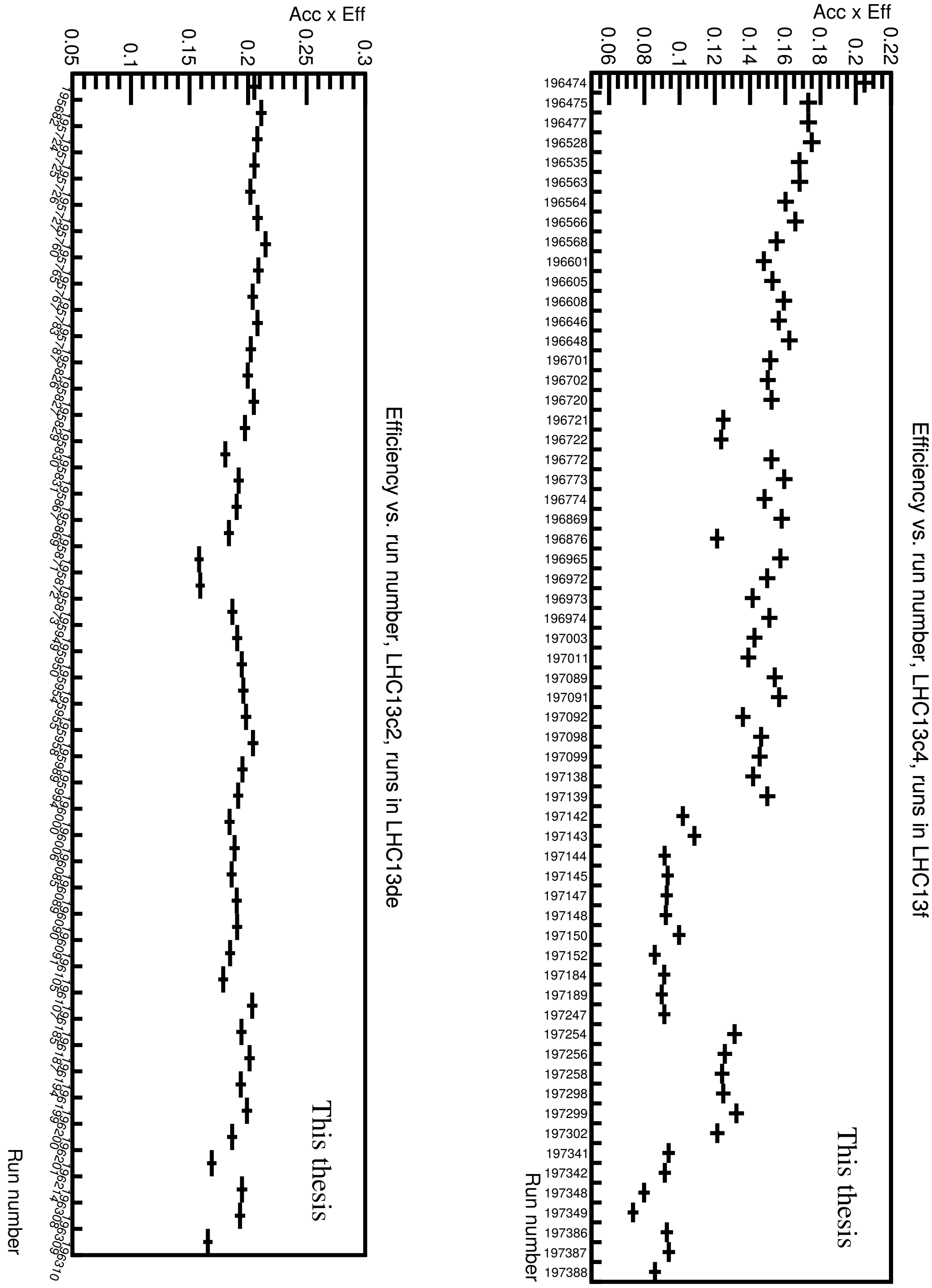

(a) (b)

Fig. B.3 Acceptance and efficiency of exclusive J/ψ at forward rapidity in p-Pb (a) and Pb-p (b).

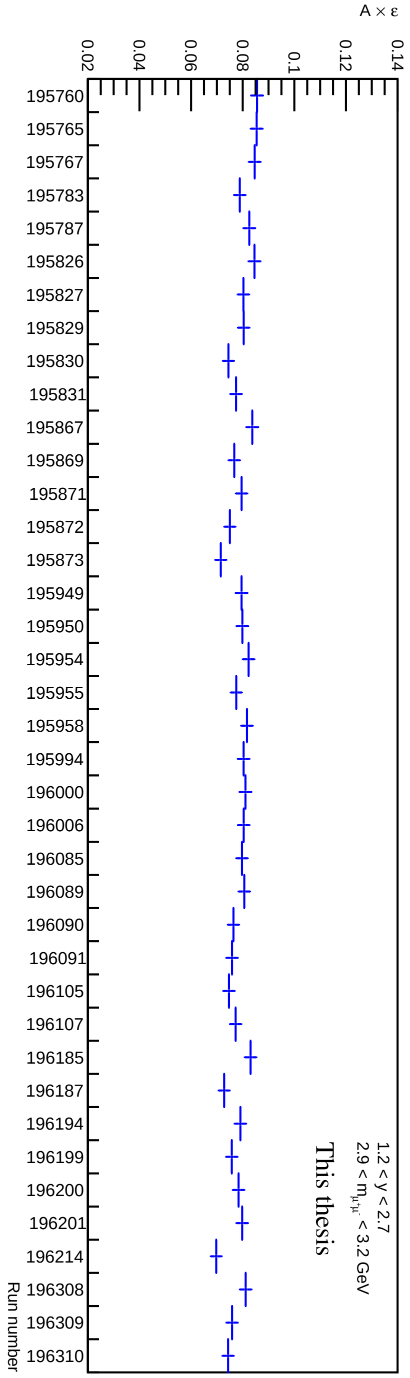

(a)

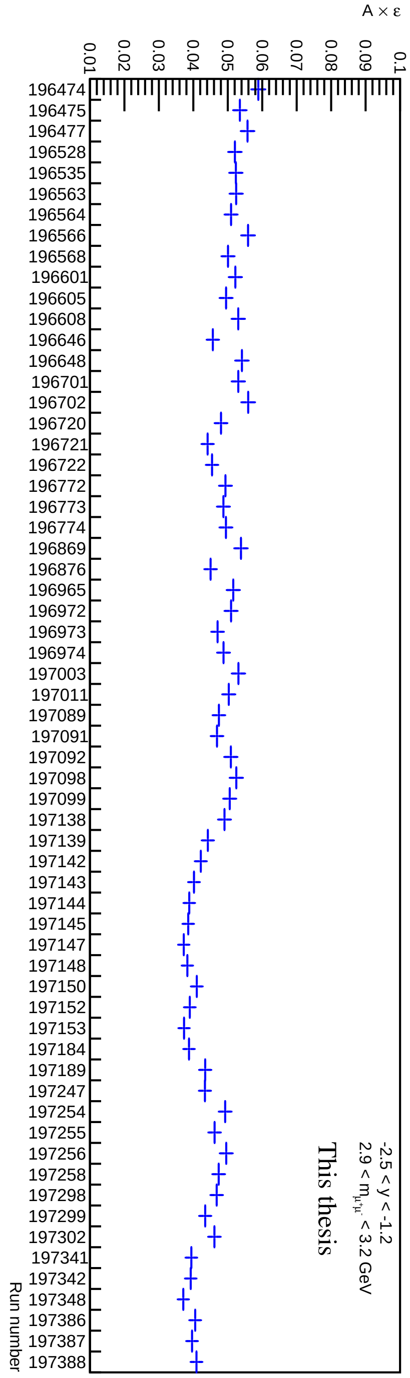

(b)

Fig. B.4 Acceptance and efficiency of exclusive J/ψ at semi-forward rapidity in p-Pb (a) and Pb-p (b).

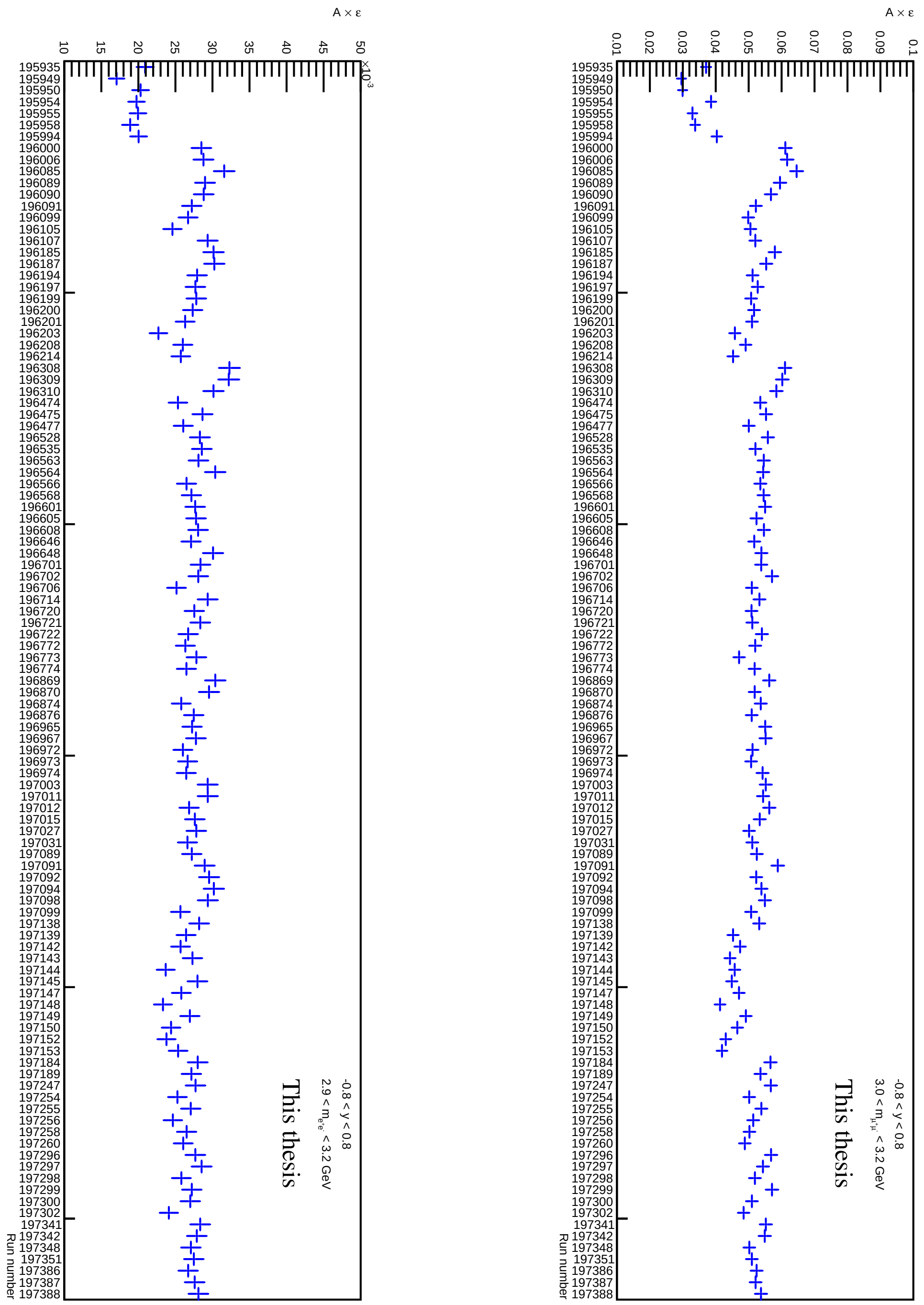

(a) (b)

Fig. B.5 Acceptance and efficiency of exclusive J/ψ at mid-rapidity in the dielectron channel (a) and in the dimuon channel (b).

Appendix C

Technical plots of selected J/ψ candidates

Aim of this appendix is to provide characteristics of the data and corresponding MC distributions, scaled to the data. Good description of the data by the MC is tested by simultaneous plots of the data and the MC.

C.1 Semi-forward rapidity

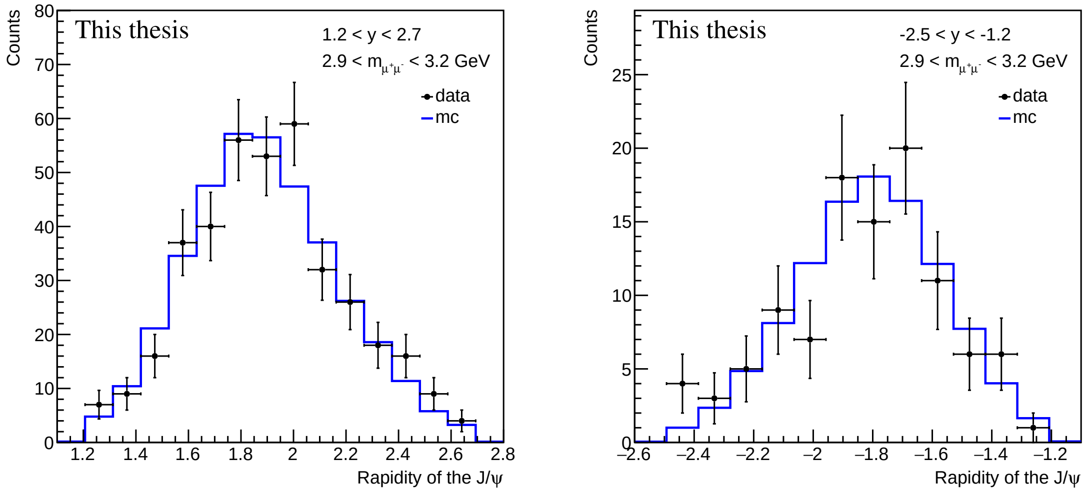

Fig. C.1 Distributions of rapidity of the J/ψ candidates for semi-forward p-Pb (left) and Pb-p (right).

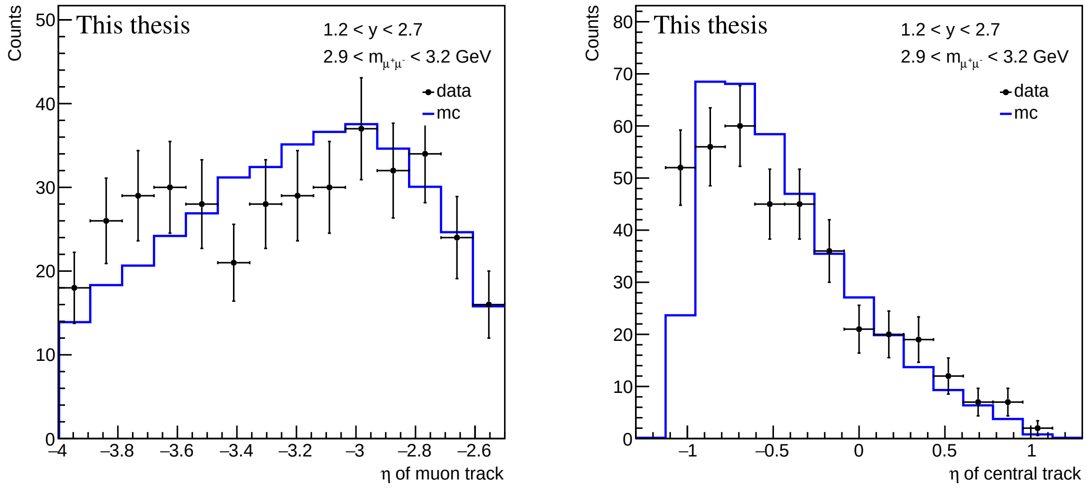

Fig. C.2 Pseudorapidity η distributions of muon (left) and central (right) tracks forming the semi-forward J/ψ candidates in p-Pb.

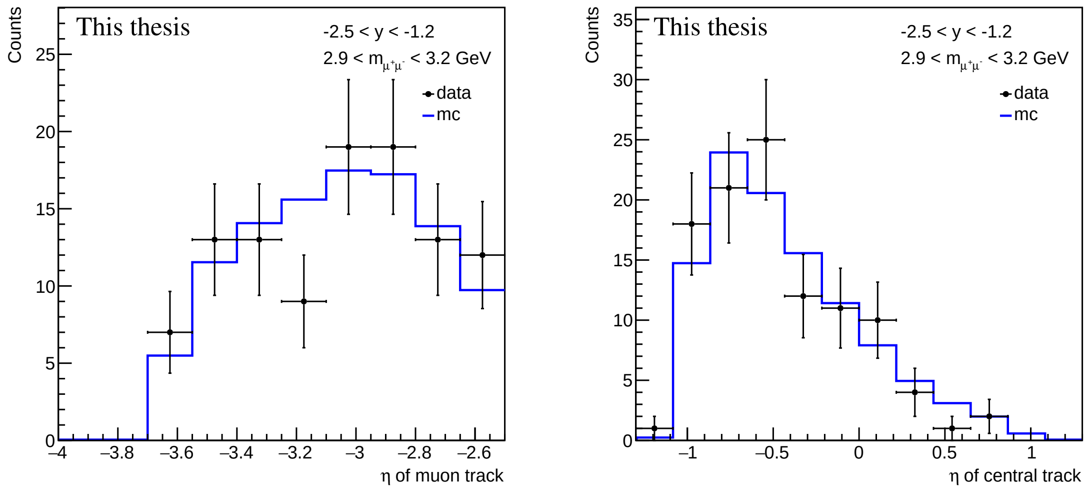

Fig. C.3 Pseudorapidity η distributions of muon (left) and central (right) tracks forming the semi-forward J/ψ candidates in Pb-p.

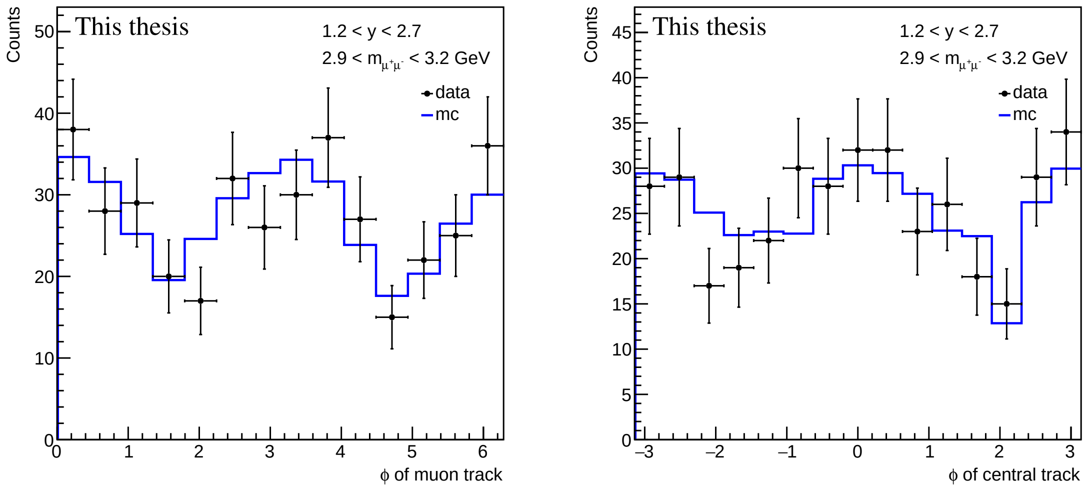

Fig. C.4 Azimuthal angle ϕ distributions of muon (left) and central (right) tracks forming the semi-forward J/ψ candidates in p-Pb.

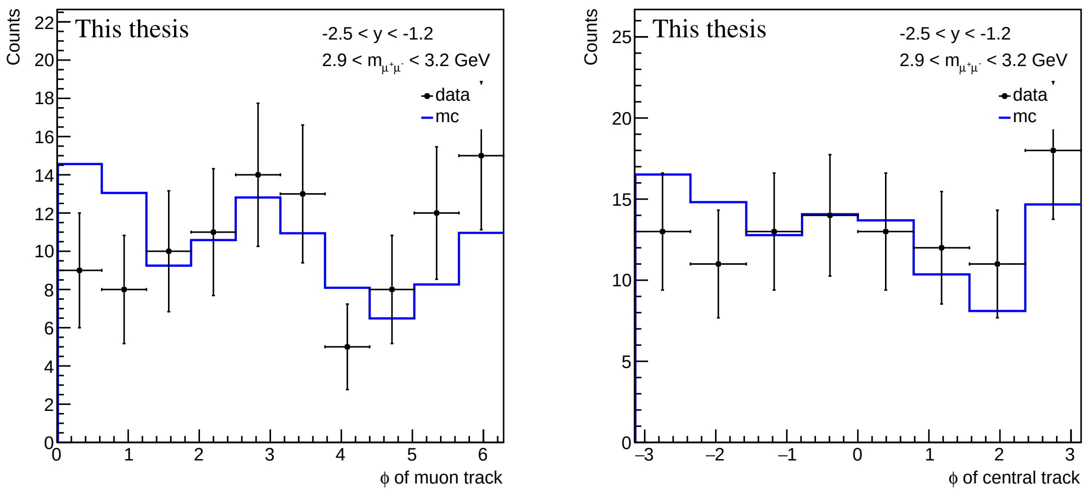

Fig. C.5 Azimuthal angle ϕ distributions of muon (left) and central (right) tracks forming the semi-forward J/ψ candidates in Pb-p.

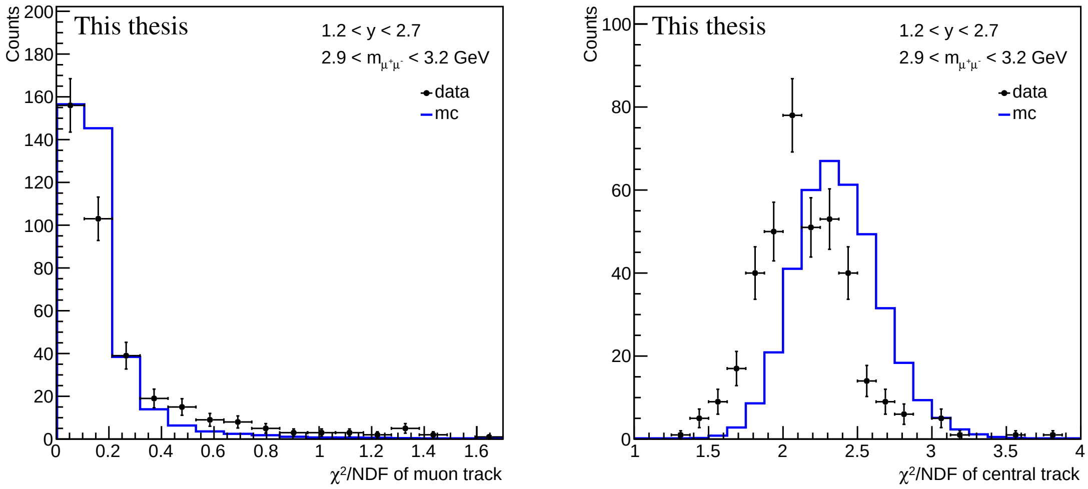

Fig. C.6 Distributions of χ^2/NDF for muon (left) and central (right) tracks in p-Pb.

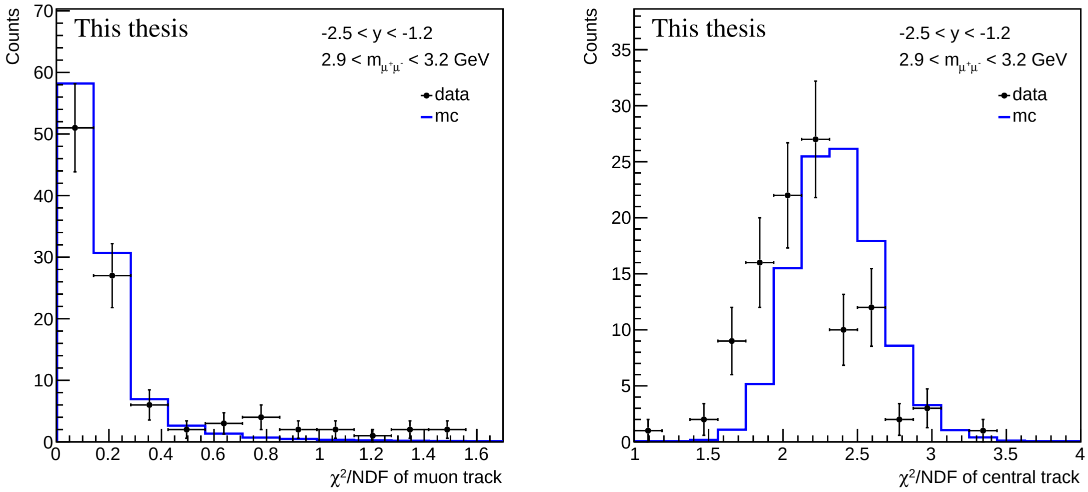

Fig. C.7 Distributions of χ^2/NDF for muon (left) and central (right) tracks in Pb-p.

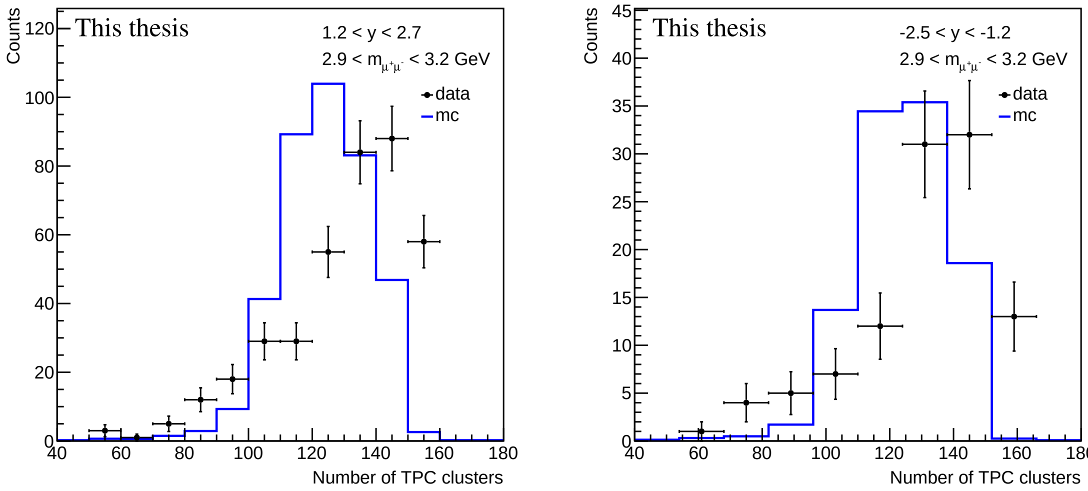

Fig. C.8 Number of space points (clusters) in TPC for central tracks in p-Pb (left) and Pb-p (right).

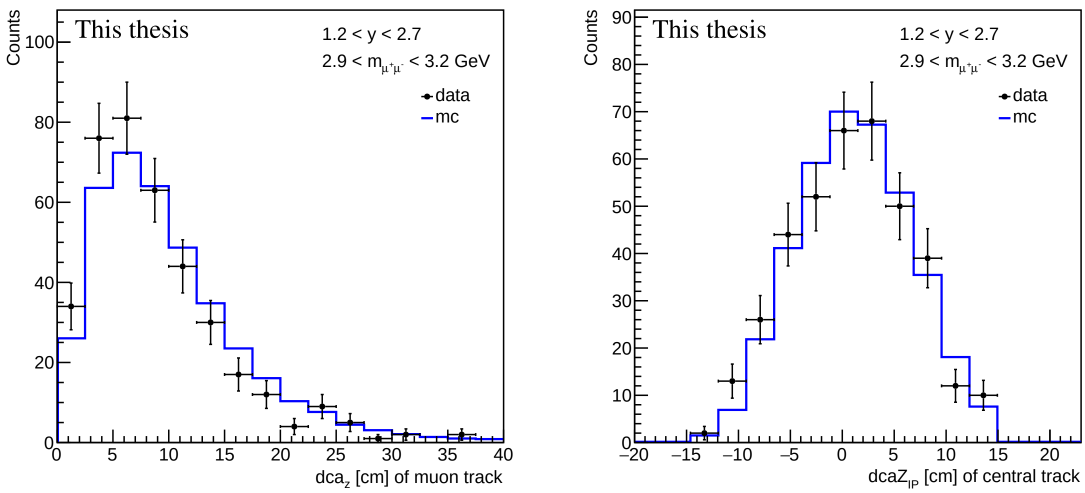

Fig. C.9 DCA along the beam direction for muon (left) and central (right) tracks in p-Pb. In the case of central tracks the DCA_Z is taken with respect to the nominal interaction point (IP) at the origin of the coordinates (0,0,0).

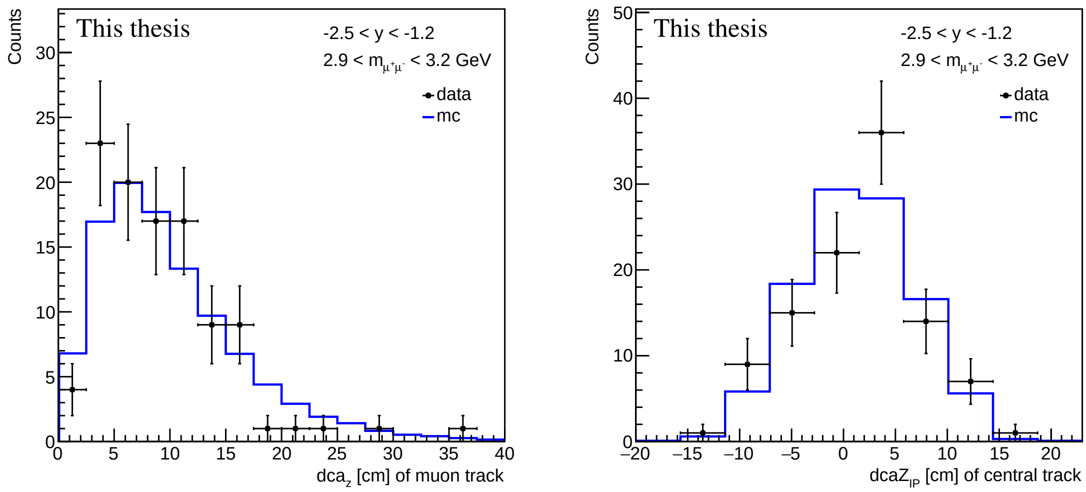

Fig. C.10 DCA along the beam direction for muon (left) and central (right) tracks in Pb-p. In the case of central tracks the DCA_Z is taken with respect to the nominal interaction point (IP) at the origin of the coordinates (0,0,0).

C.2 Mid-rapidity

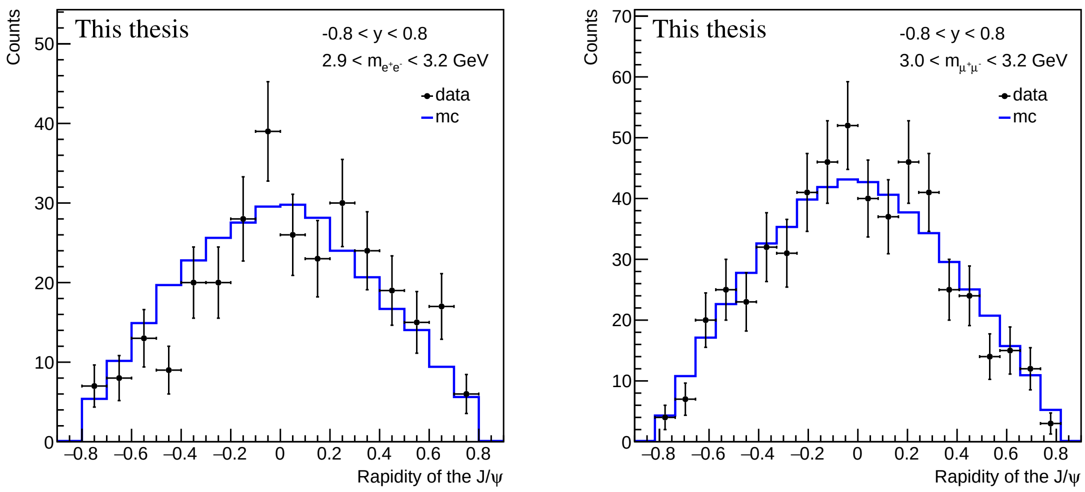

Fig. C.11 Distributions of rapidity of the J/ψ candidates for mid-rapidity dielectron channel (left) and dimuon channel (right).

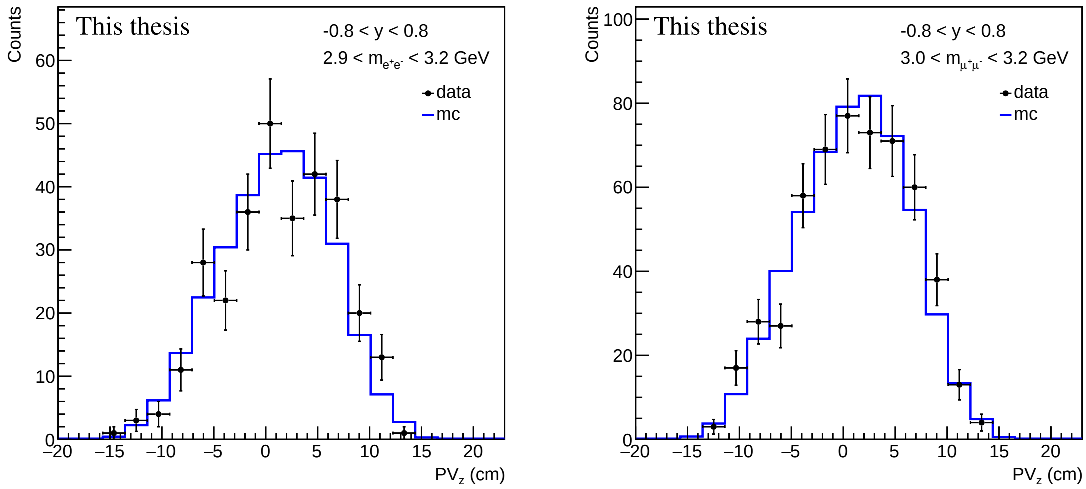

Fig. C.12 Position of the primary vertex along the beam direction in the dielectron channel (left) and dimuon channel (right).

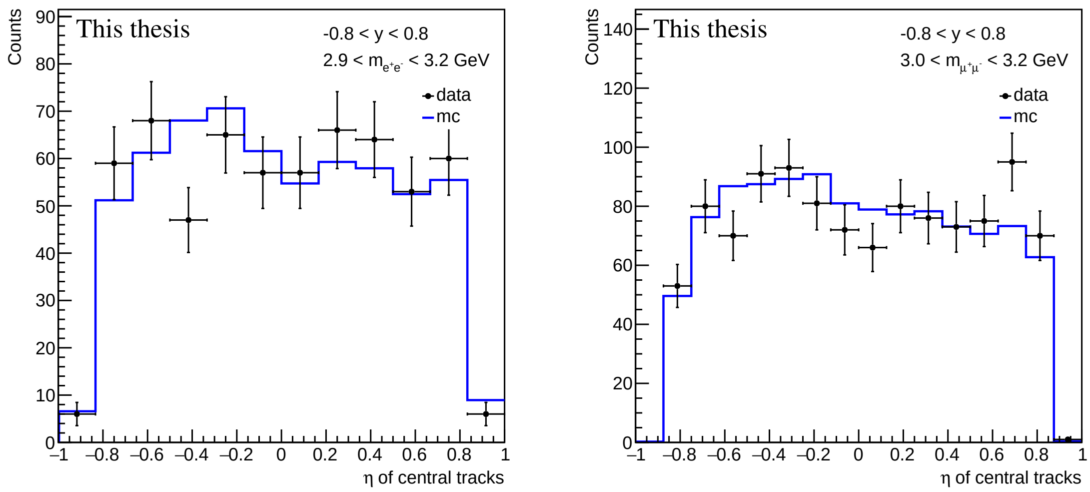

Fig. C.13 Pseudorapidity η distributions of the tracks in the dielectron channel (left) and dimuon channel (right).

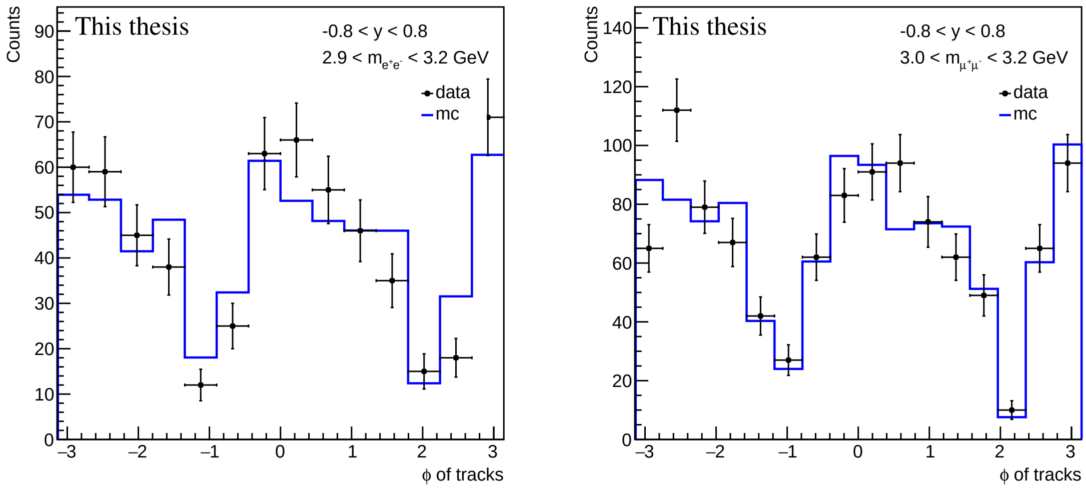

Fig. C.14 Distributions of the azimuthal angle ϕ of the tracks in the dielectron channel (left) and dimuon channel (right).

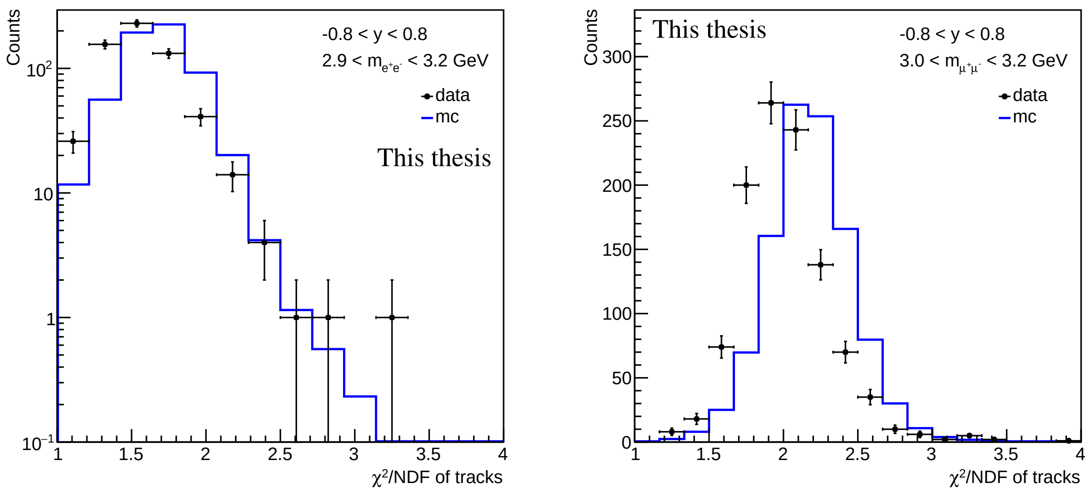

Fig. C.15 Distributions of χ^2/NDF of the tracks in the dielectron channel (left) and dimuon channel (right).

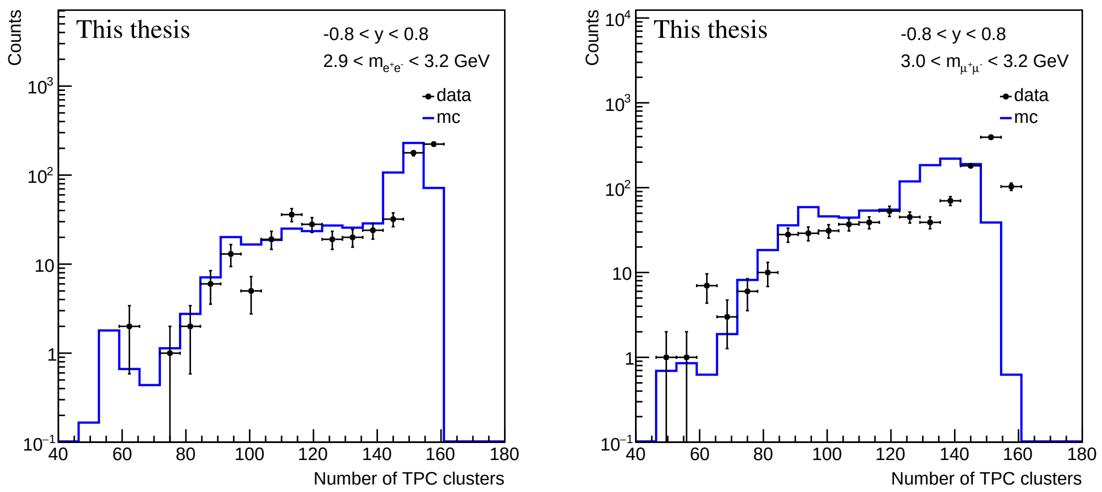

Fig. C.16 Number of space points (clusters) in TPC of the tracks in the dielectron channel (left) and dimuon channel (right).

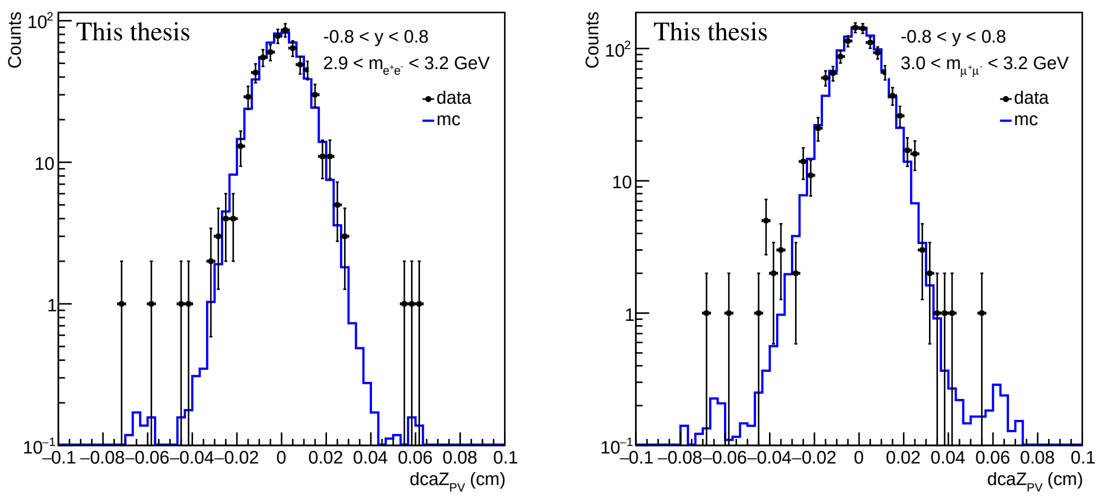

Fig. C.17 DCA of the tracks to the primary vertex along the beam direction in the dielectron channel (left) and dimuon channel (right).

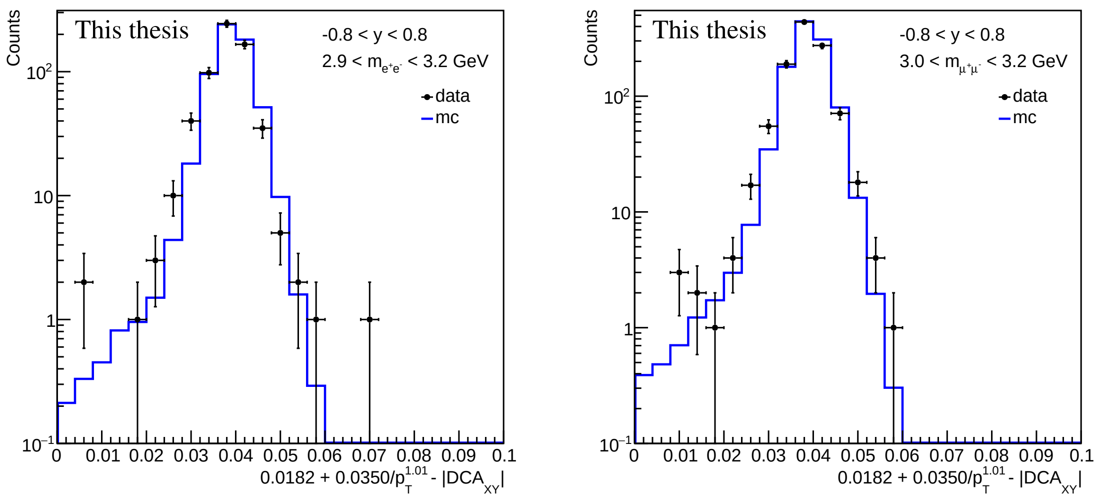

Fig. C.18 Parametrization for the DCA in the transversal direction *xy*. The parametrization is used in requirement **MR-10**. Left for the dielectron channel and right for the dimuon channel.

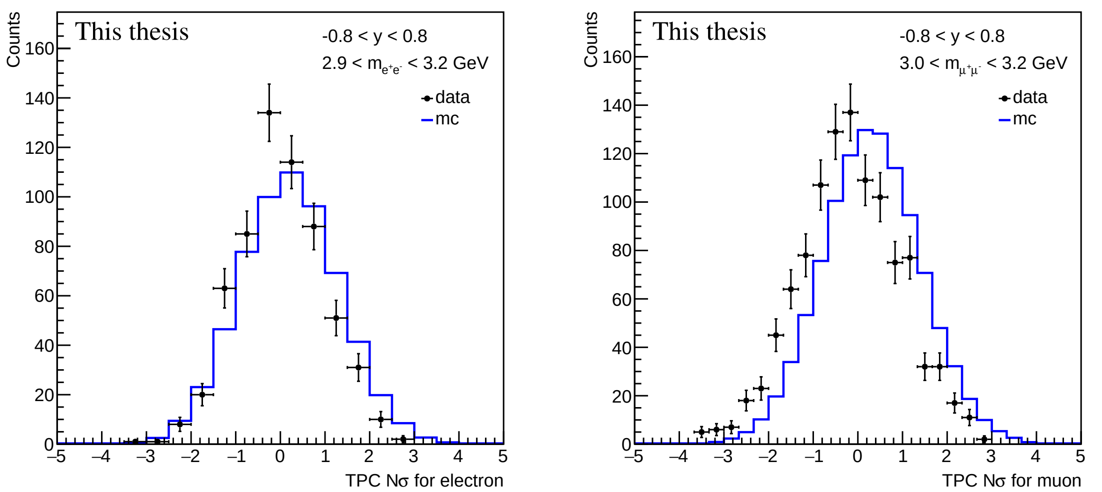

Fig. C.19 Number of standard deviations for dielectron (left) and dimuon (right) hypothesis of Bethe-Bloch expectations for the ionization losses in the TPC.

Appendix D

Supplementary analysis figures

Figures which are supplementary to the presented analyses are given in this appendix.

D.1 Parametric fits to templates of MC and non-exclusive sample

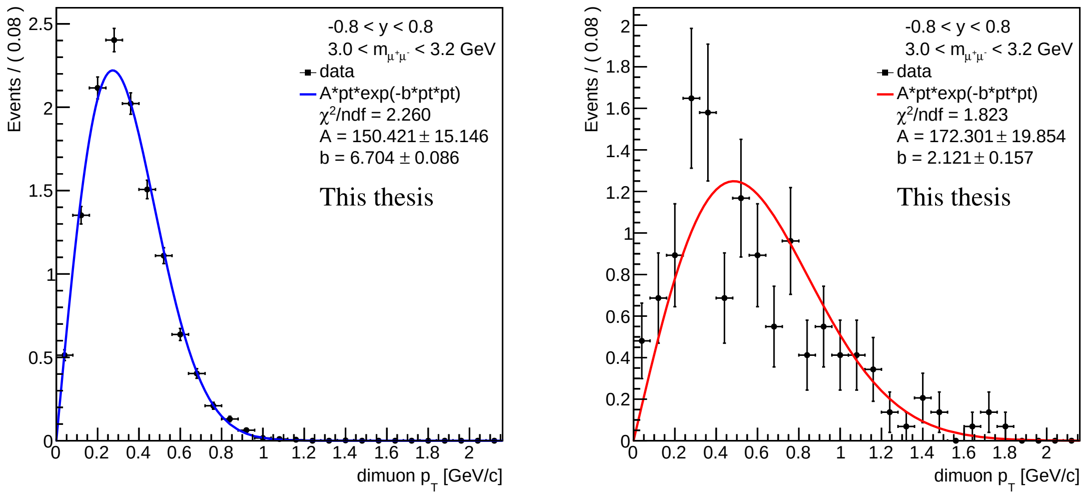

(a) (b)

Fig. D.1 Unbinned maximum likelihood fit by parametrization in Eq. (6.26) to (a) MC simulation of exclusive J/ψ and (b) non-exclusive data sample. Both fits are for the dimuon channel. Corresponding fit in the dielectron channel is shown in Figure 6.19.

D.2 Sample of non-exclusive background at mid-rapidity p-Pb

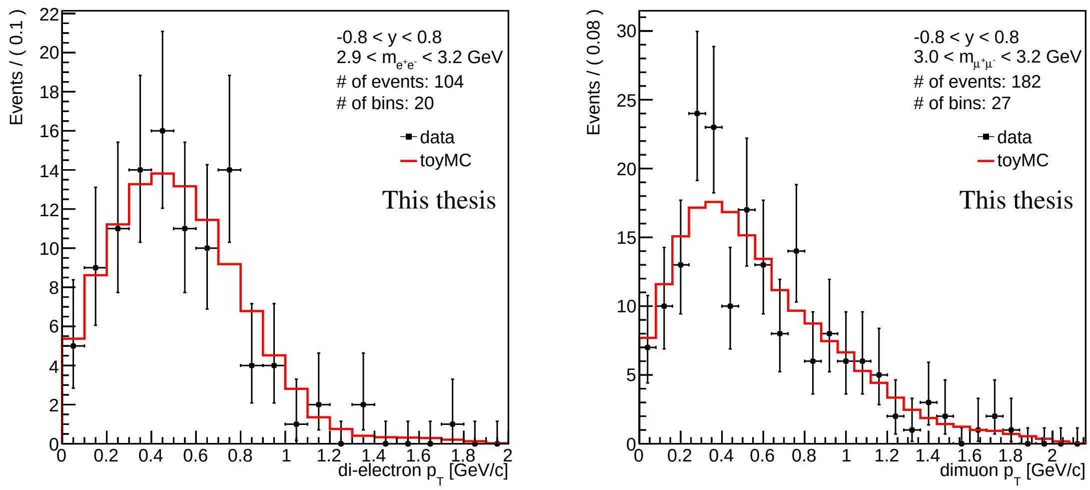

(a) (b)

Fig. D.2 Non-exclusive background and its representation by toy MC at mid-rapidity p-Pb, (a) in the dielectron channel and (b) in the dimuon channel.

D.3 Fits to p_T distribution of J/ψ candidates in the bins of rapidity

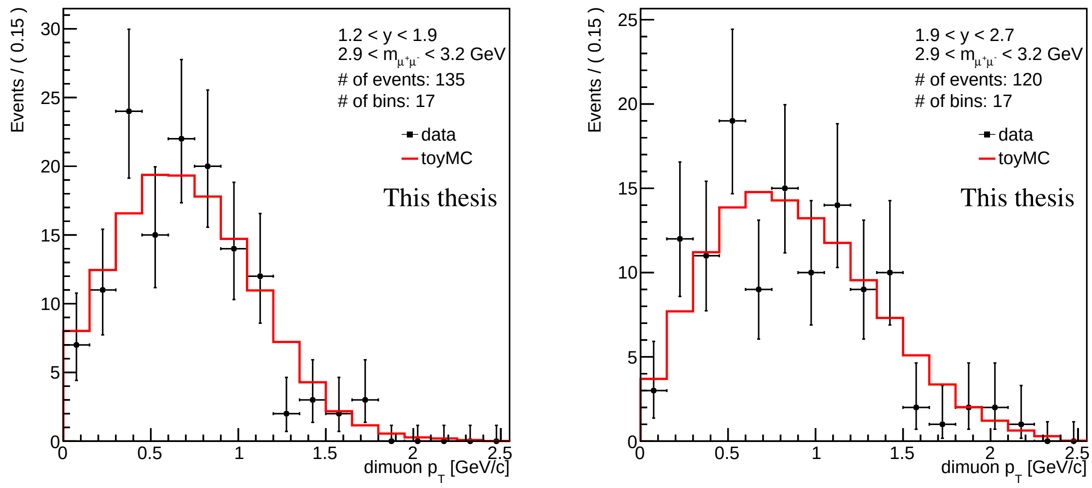

(a) (b)

Fig. D.3 Non-exclusive background and its representation by toy MC in semi-forward p-Pb in two bins of rapidity. The distributions correspond to the full interval shown in Figure 6.16a.

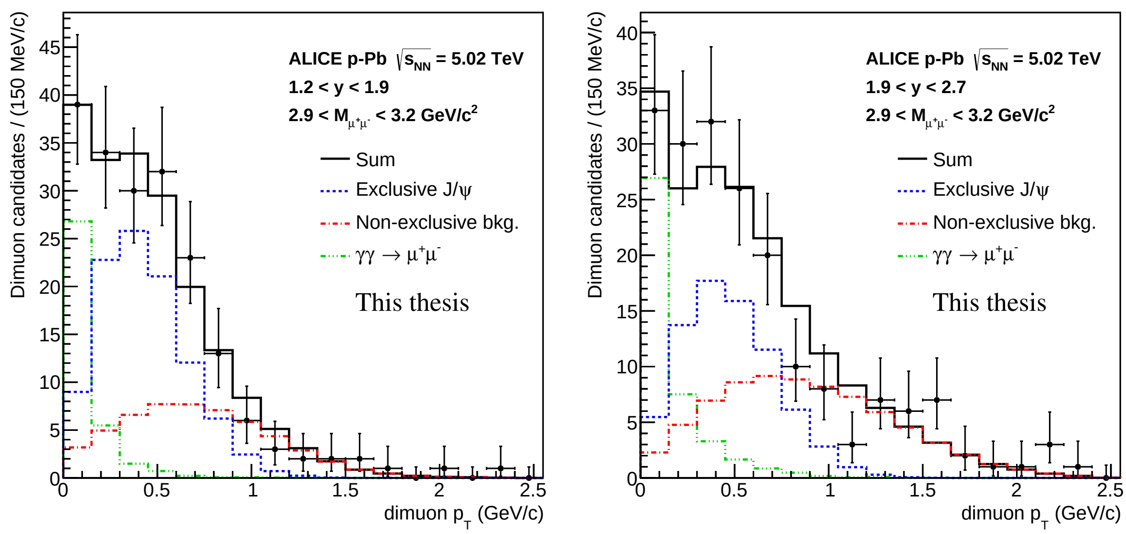

(a) (b)

Fig. D.4 Transverse momentum distribution of J/ψ candidates in semi-forward p-Pb in the bins of rapidity and fit by templates of contributing processes. The parent distribution over the full interval of semi-forward p-Pb is given in Figure 6.17a.

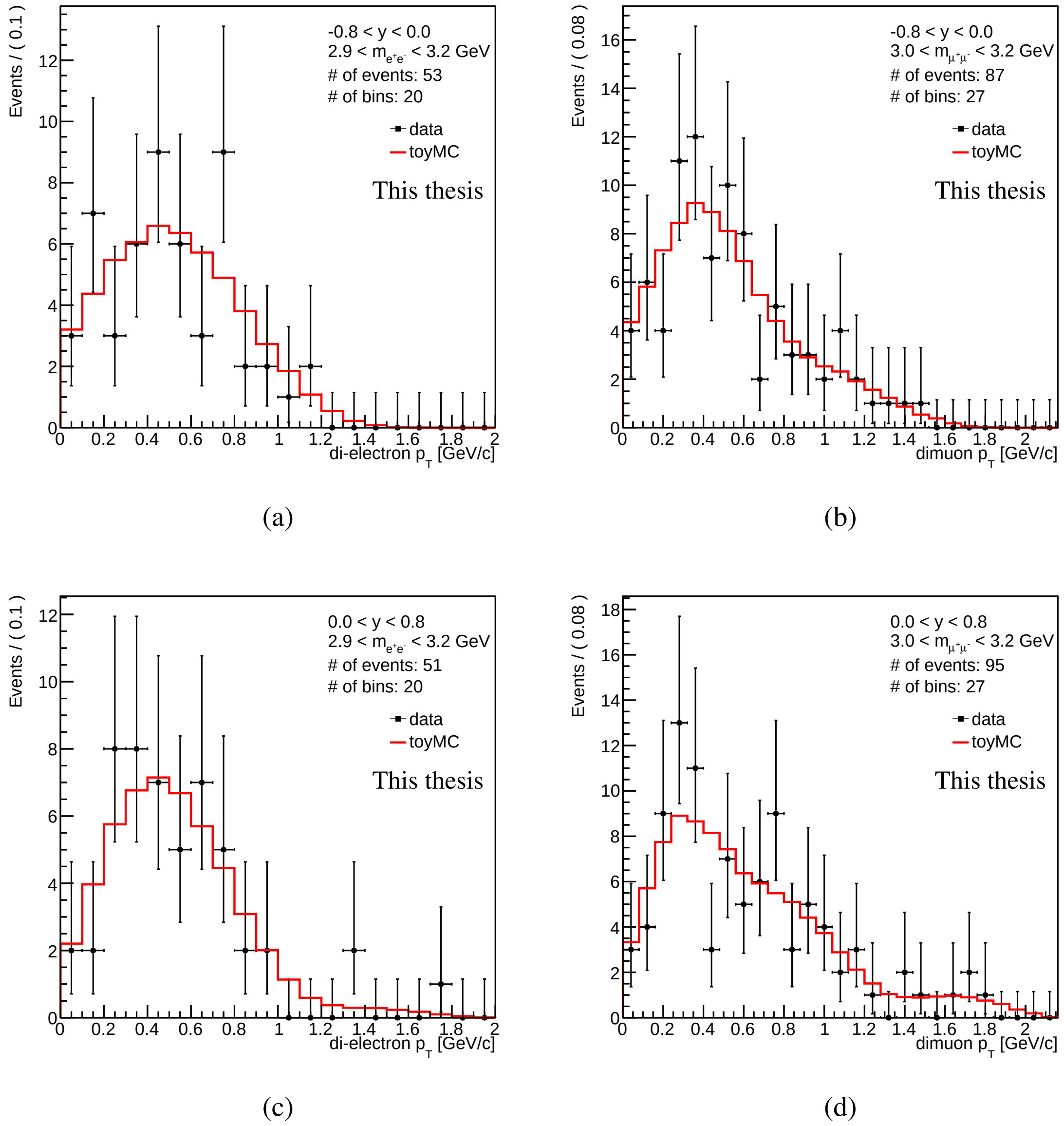

Fig. D.5 Non-exclusive background and its representation by toy MC at mid-rapidity in the bins of rapidity. Corresponding plots in the full interval are shown in Figure D.2.

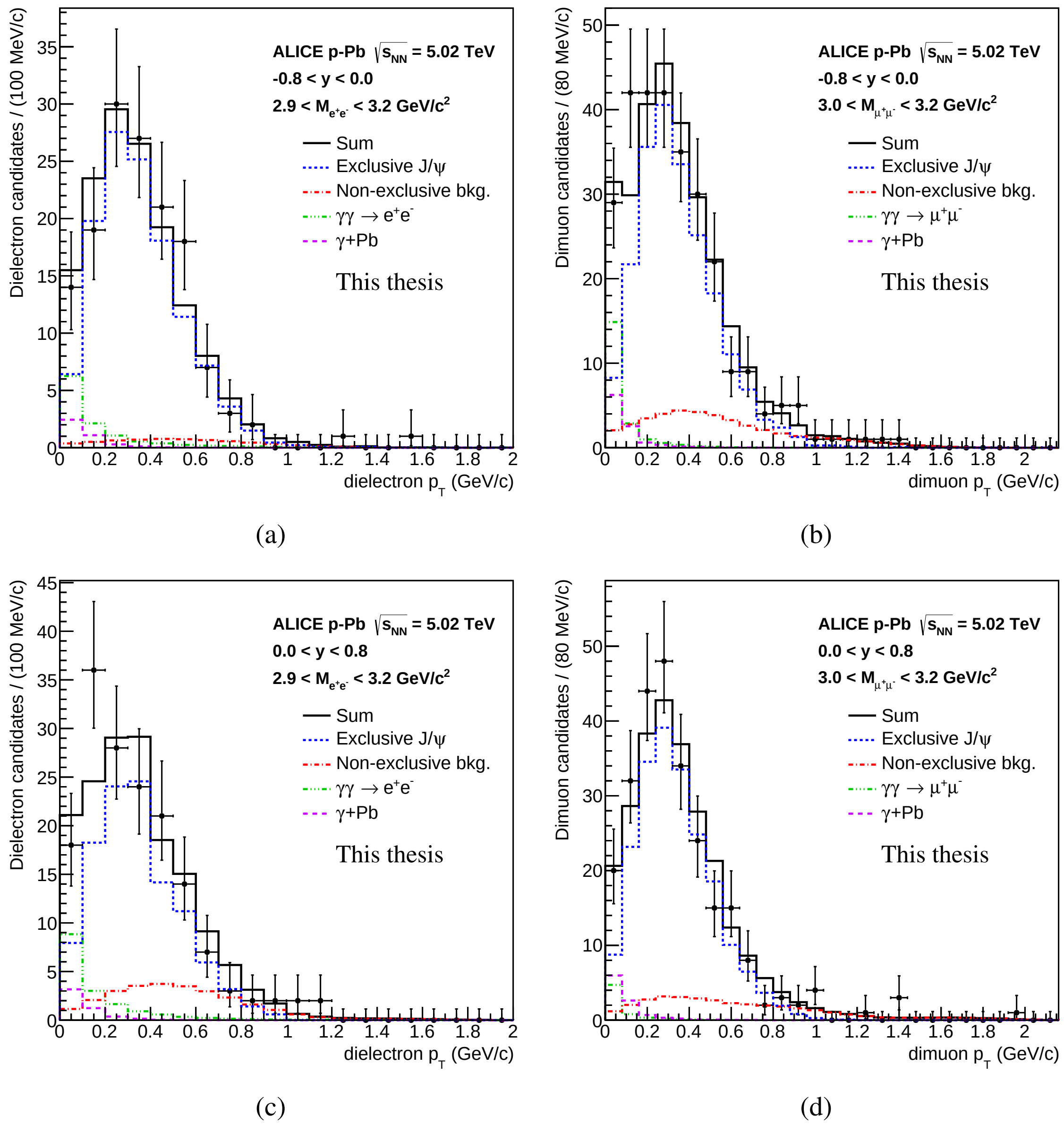

Fig. D.6 Distribution of transverse momentum of J/ψ candidates at mid-rapidity in the bins of rapidity and fit by templates of contributing processes. Corresponding fits over full mid-rapidity interval are shown in Figure 6.20.

Appendix E

List of publications

The measurements presented in this thesis have been reported in the following publications:

A) Publications in international scientific journals.

Already published:

[1] **ALICE** Collaboration, B. Abelev *et al.*, "Coherent J/ψ photoproduction in ultra-peripheral Pb-Pb collisions at $\sqrt{s_{\mathrm{NN}}}$ = 2.76 TeV," *Physics Letters B* **718** no. 4–5, (2013) 1273–1283. http://www.sciencedirect.com/science/article/pii/S0370269312012257.

[2] **ALICE** Collaboration, B. Abelev *et al.*, "Exclusive J/ψ photoproduction off protons in ultra-peripheral p-Pb collisions at $\sqrt{s_{\mathrm{NN}}}$ = 5.02 TeV," *Phys. Rev. Lett.*, **113** (Dec, 2014) 232504. http://link.aps.org/doi/10.1103/PhysRevLett.113.232504.

In preparation (draft being discussed within the Collaboration):

[3] **ALICE** Collaboration, "Energy dependence of exclusive J/ψ photoproduction off protons from p-Pb ultra-peripheral collisions at $\sqrt{s_{\mathrm{NN}}}$ = 5.02 TeV."

B) Proceedings from international meetings.

[4] J. Adam, "Coherent J/ψ photoproduction with the ALICE experiment at the LHC," *J. Phys. Conf. Ser.*, **446** (2013) 012058.

[5] J. Adam, "J/ψ photoproduction in ultra-peripheral Pb-Pb and p-Pb collisions with the ALICE detector," *EPJ Web Conf.*, **71** (2014) 00002.

[6] J. Adam, "J/ψ photoproduction in ultra-peripheral Pb-Pb and p-Pb collisions with the ALICE detector," *To be published in Nuclear Physics B Proceedings Supplement*.

[7] J. Adam, "ALICE results on ultra-peripheral p-Pb and Pb-Pb collisions," *PoS*, **DIS2015** (2015) 060.

[8] J. Adam, “Vector meson photoproduction in ultra-peripheral p-Pb collisions measured using the ALICE detector,” *To be published in Proceedings of Science.*

C) Internal Analysis Notes of the ALICE Collaboration.

[9] J. Adam *et al.*, “Analysis note on: Coherent J/ψ photoproduction in ultra-peripheral Pb-Pb collisions at $\sqrt{s_{\rm NN}}$ = 2.76 TeV,” ALICE analysis note. https://aliceinfo.cern.ch/Notes/node/138.

[10] J. Adam *et al.* “Analysis note on: Photoproduction of J/ψ vector mesons in ultra-peripheral p-Pb collisions at $\sqrt{s_{\rm NN}}$ = 5.02 TeV,” ALICE analysis note. https://aliceinfo.cern.ch/Notes/node/344.

[11] J. Adam *et al.*, “Analysis note on: Semi-forward exclusive J/ψ photoproduction off protons in ultra-peripheral p-Pb collisions at $\sqrt{s_{\rm NN}}$ = 5.02 TeV,” ALICE analysis note. https://aliceinfo.cern.ch/Notes/node/366.

[12] J. Adam *et al.* “Analysis note on: Mid-rapidity exclusive J/ψ photoproduction off protons in ultra-peripheral p-Pb collisions at $\sqrt{s_{\rm NN}}$ = 5.02 TeV,” ALICE analysis note. https://aliceinfo.cern.ch/Notes/node/459.